OUKA
The University of Osaka
Institutional Knowledge Archive

Title	Gas-flow-directed synthesis of long carbon nanotubes for network formation and carrier transport analysis
Author(s)	劉, 元嘉
Citation	大阪大学, 2026, 博士論文
Version Type	VoR
URL	https://doi.org/10.18910/105434
rights	
Note	

The University of Osaka Institutional Knowledge Archive : OUKA

https://ir.library.osaka-u.ac.jp/

The University of Osaka

Doctoral Dissertation

Gas-flow-directed synthesis of long carbon nanotubes for network formation and carrier transport analysis

Liu Yuanjia

December 2025

Graduate School of Engineering,

The University of Osaka

Abstract

Carbon nanotubes (CNTs) are one-dimensional nanomaterials with exceptional electrical, thermal, and mechanical properties, making them promising candidates for next-generation electronic devices. Among various synthesis methods, gas-flow-directed growth—a flow-directed approach characterized by tip growth influenced by buoyant gas flow forces—has gained increasing attention. This mechanism enables CNTs to extend into high laminar flow regions, promoting the formation of long, air-suspended structures that are particularly advantageous for electronic applications. This dissertation presents a comprehensive investigation into the gas-flow-directed growth of CNTs, covering catalyst-free synthesis, network morphology control, and substrate-dependent transport characterization. The results offer new insights into the fundamental mechanisms of gas-flow-directed growth and demonstrate its potential for scalable fabrication of high-performance CNT-based devices.

In the first study, a catalyst-free gas-flow-directed growth strategy is developed using nanodiamond particles as nonmetallic seeds. CNTs are synthesized using ethanol chemical vapor deposition (CVD), guided by laminar gas flow on SiO_2/Si substrates. The absence of metal catalysts prevents undesired contamination, while enabling the direct integration of CNTs into devices. Structural characterization by scanning electron microscopy (SEM), atomic force microscopy (AFM), and Raman spectroscopy confirms high alignment and crystallinity. The nature of CNT tips is evaluated via secondary electron yield contrast between carbon and metal, and AFM is used to verify nanoparticle presence. This method provides a clean and effective route to aligned CNTs suitable for electronic applications.

The second part focuses on understanding the complex interaction between gas-flow-directed growth and vibrational bridging mechanisms in pillar-assisted growth of CNT networks. When CNTs are grown in confined geometries such as between micropillars, the synthesis process is influenced not only by gas flow direction but also by thermally induced vibrations. To elucidate this behavior, systematically designed pillar arrays are used to study the crossover between the two mechanisms. It is found that the relative

contribution of gas-flow-directed growth and vibrational bridging depends strongly on the pillar spacing, CNT length, and local growth conditions. In previous studies, the bridging behavior was modeled using simplified power-law fitting, which limited predictive accuracy for non-ideal geometries. To overcome this, a complete geometric model is derived to describe CNT vibrations and anchoring under various pillar configurations. The model significantly enhances control over CNT network morphology, and experimental validation confirms its applicability across various pillar layouts.

The third study aims to exploit long CNTs grown by gas-flow-directed growth to investigate the role of substrate environments in regulating electronic transport. To isolate substrate effects from intrinsic variability among CNTs, devices are fabricated in which a single, continuous CNT spans both SiO_2 and hexagonal boron nitride (hBN) regions. This cross-substrate configuration enables direct, within-tube comparison under identical structural and electronic conditions. Electrical measurements show that, while the thermally activated transport behavior and activation energies are comparable on the two substrates, the CNT consistently exhibits higher field-effect mobility on hBN. This mobility enhancement is attributed to the cleaner dielectric environment provided by hBN, including its atomically flat surface, low density of charge impurities. The results provide quantitative evidence that substrate selection alone can substantially enhance CNT transport, underscoring substrate engineering as a key strategy for advancing high-performance CNT electronics.

In conclusion, this dissertation provides an integrated investigation of CNT synthesis and device application via the gas-flow-directed growth mechanism. The findings offer: A new catalyst-free approach using nanodiamond seeds for clean, aligned CNT growth; A comprehensive model explaining the crossover between gas-flow-directed growth and vibrational bridging in network formation; A transfer-free device platform for investigating environment-sensitive transport behavior in single CNTs. These results not only enhance the fundamental understanding of gas-flow-directed growth mechanisms but also support its potential in scalable and clean integration of CNTs into future nanoelectronic devices.

Table of Contents

Chapter 1. Introduction 1

1.1 Introduction of carbon nanotube 1

1.1.1 Structure of CNT 2

1.1.2 Properties of CNT 7

1.1.3 Synthesis of CNT 10

1.2 Growth mechanism of CNT 13

1.2.1 Chemical vapor deposition 13

1.2.2 Catalyst vs. catalyst-free 16

1.2.3 Morphologies of CNT and growth mechanisms of aligned CNT 20

1.3 Gas-flow-directed growth 25

1.3.1 Mechanisms of gas-flow-directed growth 25

1.3.2 Properties of gas-flow-directed growth CNTs 29

1.3.3 Application of gas-flow-directed growth CNTs 34

1.4 Motivation and challenges 36

1.5 Organization of the thesis 38

Chapter 2. Experiments 41

2.1 CNT synthesis: furnace, gas supply and exhaust system 41

2.1.1 Substrate preparation and catalyst/growth seed pretreatment 41

2.1.2 CVD furnace system 42

2.2 Fabrication of electrodes on aligned CNT samples 44

2.3 Characterization techniques 48

2.3.1 Raman spectroscopy 48

2.3.2 Atomic force microscopy 51

2.3.3 Scanning electron microscopy 52

2.3.4 Electrical measurements 55

Chapter 3.

Gas-flow-directed growth of aligned carbon nanotubes from nonmetallic seeds 57

3.1 Background 57

3.2. Experimental section 60

3.2.1. Deposition of ND growth seeds 60

3.2.2. Pretreatment of ND growth seeds 60

3.2.3. Synthesis of aligned CNTs from ND growth seeds 61

3.2.4. Characterization 62

3.3 Temperature and gas flow rate dependence of CNT synthesis 64

3.4 Verification of nonmetallic particles as the origin of CNT growth 70

3.5 Growth-mode determination of CNTs grown from nonmetallic NPs 76

3.6 Crystallinity and diameter analysis of CNTs grown from nonmetallic NPs 83

3.7 Conclusion 87

Chapter 4.

Crossover between gas-flow-directed growth and vibrational bridging in pillar-assisted controlled formation of carbon nanotube networks 88

4.1 Background 88

4.2. Experimental section 91

4.2.1 CNT growth and characterization 91

4.2.2 Finite element method simulations 92

4.3 Gas flow direction dependence and model fitting 93

4.4 Gas flow-induced deflection and vibrations 106

4.5 Statistical analysis of the CNT bridging types 118

4.6 Conclusion 122

Chapter 5.

Substrate-dependent electrical transport in individual single-walled carbon nanotubes grown across SiO_2 and hexagonal boron nitride 123

5.1 Background 123

5.2. Experimental section 126

5.2.1 CNT growth 126

5.2.2 Alignment markers and electrodes fabrication 127

5.2.3 Characterization 127

5.3 Morphology and device overview 129

5.4 Electrical transport on SiO_2 and hBN 132

5.5 Band evolution at metal–CNT contacts under equilibrium and biased conditions 140

5.6 Temperature-dependent transport and activation behavior 147

5.7 Conclusion 155

Chapter 6. Conclusion and future perspective 156

Reference 159

List of publications 194

List of conferences 196

Acknowledgments 198

Chapter 1. Introduction

1.1 Introduction of carbon nanotube

Since 1991, when Iijima first reported the observation of multi-walled carbon nanotubes (MWCNTs) using arc-discharge methods [1], the fascinating structural and physical properties of carbon nanotubes (CNTs) have captured worldwide attention. Shortly afterward, single-walled carbon nanotubes (SWCNTs) were successfully synthesized [2,3], revealing their quasi-one-dimensional nature and extraordinary electronic behavior, where charge carriers can exhibit ballistic transport over micrometer scales. These groundbreaking discoveries immediately positioned CNTs as promising candidates for next-generation nanoelectronic, mechanical, and energy-related applications.

As CNT research advanced, increasing efforts were devoted to tailoring their structural characteristics, including chirality, diameter, and wall number, which critically determine whether a CNT behaves as a metallic or semiconducting material [4–7]. Simultaneously, progress in synthesis methods from arc discharge [1] and laser ablation [8] to chemical vapor deposition (CVD) [9,10] that enabled controlled growth of CNTs with improved alignment and fewer defects [11]. Yet, challenges such as precise chirality control, large-area uniformity, and defect suppression remain unresolved, hindering their scalable integration into practical devices [12,13].

More than two decades ago, gas-flow-directed growth was proposed as an effective strategy to achieve long-range alignment of CNTs [14–20]. Unlike randomly oriented CNT networks, this method enables large-scale ordering, uniform orientation, and minimized junction resistance, which are essential for translating the exceptional intrinsic properties of individual CNTs into macroscopic assemblies. Through gas flow–assisted alignment, CNT arrays can be organized over centimeter-scale dimensions, significantly enhancing their mechanical, electrical, and thermal performance. In recent years,

remarkable progress has been made in applying this technique to fabricate high-performance CNT-based devices, including field-effect transistors, integrated circuits, and wafer-scale aligned arrays, demonstrating its great potential for bridging the gap between fundamental CNT research and practical applications [21–27].

1.1.1 Structure of CNT

CNTs represent a class of one-dimensional (1D) nanomaterials that can be structurally envisioned as rolled-up graphene sheets with seamless cylindrical geometry. To understand their atomic configuration, it is essential to first recall the structure of graphene itself. In a single-layer graphene sheet, carbon atoms are covalently bonded in a two-dimensional (2D) honeycomb lattice through sp^2 hybridization [28], where each carbon atom contributes three in-plane σ bonds forming the hexagonal framework, while the remaining unhybridized p_z orbital extends out of the plane, overlapping with neighboring p_z orbitals to create a delocalized π-electron system. This unique bonding topology endows graphene with its remarkable mechanical strength and exceptional electronic properties, including the massless Dirac fermion behavior near the K and K′ points in its Brillouin zone. Fig. 1.1 schematically illustrates the hybridization of σ and π bonds in graphene, together with its energy dispersion relations and the location of the Dirac points in reciprocal space. At the Fermi level, the valence and conduction bands meet at six points in the Brillouin zone, of which only two are inequivalent, known as the K and K′ points. At these Dirac points, the density of states (DOS) becomes zero, so graphene is often described as a zero-gap semiconductor or a semimetal.

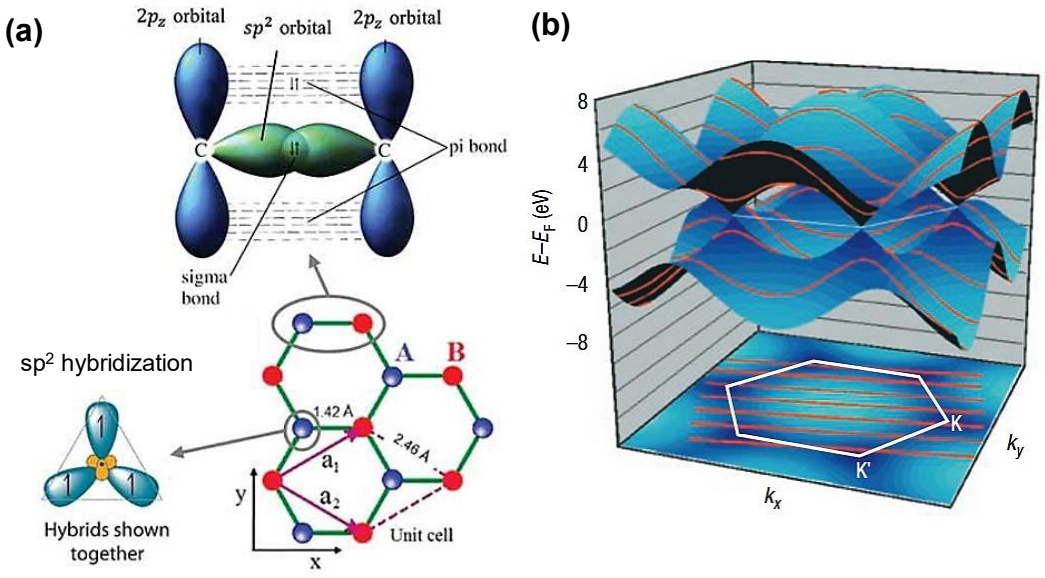


Figure 1.1 (a) Schematic illustration of sp² hybridization in graphene [29]. (b) Schematic illustration of the Brillouin zone and band structure of graphene [30].

When a graphene sheet is conceptually "rolled up" along a specific crystallographic direction defined by the chiral vector $C_h = na_1 + ma_2$, where n and m are integers and a_1, a_2 are graphene's primitive lattice vectors, the open edges of the sheet are seamlessly connected to form a nanotube with diameter d and chiral angle θ. The pair of integers (n, m) uniquely determines the tube's structure, including its diameter, helicity, and most importantly, its electronic properties [4]. Based on the (n,m) indices, CNTs are classified into three canonical types: armchair ($n = m, \theta = 30°$), zigzag ($m = 0, \theta = 0°$), and chiral ($n \neq m, 0° < \theta < 30°$) configurations [31] (Fig. 1.2). This simple yet powerful (n,m) notation not only provides a geometric description but also directly links the real-space atomic structure to the electronic band structure through zone-folding analysis.

The electronic properties of CNTs are determined by their chiral indices (n,m), which define both diameter and chiral angle. A general rule is that when $n - m = 3q$ (q being an integer), the nanotube is metallic; otherwise, it is semiconducting. Due to curvature

effects, however, only armchair ($n = m$) tubes are truly gapless, while other nominally metallic species display a small chirality-dependent bandgap at low temperatures [32]. In semiconducting CNTs, the bandgap scales inversely with diameter and typically lies in the range of 0–2 eV [5], thereby enabling tunable electronic properties. This direct correlation between structure and electronic behavior makes CNTs a distinctive platform for bandgap engineering.

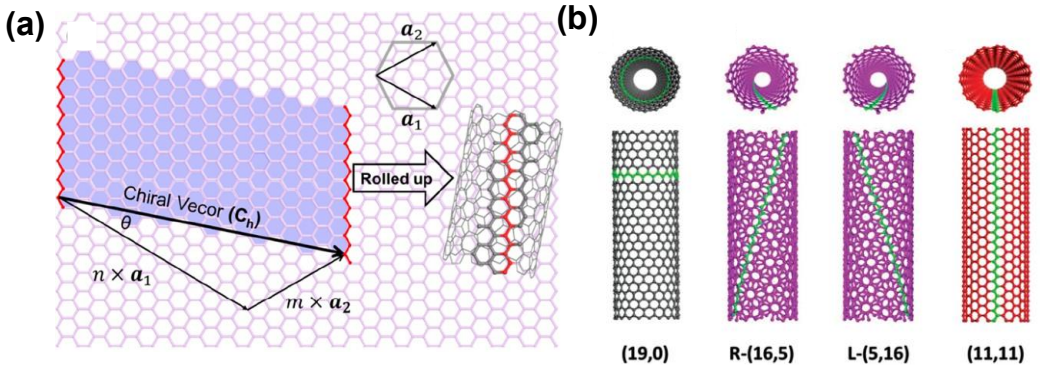


Figure 1.2 (a) A CNT is viewed as rolling a graphene ribbon along chiral vector $\boldsymbol{C_h}$. (b) Examples of CNTs with different chiralities, including zigzag, armchair, and chiral forms.

Fig. 1.3 shows the Brillouin zone and DOS of CNT. In CNTs, the energy dispersion collapses into a set of 1D subbands superimposed on the 2D graphene dispersion. Subbands that pass through the K and K′ points yield metallic behavior, while those that avoid these points produce semiconducting behavior. The DOS of CNTs clearly reflects these electronic characteristics [33]. The optical properties of CNTs arise from their underlying band structure. In these 1D systems, the DOS features pronounced van Hove singularities in both the valence and conduction bands, and optical transitions occur between pairs of these singularities. The corresponding transition energies, denoted as E_{ii} (i = 1, 2, 3…), represent allowed interband transitions with matched symmetry, whereas crossover transitions are dipole-forbidden and therefore very weak. Using a tight-binding approach, Kataura and co-workers calculated E_{ii} for CNTs with diameters in the range of

0.6–1.8 nm, producing what later became known as the Kataura plot [34]. The existence of discrete, diameter-dependent optical transitions makes CNTs highly attractive for optoelectronic applications, with techniques such as Raman and photoluminescence spectroscopy serving as powerful tools for chirality identification and experimental validation of the zone-folding model.

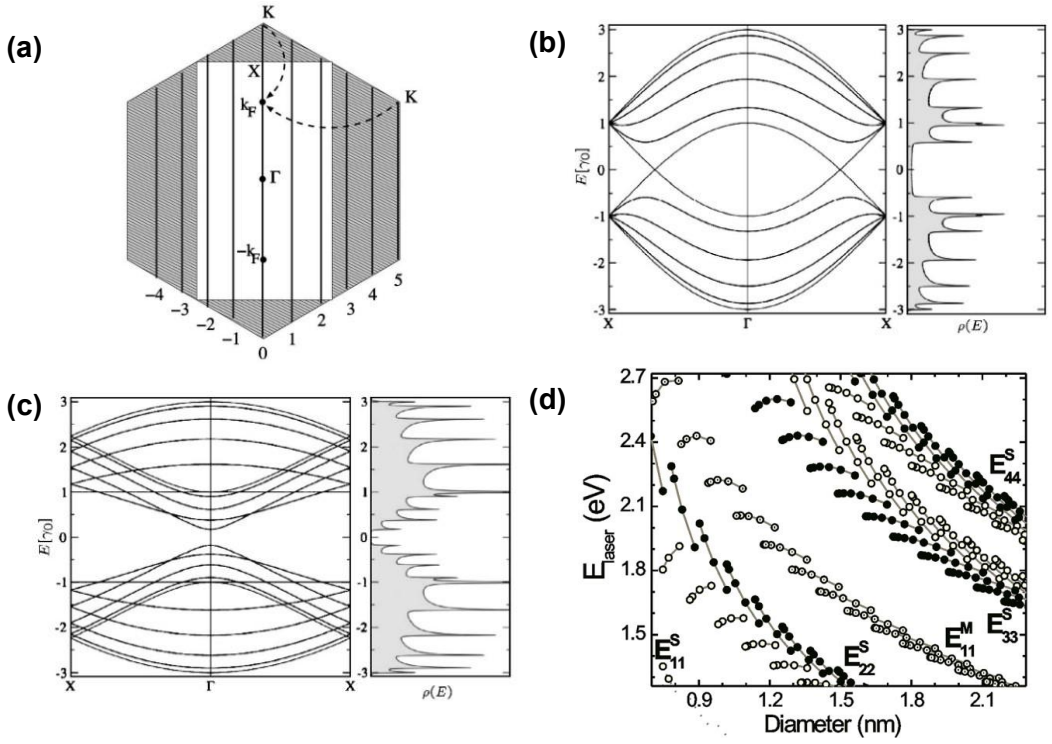


Figure 1.3 (a) Brillouin zone of graphene. The white rectangle is the Brillouin zone associated with the four-atom cell with lattice vectors for an armchair tube. Thick lines are the allowed k lines for the (5,5) armchair tube. (b) Band structure and DOS of a (5, 5) armchair nanotube. (c) Band structure and DOS of a (10,0) zigzag nanotube **[6]**. (d) Kataura plot showing optical transition energies as a function of nanotube diameter **[35]**.

In terms of morphology, CNTs can be broadly divided into two categories: single-walled SWCNTs and MWCNTs. SWCNTs consist of a single graphene cylinder with typical diameters ranging from 0.6 to 1.8 nm and lengths up to several millimeters under

optimized growth conditions. Their atomically thin structure offers well-defined electronic properties highly sensitive to chirality, making them ideal model systems for fundamental studies of quantum transport, mechanical resonance, and thermal conduction [6,36]. In contrast, MWCNTs comprise multiple concentric graphene cylinders with interlayer spacing close to that of graphite (~0.34 nm) [37], as depicted in Fig. 1.4. The outer shells of MWCNTs often dominate the electrical conduction due to screening effects, while the inner shells contribute to mechanical reinforcement and thermal transport. Transmission electron microscopy (TEM) images reveal their characteristic coaxial morphology, providing direct structural evidence for their multi-layered architecture.

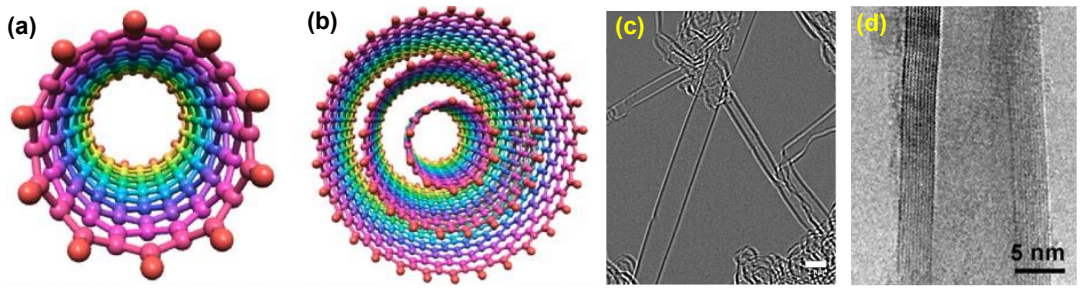


Figure 1.4 (a) Model structure of an SWCNT. (b) Model structure of an MWCNT **[38]**. (c) TEM image of an SWCNT **[39]**. (d) TEM image of an MWCNT **[40]**.

Another important structural aspect is the defect density and functionalization of CNT sidewalls. Perfect CNTs ideally consist of only hexagonal carbon rings; however, during synthesis or post-growth processing, topological defects such as pentagon–heptagon pairs (Stone–Wales defects) or vacancies may be introduced. These defects locally modify the electronic structure, scatter charge carriers and phonons, and thus deteriorate the exceptional transport properties of pristine CNTs [6,41–43]. On the other hand, controlled chemical functionalization enables the attachment of various molecular groups to CNT sidewalls, expanding their utility in sensing, catalysis, and composite materials while simultaneously altering their electronic and optical characteristics [44].

Finally, the alignment and bundle formation of CNTs deserve special mention. In solution or during growth, van der Waals interactions often drive individual CNTs to assemble into bundles or "ropes," modifying their effective band structure through inter-tube coupling [8,45]. Conversely, techniques such as gas-flow-directed growth and templated assembly on nanostructured substrates can produce highly aligned CNT arrays with uniform orientation and spacing [46,47]. Such structural control at both the single-tube and ensemble levels is crucial for integrating CNTs into scalable electronic and photonic devices, as random networks typically suffer from uncontrolled junction resistance and device-to-device variability [48].

In summary, the structure of CNTs encompasses multiple hierarchical levels, from atomic bonding and chirality to wall number, defect topology, and ensemble organization. Each level profoundly influences their electronic, mechanical, and thermal properties, establishing a direct link between synthesis, structure, and functionality. The following sections will further elaborate on how these structural features translate into the remarkable properties and diverse synthesis strategies of CNTs.

1.1.2 Properties of CNT

Having introduced the atomic structure, chirality, and electronic band characteristics of CNTs, it is important to highlight how these structural features translate into their remarkable physical properties. The exceptional properties of CNTs originate from their unique one-dimensional structure, strong sp^2 carbon–carbon bonding, and quantum confinement effects. These properties can be generally divided into several categories, including mechanical, electrical, thermal, surface-related, and energy-related characteristics, each providing distinct advantages for various technological applications as shown in Fig. 1.5 [49–51].

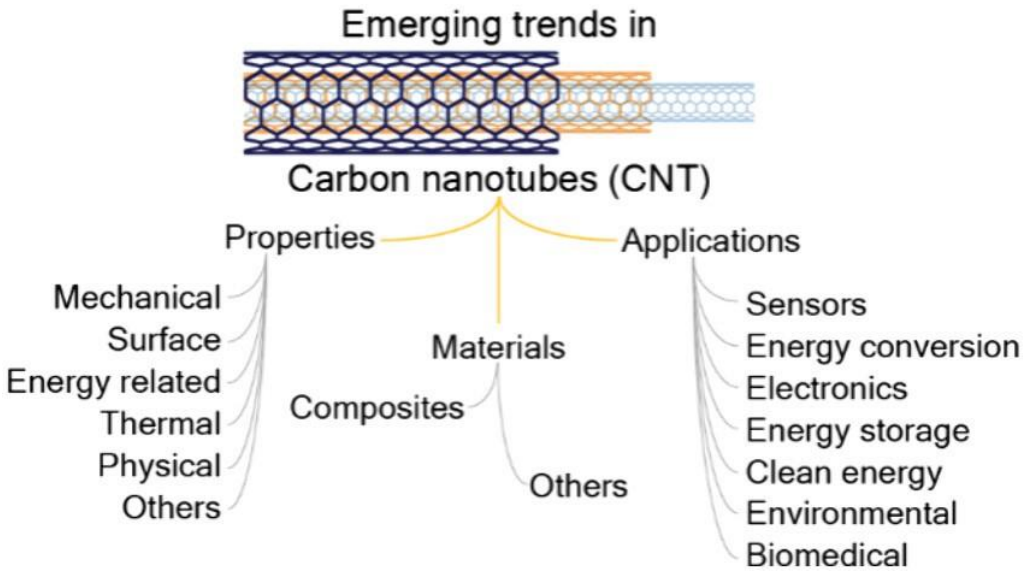


Figure 1.5 Overview of the diverse properties of CNTs and their corresponding application areas **[51]**.

Mechanically, CNTs are among the strongest and stiffest materials known, with Young's modulus reaching up to 1 TPa for individual SWCNTs [52,53]. These values are nearly an order of magnitude higher than those of high-strength steels while maintaining an ultralow density of about 1.3–1.4 g cm^{-3}, leading to a specific strength far surpassing conventional engineering materials [54]. The exceptional mechanical robustness originates from the strong in-plane σ bonds of sp^2 carbon and the seamless cylindrical geometry that minimizes stress concentration points. Moreover, CNTs exhibit remarkable flexibility and resilience, allowing them to sustain large elastic deformations without fracturing [55]. This unique combination of high strength, low density, and flexibility has led to widespread research on CNT-reinforced composites for aerospace, automotive, and structural applications where weight reduction and mechanical reliability are critical [56].

Electrically, CNTs display highly tunable behavior depending on their chirality and diameter. Metallic CNTs can sustain current densities on the order of 10^9–10^{10} A/cm^2, far exceeding those of conventional metals such as copper [57]. Due to minimal scattering and possible ballistic transport over micrometer distances at room temperature, CNTs

offer exceptionally high conductance [58]. Semiconducting SWCNTs with diameters in the range of 1–2 nm often exhibit direct bandgaps of ~0.4–1 eV; in ideal conditions their carriers may achieve mobilities on the order of 10^4–10^5 $cm^2/V \cdot s$ [59], though experimentally observed values are often somewhat lower, depending on purity, contact quality, and scattering.

In terms of thermal properties, CNTs exhibit ultrahigh thermal conductivity, with reported values up to 3000–6000 W/mK for individual SWCNTs [60,61], approaching or even exceeding that of diamond. This outstanding thermal transport behavior arises from strong covalent bonding and long phonon mean free paths along the tube axis, enabling efficient heat dissipation in nanoscale electronics and optoelectronics. Moreover, CNTs maintain excellent thermal stability in vacuum or inert environments up to approximately 2000–3000 K [62], far beyond the thermal limits of most metals and polymers. This combination of high thermal conductivity and temperature resilience makes CNTs promising for thermal interface materials, heat spreaders, and energy conversion devices where both efficient heat transport and high-temperature stability are required [63].

CNTs possess versatile surface and chemical characteristics arising from their high aspect ratio, large specific surface area, and chemically inert sp^2 carbon framework. Their sidewalls can be functionalized or doped to tailor dispersibility, electronic structure, and surface reactivity, enabling applications in sensing, catalysis, and energy systems [64,65]. These same features, combined with high electrical and thermal conductivities, support CNT use in electrochemical storage, photocatalysis, thermoelectrics, and hybrid energy-conversion devices. As a result, CNTs have been incorporated into technologies ranging from gas and biosensors to batteries, supercapacitors, solar cells, clean-energy catalysts, and biomedical platforms such as drug delivery and tissue engineering [66–68].

This rich interplay between the structure, properties, and applications of CNTs highlights the importance of precise synthesis control and property tailoring, topics that

will be discussed in the next section on growth methods and challenges.

1.1.3 Synthesis of CNT

Since the discovery of CNTs, various synthesis methods have been developed to obtain CNTs with controlled morphology, structure, and properties. These methods differ significantly in terms of growth mechanism, synthesis temperature, carbon source, and catalyst requirements. The most common techniques include the arc discharge method, laser ablation, CVD and its variants, template-assisted growth, and some physical or chemical treatments such as ball milling combined with annealing (Fig. 1.6) [11,38]. Each of these approaches has played a crucial role in advancing CNT research and enabling specific applications, yet they also face challenges in terms of scalability, structural control, and defect minimization.

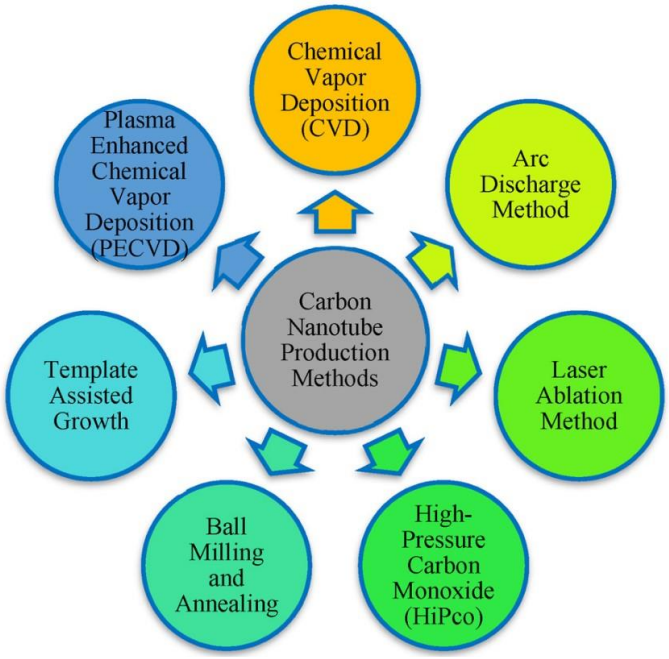


Figure 1.6 Various techniques for synthesizing CNTs **[38]**.

The arc discharge method was the earliest technique used to produce CNTs, dating back to Iijima's original work in 1991 [1]. In this method, a high-current arc is struck between two graphite electrodes in an inert atmosphere, typically helium or argon, leading to the evaporation of carbon atoms that subsequently condense to form CNTs. Arc discharge can produce high-quality MWCNTs with few structural defects, while SWCNTs can be obtained by incorporating metal catalysts such as iron, cobalt, or nickel into the electrodes [69–71]. However, the limited control over alignment, diameter, and chirality restricts its applicability for large-scale electronic or optoelectronic devices where uniformity is critical [72].

The laser ablation method, developed shortly after the arc discharge approach, employs a high-power pulsed laser to vaporize a graphite target containing transition metal catalysts in a high-temperature furnace [73,8]. The carbon vapor then condenses on a cooler substrate to form CNTs. Laser ablation typically produces high-quality SWCNTs with relatively narrow diameter distributions compared to arc discharge. The process allows for certain control over tube diameter by adjusting the furnace temperature and catalyst composition. Nevertheless, the high equipment cost, energy consumption, and relatively low yield hinder its large-scale industrial deployment [74].

Template-assisted growth offers a controllable strategy for preparing carbon nanotubes with defined dimensions [75,76]. In this method, porous materials such as anodic aluminum oxide membranes or mesoporous silica are employed as templates. Their nanoscale channels confine carbon deposition during CVD and guide the formation of tubular structures. This approach enables partial control over the diameter and length of CNTs, and it can also support the formation of ordered arrays when the template architecture is well defined. These features make template-assisted growth attractive for applications that rely on regular pore structures, including nanofluidics, sensing, and energy-related systems. However, template removal often requires chemical etching, which may introduce residues or structural imperfections. In addition, the crystallinity

and purity of the resulting CNTs are sometimes lower than those obtained from established gas-phase growth methods, and most reported CNTs are multiwalled rather than single-walled [77].

Physical treatments such as high-energy ball milling followed by high-temperature annealing offer a low-cost route to CNT–like structures. In this approach, graphite powder is first mechanically milled to induce severe deformation and amorphization; subsequent annealing under inert gasat high temperature can lead to the formation of tube-like carbon structures. Several studies have reported the formation of multiwalled nanotubes with diameters in the range of ~50–200 nm and lengths on the order of micrometers [78,79]. This method is suitable for bulk powder production because it uses inexpensive graphite as precursor and common milling / annealing equipment. However, the produced tubes often exhibit considerable structural defects, non-uniform wall thickness, and mixed morphologies, which limit their performance in applications requiring high crystallinity, purity, or precise structure control.

Chemical vapor deposition (CVD) and its variants have become the most widely adopted methods for synthesizing carbon nanotubes due to their versatility and scalability. In a typical process, a carbon-containing precursor such as methane, ethylene, or ethanol is decomposed at elevated temperatures, usually between 600 and 1000 °C, in the presence of transition-metal nanoparticles supported on substrates such as silicon, quartz, or alumina [10,80–85]. These catalyst particles initiate the nucleation and guide the subsequent growth of nanotubes. CVD offers several advantages, including relatively low synthesis temperatures compared with arc-based methods, compatibility with lithographic patterning, and the capability to grow vertically aligned arrays or horizontally aligned tubes over large areas. Control over parameters such as catalyst size, precursor concentration, gas flow rate, and growth temperature enables adjustment of tube diameter, length, and areal density. However, precise control over chirality remains

challenging, and the quality of the resulting CNTs depends strongly on catalyst stability and process conditions [86].

Given its scalability, compatibility with microfabrication, and potential for alignment control, CVD has become the dominant technique for both fundamental research and industrial-scale production of CNTs. The next section will therefore focus on the growth mechanisms of CNTs using CVD, including the roles of catalysts, substrates, and growth parameters, as well as the specific challenges in achieving aligned, defect-free CNTs for electronic and optoelectronic applications.

1.2 Growth mechanism of CNT

1.2.1 Chemical vapor deposition

CVD has become the most widely used method for the synthesis of CNTs because of its scalability, controllability, and compatibility with microfabrication techniques. The fundamental principle of CVD involves the decomposition of a carbon-containing precursor gas at elevated temperatures in the presence of a transition metal catalyst, leading to the nucleation and growth of CNTs directly on a solid substrate. The schematic diagram in Fig. 1.7 illustrates the basic components of a typical CVD system, including the hydrocarbon source, inert carrier gas, gas mixer, heating zone with catalyst substrate, and downstream exhaust analysis.

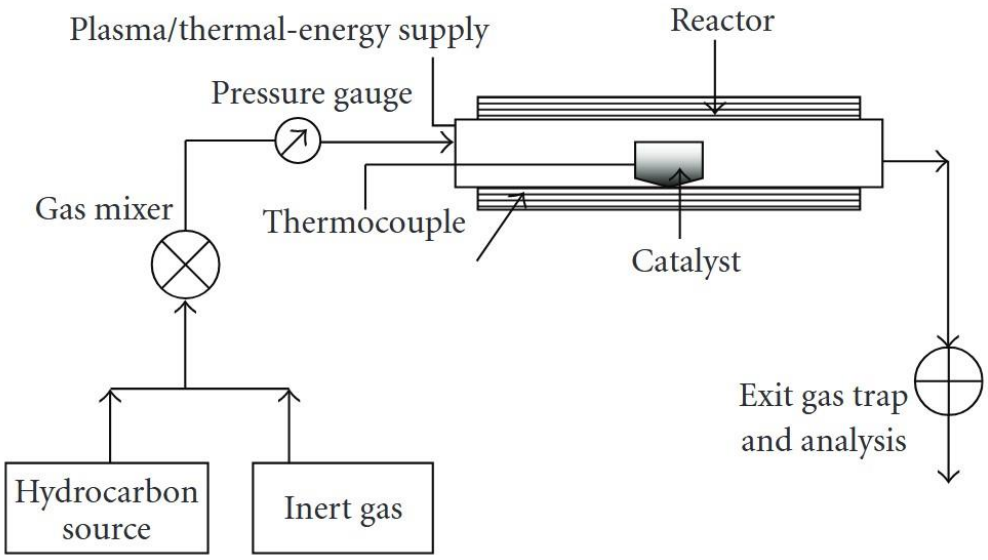


Figure 1.7 Schematic diagram of a CVD process for CNT synthesis **[87]**.

In a standard thermal CVD process, a hydrocarbon gas such as methane, acetylene, ethylene, or ethanol is introduced into a reaction chamber along with an inert carrier gas such as argon, nitrogen, or hydrogen [10,88–90]. The mixture flows over a substrate coated with nanoscale metal catalyst particles, typically Fe, Co, or Cu [15,18,91], supported on materials such as SiO_2, Al_2O_3, or MgO [92,93]. When the system is heated to growth temperatures in the range of 600–1000 °C, the hydrocarbon molecules decompose on the catalyst surface, releasing carbon atoms that dissolve into the catalyst nanoparticles. Upon reaching supersaturation, carbon atoms precipitate from the catalyst–substrate interface or from the catalyst top surface, depending on the adhesion between the catalyst particle and the substrate. The diameter of the resulting CNTs is largely determined by the size of the catalyst nanoparticles, while the growth rate and length are controlled by factors such as hydrocarbon flow rate, reaction temperature, and growth duration [86].

Beyond conventional thermal CVD, several variants have been developed to address specific challenges or improve control over CNT growth. plasma-enhanced CVD

(PECVD) introduces a plasma source to generate highly reactive radicals from the precursor gases at lower substrate temperatures, typically below 600 °C [94–96]. The electric field in PECVD systems can also align CNTs vertically, producing dense forests of aligned CNTs with uniform orientation. This is particularly advantageous for field emission devices, sensors, and interconnect applications where vertical alignment and low-temperature growth on temperature-sensitive substrates are required.

Another modification is alcohol catalytic CVD (ACCVD), which uses ethanol or other alcohols as carbon precursors [88,97–100]. Alcohol molecules decompose to produce not only carbon radicals but also hydroxyl species, which can selectively remove amorphous carbon from the catalyst surface, thereby prolonging the catalyst lifetime and improving CNT crystallinity. This self-cleaning effect enables the growth of high-quality SWCNTs with fewer defects, making ACCVD a preferred method for fundamental studies of electronic and optical properties.

Water-assisted CVD, also known as “supergrowth CVD,” introduces a small amount of water vapor into the reaction chamber along with hydrocarbon gases [84,101–103]. The water molecules continuously etch amorphous carbon from the catalyst surface, maintaining its activity for extended growth periods. This technique has enabled the synthesis of millimeter-scale vertically aligned CNT arrays with ultrahigh growth rates exceeding several micrometers per second. Such CNT forests have been used for mechanical reinforcement, thermal interface materials, and large-scale energy storage electrodes.

Catalyst-free CVD methods have also been explored to avoid metal contamination that can degrade the electronic properties of CNTs. These approaches often rely on substrates with inherent catalytic activity, such as certain crystalline carbides or nitrides, or employ high-temperature decomposition of hydrocarbons in confined geometries [104–107]. However, achieving uniform, high-quality CNT growth without catalysts

remains challenging, and such methods are less developed compared to catalyst-assisted CVD.

After reviewing various CVD variants, a common theme emerges: nearly all successful CNT syntheses rely on the presence of a catalyst. The catalyst particle plays a central role not only in decomposing the carbon precursor, but also in mediating carbon dissolution, precipitation, and the initial nucleation of tubular graphene layers. The choice of catalyst material, its particle size and dispersion, and interaction with the substrate or support strongly influence the nanotube's diameter, wall number, crystallinity, growth rate and overall yield [108]. Nevertheless, the reliance on transition-metal catalysts raises persistent concerns. Residual metal impurities may impair the intrinsic electronic, optical, or chemical properties of CNTs, and often necessitate post-growth purification steps. This is a particular issue when CNTs are intended for high-performance electronic, optoelectronic or biomedical applications. Understanding these limitations motivates research into alternative routes. Accordingly, the next section will examine the contrast between conventional catalyst-assisted CVD and emerging catalyst-free CVD approaches, exploring their respective mechanisms, advantages, and current challenges.

1.2.2 Catalyst vs. catalyst-free

In CVD, CNT growth can be organized by the physical state/location of the active particle and by whether a metal catalyst is present. For metal-catalyzed growth, the canonical vapor–liquid–solid (VLS) (Fig. 1.8 (a)) [109–111] and vapor–solid–solid (VSS) [112] routes apply. In VLS, a molten or semi-molten transition-metal nanoparticle (often Fe, Co) dissolves carbon and precipitates a graphitic wall at the particle/tube interface; fast bulk diffusion through the liquid explains high growth rates but also particle reshaping at elevated temperature. In VSS, the nanoparticle remains solid (metal or carbide), with carbon diffusing on or through the solid and precipitating at the growth

interface; this typically improves diameter stability at the cost of lower diffusion rates.

Within the metal-catalyzed family, Fe, Co or Ni are widely effective owing to their high carbon solubility and diffusion coefficients and favorable adhesion to growing graphitic caps for small diameters [15,18,113]. Beyond these, many “uncommon” metals (Cu, Pt, Pd, Au, etc.) can catalyze CNTs when downsized to a few-nanometer scale, and alloying can further modulate activity and temperature windows [91,113–115].

A distinct class of catalyst-free or non-metal-seeded CNT growth involves solid nonmetal seeds that remain chemically and structurally stable during CVD. Because the precursor does not dissolve into the seed, and the seeds remain solid throughout growth, this pathway is better described as a vapor–solid surface–solid (VSSS) mechanism rather than the classical VSS model (Fig. 1.8 (b)). In VSSS growth, carbon species generated in the vapor phase adsorb onto the surface of the nonmetal seed and diffuse along the seed or substrate surface, without penetrating or dissolving into the seed. The nanotube structure nucleates at the seed–surface interface through reconstruction of sp^2 carbon, driven purely by surface diffusion and local carbon supersaturation on the seed exterior. Nanodiamond (ND)-seeded CVD is a prototypical VSSS case: ND particles remain solid and chemically inert during CVD, do not allow carbon dissolution, and yet their graphitization-prone surface can supply the necessary sites for CNT nucleation and wall formation [106,116,117]. Other reported metal-free CNT growth systems follow similar solid-surface-mediated pathways. Active examples include SiOx nanoparticles [107,118], a range of nonmetal oxides such as TiO_2, Cr_2O_3, and ZrO_2 [119,120] have also been demonstrated to act as solid-state catalytic centers for SWCNT nucleation, highlighting that oxygenated solid surfaces can host the rate-determining chemistry without requiring metal nanoparticles or liquid/solid alloy formation.

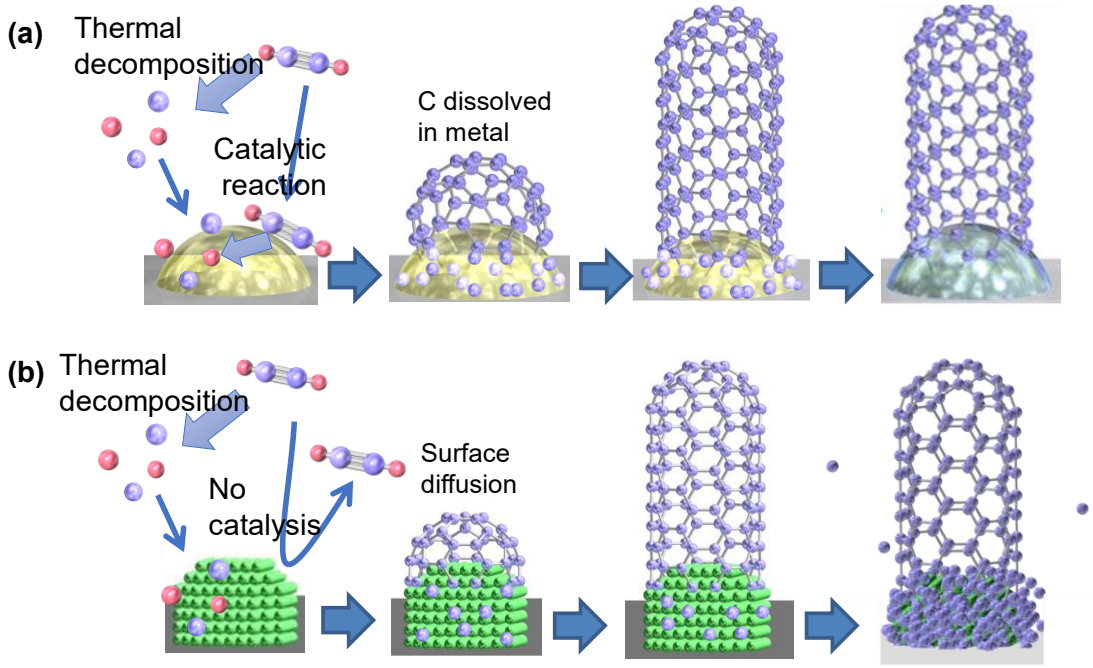


Figure 1.8 (a) Vapor-Liquid-Solid mechanism. (b) vapor–solid surface–solid mechanism.

Another important aspect of catalyst-mediated CNT growth is the position of the catalyst particle during elongation, which yields two characteristic growth modes: tip-growth and base-growth, as illustrated in Fig. 1.9. In the tip-growth mode, the adhesion between the catalyst nanoparticle and the substrate is weak, allowing the particle to lift off the surface once carbon begins to precipitate at the particle–substrate interface [121]. As the tube elongates, the catalyst remains at the leading end of the CNT, where it continues to decompose the incoming hydrocarbon and incorporate carbon species. This mode is frequently observed when catalyst–substrate interactions are minimal or at higher temperatures where the catalyst becomes partially molten, a behavior often associated with VLS-like growth.

In the base-growth mode, the catalyst particle remains strongly anchored to the substrate, and the CNT grows upward while the particle stays fixed at the base [122]. Carbon precursors dissociate on the exposed catalyst surface, and carbon diffuses across

or around the solid or partially molten particle before assembling into graphitic layers at the tube–substrate interface. This behavior is typical of VSS-type processes, in which strong catalyst–substrate interactions suppress catalyst mobility. Because the catalyst position is fixed, base-growth is well suited for patterned CNT arrays and vertically aligned structures formed on lithographically defined catalyst islands.

Although metal nanoparticles remain the most established catalysts for producing high-quality CNTs, interest in catalyst-free or metal-free growth routes has continued to rise, motivated by the need to avoid metallic residues and to access alternative nucleation environments. Catalyst-free CNT formation usually relies on specialized conditions—such as high-temperature hydrocarbon pyrolysis, oxygen-containing surfaces, crystalline carbides or nitrides, or graphitic templates with intrinsic reactive sites—where step edges, defect terminations, or oxygenated surface groups can act as nucleation centers. While the structural uniformity achieved so far may not yet match that of optimized metal-assisted CVD, these metal-free pathways open a distinct space of surface-mediated mechanisms and offer opportunities to tailor CNT properties through substrate chemistry rather than catalyst composition. This alternative paradigm is particularly relevant for applications that demand ultraclean electronic or optical behavior, and it motivates a broader examination of how different growth pathways influence the resulting CNT morphology.

In this context, understanding the diverse structural forms that CNTs can adopt becomes essential. The next section therefore surveys the major CNT morphologies—ranging from vertically aligned arrays to horizontally oriented and guided nanotubes—with a particular focus on strategies for achieving controlled horizontal alignment, which is central to both fundamental studies and device-level integration.

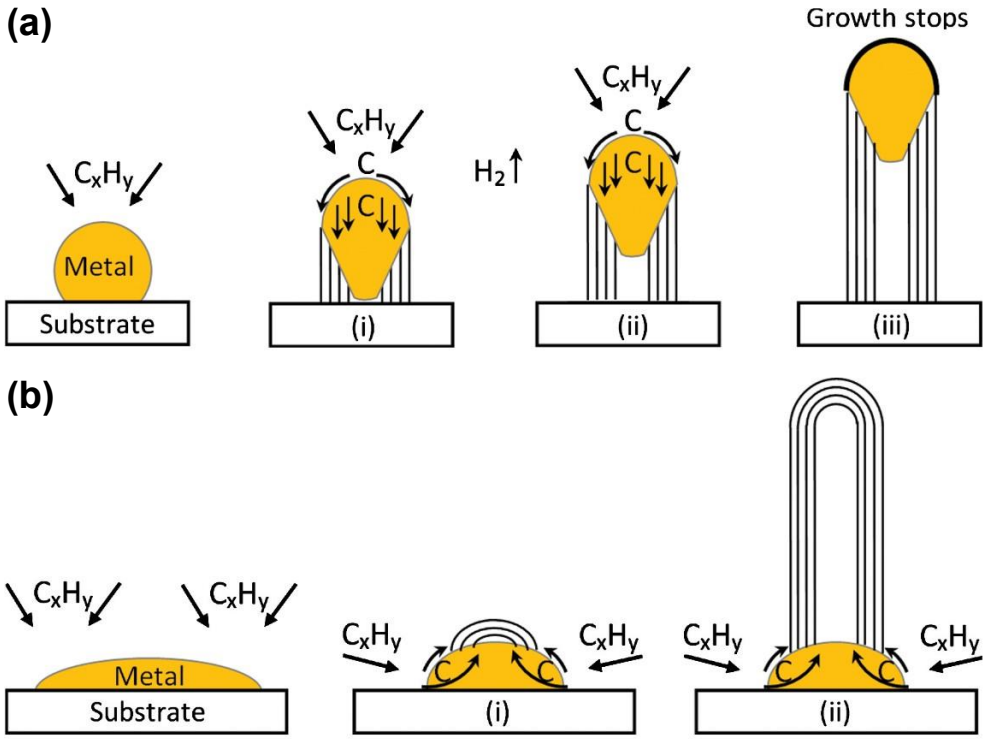


Figure 1.9 Growth mechanisms for CNTs: (a) tip-growth model, (b) base-growth model **[86]**.

1.2.3 Morphologies of CNT and growth mechanisms of aligned CNT

The morphology of CNTs synthesized by CVD or related methods can vary significantly depending on the growth conditions, catalyst distribution, and external guiding fields. As shown in Fig. 1.10, CNTs may form as randomly entangled networks, vertically aligned arrays, horizontally aligned individual nanotubes, or dense films with controlled density and thickness [80,84,123–126]. Randomly oriented CNT networks are often obtained when catalyst particles are distributed nonuniformly or when no external alignment mechanisms are imposed during growth. Such networks resemble a "spaghetti-like" morphology, where CNTs grow in arbitrary directions and form junctions due to van der Waals interactions [123]. Although these structures are advantageous for applications such as field emission cathodes, supercapacitor electrodes, or catalyst supports where isotropic properties are acceptable or even desirable, they lack the long-range order

required for high-performance nanoelectronic devices.

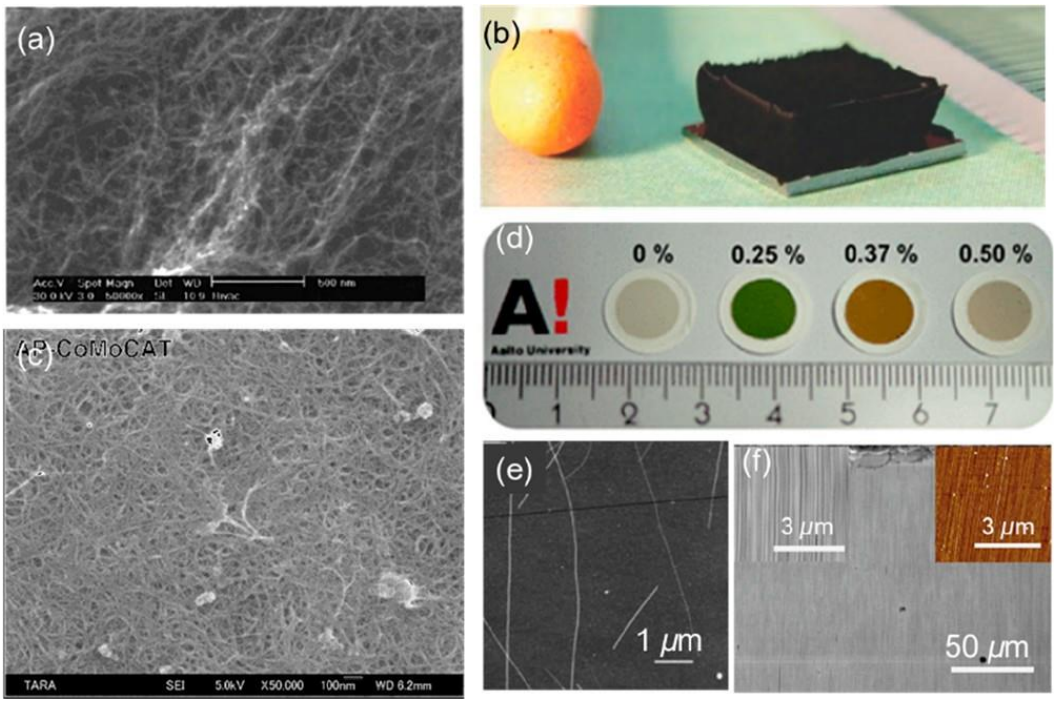


Figure 1.10 CNTs in different morphologies **[127]**. (a) SEM image of randomly oriented, bundled CNTs. (b) Optical image of a 2.5 mm tall CNT forest. (c) SEM image of CoMoCAT CNTs. (d) Optical image of colorful CNT films on filters. (e) Atomic force microscopy image of individual CNTs grown on surface. (f) SEM image of horizontally aligned CNT array.

Vertically aligned CNT arrays, often referred to as “CNT forests,” represent another widely studied morphology. They are typically synthesized under conditions where catalyst particles are uniformly distributed and strong tip-growth modes prevail, often assisted by plasma-enhanced CVD or water-assisted CVD techniques. These CNT forests can reach millimeter-scale heights with controlled density and alignment, exhibiting exceptional mechanical resilience, thermal conductivity, and electrical connectivity along the vertical direction. As shown in Fig, 1.10 (b), macroscopic CNT blocks composed of vertically aligned arrays can even be handled as bulk materials, offering opportunities for thermal interface materials, energy storage electrodes, and structural composites [84].

In contrast, horizontally aligned CNTs grown across substrates represent the most desirable morphology for nanoelectronic and optoelectronic applications, where individual CNTs or parallel CNT arrays serve as conducting channels, interconnects, or optical waveguides. Fig. 1.10 (e–f) illustrates examples where horizontally aligned CNTs bridge predefined electrode gaps or extend across crystalline substrates in highly ordered orientations [80,125]. Such structures enable the fabrication of CNT field-effect transistors (FETs), logic circuits, and photodetectors with reproducible performance metrics. However, achieving wafer-scale horizontal alignment with controlled spacing and orientation remains challenging and has motivated the development of several guiding strategies.

The alignment of CNTs during growth can be achieved through multiple mechanisms. As Fig. 1.11, one approach is electromagnetic alignment, where external electric or magnetic fields are applied during CVD growth to orient CNTs along field lines [128–130]. Electric field alignment has been demonstrated in plasma-enhanced CVD systems, where the plasma sheath provides a vertical electric field guiding CNT growth upward, yielding dense vertically aligned arrays. Magnetic field alignment, on the other hand, typically requires functionalization of CNTs with magnetic nanoparticles or the use of ferromagnetic catalyst materials, limiting its general applicability. While electromagnetic methods can achieve large-scale alignment, they often involve complex setups and may not be compatible with all substrate geometries or growth conditions.

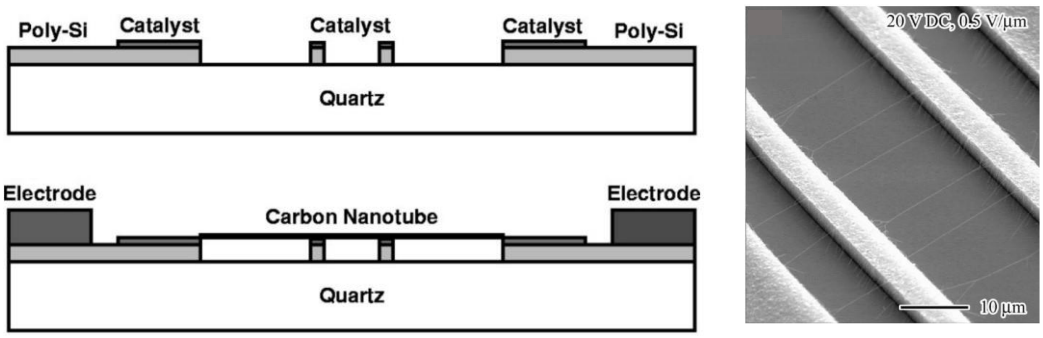


Figure 1.11 Horizontally aligned CNT arrays grown by applying in situ electric fields **[128]**.

Another widely explored mechanism is lattice-guided growth, where the epitaxial relationship between the CNT catalyst and the underlying crystalline substrate provides preferential growth directions [46,131]. For example, quartz and sapphire substrates exhibit well-defined crystallographic orientations that can template the alignment of CNTs along specific lattice directions, as shown in Fig. 1.12. When catalyst nanoparticles nucleate CNTs on such substrates, interfacial energy minimization drives the CNT growth direction to align with low-energy crystallographic axes. This method has enabled the synthesis of centimeter-long, perfectly aligned CNT arrays on single-crystal quartz, representing a significant breakthrough for high-performance CNT electronics. However, lattice-guided growth requires expensive single-crystal substrates and typically produces alignment only along discrete crystallographic orientations, limiting flexibility for arbitrary device layouts.

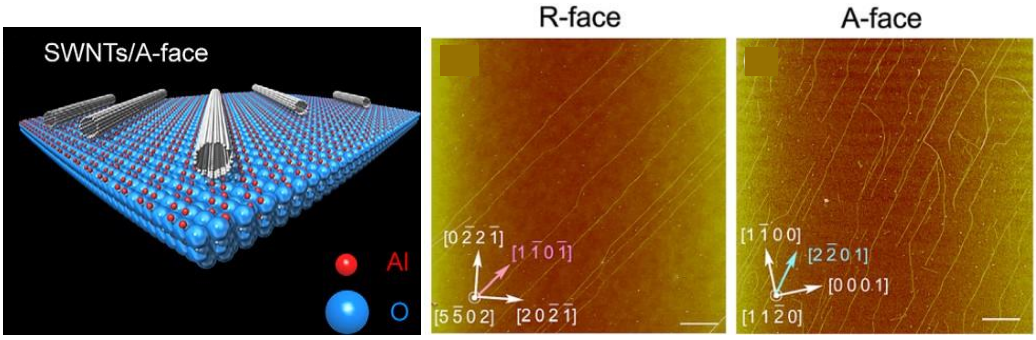


Figure 1.12 Lattice oriented CNT growth on sapphire **[131]**.

Gas-flow-directed growth represents a third and increasingly popular approach for aligning CNTs over large areas with high uniformity. In this method, a controlled gas flow is introduced across the substrate during CVD growth, exerting aerodynamic forces on the growing CNTs and orienting them along the flow direction [14–20]. Compared to electromagnetic or lattice-guided methods, gas-flow-directed growth offers a simpler and

more scalable route, as it does not require external fields or single-crystal substrates. Moreover, by tuning flow velocity, direction, and reactor geometry, it is possible to control CNT spacing, alignment degree, and network topology, providing a versatile platform for integrated nanoelectronic and optoelectronic devices.

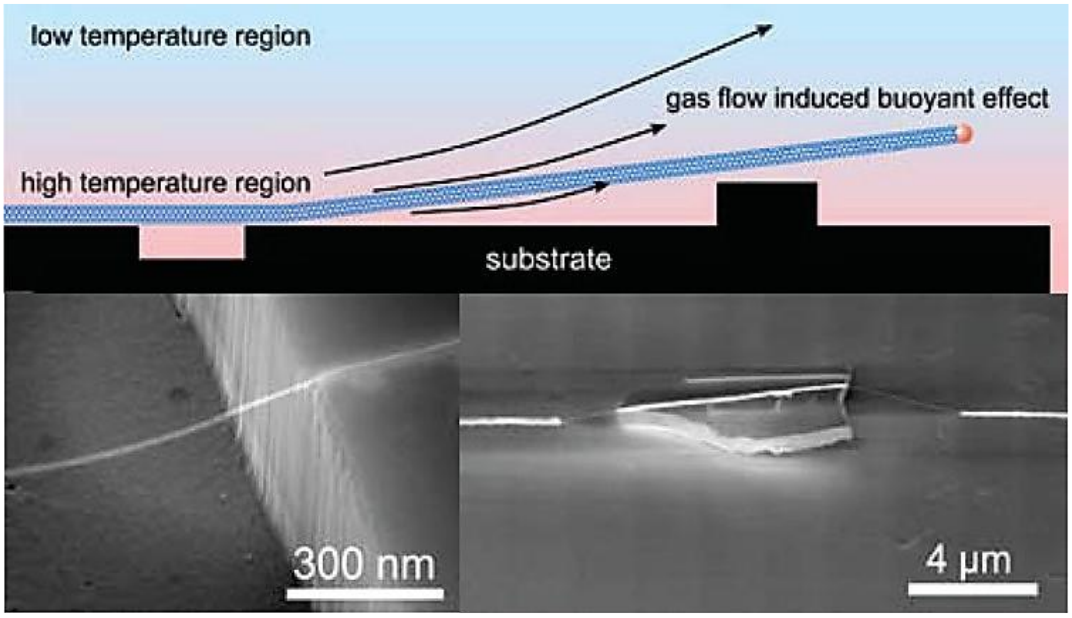


Figure 1.13 Horizontally aligned CNT synthesized by gas-flow-directed growth **[47]**.

In summary, CNT morphology ranges from randomly entangled networks to highly aligned individual nanotubes or arrays, with alignment playing a crucial role in determining electrical, thermal, and mechanical anisotropy. Among the various alignment strategies, gas-flow-directed growth combines simplicity, scalability, and compatibility with existing CVD systems, making it an attractive focus for further investigation. The next section will therefore explore the fundamental mechanisms, structural properties, and potential applications of CNTs grown via gas-flow-directed methods.

1.3 Gas-flow-directed growth

1.3.1 Mechanisms of gas-flow-directed growth

Gas-flow-directed CVD has evolved into a powerful approach for synthesizing horizontally aligned CNTs (Fig. 1.14). Early work established the fundamental idea that a growing CNT can be partially lifted by gas flow, allowing its free end to float and align along the flow direction while elongation proceeds. Cassell and co-workers first demonstrated this principle in 1999 by showing that CNTs grown from patterned tower structures could span adjacent pillars as their free ends waved in the carrier-gas stream [132]. Although directional suspended CNTs were obtained, the overall yield remained low, and dense interconnected networks were difficult to achieve. A major leap was achieved in 2004 when Huang and colleagues reported that rapid heating at the onset of CVD enabled millimeter-long, flow-aligned CNTs [15]. Their results established the "flying-kite" mechanism, in which transient buoyant convection lifts catalyst particles into a tip-growth mode, allowing the CNT ends to remain airborne and aligned by laminar flow. These long CNTs were able to cross trenches and vertical barriers, demonstrating the ability of gas flow to guide growth over macroscopic distances. As the understanding of the mechanism improved, researchers recognized that flow stability—characterized by low Reynolds numbers and minimized secondary vortices—was essential for obtaining long and straight nanotubes [133]. This led to engineering solutions such as inserting inner tubes or modifying reactor geometry to stabilize laminar flow. These developments set the stage for ultralong CNT growth beyond the centimeter scale.

A watershed moment came in 2013, when Zhang et al. demonstrated half-meter-long CNTs using optimized gas-flow-directed CVD and a furnace-moving strategy [21]. Their analysis revealed that CNT length distributions follow the Schulz–Flory distribution, with catalyst activity probability determining the decay rate of CNT counts with length. In 2019, Zhu et al. expanded the theoretical and practical implications of SF statistics by

showing that metallic and semiconducting CNTs decay at markedly different rates during ultralong growth [23]. Because semiconducting CNTs possess an order-of-magnitude higher atomic assembly rate, metallic CNTs “die out” more quickly, leading to a spontaneous enrichment of semiconducting CNTs along the growth direction. This rate-selected growth enabled predicted purities approaching 99.9999% semiconducting CNTs at lengths around 154 mm and produced CNTs as long as 650 mm, setting a new length record. Most recently, 2023, Jiang et al. addressed one of the most persistent limitations in gas-flow-directed growth: the extremely low yields of ultralong CNTs [27]. By integrating floating-catalyst CVD with a substrate interception and direction strategy, they transformed initially floating short CNTs into tip-growing, gas-flow-oriented ultralong CNTs. This method dramatically increased catalyst utilization and suppressed nanoparticle aggregation, yielding an ultralong CNT array density of ~6700 CNTs mm^{-1}, which is 2–3 orders of magnitude higher than all previous reports. The CNTs retained high crystallinity and exhibited a self-purifying trend, with semiconducting purity increasing with length.

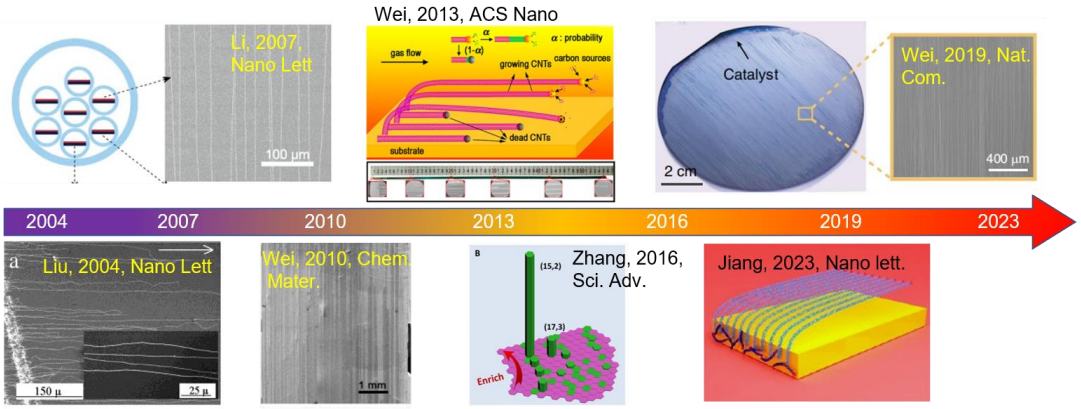


Figure 1.14 Timeline of major milestones in the controlled synthesis of gas-flow-directed growth CNTs **[15,21,23,27,47,133,134]**.

Building on the historical development of gas-flow-directed CNT growth, a more

unified mechanistic picture has emerged that clarifies how CNTs transition from substrate-anchored structures into freely suspended, flow-aligned filaments. As illustrated in Fig. 1.15, the first stage is lift-off of the catalyst–CNT assembly from the substrate, followed by a second stage in which the floating CNT is aligned and extended by the imposed gas flow. Historically, lift-off was attributed to thermal buoyancy arising from vertical temperature gradients [135,136]. However, recent quantitative heat-balance analysis and CFD modeling reveal that such gradients originate primarily from the inherent thermal effect of the substrate, rather than from gas-phase heating [137]. Because the substrate absorbs and emits thermal radiation far more effectively than the surrounding gas, it becomes substantially hotter than the bulk flow. This temperature difference is strongly dependent on substrate emissivity, with high-emissivity materials such as silicon producing much larger temperature elevations than low-emissivity substrates such as quartz. These findings explain why ultralong, tip-grown CNTs are commonly obtained on silicon but rarely on quartz. The local temperature gradient generated by this inherent thermal effect gives rise to two independent temperature-gradient-induced forces: natural convection, which produces an upward drag force, and thermophoresis, which pushes the CNT away from the hotter substrate surface toward the cooler gas region. Direct computational and experimental decoupling of these effects shows that natural-convection drag is negligible within the narrow boundary layer near the surface, where gas velocity approaches zero. In contrast, the thermophoretic force reaches its maximum at the substrate interface because the temperature gradient is steepest there. As a result, thermophoresis overwhelmingly dominates the lift-off process, providing the only force capable of detaching CNTs from the substrate and initiating the flying-kite-like tip-growth mode.

The second stage of gas-flow-directed growth is the flow alignment and sustained elongation of the suspended CNT in the gas stream. The stability of this streamline field can be described by two classical dimensionless numbers: the Reynolds number R_e [138]

and the Richardson number R_i [139]. In CVD tubes, R_e and R_i can be written as $R_e = \rho v d/\mu$ and $R_i = \Delta\rho g h/(\rho v^2)$, where ρ is gas density, v is average flow speed, d is tube diameter, μ is gas viscosity, $\Delta\rho$ is density difference across a vertical length h, and g is gravitational acceleration. Increasing temperature raises R_i but lowers R_e; increasing flow speed lowers R_i but raises R_e. Practically, lowering R_e (e.g., by reducing v and/or raising T within the growth window) helps maintain laminar flow, while tuning R_i to a moderate value provides sufficient "lift" without triggering strong convection that would destabilize alignment. This trade-space explains why optimal growth windows feature slow, steady carrier flows at relatively high substrate temperatures, which simultaneously reinforce thermophoretic lift and laminar guidance.

Beyond force balance, reactor and substrate parameters strongly modulate outcomes. Because the substrate tends to be hotter than the gas, its emissivity directly sets the magnitude of the near-surface ∇T and therefore the thermophoretic field; higher-emissivity surfaces (e.g., Si) enhance lift-off and sustain the floating state, whereas low-emissivity quartz favors "crawling" growth. Moreover, under laminar conditions the forced-convection intensity has limited impact on the temperature distribution near the substrate, so the thermophoretic driving force remains nearly constant across a wide range of flow velocities—one reason ultralong arrays can be grown robustly once the thermal environment is properly engineered [137].

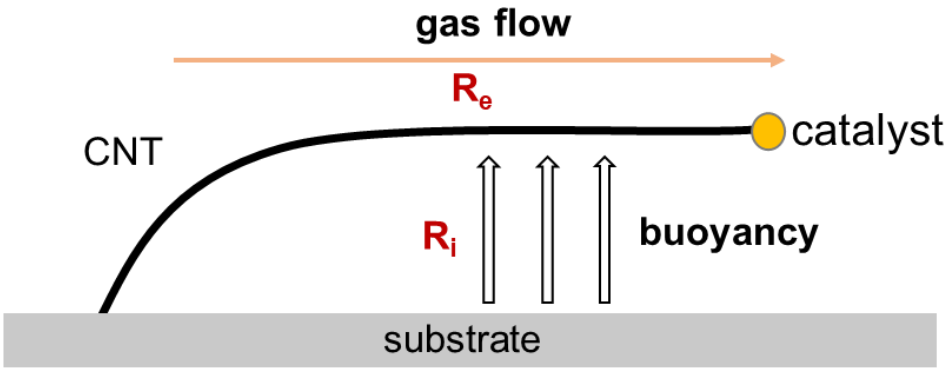


Figure 1.15 Schematic diagram of the formation mechanism of gas-flow-directed growth.

Historically, this growth mode relied almost exclusively on liquid-like transition-metal nanoparticles such as Fe, Co, or Cu [15,18,20], which naturally enter a VLS-type tip-growth regime at elevated temperatures. Although effective, metal catalysts can reshape or redistribute during growth and may introduce defects or leave residues that limit electronic purity. Recently, nonmetallic seeds such as nanodiamond (ND) have been shown to support gas-flow-directed, tip-growth alignment with high crystallinity while eliminating metal contamination, provided that the same fluid-mechanic and thermal criteria are met [140]. These advances broaden gas-flow-directed growth from purely catalytic to catalyst-free regimes and underscore that alignment/length are governed as much by reactor physics as by seed composition.

Putting these pieces together, gas-flow-directed growth is best viewed as a coupled thermal–fluid-mechanic process atop conventional CVD chemistry: substrate-emissivity–driven thermophoresis initiates lift-off; a carefully tuned R_i provides just enough "buoyancy"; a low R_e laminar field delivers directional drag for long-range alignment; and appropriate catalyst or seed activity plus carbon flux sustains defect-lean elongation over macroscopic distances. This integrated framework explains how the field has progressed from early micrometer-scale alignments to today's centimeter–decimeter ultralong arrays, and it establishes a general design space for achieving wafer-scale, horizontally aligned CNTs.

1.3.2 Properties of gas-flow-directed growth CNTs

The alignment and high structural quality achieved through gas-flow-directed growth significantly enhance the intrinsic properties of CNTs. Compared to randomly oriented CNT networks, aligned CNT arrays exhibit superior performance in mechanical strength, electrical transport, and thermal conductivity due to minimized junction resistance,

reduced defect density, and improved load transfer between individual nanotubes. The figures provided illustrate representative studies demonstrating these property enhancements across multiple physical domains.

Mechanically, individual CNTs produced by gas-flow-directed growth exhibit exceptional axial stiffness, with Young's moduli approaching the in-plane modulus of graphite. As measured by Wu et al., structurally defined suspended CNTs exhibit a Young's modulus of 0.97 ± 0.16 TPa, with little dependence on chirality, demonstrating that individual nanotubes approach the intrinsic stiffness of graphene (Fig. 1.16) [141]. Beyond stiffness, Bai et al. quantified the tensile behavior of ultralong, defect-free CNTs and CNT bundle. Single CNTs with gauge lengths of ~1.5 mm showed a tensile strength of 121.6 GPa and a fracture strain of 14.1%, confirming the near-theoretical mechanical performance of high-quality, aligned CNTs [142]. These results collectively show that while individual CNTs possess ultrahigh intrinsic stiffness and tensile strength, aligned and well-processed CNT bundles can retain a substantial fraction of this performance at the macroscopic scale. The strong mechanical coupling enabled by parallel orientation, continuous lengths, and minimized strain heterogeneity allows CNT assemblies to transcend the limitations of conventional carbon fibers, offering a pathway toward ultra-strong macroscopic materials.

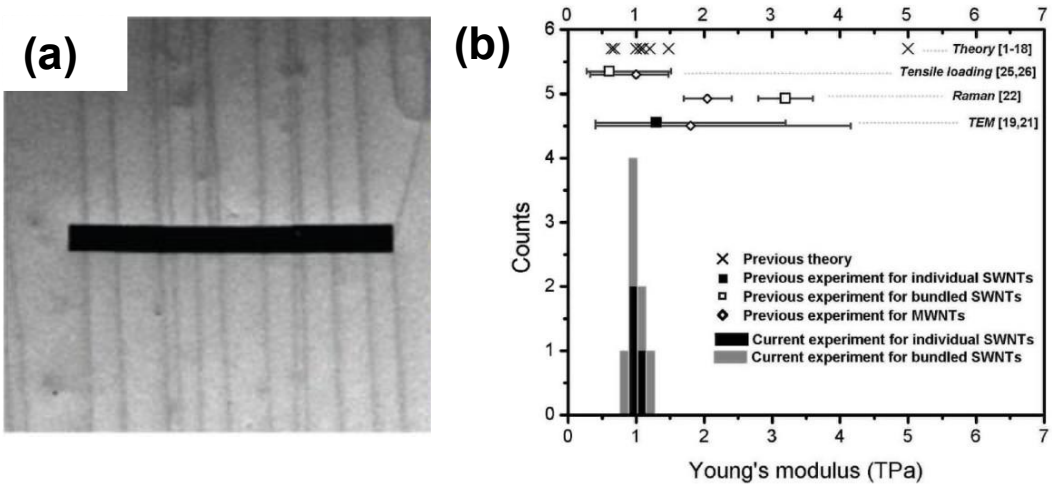


Figure 1.16 (a) Scanning electron microscope image of aligned CNT. (b) Values of the Young's modulus for carbon nanotubes from this study **[141]** and previous experimental and theoretical investigations.

Electrically, aligned semiconducting CNT arrays produced by gas-flow-directed growth exhibit uniform and high-quality transport characteristics. Fig. 1.17 of Zhu et al. shows that transistors fabricated on CNTs longer than 154 mm deliver an on-state current of about 14 μA μm^{-1} together with an on/off ratio of approximately 10^8, confirming both the high purity and structural perfection of the ultralong tubes [23]. he high degree of alignment ensures that carrier transport occurs along continuous, junction-free paths, avoiding the random percolation bottlenecks commonly found in solution-processed CNT networks. At the array level, the uniform electrostatic gating also leads to reproducible device behavior across large device sets. These characteristics demonstrate that gas-flow-directed growth, once combined with rate-selected purification at long lengths, can supply CNTs suitable for high-performance logic applications where both purity and structural integrity are essential.

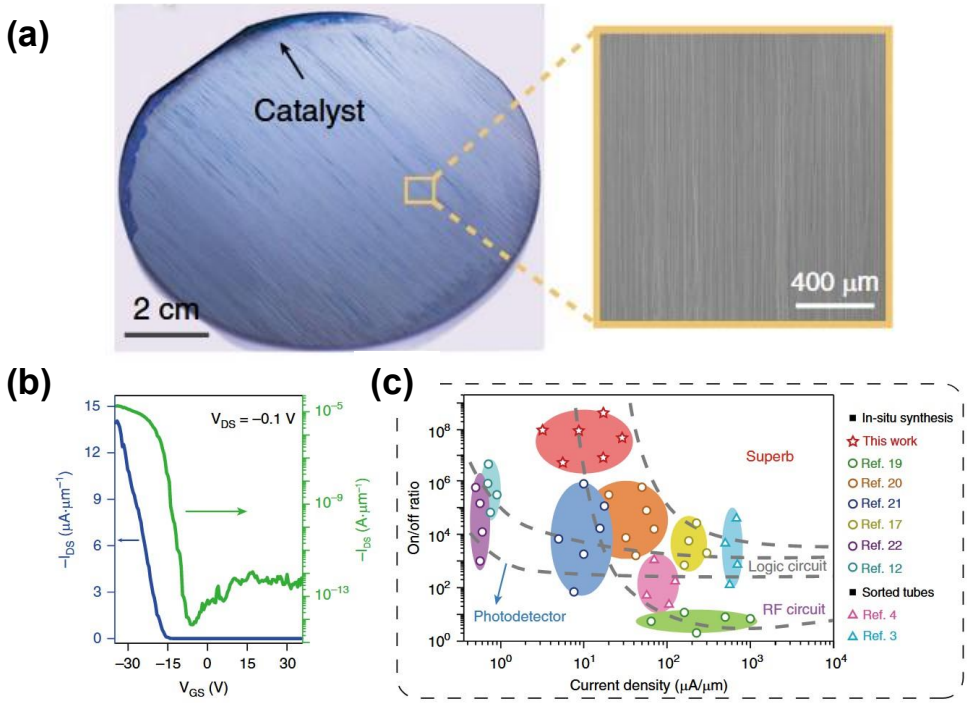


Figure 1.17 (a) Device fabrication with highly pure aligned semiconducting CNTs. (b) Transfer characteristics of the width-normalized transistor. (c) Benchmarking the width-normalized device fabricated on ultralong CNT arrays for a single channel with those previously reported **[23]**.

Thermal transport in aligned CNTs produced by gas-flow-directed growth reflects the intrinsic phonon conduction capability of structurally pristine one-dimensional materials. As quantified by Lee et al., the room-temperature thermal conductivity of an individual millimeter-long CNT increases continuously with tube length, reaching 8640 W m^{-1} K^{-1} at a measured length of 1.039 mm, and exceeding 13 000 W m^{-1} K^{-1} after correcting for radiative losses (Fig. 1.18) [143]. This anomalous length-dependent behavior follows a power-law divergence $\kappa \sim L^{\alpha}$, where κ is the thermal conductivity, L is the suspended CNT length, and α (typically 0.2–0.5) quantifies the degree of anomalous, non-Fourier thermal conduction. Such a relationship indicates that long-wavelength phonons propagate quasi-ballistically over macroscopic distances when the nanotube remains continuous and defect-lean—conditions naturally satisfied in ultralong,

flow-guided CNTs. Notably, the observed divergence persists despite structural imperfections such as isotope disorder or thin amorphous-carbon coatings, implying that the phonon mean free path in ultralong CNTs is remarkably robust. These findings demonstrate that flow-directed growth, by enabling millimeter-scale continuity with minimal scattering centers, provides an effective route toward CNTs approaching their intrinsic thermal limits. Such ultrahigh thermal conductivities, combined with mechanical flexibility and scalability, position ultralong CNTs as attractive candidates for advanced heat-spreading technologies and thermal interface applications.

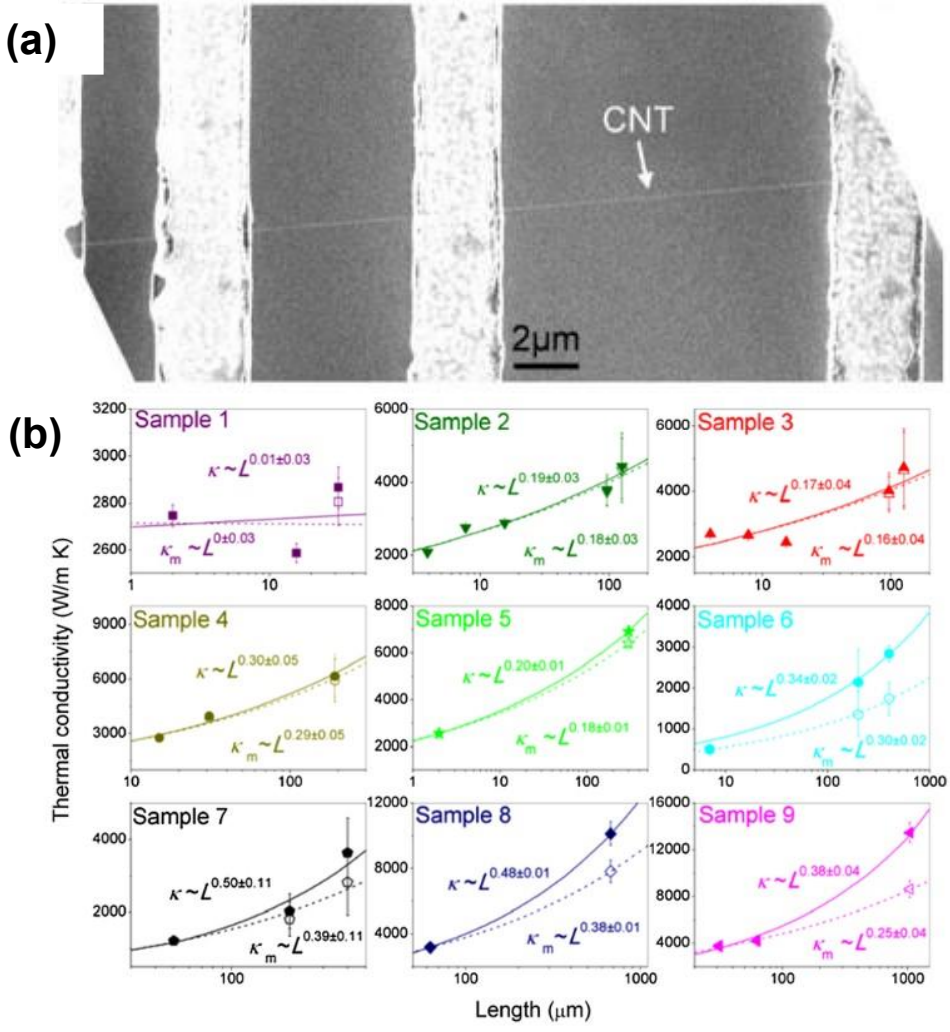


Figure 1.18 (a) Scanning electron microscope image of a CNT anchored on a test fixture consisting of parallel resistive thermometers. (b) CNT length and thermal conductivity relations for nine different

CNTs.

The synergistic optimization of mechanical, electrical, and thermal properties in gas-flow-directed CNTs arises from their unique structural characteristics: macroscopic alignment, ultralong lengths, and low defect densities. Together, these features enable multifunctional materials that simultaneously provide mechanical reinforcement, electrical conduction, and thermal management in lightweight, flexible platforms. The next section will explore how these properties translate into specific technological applications, ranging from energy devices to nanoelectronics and multifunctional composites.

1.3.3 Application of gas-flow-directed growth CNTs

The superior structural order and long-range alignment of gas-flow-directed CNTs have enabled a series of breakthrough applications in nanoelectronics. Unlike randomly oriented CNT networks, aligned arrays provide deterministic conduction pathways, minimized intertube junction resistance, and enhanced device uniformity, which are essential for large-scale integration.

One of the most prominent applications is in field-effect transistors (FETs). Fig. 1.19 (a) shows a CNT bridging source and drain electrodes with nanoscale channel lengths [144]. The well-aligned CNT channels ensure high carrier mobility and excellent switching performance, with subthreshold slopes approaching the thermionic limit of 60 mV/decade. CNT FETs exhibit steep subthreshold swings and high on–off current ratios, which make them highly competitive compared to silicon-based complementary metal-oxide semiconductor (CMOS) FETs, particularly for low-power electronics. Moreover, their nanoscale diameters enable ultimate device scaling to sub-10 nm channel lengths

while maintaining superior electrostatic control, positioning CNT FETs as a key candidate for beyond-CMOS technologies.

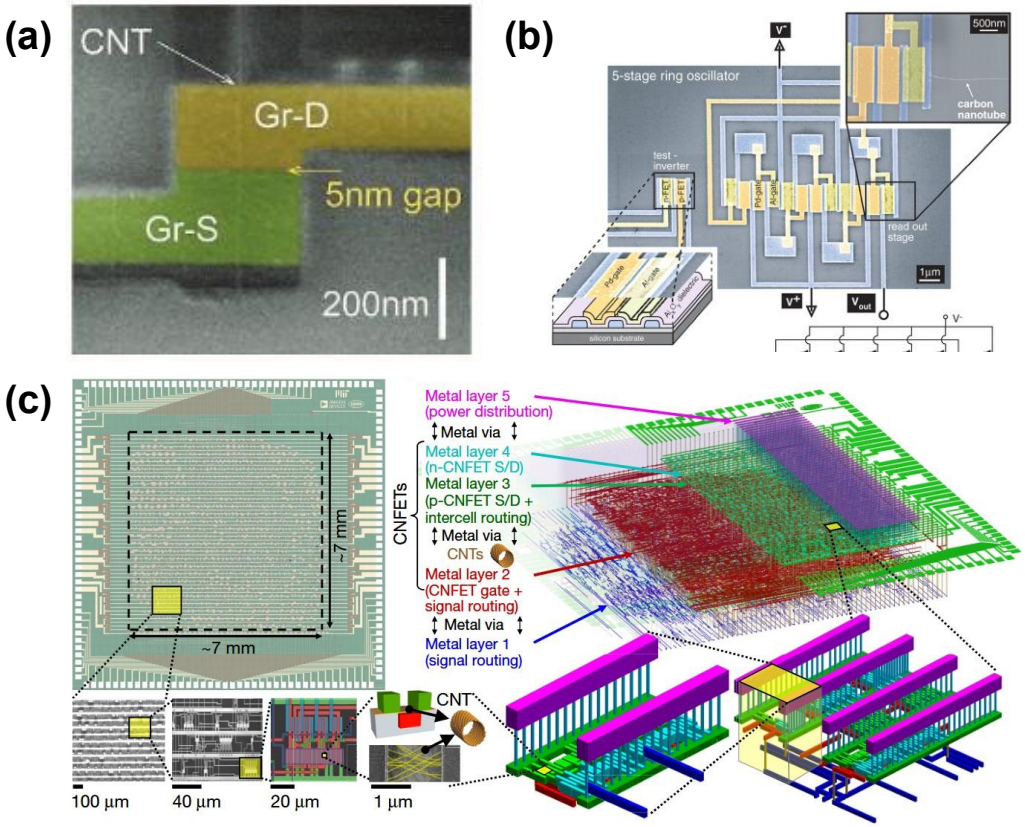


Figure 1.19 (a) Scanning electron microscope image of a graphene-contacted CNT FET with channel length of 5 nm **[144]**. (b) Scanning electron microscope image of a CNT ring oscillator consisting of five CMOS inverter stages **[145]**. (c) Image of a fabricated CNT chip **[146]**.

Beyond individual devices, aligned CNTs have been integrated into functional circuits. Fig. 1.19 (b) demonstrates a five-stage ring oscillator constructed from CNT FETs, which exhibits stable oscillation frequencies in the MHz regime. This achievement highlights the feasibility of CNT-based logic gates and small-scale integrated circuits, overcoming a long-standing bottleneck in the reproducibility of CNT devices. More advanced demonstrations, such as CNT complementary logic circuits, further underscore the potential of CNTs to replace or complement silicon in high-performance computing

systems.

Recent progress has extended these concepts to wafer-scale integration of CNT-based chips. Fig. 1.19 (c) presents a prototype CNT microprocessor fabricated using aligned CNT arrays, incorporating over 10,000 transistors distributed across multiple metal routing layers [146]. The chip demonstrates functional logic operations, memory storage, and power management, marking a milestone in translating CNT properties into real-world computing hardware. Importantly, the large-area alignment enabled by gas-flow-directed growth ensures uniform electrical performance across thousands of devices, a critical prerequisite for scalable manufacturing.

In addition to digital electronics, gas-flow-directed CNTs also hold promise for applications in high-frequency analog and radio-frequency (RF) devices. Their high carrier mobility and low parasitic capacitance enable RF transistors capable of operation beyond 100 GHz, opening opportunities in next-generation wireless communication technologies [147]. Furthermore, the combination of mechanical flexibility and outstanding electronic performance makes CNTs attractive for flexible and wearable electronic [148].

1.4 Motivation and challenges

In this study, we focus on gas-flow-directed growth of aligned CNTs because it offers unique advantages for next-generation nanoelectronic and energy devices. First, the choice of catalysts/seeding materials strongly affects CNT quality. Metal catalysts [15,18,91], though effective, often introduce contamination that degrades intrinsic electronic properties. These limitations have motivated the search for metal-free routes capable of producing clean, high-quality gas-flow-directed growth CNTs. Before our work, however, metal-free growth strategies remained difficult to implement for aligned CNTs. Our recent studies addressed these issues by demonstrating that nanodiamond can

function as an effective nonmetallic seed, enabling gas-flow-directed CNT growth through a vapor–solid–solid surface pathway [106,140]. This approach produces aligned CNTs without introducing metallic contamination, providing a promising foundation for clean CNT electronics. Establishing such a clean and controllable growth platform is a necessary first step for exploring more complex growth behaviors and device-relevant CNT architectures.

Second, the interplay between different alignment mechanisms during CNT growth remains insufficiently understood. In principle, gas-flow-directed growth can produce highly aligned, millimeter-long CNTs by maintaining a steady aerodynamic force that guides the floating tip during elongation [15,140]. However, in pillar-assisted architectures, an additional mechanism—vibrational bridging—can arise from small-amplitude oscillations of the CNT tip, allowing the tube to intermittently contact and anchor onto neighboring structures [132,149]. This effect tends to dominate at shorter CNT lengths, introducing structural variations that coexist with gas-flow alignment. Before our recent work [150], the relative contributions of these two mechanisms and the conditions under which one transitions to the other were not clearly established. The lack of a quantitative framework for this crossover has hindered deterministic control over CNT alignment, network topology, and device-level reproducibility. Our study clarified that alignment arises from a competition between aerodynamic guidance and mechanically induced bridging, and that the dominant mechanism depends sensitively on CNT length, local flow conditions, and the geometric environment. Establishing this mechanistic crossover is therefore essential for rationally engineering aligned CNT architectures with predictable connectivity. Importantly, this analysis contributes to a deeper understanding of gas-flow-directed CNT growth and offers useful context for the substrate-dependent transport investigations presented in the following section.

Third, substrate effects play a decisive role in determining charge transport in CNT electronics [6,151,152], yet our current understanding remains incomplete. Prior studies

have shown that CNTs supported on atomically flat and low-disorder substrates such as hexagonal boron nitride (hBN) [153] can exhibit substantially higher mobilities compared with devices on conventional SiO_2, largely due to the suppression of surface roughness scattering, charge impurities, and remote phonon coupling [154–156]. However, these results are typically based on different CNTs fabricated on different substrates, making it difficult to isolate substrate contributions from variations in tube quality, chirality, or defect density. Direct, within-tube comparisons—where the same CNT spans two substrates and is measured under identical conditions—are still rare, leaving a critical gap in quantifying the intrinsic impact of substrate choice on carrier transport. In our work, we directly address this gap by using gas-flow-directed long CNTs to span SiO_2 and hBN. Because the CNT remains continuous across both regions, its intrinsic properties are held constant, allowing unambiguous evaluation of substrate-dependent transport. Our measurements show that the same CNT exhibits higher mobility on hBN than on SiO_2, providing the first direct experimental evidence that substrate quality alone can modulate carrier transport without changing nanotube structure.

In summary, the motivation of this dissertation is to establish a deeper understanding of the mechanisms governing gas-flow-directed growth of aligned CNTs, with particular emphasis on (i) the role of nonmetallic seeds in gas-flow-directed growth, (ii) the crossover between gas-flow-directed growth and vibrational bridging, and (iii) the analysis of substrate effects on transport properties using gas-flow-directed growth CNT. By addressing these challenges, this work aims to provide new strategies for achieving high-quality, transfer-free, and device-compatible CNTs for future nanoelectronics.

1.5 Organization of the thesis

This thesis consists of six chapters.

Chapter 1 begins by introducing the fundamental concepts of CNTs, including their

structure, properties, and synthesis methods. Special attention is given to the growth mechanisms of CNTs, such as CVD, catalyst- and non-catalyst-based growth, and the influence of different growth modes on morphology. The chapter then discusses alignment mechanisms, including electromagnetic, lattice, and gas-flow-directed growth, leading to a detailed focus on the advantages and potential of gas-flow-directed CNTs. Finally, the motivation and challenges associated with scalable CNT growth are presented, setting the stage for the subsequent research.

Chapter 2 outlines the experimental setup and characterization methods employed in this study. It begins by describing the design of the CVD growth system, including the gas flow control modules, heating configurations, and substrate preparation methods, which are critical for achieving gas-flow-directed alignment. In addition to CNT synthesis, the chapter describes the fabrication of device structures used for electrical measurements. This includes the photolithography-based patterning of alignment markers and the fabrication of metal electrodes. The chapter then introduces the structural and property characterization techniques, such as scanning electron microscopy (SEM), Raman spectroscopy, and electrical transport measurements. The working principles of these methods are briefly explained, along with their specific applications in analyzing CNT morphology, alignment, and properties.

Chapter 3 investigates the gas-flow-directed growth of aligned CNTs from nonmetallic seeds. Building upon the limitations of metal catalysts, this chapter demonstrates that nanodiamond can enable aligned CNT growth through gas-flow-directed growth. We systematically examine the effects of seed pretreatment, growth temperature, and gas flow rate on CNT nucleation, lift-off, and alignment. Secondary-electron yield mapping combined with AFM analysis eliminates the contribution of metal impurities and confirms that long CNTs predominantly grow in a tip-growth mode from nonmetallic particles. Structural characterization further shows that the resulting CNTs possess high crystallinity and small diameters suitable for electronic applications. Overall,

this chapter establishes that nonmetallic seeds can reliably support gas-flow-directed alignment, thereby extending the gas-flow-directed growth mechanism into a catalyst-free regime and enabling high-purity, transfer-free CNTs for device integration.

Chapter 4 builds on these findings by focusing on the crossover between gas-flow-directed growth and vibrational bridging mechanisms in pillar-assisted system. Through a combination of in situ observations, structural characterization, and theoretical analysis, this chapter clarifies how gas flow dynamics, thermal gradients, and tip oscillations collectively determine CNT alignment and connectivity. A growth model is proposed to describe the transition between gas-flow-directed and bridging regimes, providing new insights into the self-organization of CNT networks under flow fields.

Chapter 5 extends the discussion to the influence of substrate environments on the electronic transport properties of aligned CNTs grown by gas-flow-directed growth. By fabricating devices in which a single long CNT spans different substrates, such as SiO_2 and hBN, this chapter describes the measurement protocols used to extract field-effect mobility and thermally activated transport parameters, as well as the analysis framework for evaluating substrate-induced scattering. The results show that, while the activation energies on the two substrates are comparable, CNT segments on hBN consistently exhibit higher mobility than those on SiO_2. Through this direct within-tube comparison, the chapter demonstrates that substrate engineering provides an effective means of improving CNT device performance and offers quantitative insight into how dielectric environments influence electronic transport in aligned CNTs.

The final chapter summarizes the main findings of the preceding chapters and discusses remaining challenges. Key issues such as large-area uniformity, growth reproducibility, and integration with device-compatible substrates are identified, outlining directions for future development of gas-flow-directed CNTs in advanced applications.

Chapter 2. Experiments

2.1 CNT synthesis: furnace, gas supply and exhaust system

2.1.1 Substrate preparation and catalyst/growth seed pretreatment

The substrates used were Si/SiO_2 wafers or quartz plates. Prior to seed deposition, all substrates were cleaned by sequential ultrasonication in acetone, ethanol, and deionized water for 5 min each, followed by nitrogen blow-drying. Additional UV–ozone cleaning was performed for 10 min to remove organic residues and improve surface wettability.

For nanodiamond (ND) growth seed preparation, commercial detonation ND [157] colloidal suspension in ethanol ((provided by Nippon Kayaku, impurity concentrations of 80 ppm for Fe, 2100 ppm for Zr, and 6–20 ppm for Pd)) was used. The suspension typically contained ND particles with diameters of 4–14 nm. A small amount of the ND–ethanol solution (10–20 μL) was drop-cast onto the substrate, followed by drying in ambient air. The ND dispersion and its drop-cast coating on Si are shown in Fig. 2.1, followed by pretreatment at 600 °C in air for 10 min. This treatment removed surface impurities and simultaneously reduced the ND particles to a suitable size distribution for CNT growth [158]. These nanoscale diamond clusters then acted as non-metallic seeds for CNT nucleation, providing stable growth sites at elevated temperatures without introducing metallic contamination.

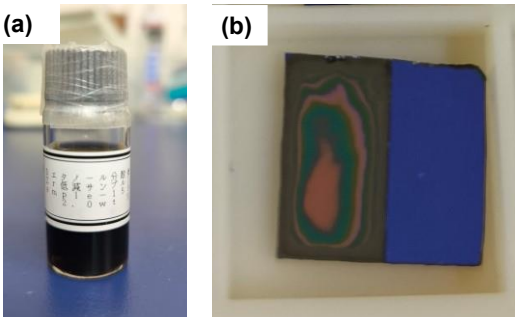


Figure 2.1 (a) Photograph of the ND dispersion. (b) Photograph of a Si substrate after drop-casting and drying the ND dispersion on the left region.

For metallic catalyst preparation, an aqueous $FeCl_3$ solution (0.03 M) was drop-cast onto the designated substrate area and dried under ambient conditions. Pretreatment was performed in two steps: first, heating in air to the reduction initiation temperature to remove residual solvent and surface impurities; second, annealing under vacuum with Ar/H_2 flow to reduce Fe^{3+} ions to catalytically active Fe nanoparticles. The resulting Fe nanoparticles provided highly active sites for hydrocarbon decomposition and CNT nucleation.

2.1.2 CVD furnace system

Fig. 2.2 presents both the external appearance and a schematic diagram of the furnace. CNT synthesis in this study was carried out using a horizontal multi-temperature zone chemical vapor deposition (CVD) furnace (GE-1000, GII Techno). The quartz reactor tube has a length of 1040 mm with an internal semicircular cross-section of 44 mm, and the heating length of the furnace is 890 mm. The system is equipped with independent heating zones at the upstream, midstream, and downstream regions, allowing controlled temperature gradients of up to ~100 °C between the upstream and midstream, and ~50 °C between the midstream and downstream. By gradually increasing the temperature difference during the heating stage, a maximum gradient of ~180 °C can be achieved between upstream and midstream regions, which is particularly effective for controlling the pyrolysis of carbon precursors and the subsequent CNT growth.

The piping system is connected to multiple gas lines, enabling the introduction of high-purity argon (99.99%), diluted hydrogen (3% H_2/Ar), hydrocarbon gases (C_2H_2 or C_2H_4), ethanol vapor, and optional additives such as H_2O or CO_2. The use of a multi-zone heating profile is critical when using ND growth seeds, since ND lacks catalytic activity and requires efficient upstream pyrolysis of the ethanol precursor before CNT nucleation.

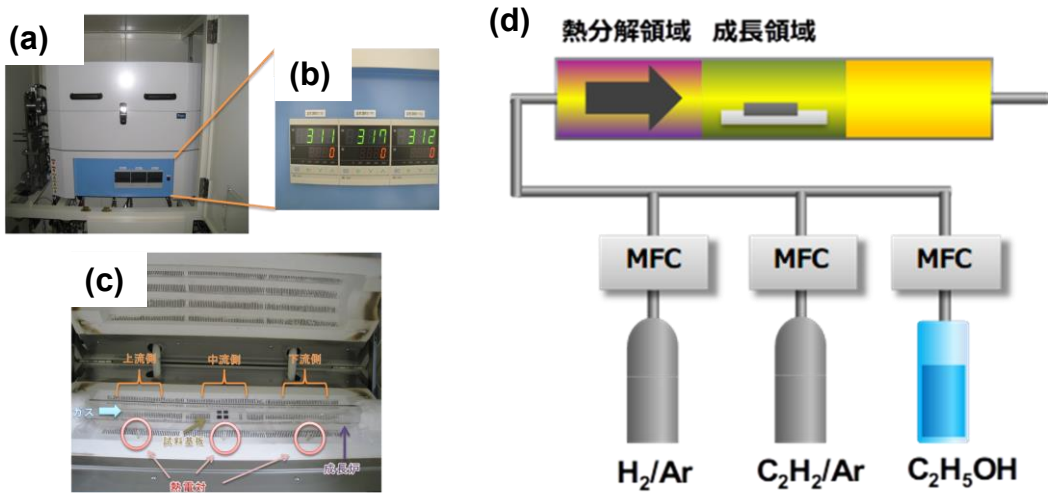


Figure 2.2 (a) Outside of the growth furnace, (b) Thermostat, (c) Inside of the growth furnace. (d) Schematic diagram of a multi-temperature zone CVD system.

Fig. 2.3 illustrates the designed and modified gas supply and exhaust system connected to the CVD furnace. Ethanol (purity 99.5%, Wako Pure Chemical Co., Ltd.) was introduced into the reactor by a bubbling method. Argon or H_2/Ar carrier gas was passed through an ethanol reservoir maintained at 40 °C to ensure stable vaporization. The ethanol vapor concentration was controlled by adjusting the carrier gas flow rate. To prevent condensation, all ethanol delivery lines were heated to 50–80 °C.

At the start of each experiment, the system was evacuated and backfilled with Ar to remove residual gases. During the heating stage, only Ar or diluted H_2/Ar was introduced until the target temperature was reached. Once stabilized, ethanol vapor carried by H_2/Ar was supplied into the reactor to initiate CNT growth. Growth was typically carried out at 850–950 °C for 30 minutes at atmospheric pressure. After the reaction, the carbon source was stopped and the system was purged with Ar while cooling to room temperature.

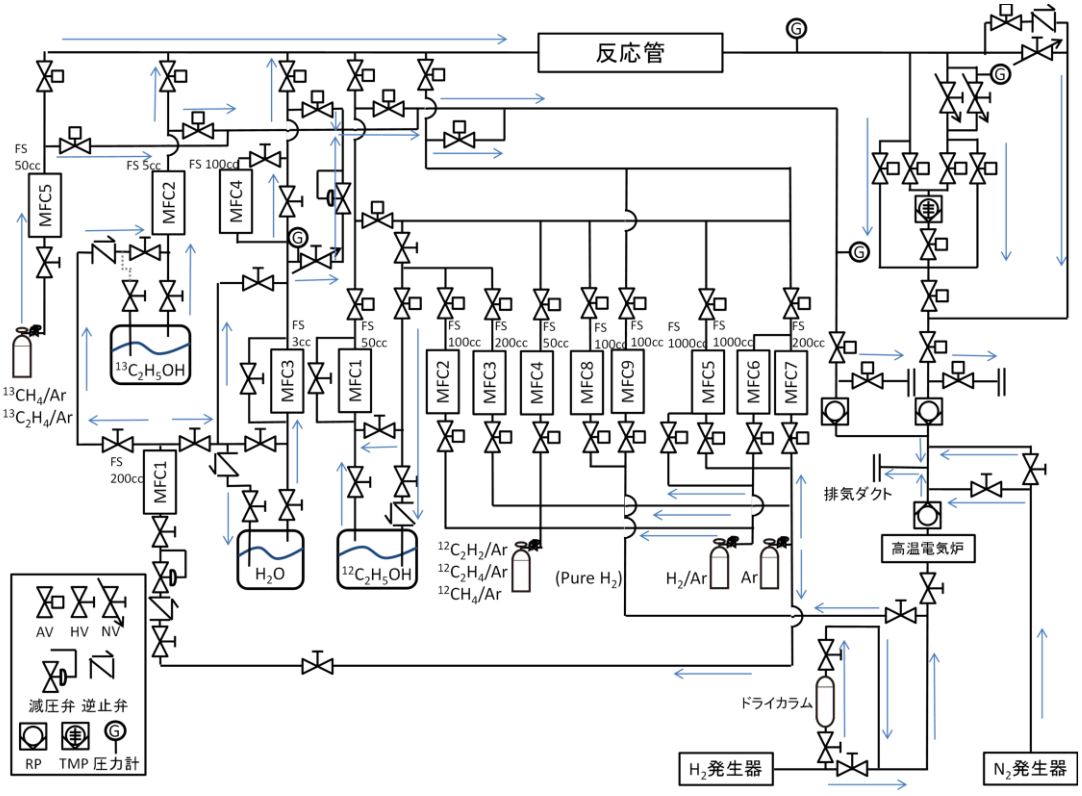


Figure 2.3 Gas piping diagram of multi-temperature zone CVD system.

2.2 Fabrication of electrodes on aligned CNT samples

Following CNT growth, electrodes were fabricated through a combination of photolithography and electron-beam lithography (EBL) to define both alignment markers and nanoscale contacts. The overall process included photoresist coating, lithographic patterning, metal deposition via electron-beam evaporation, and subsequent lift-off.

For the optical lithography step, a three-layer resist structure consisting of hexamethyldisilazane (HMDS), LOR-3A, and OFPR-800 was employed to facilitate clean lift-off. Substrates were first dehydrated by baking at 110 °C to remove surface moisture. HMDS was spin-coated and baked at 120 °C to promote resist adhesion, followed by the application of LOR-3A at 150 °C to provide an undercut profile. Finally, OFPR-800 was spin-coated and baked at 110 °C to form the top imaging layer. Exposure

was carried out using the digital light processing (DLP) projection system (Fig. 2.6 (a)), with exposure times adjusted according to the optical magnification, and subsequent development was performed in a TMAH-based developer for 60 s. After rinsing in deionized water and drying, the patterned resist was ready for metallization.

Alignment markers were deposited on the substrates prior to SEM imaging. The fabrication process and design of the alignment markers used for CNT localization are summarized in Fig. 2.4. For this purpose, a DC magnetron sputtering system (Quick Coater SC-701MkII ADVANCE, Sanyu Electron) was employed (Fig. 2.5). The device uses Ar plasma to sputter target materials onto the sample surface under controlled vacuum conditions. Au was used as the target material, and plasma sputtering was carried out for approximately 1 min at an Ar pressure of ~1.5 Pa. During deposition, a stable purple plasma was generated in the chamber, ensuring uniform coverage of the exposed substrate surface. The resulting Au markers exhibited sufficient conductivity and optical contrast, which allowed for clear visualization under both optical microscopy and SEM. Lift-off was performed by immersing the samples in N-methyl-2-pyrrolidone (NMP) at 90 °C for 1 h.

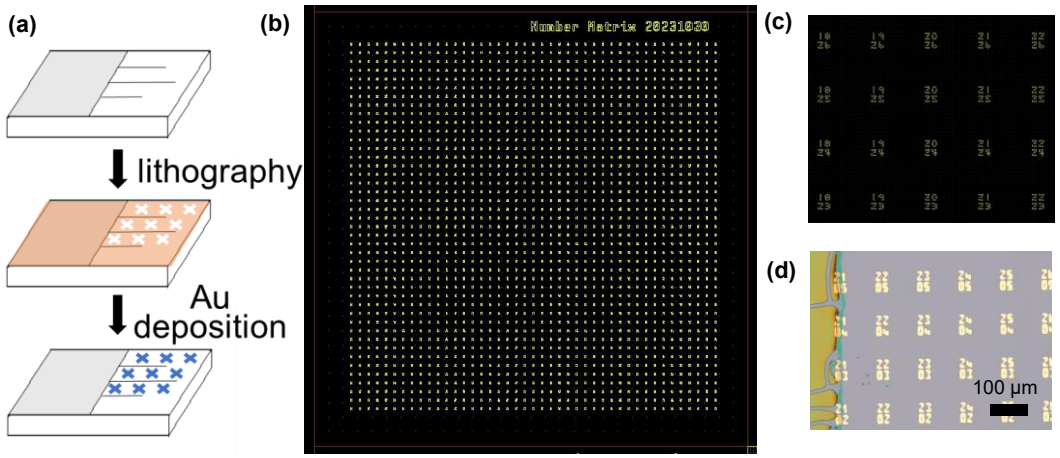


Figure 2.4 (a) Fabrication procedure of the alignment markers, consisting of photolithographic patterning followed by Au deposition. (b) Layout of the photomask used to define the marker array.

(c) Magnified view of the photomask pattern showing the numerical marker elements. (d) Optical microscopy image of the fabricated Au alignment markers on the substrate.

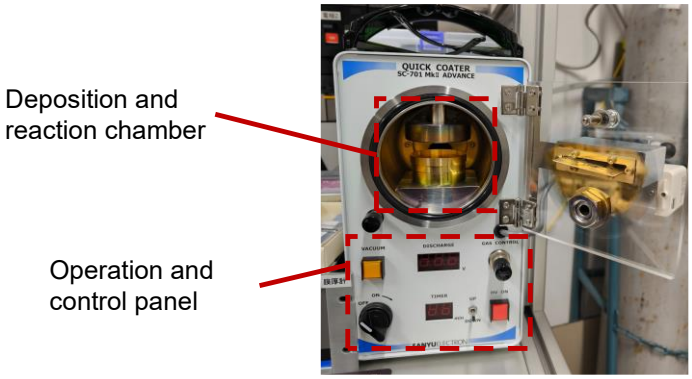


Figure 2.5 Photograph of the quick coater system.

After CNT localization, nanoscale electrodes were fabricated using EBL at the university's nanofabrication platform. A high-resolution resist, ZEP520A diluted in anisole at a 1:3 ratio, was spin-coated at 2000 rpm for 60 s and baked at 180 °C for 3 min. The patterns were written at 150 keV using EBL system (ELS-BODEN OU4801) (Fig. 2.6 (b)), taking advantage of the high beam energy for sub-100 nm feature definition. Following exposure, the resist was developed in ZED-N50 for 90 s and rinsed in isopropanol before nitrogen drying. Metal electrodes, typically consisting of Ti/Au, were deposited by electron-beam (EB) evaporation.

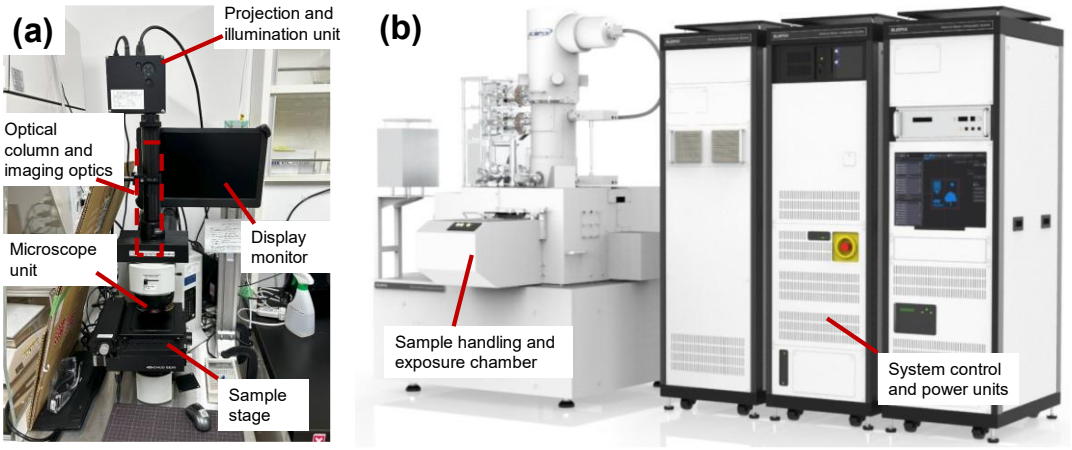


Figure 2.6 (a) DLP-based photolithography system. (b) EBL system (ELS-BODEN OU4801) employed for high-resolution patterning of nanoscale features.

Metal electrodes were deposited using an Anelva L-043E EB evaporation system (Fig. 2.7). Prior to deposition, the chamber was evacuated to ~10^{-4} Pa. Titanium of 50 nm was used as the adhesion layer, followed by Au with typical thicknesses of 450 nm or, in some cases, 950 nm. The deposition rate and thickness were monitored by a quartz crystal microbalance integrated in the EB system. Care was taken to maintain stable beam current and substrate position during deposition to ensure uniform film coverage. Lift-off was performed by immersing the samples in NMP at 90 °C for 1 h.

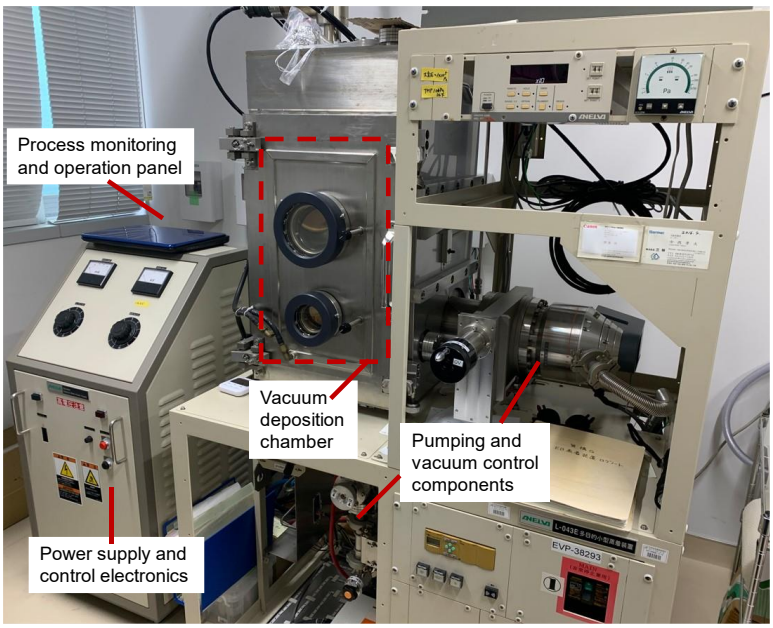


Figure 2.7 Photograph of the Anelva L-043E EB evaporation system.

This two-step lithography approach—using optical lithography for large-area alignment markers and electron beam lithography for nanoscale electrode definition—enabled reliable localization of individual CNTs and precise fabrication of source–drain contacts. The integration of SEM-based CNT mapping with lithographic alignment ensured that electrodes could be reproducibly positioned on isolated CNTs for subsequent electrical measurements.

2.3 Characterization techniques

2.3.1 Raman spectroscopy

Raman spectroscopy is a widely used characterization method based on inelastic light scattering. When monochromatic light interacts with a material, most photons are elastically scattered, while a small fraction undergoes an energy change due to interactions with vibrational, rotational, or electronic states of the system, as illustrated in

Fig. 2.8 (a). The resulting energy difference between the incident and scattered photons is defined as the Raman shift, expressed in units of cm^{-1}. By recording the intensity of the scattered light as a function of the Raman shift, a Raman spectrum is obtained, which serves as a sensitive probe of the material's molecular structure and chemical composition, as shown in (Fig. 2.8 (b).

For CNTs, Raman spectroscopy is a highly sensitive and widely used technique for probing structural quality, vibrational modes, and electronic characteristics of sp^2 nanocarbon materials [159–161]. It provides detailed information on defect density, tube diameter, chirality distribution, and intertube interactions. Characteristic CNT Raman features include the D-band (associated with disorder-induced scattering), the G-band (originating from in-plane vibrational modes of sp^2 carbon), the 2D-band (a second-order double-resonance feature), and the radial breathing mode (RBM), which is uniquely sensitive to nanotube diameter. Representative Raman signatures of semiconducting and metallic CNTs, used as references for interpreting RBM and G-band features in this study, are shown in Fig. 2.8 (d). Because these vibrational signatures respond to strain, defects, doping, and environmental interactions, Raman spectroscopy is particularly effective for evaluating the structural integrity of gas-flow-directed CNTs, which often grow as ultralong, low-defect, individual nanotubes.

In this study, Raman spectroscopy was employed to assess the crystallinity, defect levels, and diameter distribution of aligned CNTs at room temperature. Two Raman systems were used. Measurements were first carried out with the laboratory HORIBA LabRAM HR-800 spectrometer equipped with a 633 nm laser and a 100× objective lens (spot size ~1 μm) (Fig. 2.8 (c)). This setup was used primarily for rapid characterization of CNT growth regions and evaluation of D-/G band evolution under different synthesis conditions. For high-precision measurements on individual CNTs, especially ultralong tubes produced by gas-flow-directed growth, additional experiments were conducted using the shared-facility RAMANtouch VIS-NIR-OUN system (532 nm excitation). This

instrument offers line-scan capabilities, which are advantageous for mapping Raman signals along a single CNT and assessing diameter variations, defect distributions, and local strain profiles. The higher excitation efficiency at 532 nm also enhances RBM detection, enabling more accurate determination of CNT diameter and semiconducting/metallic assignment.

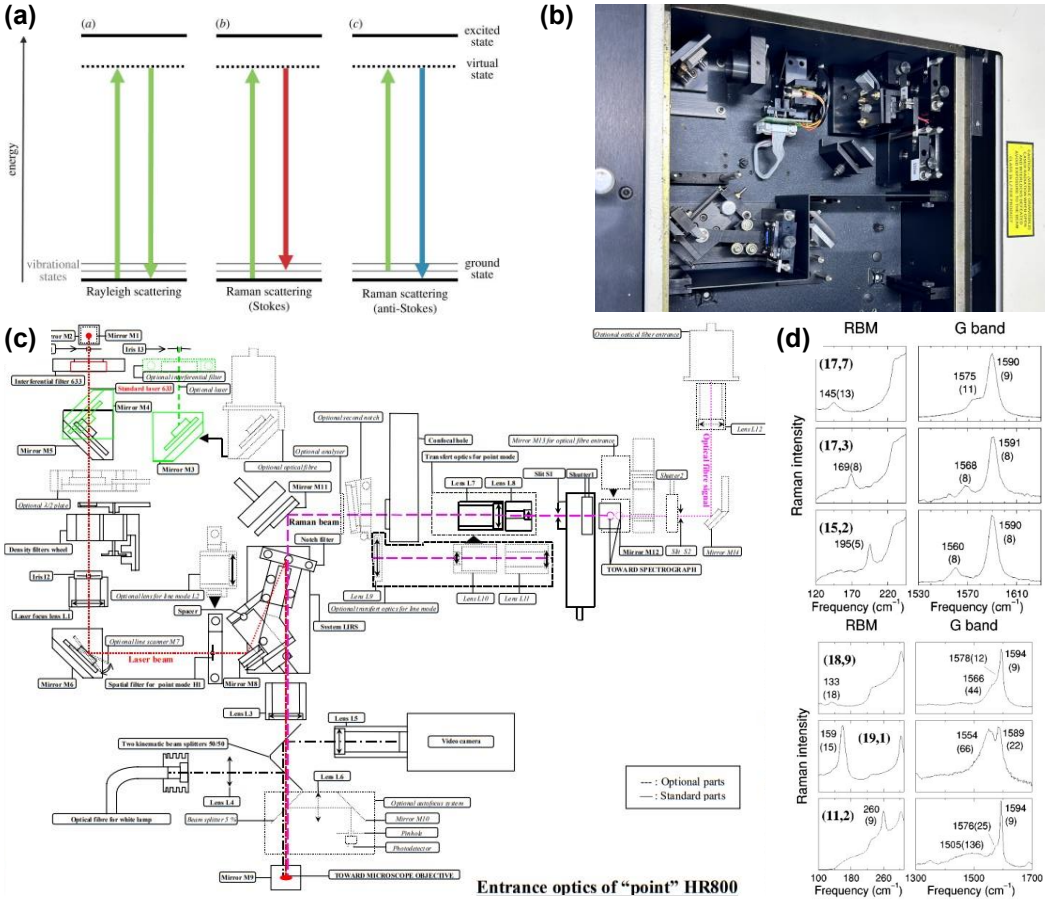


Figure 2.8 (a) Rayleigh scattering and Raman scattering **[162]**. (b) Interior view of the HORIBA LabRAM HR-800 spectrometer. (c) Schematic presentation of typical Raman spectroscopy instrument. (d) The RBM and G-band Raman spectra for three isolated semiconducting CNTs and three isolated metallic CNTs **[160]**.

2.3.2 Atomic force microscopy

The operating principle of atomic force microscopy (AFM) is governed by the interaction between a sharp probe tip attached to the end of a cantilever and the sample surface [163]. As the tip approaches or comes into contact with the surface, various short range and long range forces act on the cantilever, including van der Waals interactions, electrostatic forces, and, in some cases, chemical bonding forces. These interactions induce a mechanical deflection of the cantilever, which can be quantitatively described using Hooke's law. The deflection leads to a change in the position of a laser beam reflected from the cantilever onto a position sensitive photodiode, resulting in a measurable variation in the detected light signal. This signal is used as a feedback parameter to continuously adjust the vertical position of the cantilever during scanning (Fig. 2.9 (a)). By regulating the interaction force or the corresponding response signal, AFM enables high resolution mapping of surface topography at the nanometer scale.

The cantilever is commonly fabricated from silicon or silicon nitride and terminated with an ultra sharp tip whose radius is typically on the order of a few nanometers (Fig. 2.9 (b)). Such a small tip radius is critical for accurately resolving the nanoscale geometry of carbon nanotubes. Because CNTs exhibit diameters on the order of 1–3 nm for single-walled tubes, AFM is one of the most reliable methods for determining their diameter, mapping their alignment, and assessing surface cleanliness. AFM is especially valuable for ultralong, gas-flow-directed CNTs because it allows direct visualization of individual tubes over extended distances and provides insight into local variations such as bundling, surface adsorbates, or substrate interactions.

In this study, AFM measurements were carried out to characterize the height, diameter, and morphology of aligned CNTs. The HITACHI AFM5100N system was operated in dynamic (tapping) mode at room temperature (Fig. 2.9 (c)). This mode minimizes lateral forces on the CNT and reduces the likelihood of displacing or damaging

suspended or weakly adhered segments. Both topographic and phase images were acquired simultaneously, allowing us to distinguish CNTs from surface residues and to examine tip–CNT interaction contrast. Scan resolutions of 512 × 512 or 1024 × 1024 pixels were used, with scan sizes ranging from 500 nm to 10 μm per frame depending on the target feature. Fig. 2.9 (d) shows a representative topographic AFM image of a single CNT lying on the substrate, while Fig. 2.9 (e) provides a corresponding height line profile used to extract CNT diameter and evaluate imaging quality. Together, these AFM measurements provide essential structural information for analyzing the morphology and continuity of gas-flow-directed CNTs.

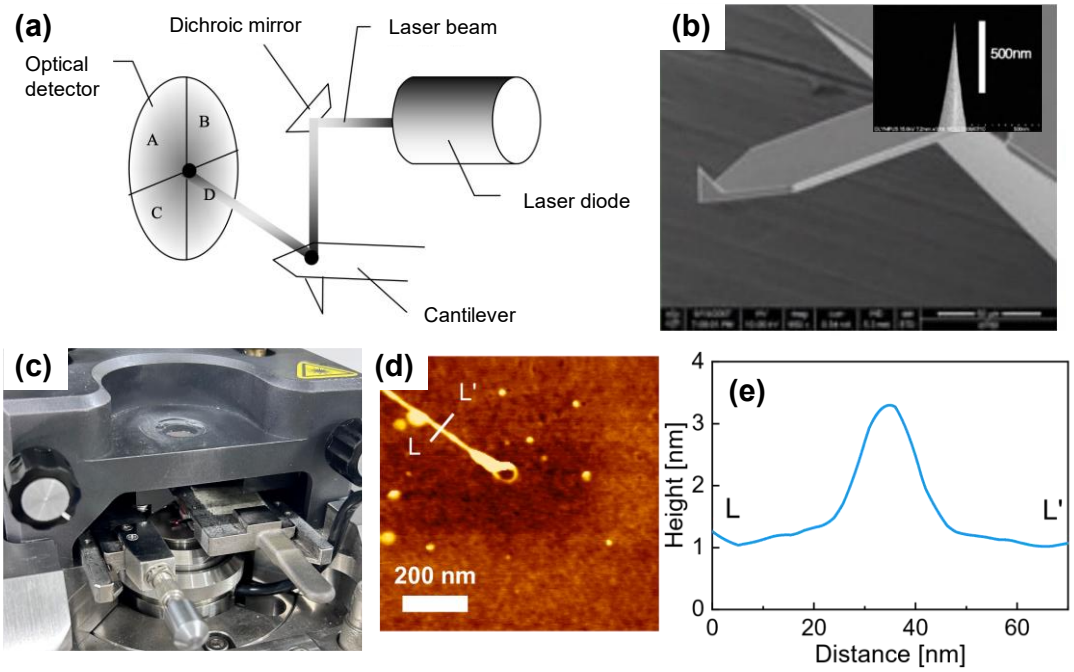


Figure 2.9 (a) Schematic of the AFM operating principle. (b) SEM image of the AFM cantilever. (c) Work platform of the HITACHI AFM5100N used for AFM measurements. (d, e) Typical AFM phase image and corresponding height profile of a gas-flow-directed CNT.

2.3.3 Scanning electron microscopy

Scanning electron microscopy (SEM) is a powerful surface characterization

technique based on the raster scanning of a highly focused high-energy electron beam across the sample. The interaction between the incident electrons and the sample generates multiple types of signals, including secondary electrons, backscattered electrons, and characteristic X-rays, which can be detected to construct an image (Fig. 2.10 (a)). Among these signals, secondary electrons are most commonly employed because of their strong surface sensitivity and their effectiveness in revealing fine morphological details, particularly for one-dimensional nanostructures such as CNTs.

In the context of CNTs, SEM imaging relies on contrast mechanisms that arise from electron–sample interactions that differ markedly depending on whether the CNTs are suspended, supported on conducting substrates, or lying on insulating substrates [164,165]. For suspended CNTs, direct secondary-electron emission from the nanotube dominates the contrast, allowing individual tubes to be visualized even when their diameters (~1–3 nm) are smaller than the electron-beam diameter. Low primary electron energies (~0.5–1 keV) are particularly effective for imaging suspended CNTs, as the secondary-electron yield of carbon peaks in this range and enhances visibility. However, prolonged irradiation can induce hydrocarbon deposition that thickens the apparent CNT diameter, making diameter estimation unreliable. When CNTs rest on insulating substrates such as SiO_2, the dominant contrast mechanism shifts to electron-beam-induced currents (EBIC) charging. Irradiation generates electron–hole pairs in the insulator, resulting in local positive charging that suppresses secondary-electron emission from the substrate. A CNT that is electrically connected—either to the substrate or indirectly to the environment—provides a conductive pathway for charge dissipation. This restores secondary-electron emission near the CNT, producing a bright, broadened feature around the tube. The width of this bright halo is governed by the lateral range of the incident electron beam in the substrate, typically on the order of tens of nanometers at ~1 keV. This charging-contrast mechanism enables individual CNTs to be identified even at low magnification and is widely used to map CNT distributions on insulating

substrates

In this study, SEM imaging was performed using the ZEISS Nvision 40D system equipped with NPVE capability (Fig. 2.10 (c)), which provides higher resolution and more advanced detection modes compared with standard SEM platforms. This system was used for most high-resolution CNT imaging. For routine inspection and device-level imaging, a secondary S-4800 SEM (Hitachi) was also used. Imaging was conducted at low accelerating voltages (typically 0.5–2 kV) to enhance surface contrast while minimizing potential electron-beam damage to suspended or thin CNTs. Representative SEM images of aligned CNT grown by gas-flow-directed growth is shown in Fig. 2.10 (d), illustrating their uniform alignment and continuous morphology across the substrate. SEM thus serves as an essential tool for evaluating the growth quality of gas-flow-directed CNTs, complementing Raman spectroscopy and AFM in providing a comprehensive understanding of CNT structure and alignment.

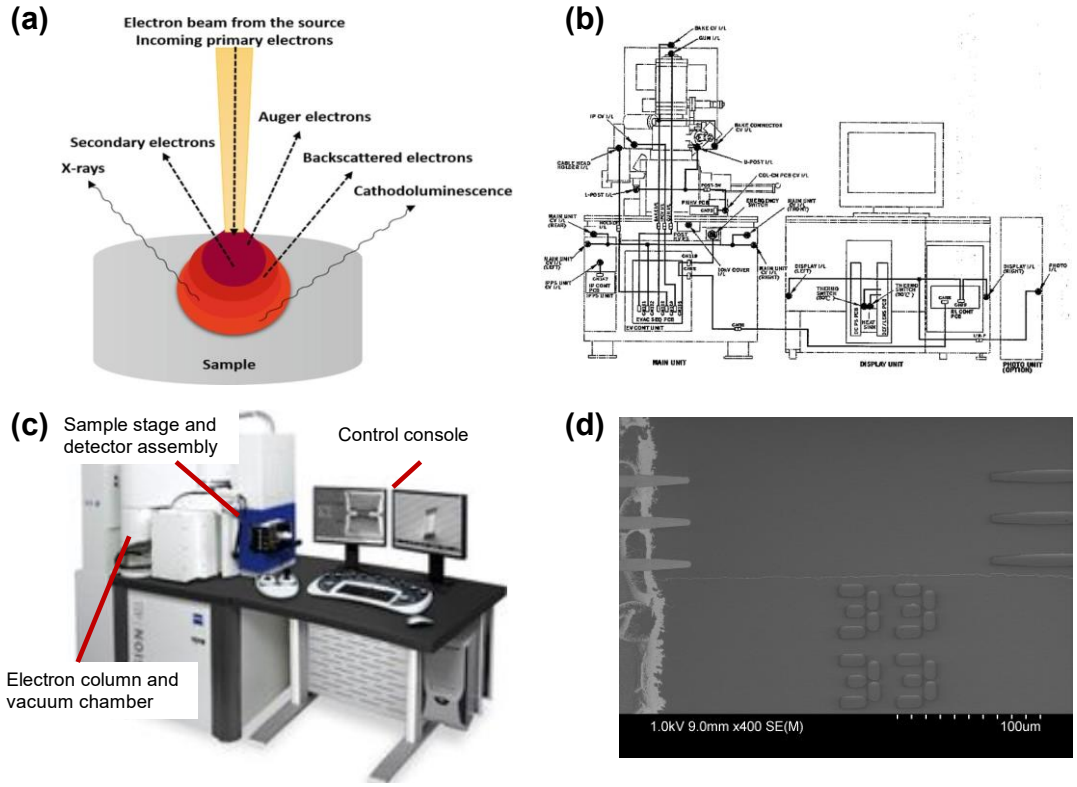


Figure 2.10 (a) Schematic representation of various signals for SEM imaging **[166]**. (b) Schematic

instruments of S-4800 SEM. (c) Photograph of the Anelva L-043E EB evaporation system. (d) Typical SEM image of gas-flow-directed CNT sample.

2.3.4 Electrical measurements

Electrical transport measurements were performed using a semiconductor characterization system consisting of a precision source/measure unit (SMU; Keysight B2912A) and two types of probe stations. For measurements at ambient conditions, a standard manual probe station equipped with a micromanipulator stage was employed, enabling direct contact between probes and device electrodes under an optical microscope (Fig. 2.11 (a)). The probe configuration allowed assignment of source, drain, and gate electrodes, with the SMU channels connected accordingly to perform current–voltage (I–V) characterization.

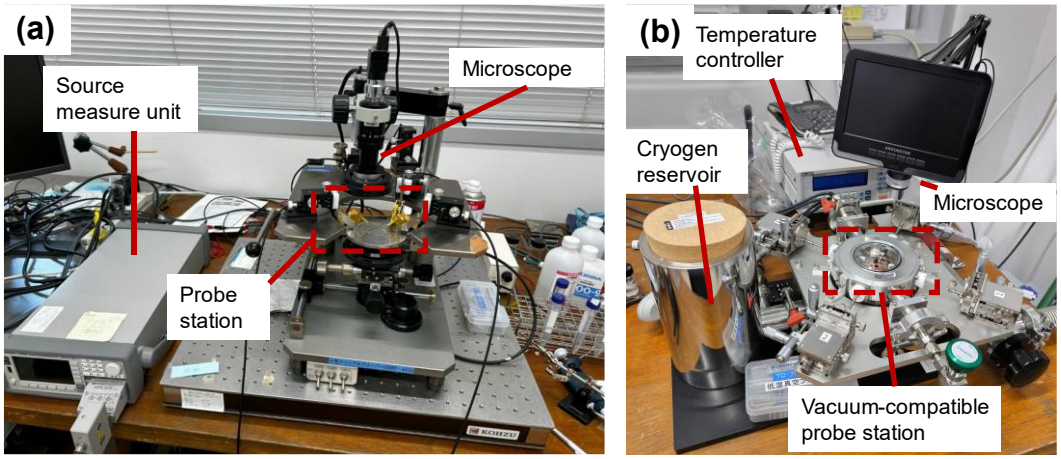


Figure 2.11 (a) Setup for electrical transport measurements performed at room temperature, equipped with a probe station and semiconductor parameter analyzer. (b) Vacuum-compatible probe system used for low-temperature electrical measurements.

For variable-temperature measurements, a temperature-controlled vacuum probe station (manufactured by Nagase Techno-Engineering, model HMP400/600) was utilized

(Fig. 2.11 (b)). The system is equipped with a sealed vacuum chamber and a turbomolecular pumping unit, enabling measurements under pressures down to ~10^{-3} Pa. A liquid nitrogen cooling system allowed temperature control from 80 K to 300 K, with a resistive heater integrated in the sample stage for temperature stabilization at elevated conditions. During measurements, the device chip was mounted on an insulating sapphire substrate to ensure thermal contact while preventing leakage currents. Electrical probes were carefully positioned on the designated source, drain, and gate electrodes using a built-in microscope, and SMU biasing/measurement was performed once thermal equilibrium was established at the desired temperature.

This combined setup enabled reliable electrical characterization of carbon nanotube devices across a wide range of conditions, from room temperature in air to cryogenic temperatures in vacuum.

Chapter 3. Gas-flow-directed growth of aligned carbon nanotubes from nonmetallic seeds

3.1 Background

Carbon nanotubes (CNTs) [1,2] have garnered attention due to their excellent properties [5,33] and various promising applications [167–171]. In particular, aligned CNTs grown on surfaces by chemical vapor deposition (CVD) with macroscale lengths, low defects, and parallel alignment are ideal candidates for next-generation electronics applications [22,172] and have attracted research interest [127,136]. In the past decades, significant progress has been made toward the controlled synthesis of aligned CNTs on substrate surfaces [128,131,173]. Gas-flow-directed growth, also known as kite growth, is a well-established method [21] and has several advantages over other methods, including ultralong CNT length and wide applicability of the as-formed air-suspended CNTs. The “kite mechanism” was first proposed by Huang et al. to explain the growth of aligned CNTs [15]. In this mechanism, convective effects caused by vertical temperature gradients overcome the catalyst–substrate interaction and lift both the catalyst at the CNT tip and the CNT; then, the horizontal laminar flow carries the CNTs and aligns the growing CNTs [47]. During the growth process, the catalyst floats above the substrate and moves with the growing CNT tip, also known as the tip-growth mode. In contrast, in base growth, the catalyst is at the root of the CNT and does not move with the growing CNT. During tip growth along with gas-flow-directed growth, the strong van der Waals interaction between CNTs and substrates fixes the originally floating CNTs on the substrates after their growth. Significant advances have been made recently toward the controlled synthesis of CNTs by gas-flow-directed growth due to continuous research efforts [23,24,26,27].

Catalyst nanoparticle (NP) preparation, particularly the selection of their elements, has a significant impact on the growth behavior of CNTs via CVD. A typical gas-flow-

directed growth process uses metal NPs as catalysts, such as Fe [15], Co [18], and Cu [91]. Typical transition metal catalysts, such as Fe and Co, mediate the CNT growth through their NPs in the liquid phase [110]. CNT growth from liquid NPs usually occurs via a so-called vapor–liquid–solid (VLS) mechanism [111], where carbon atoms are supplied to the CNT through the bulk diffusion of carbon in the NPs. These molten NPs tend to deform during the synthesis of CNTs at high temperatures, which is considered the main origin of defect formation in CNTs [42]. The CNT tips connected to catalysts may not be used for usual device fabrication. However, during growth, metal catalysts may be once evaporated in the chamber and redeposited on CNTs, resulting in contamination by metal NPs as reported in a literature [18,27]. Purification processes are necessary to remove these contaminants before further utilization, but such processes often introduce additional defects in the CNTs[174]. A possible solution to overcome the drawbacks of metal catalysts is to grow CNTs from nonmetallic NPs. Hereafter, the NP used for CNT growth is referred to as the "growth seed" instead of a "catalyst"; the nonmetallic NP has negligible catalytic activity but plays a role as a template for CNT growth [116]. As a representative nonmetallic growth seed, nanodiamond (ND) [106,117,158] has attracted research interest due to its unique properties. As the diffusion of carbon in diamond is negligibly small compared to metals such as Fe [175,176], the bulk diffusion of carbon is unlikely to promote the growth of CNTs. Therefore, the growth of CNTs from ND must be driven by the surface diffusion of carbon, known as vapor–solid surface–solid (VSSS) mechanism [106,116]. ND as a growth seed offers excellent thermal stability at high temperatures and facilitates the growth of low-defect CNTs without any residual metal impurities. ND is also beneficial for device fabrication because it can facilitate CNT growth on any substrate type, including metal electrodes [106]. Despite these advantages, the gas-flow-directed growth of CNTs from ND has not been reported yet, presumably because of low CNT growth yields due to the limited catalytic activity of ND and narrow window of growth conditions. Moreover, CNT yield from the

gas-flow-directed growth is low even when metal catalysts are used, and the co-influence of ND and gas-flow-directed growth further worsens this issue. To overcome this issue, we have attempted to further understand the CNT growth mechanism, especially the nucleation of cap structure at the initial growth stage [117,158]. This strategy can be extended to improve the yield of CNTs from ND via gas-flow-directed growth.

In this study, we achieved the gas-flow-directed growth of aligned CNTs from nonmetallic growth seed, most likely ND-derived carbon NPs. After confirming the successful growth of aligned CNTs on ND-deposited substrates, we conducted a parametric study to investigate the effects of temperature and gas flow rate on the gas-flow-directed growth of CNTs. Scanning electron microscopy (SEM) is used to eliminate the possible contribution of metal impurities. Furthermore, the gas-flow-directed growth mechanism is further evaluated using SEM and atomic force microscopy (AFM) images to determine whether the growth occurred via the tip-growth or base-growth modes. Finally, structural analysis of the aligned CNTs grown from nonmetallic NPs was performed using Raman spectroscopy and AFM, providing a comprehensive understanding of the structural properties of the synthesized CNTs.

3.2. Experimental section

3.2.1. Deposition of ND growth seeds

Purified ND particles prepared via the detonation method (original diameter: 4–14 nm) [157] and dispersed in ethanol (2.0 wt%) were used as the growth seeds to synthesize aligned CNTs. To support the ND particles, ~1 cm × 1 cm Si substrates with a 300-nm-thick thermal oxide layer were cleaned by ultrasonication sequentially with acetone, ethanol, and deionized water, followed by an ozone treatment process (L-UV253, Japan Electronics Industry) by flowing oxygen at a flow rate of 6 L/min under ultraviolet light for 48 min. After cleaning, adhesive tapes were applied to half of the substrate as a mask, and 10 μL of ND/ethanol solution was dropped on the other half of the substrate and dried naturally. After peeling off the tapes, followed by the heat treatment described in Section 2.2 to remove the glue, half of the substrate without ND was designated for aligned CNT growth.

3.2.2. Pretreatment of ND growth seeds

Herein, a 1040-mm-long quartz tube with a semicircular cross section of 44-mm diameter fixed in a tubular CVD furnace (GE-1000, GII Techno) with a heating length of 890 mm was used as the reactor. Figure 1 illustrates the growth process of long, aligned CNTs on the substrate via the gas-flow-directed growth mechanism comprising two steps. In step 1, ND was pretreated for preparation as a growth seed. The quartz tube was heated to 600°C in advance without the samples; then, the substrates with ND particles were pushed into the quartz tube in the middle of the furnace and kept at 600°C in air for 10 min to remove any residual impurities. In this treatment, the diameter of the ND particles decreased to less than ~4 nm, which is the appropriate size for CNT growth [158].

3.2.3. Synthesis of aligned CNTs from ND growth seeds

Step 2 was the gas-flow-directed growth of CNTs, where optimized conditions were investigated by controlling the temperature and flow rate. After the heat treatment of the ND-deposited substrates (Fig. 3.1, step 1), the furnace temperature was increased to the synthesis temperature (850°C–950°C) under continuous 20-sccm H_2 (3%)/Ar flow at 85 kPa. The CNT growth was initiated by introducing 35 sccm H_2 (3%)/Ar bubbling through an ethanol reservoir at 40°C and 420 sccm H_2 (3%)/Ar through another gas line (Fig. 1, step 2). The growth process was conducted at atmospheric pressure, and the partial pressure of ethanol was estimated to be ~1.4 kPa. After 30 min of growth, the reaction was terminated by switching the gas to Ar. We employed relatively long growth time to compensate for the low efficiency of CNT growth from ND. Finally, the furnace was cooled to room temperature with a continuous flow of Ar. Fe catalyst was also used in the control experiment, as shown in Fig. 3.2.

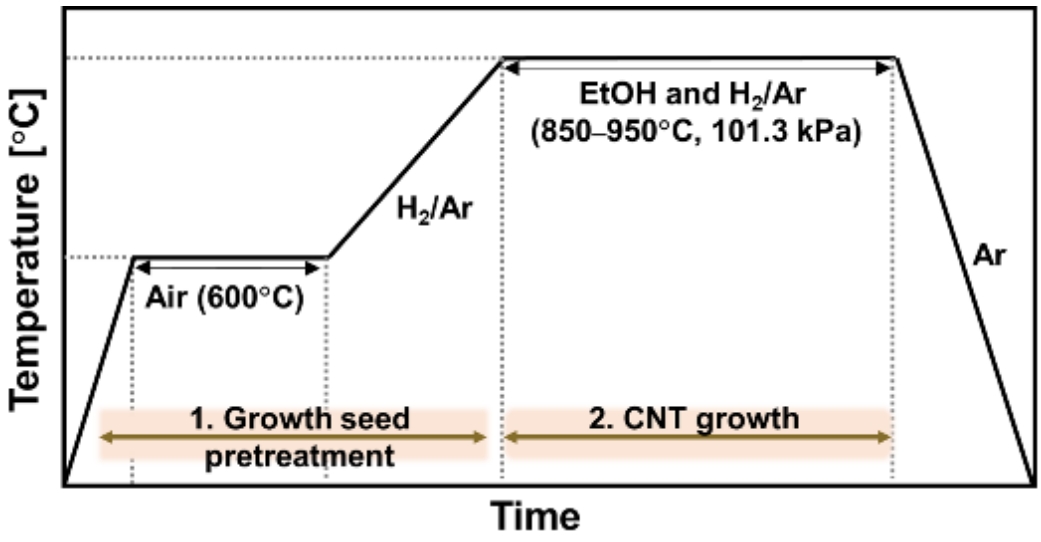


Figure 3.1 Schematic of the pretreatment of ND growth seed in the reactor (step 1) and the subsequent gas-flow-directed growth of aligned CNTs on the substrates (step 2).

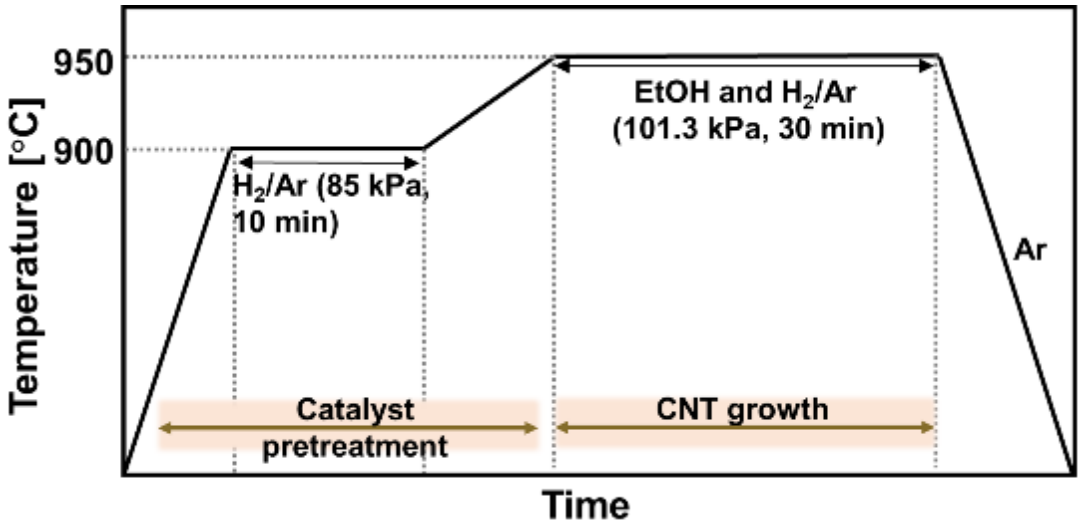


Figure 3.2 Schematic of the gas-flow-directed growth process of CNTs from a metal catalyst (Fe). Fe catalyst was patterned by a dip-pen method using FeCl3 ethanol solution (0.03 mol/l) and a wooden stick. The CNT growth was initiated by introducing 70 sccm of H2 (3%)/Ar bubbling through an ethanol reservoir at 40°C and 840 sccm of H2 (3%)/Ar through another gas line.

3.2.4. Characterization

SEM (S-4800, Hitachi High-Tech) was used to characterize the grown CNTs (acceleration voltage of 1 kV and emission current of 10 μA, upper detector). The growth seeds/catalyst NPs at the tip of the grown CNTs were analyzed in detail based on the SE yield of SEM (acceleration voltage of 5 kV and emission current of 10 μA, upper detector); details are provided in Section 3.2, where we discuss how the SE yield allowed us to distinguish the elements located at the tip of the CNTs. The structure of the CNTs was characterized by Raman spectroscopy (RAMANtouch, Nanophoton) with an excitation laser wavelength of 532 nm and an objective lens of 100x and 0.90 NA, which results in a spatial resolution of approximately 350 nm. Dynamic force mode measurement of AFM (AFM5000, Hitachi High-Tech) was also used to characterize the grown CNTs and the growth seed/catalyst NPs at the tip of the CNTs.

To characterize grown CNTs at the same positions using multiple methods, such as SEM, AFM, and Raman spectroscopy, marker structures (Fig. 3.3) were patterned on the substrates after CNT growth using photolithography, subsequent metal deposition, and lift-off.

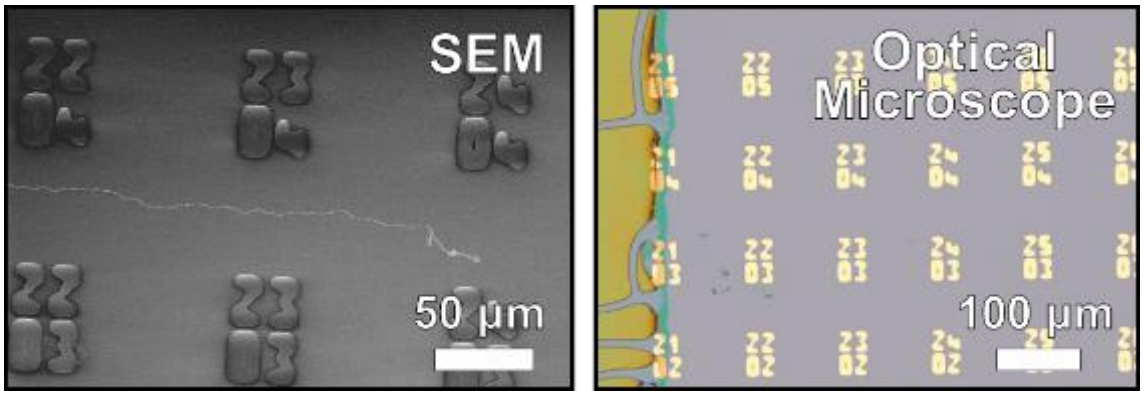


Figure 3.3 SEM and optical microscopy images of the same region where a target CNT exists. The position was adjusted by number-shaped metal markers on the substrate. The vertical boundary toward the left in the optical microscopy image indicates the ND-deposited area (left) and the aligned CNT growth area without ND (right).

3.3 Temperature and gas flow rate dependence of CNT synthesis

We synthesized aligned CNTs on ND-deposited substrates using the aforementioned process under varying growth conditions. Fig. 3.4 (a) shows the SEM images of aligned CNTs grown on SiO_2/Si substrates under optimized temperatures and gas flow rates. As shown, the aligned CNTs extended from the area of deposited ND particles and are longer than 100 μm. The alignment direction of the CNTs is parallel to that of the gas flow. These growth results are similar to those reported previously on gas-flow-directed growth of CNTs using metal catalysts [14–20]. Considering that the substrate is silicon with a thermal oxide layer, there is no possibility of crystal lattice–directed growth, indicating that the growth of the aligned CNTs follows the gas-flow-directed growth mechanism. The confirmation of CNT growth from nonmetallic seed and exclusion of the contribution from metal impurities are provided in Section 3.2.

The occurrence of the gas-flow-directed growth is further understood via fluid dynamics; therein, buoyancy lifts the CNT tips and then the laminar flow guides the stable lengthening of CNTs. Proper buoyancy and laminar flow are essential for stable gas-flow-directed growth. At the same time, CNT growth is governed by the activity of the growth seeds and the carbon supply rate [21], which are closely related to the growth rate even for the gas-flow-directed growth. Thus, the growth condition should be optimized comprehensively from these aspects. The buoyancy and laminar characteristics of the gas flow are evaluated by the Richardson number *Ri* and Reynolds number *Re*. They can be expressed as $Ri = \Delta\rho g h/\rho v^2$ and $Re = \rho v d/\mu$, where $\Delta\rho$, g, ρ, v, d, and μ represent the density difference in vertical length h, gravitational acceleration constant, gas density, gas flow velocity, inner diameter of the reactor tube, and coefficient of gas viscosity, respectively [139,138]. According to these formulae, as the process temperature T increases, the *Ri* increases while the *Re* decreases. On the other hand, as the v increases, the *Ri* decreases while the *Re* increases. These relationships are based on the equations of state assuming the ideal gas and the viscosity formula [177]. A decrease in the *Ri*

corresponds to a reduction in buoyancy, whereas a decrease in *Re* promotes a more stable laminar flow. As per the aforementioned relation, achieving proper buoyancy requires an appropriate value of *Ri* and minimum *Re* to promote stable laminar flow. Two strategies can be employed to decrease the *Re* for the efficient growth of aligned CNTs: reducing the gas flow velocity (*v*) and increasing the temperature (*T*). A larger buoyancy (large *Ri*) is simultaneously obtained; however, a too large buoyancy will cause strong gas convection. Therefore, optimizing the growth conditions is crucial to obtain a suitable buoyancy that can lift the growth seed and the grown CNTs into the laminar flow without affecting its stability. We thus examined the effects of the main factors, i.e., the temperature and gas flow rate, on the growth of aligned CNTs separately.

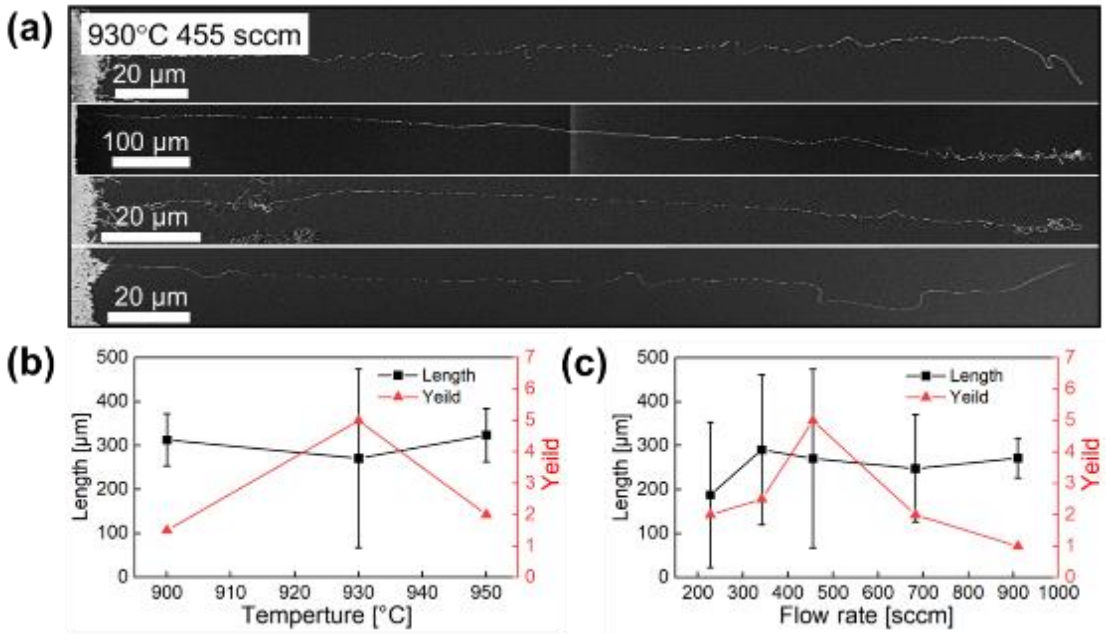


Figure 3.4 (a) SEM images of the aligned CNTs grown on ND-deposited substrates under the optimized condition (445 sccm and 930°C). The horizontal direction from left to right in the images corresponds to the direction of the gas flow. The ND-deposited areas look bright at the left end of the images. (b, c) The average length and the yield of aligned CNTs. CNTs are grown (b) at different temperatures with a flow rate of 455 sccm and (c) with different flow rates at 930°C. The yield was calculated as the average number of aligned CNTs observed per substrate (~1 cm × 1 cm size). The

error bars represent the standard deviation of the length of all aligned CNTs measured for each condition.

We investigated the dependence of temperature on the aligned growth of CNTs. CVD using ethanol as the carbon source is a widely adopted method for aligned CNT growth, owing to the etching effect of hydroxyl radical [88]. Initially, the temperature and gas flow rate were set to 950°C and 455 sccm, respectively, based on the process described by Liu et al. [19] However, in contrast to their study, we chose to employ a lower flow rate in order to achieve a more stable laminar flow under our experimental conditions. Aligned CNTs were grown at varying growth temperatures from 850°C to 950°C and a constant gas flow rate of 455 sccm to evaluate the average length and the yield of aligned CNTs. Two or more substrates with a size of approximately 1 cm × 1 cm were employed for each condition. We defined aligned CNTs as CNTs longer than 50 μm extending from the ND-deposited region that are grown in the gas flow direction. The yield of aligned CNTs was determined by calculating the average number of CNTs observed per substrate under a given condition. This was done by dividing the total number of aligned CNTs observed across all the substrates by the total number of substrates. SEM images of the aligned CNTs grown at different temperatures are shown in Fig. 3.5, and the average length and the yield of the aligned CNTs are plotted against temperatures in Fig. 3.4 (b). Considering fluid dynamics, higher temperatures cause more stabler laminar flows (small *Re*) but also possibly lead to excessive buoyancy (large *Ri*), whereas lower temperatures lead to more unstable flows (large *Re*). CNTs were not grown directionally below 900°C (Fig. 3.5 (a)). At 900°C, CNTs grew more than 200 μm in length but were not well aligned (Fig. 3.5 (b)). The CNTs grown between 930°C and 950°C were generally well aligned; the highest growth yield was obtained at 930°C (Fig. 3.4 (b)).

Gas flow rate dependence was examined at a fixed temperature of 930°C (Figs. 3.4

(c) and Fig. 3.6). The effect of gas flow rate on *Ri* and *Re* is similar to that of temperature. For a lower gas flow rate, *Re* becomes small and the smaller *Re* tends to cause stabler laminar flow. Contrarily, *Ri* possibly becomes large, resulting in significant buoyancy, which is not suitable for stable gas-flow-directed growth. Higher gas flow rates lead to larger *Re* values and cause more unstable flow. Thus, it becomes challenging to grow longer CNTs below 300 sccm (Fig. 3.6 (a)). Above 600 sccm, although long CNTs were grown in the direction of the gas flow, the degree of alignment was not high (Fig. 3.6 (e)). The optimal growth occurred within the range of 300 to 600 sccm, as the CNTs were longer and well aligned. The highest growth yield was realized at 455 sccm (Fig. 3.4 (c)).

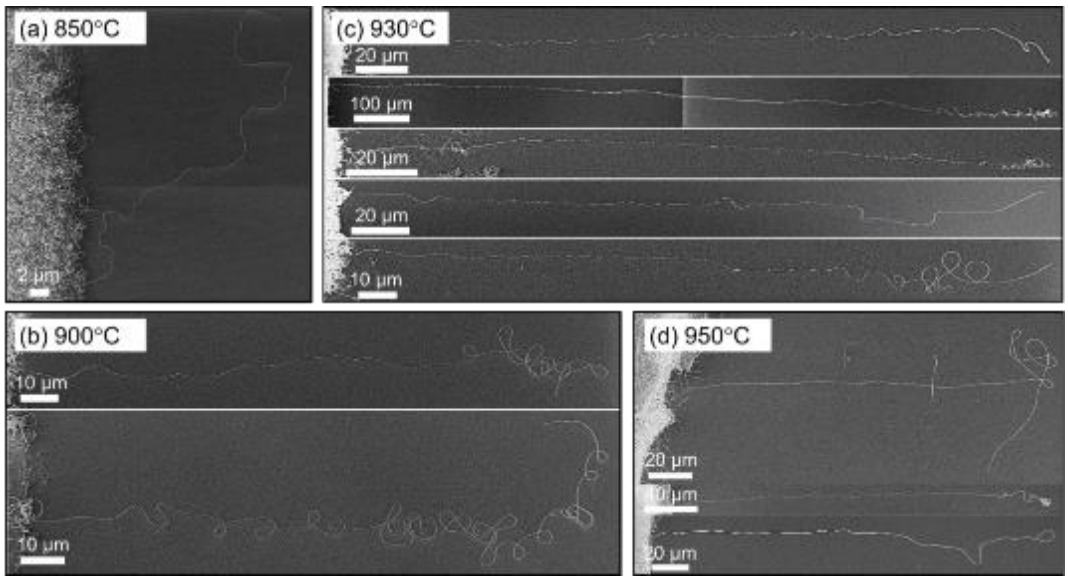


Figure 3.5 SEM images of the aligned CNTs grown on the SiO_2/Si substrate at different temperatures with a flow rate of 455 sccm: (a) 850°C, (b) 900°C, (c) 930°C, and (d) 950°C.

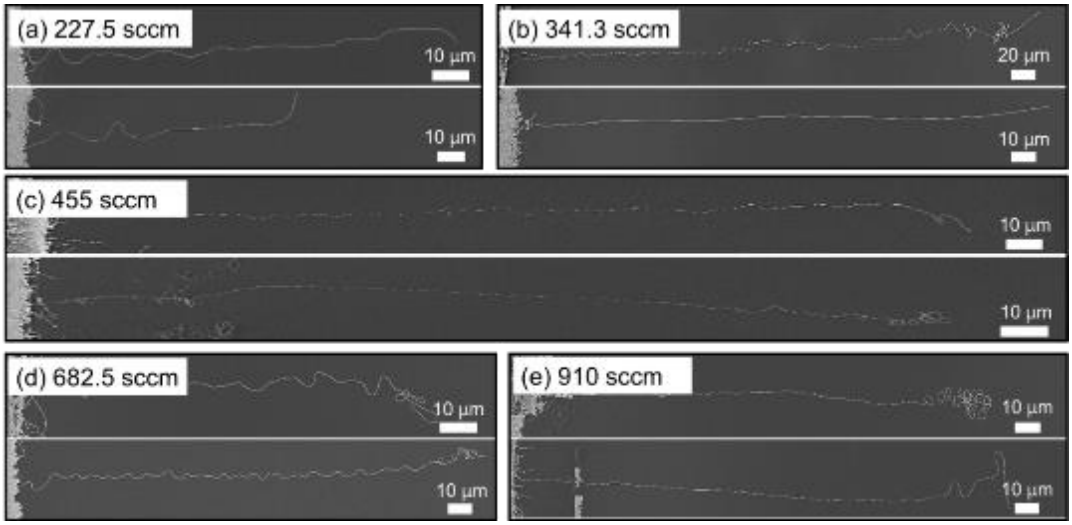


Figure 3.6 SEM images of the aligned CNTs grown on the SiO_2/Si substrate with different flow rates at 930°C: (a) 227.5 sccm, (b) 341.3 sccm, (c) 455 sccm, (d) 682.5 sccm, and (e) 910 sccm.

For CNT growth from ND, the growth behavior is primarily governed by the thermodynamic and kinetic growth driving force [158] rather than by sharply defined phase boundaries. Previous studies have shown that the nucleation and elongation of CNTs on ND are controlled by the balance between carbon chemical potential, temperature, and reaction kinetics, which together determine whether cap formation, continuous elongation, or growth suppression occurs. As a result, the growth process is more appropriately described by continuous growth regimes instead of discrete phases. In the present study, we adopt this growth driving force framework to interpret the experimental growth conditions. Temperature and carbon source partial pressure define the magnitude of the driving force for CNT nucleation and elongation, while gas flow acts as an additional parameter that modifies the effective growth regime by influencing CNT orientation, stability of suspended segments, and local reactant transport. Under sufficiently strong driving force, CNT elongation is sustained, and the presence of laminar gas flow directs the growing CNT into a stable suspended configuration, resulting in gas-flow-directed growth.

We also observe that, although most CNTs grown under gas-flow-directed conditions are well aligned along the flow direction, some CNTs exhibit pronounced entanglement near the tip or even a wavy morphology along the entire length. This behavior indicates that perfect axial alignment is not always maintained during growth and suggests the involvement of local perturbations in the growth environment. The densely bending structures of gas-flow-directed CNTs can therefore be reasonably attributed to disturbances occurring during growth rather than deformation after substrate contact. Strong evidence supporting this interpretation is provided by the work of Zhu et al. [134], who demonstrated that individual ultralong CNTs can form tightly wound and looped structures while remaining fully suspended in the gas phase under acoustic excitation. Although the perturbation in their study was intentionally introduced by an external acoustic field, the formation process of the coiled structures clearly occurred in midair, indicating that suspended CNTs are highly sensitive to flow-field disturbances. In their experiments, they showed that small-scale vortices and velocity fluctuations in the surrounding gas can induce repeated lateral deflections of the CNT tip, leading to the accumulation of closely spaced bends and self-entanglement during continuous growth. Importantly, they emphasized that such structures cannot be explained by post-growth deposition or surface-induced collapse, but instead arise from dynamic interactions between the growing CNT and an unstable flow environment. By analogy, even in the absence of externally applied acoustic waves, local flow instabilities or transient perturbations in conventional gas-flow-directed growth can generate similar bending features. Therefore, the densely curved structures in this work are most consistently interpreted as being formed during growth under gas-flow perturbations, rather than being produced after the nanotubes have contacted the substrate.

3.4 Verification of nonmetallic particles as the origin of CNT growth

Since there remains the possibility that metal impurity in ND contributes to the CNT growth, the NPs at the tip of the aligned CNTs should be carefully examined. The ND solution used herein contained a small but not negligible amount of metal impurities due to the limitations of the production process, with Fe being one of the main components [117]; Fe is an active catalyst for CNT growth. Our previous study indicated that a small concentration of metal impurities (Fe, 80 ppm) in the ND samples do not contribute to the synthesis of CNTs at high temperatures [117,158]. In this study, a lower temperature was used compared to the previous studies, and thus, the impurity metal NPs may possess catalytic activity. Potential methods for identifying the element and structure of the growth seeds include transmission electron microscopy (TEM) and Raman spectroscopy. However, TEM requires a suspended structure of the specimen, and preparing samples to observe the tips of long CNTs is highly challenging. Raman spectroscopy also presents difficulties when applied to individual NPs due to their minute size, which results in an extremely weak signal. Thus, it is difficult to directly distinguish the elements of the NPs at the tip of the CNTs on the substrates. For SEM observation, secondary electrons (SEs) are the most widely used probe in imaging due to their high sensitivity to surface topography and specimen composition [178]. As the elemental difference of carbon and Fe would result in different SE yields, we used SE yield mapping to detect the presence of impurity Fe NPs. Takagi et al. utilized SE yield to investigate the existence of metal catalysts on CNTs [179]. In this study, we extended this method to confirm the presence of nonmetallic seeds.

The SE yield of SiO_2 is higher than that of carbon at any given acceleration voltage [178]. However, a SiO_2 substrate usually appears darker than a CNT in SEM images. SEM observation of CNT is generally performed at a primary electron (PE) energy of around 1 keV. At this energy, the SE yield of SiO_2 is >1 (Fig. 3.7). Under continuous irradiation of the electron beam, the electrons emitted from the irradiated area as SEs are

not supplemented by electrical conduction from surrounding unirradiated areas due to the insulating nature of SiO_2. This results in a positive charge-up on the irradiated area of the SiO_2 substrate, which hinders the emission of SEs with a negative charge from the SiO_2 surface and causes a darker contrast although the intrinsic SE yield of SiO_2 is relatively high. However, when the CNT is in direct contact with the SiO_2 substrate, electrons are supplied from the CNT to the substrate surrounding it through the electron beam-induced current (EBIC), resulting in the recovery of the SE yield. This leads to a brighter contrast of the substrate around the CNT, making the CNT appear thicker; this width depends on the EBIC range [164]. While EBIC imaging is useful for observing CNT, the intense SE emission of the substrate around the CNT can make it difficult to observe a NP connected to the CNT tip. Thus, the effect of the EBIC on the CNT should be eliminated. As the PE energy increases, the EBIC range also increases until it reaches the Si conductor substrate underneath the SiO_2 layer. At this point, electrons are supplied from the Si substrate to the entire SiO_2 surface through the EBIC, which recovers the SE yield and makes the entire substrate appear with the same contrast. To ensure the penetration of the 300-nm-thick SiO_2 layer and eliminate the effect of EBIC, a higher PE energy could be used. However, this may result in significant damage to the CNTs [180]. Therefore, a PE energy of 5 keV was selected as it reduces the effect of EBIC current while minimizing damage to the CNTs (Fig. 3.7). Since the SE yield of Fe is higher than that of carbon [178], it is easy to confirm the presence and absence of Fe NPs at CNT tips at a PE energy of 5 keV. Both ND and CNT are composed of carbon, and although they have different SE yields due to their different structures, they have approximately the same SE yield [181]. Their SE yields are lower than that of Fe, thus resulting in CNT tips with a similar contrast to their bodies if CNT tips are connected with ND particles or free from any NPs, including metals.

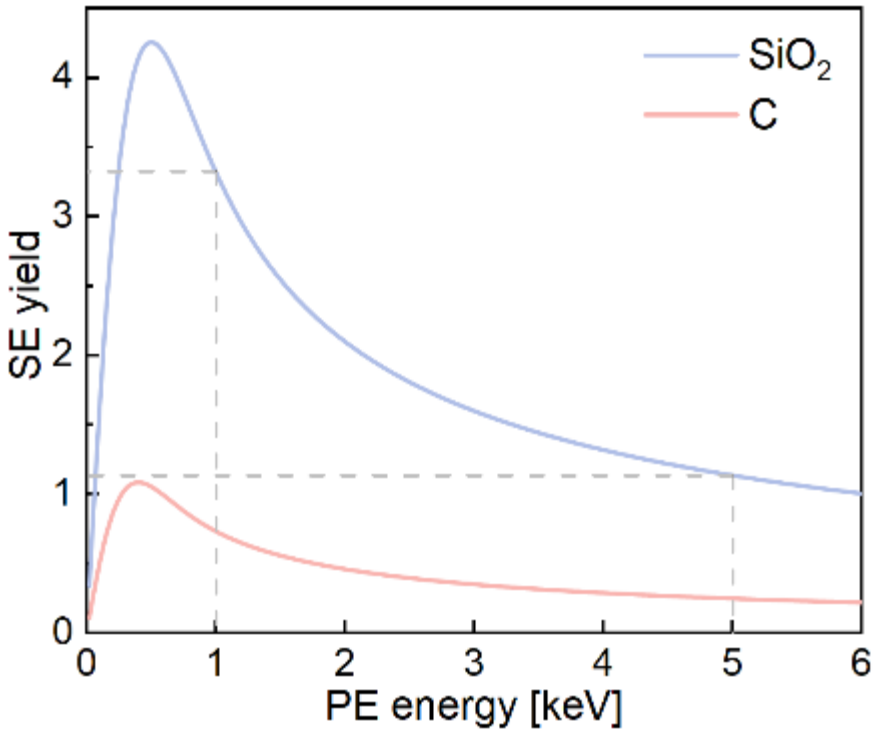


Figure 3.7 Plot of SE yield at different PE energies. The calculation formula and data for C **[182]** and the data for SiO_2 **[183]** were obtained from previous studies.

Based on the discussion above, we investigated the presence of impurity metal NPs at the CNT tips by SE yield mapping at an accretion voltage of 5 kV (PE energy of 5 keV). Fig. 3.8 (a) shows the SEM images and SE intensity profile of a typical CNT synthesized by depositing ND growth seeds. We also conducted the same observation of the control samples synthesized by depositing Fe catalysts (Fig. 3.8 (b)). Care was taken to avoid the saturation of the brightness at the tips of the CNTs during the SE yield map measurements. In the subsequent discussions, the terms “bright” and “dark” are used to describe CNT tips, which respectively imply that a CNT tip is observed to be brighter than and as dark as the corresponding CNT body in SE yield mapping. For a concise expression of the CNT samples, the term “ND-deposited samples” and “Fe-deposited samples” are used to refer to the samples grown from ND, which may contain metal impurities, and the

samples grown from Fe, respectively. For the ND-deposited samples, dark tips were frequently observed from long CNTs (Fig. 3.8 (a)). For the Fe-deposited samples, bright particles were observed at the tips of long CNTs (Fig. 3.8 (b)), whose appearance was consistent with that reported in a previous study on SE yield mapping of CNTs grown from metal catalysts [184]. The bright tips indicate that Fe NPs are attached to the CNT tips because the SE yield of Fe is higher than that of carbon. Figs. 3.8 (c) and (d) summarize the observed ratio of bright and dark tips of CNTs for the samples grown from ND and Fe. We first plotted the ratio of bright and dark tips for all CNTs indicated as "total" in the figures. For the Fe-deposited samples, although many CNT tips were bright due to the Fe NPs at the tip, a small portion of the CNT tips was found to be dark ("total" in Fig. 3.8 (d)). We infer that these CNTs with dark tips are not grown by the tip-growth mode but by the base-growth mode because of their relatively short length. Observation of approximately 30 CNTs on the Fe-deposited samples revealed that all the CNTs with dark tips were <50 μm. Thus, we defined 50 μm as the boundary to distinguish long and short CNTs and separately plotted the ratio of bright and dark tips in Figs. 3.8 (c) and (d) for "short" and "long." In the case of Fe-deposited samples, both the tip- and base-growth modes coexisted for the short CNTs ("short" in Fig. 3.8 (d)), whereas only the tip-growth mode exists for the long CNTs ("long" in Fig. 3.8 (d)).

The above results show that Fe-grown CNTs longer than 50 μm are consistently formed via a tip-growth mode. To further clarify whether this behavior arises from fundamental physical constraints rather than experimental coincidence, it is instructive to consider long CNT growth reported in the literature. A particularly stringent argument for the necessity of tip-growth in long CNT synthesis is provided by the furnace-moving method reported by Zhang et al. [21], where CNTs with lengths up to half a meter were grown under gas-flow-directed conditions. In this approach, only a localized heating zone is translated along the substrate, such that active growth occurs exclusively at the tip of the CNT. CNT segments that have already formed are rapidly removed from the high-

temperature region, lose thermal buoyancy, and consequently settle onto the substrate surface. Under these conditions, the majority of the CNT body is in direct contact with the substrate and experiences strong van der Waals adhesion. If growth were to proceed via a base-growth mode, continued elongation would require the already-deposited CNT segment to overcome substrate adhesion and be dragged forward against van der Waals forces. Such a scenario is physically implausible, as the cumulative adhesion force scales with contact length and rapidly exceeds any available aerodynamic or thermophoretic driving force. In contrast, a tip-growth configuration naturally circumvents this limitation: only the growth tip remains active and suspended within the heated, flowing gas environment, while the previously grown CNT body plays no mechanical role in sustaining elongation. Therefore, the success of the furnace-moving strategy provides compelling physical evidence that long gas-flow-directed CNT growth can only be sustained by a tip-growth mechanism.

In the case of the ND-deposited samples, most of the CNTs showed dark tips ("total" in Fig. 3.8 (c)). There are two possible explanations for the dark tips for the ND-deposited samples: CNTs grown via the tip/base-growth mode from nonmetallic NPs and CNTs grown via the base-growth mode from metal impurities. Because long CNTs over 50 μm with Fe catalyst were always grown via the tip-growth mode ("long" in Fig. 3.8 (d)), the possibility of long CNT growth via the base-growth mode from metal impurities was excluded. Thus, CNTs longer than 50 μm with dark tips were grown from nonmetallic growth seeds ("long" in Fig. 3.8 (c)). Some bright tips existed for ND-deposited samples regardless of the lengths, which should be attributed to CNTs grown via the tip-growth mode from metal impurities ("short" and "long" in Fig. 3.8 (c)). Therefore, for the ND-deposited samples, it is concluded that 80% of the long CNTs were grown not from metal impurities but from nonmetallic seeds via the gas-flow-directed growth mechanism.

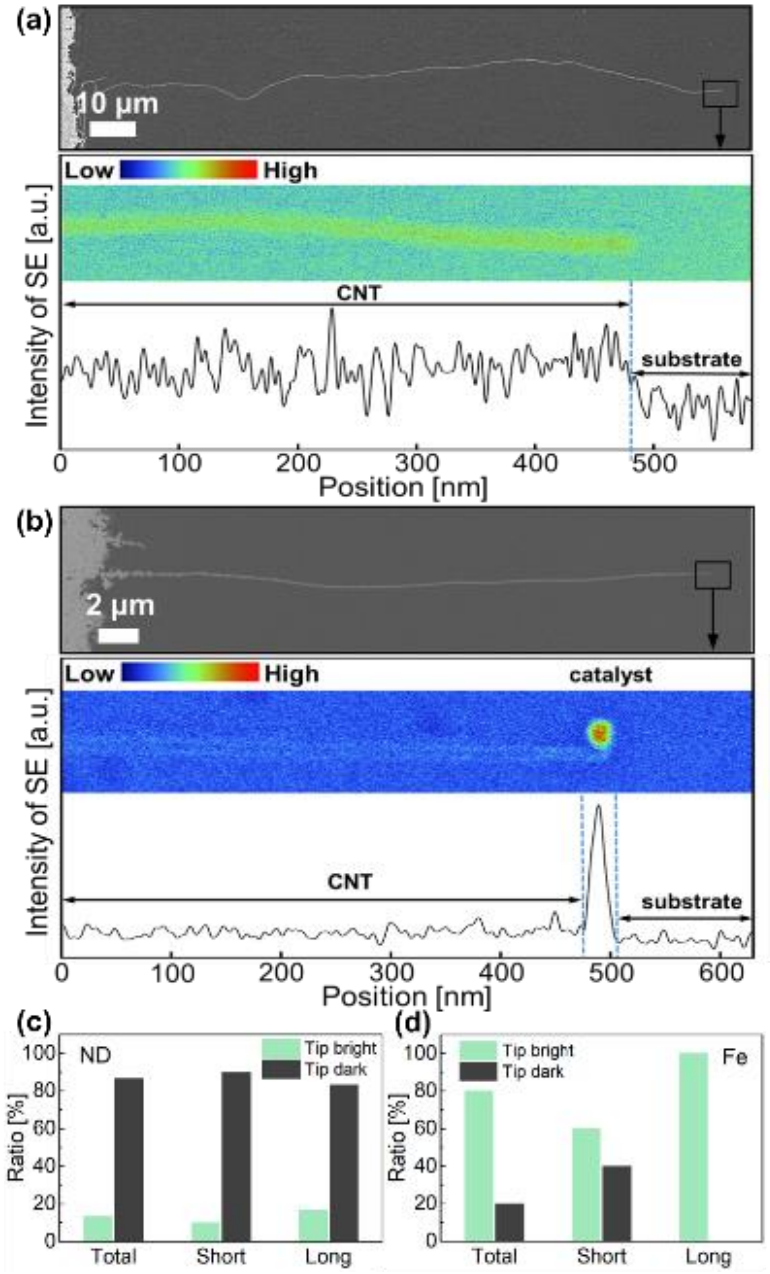


Figure 3.8 SEM images of typical CNTs for (a) ND-deposited samples and (b) Fe-deposited samples measured at a PE energy of 1 keV. The images show the SE yield maps of the magnified CNT tips in color measured at a PE energy of 5 keV. Ratio of bright/dark CNT tips for (c) ND-deposited samples and (d) Fe-deposited samples with different CNT lengths. Total represents the sum of all CNTs. Short and long, respectively, denote CNTs with lengths shorter and longer than 50 μm.

3.5 Growth-mode determination of CNTs grown from nonmetallic NPs

Although we confirmed the absence of metallic NPs at the tip of aligned CNTs, it is challenging to directly confirm nonmetallic NP attachment using SEM because both ND-derived NPs and CNTs are composed of carbon. Thus, the presence of nonmetallic NPs is further verified. To clarify the growth mode of the CNTs grown from nonmetallic NPs (tip- or base-growth modes), AFM was employed to analyze topographic images around CNT tips on the nanometer scale in combination with SEM observation. Figs. 3.9 (a) and (b) show the SE yield map and AFM image of a tip of an identical CNT longer than 50 μm (more information in Fig. 3.10). For the SE yield map, the tip of the CNT is dark, indicating the absence of metal NPs. For the AFM image of the same location on the CNT, a 5-nm-high protrusion is found at the CNT tip, indicating that the CNT was grown from nonmetallic NPs using the tip-growth mode. Due to the aforementioned challenges and the lack of direct observations such as TEM, a definitive characterization of the nonmetallic NPs at the tip of CNTs cannot be provided.

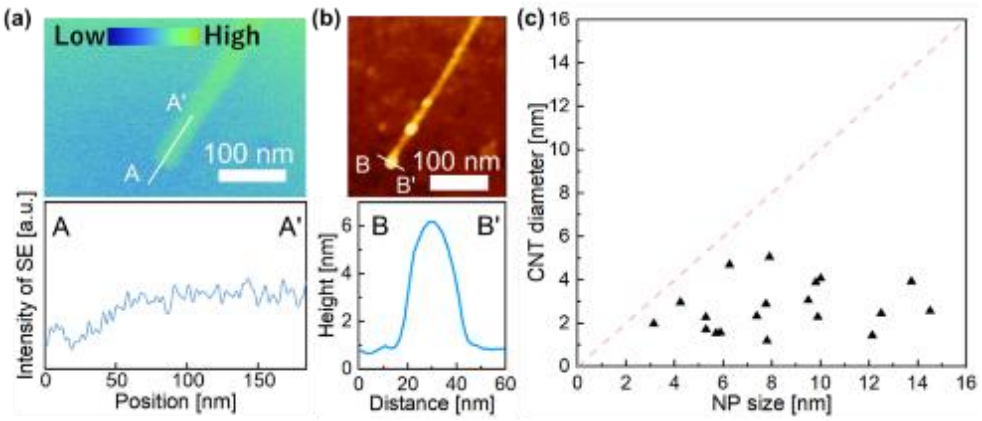


Figure 3.9 (a) SE yield map and line profile of an aligned CNT tip. The line profile was obtained along a segment of the SE yield map represented by a line between two points, denoted as A and A′. (b) AFM image and line profile of the same CNT tip. The line profile was obtained along a segment of the AFM image represented by a line between two points, denoted as B and B′. (c) The distribution of nonmetallic NP sizes and the corresponding diameters of CNTs grown via gas-flow-directed growth.

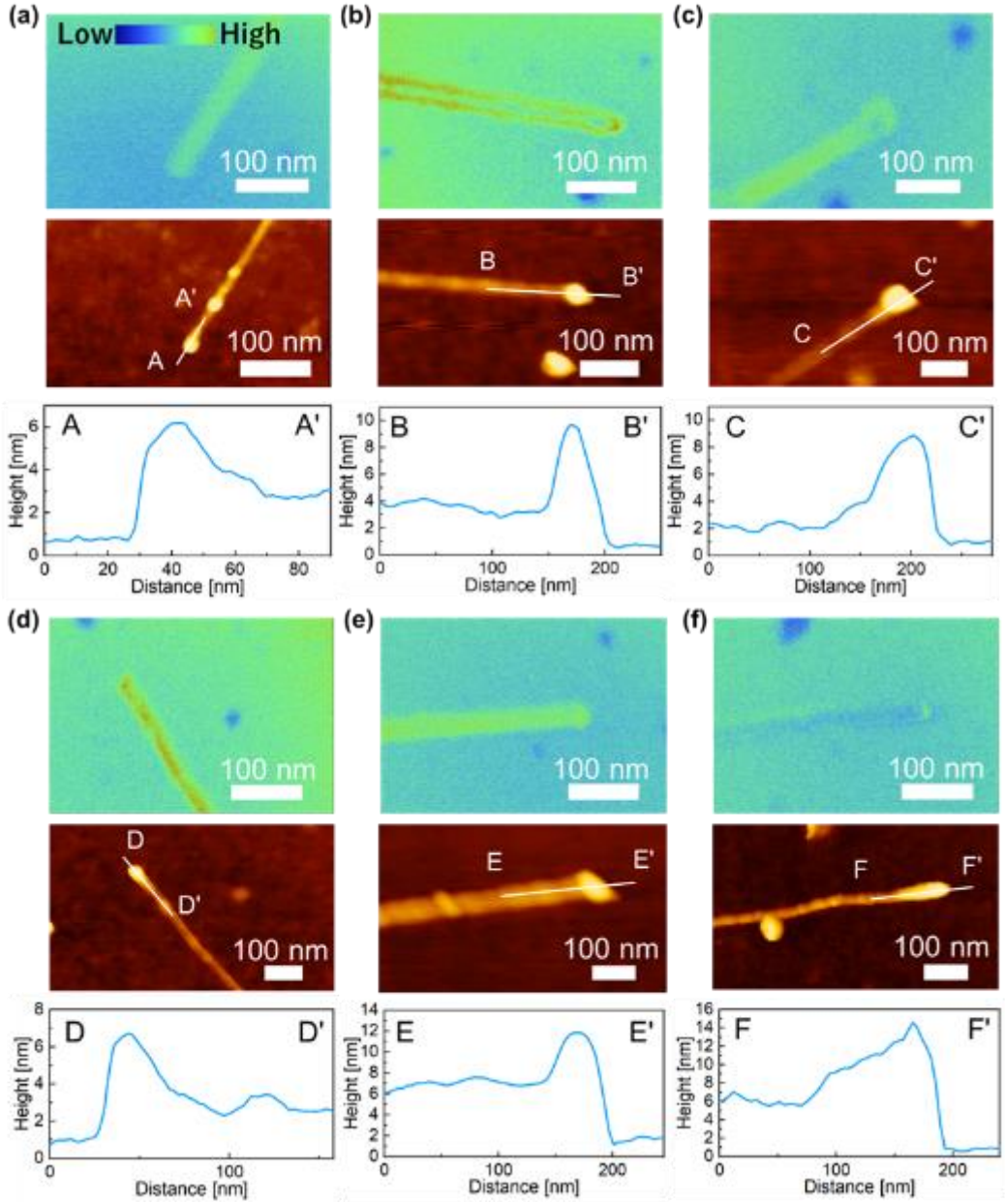


Figure 3.10 SE yield maps and AFM images and line profiles of aligned CNT tips (>50 μm). The line profile was obtained along a segment of the AFM image represented by a line between two points. While the presence of metal nanoparticles was denied by SE yield maps, the presence of some kind of nanoparticles at the tip of CNTs was confirmed by AFM, suggesting that CNTs were grown from nonmetallic NPs via the tip-growth mode. Note that some particles surrounding the CNTs can be attributed to the formation of amorphous carbon during the CVD process.

Considering that other candidates of nonmetallic NPs, such as amorphous carbon, are unlikely to serve as a seed for CNT growth, it is believed that there is a strong possibility that the nanoparticles at the CNT tips are NDs or ND-derived NPs. By observing other CNTs, we elucidated that ~95% of the aligned CNTs longer than 50 μm grown from nonmetallic NPs follow the tip-growth mode. A small portion (~5%) of the CNTs exhibited dark tips in the SE yield maps, without distinct protrusions in AFM images. The most plausible hypothesis is that the diameters of the CNTs are comparable with those of the NPs [184], making it difficult to discriminate the particles from the CNT by AFM (Fig. 3.11). Another possibility is the detachment of NPs just before growth termination [185], which has been reported in the case of metal catalysts.

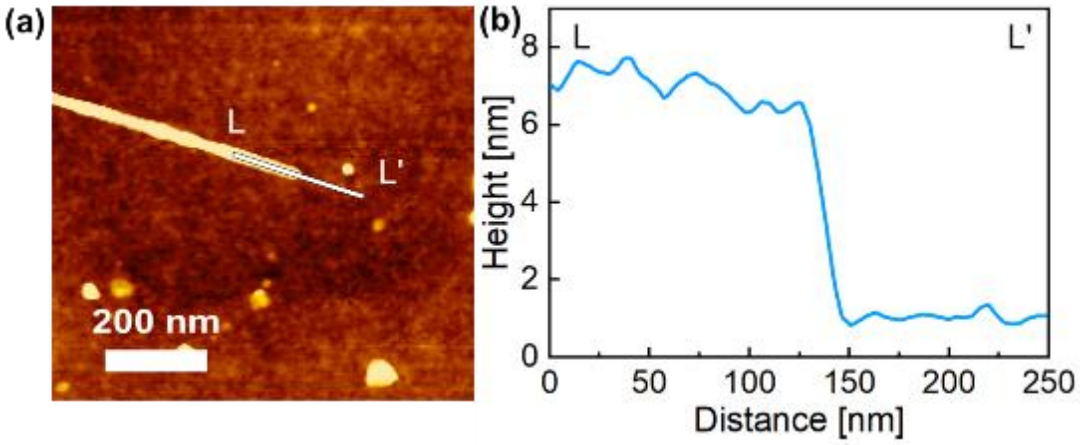


Figure 3.11 (a) AFM image and (b) line profile of the CNT. The line profile was obtained along a segment of the AFM image represented by a line between two points, denoted as L and L′.

It is noteworthy that the diameters of CNTs grown via the gas-flow-directed growth are consistently smaller than the size of the nonmetallic NP, indicating that the maximum CNT diameter is limited by the size of the nonmetallic NP (Fig. 3.9 (c)). This finding is consistent with previous research on CNT growth using metal catalysts [179,186].

Furthermore, these results suggest that the CNTs in this study were grown not in the tangential mode but in the perpendicular mode [184]. The relationship between nonmetallic NP size and CNT diameter appears to be independent, which is consistent with previous study on solid catalyst [187].

To further assess the contact state of CNTs after gas-flow-directed growth, we focus on the near-tip region where the transition from growth to substrate interaction is expected to occur. As shown in Fig. 3.10, AFM height profiles acquired over several hundred nanometers along the CNT axis near the tip exhibit relatively uniform height variations, without abrupt lift-off or large out-of-plane undulations. This observation suggests that, at least locally near the CNT tip, the nanotube adopts a stable geometric configuration with no pronounced suspended segments. It should be noted, however, that the CNT–substrate contact state relevant to device operation may not be identical to the as-grown morphology. In particular, during the subsequent electrode fabrication process discussed in Chapter 5, spin coating and solvent evaporation of photoresist can impose capillary and shrinkage-induced forces that promote additional CNT–substrate coupling and partially fill any remaining interfacial gaps. As a result, the effective contact condition in the completed devices is likely determined by a combination of the growth process and the lithographic processing steps.

Fig. 3.12 shows the length distribution of grown CNTs from nonmetallic NP growth seeds with the different states of the tips. Type I represents the CNTs with tips showing dark contrast in SE yield maps and particle structures in AFM images, corresponding to the CNT grown from nonmetallic NPs via the tip-growth mode. Type II is the CNT with a dark SE contrast and no distinct protrusion structure at the tip, which is considered as tip-growth from nonmetallic NPs but with no distinct diameter difference between the particle and CNT. Type III is the CNT with bright SE contrast at the tip, which is regarded as tip growth from metal impurities. After distinguishing types II and III from type I, the lengths of CNTs grown from nonmetallic NPs via the tip-growth mode (type I) are found

to range from 50 to 900 μm. In contrast, the CNTs grown from ND in previous studies [106,117,158] were just below 5 μm, highlighting the significant advantages of the gas-flow-directed growth mechanism in the synthesis of longer CNTs. The distribution of CNT lengths in this study indicates a potential accordance with the Schulz-Flory distribution [21] (Fig. 3.13), but more sample numbers are needed for detailed discussion. The relationship between the diameter and length of CNTs has also been studied, but there is no direct correlation between them (Fig. 3.14).

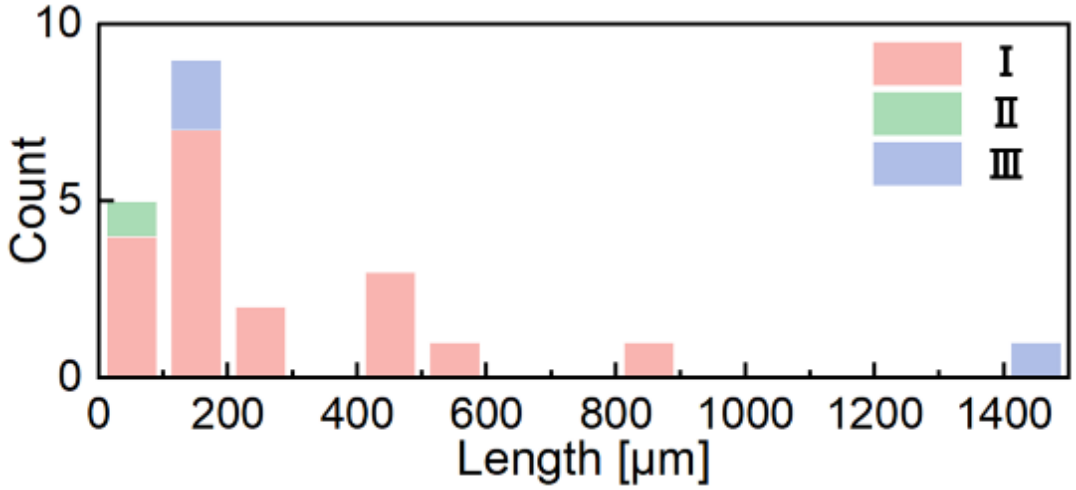


Figure 3.12 Length distribution of CNTs formed by gas-flow-directed growth mechanism on ND-deposited samples with different types of tips. Type I corresponds to CNTs with a dark SE contrast and distinct protrusion structures at the tips (tip growth from nonmetallic NPs). Type II indicates a CNT with a dark SE contrast and no distinct protrusion structures at the tip (presumably tip growth from nonmetallic NPs whose diameter is comparable with that of CNT). Type III indicates CNTs having tips of bright SE contrast (tip growth from metal impurities).

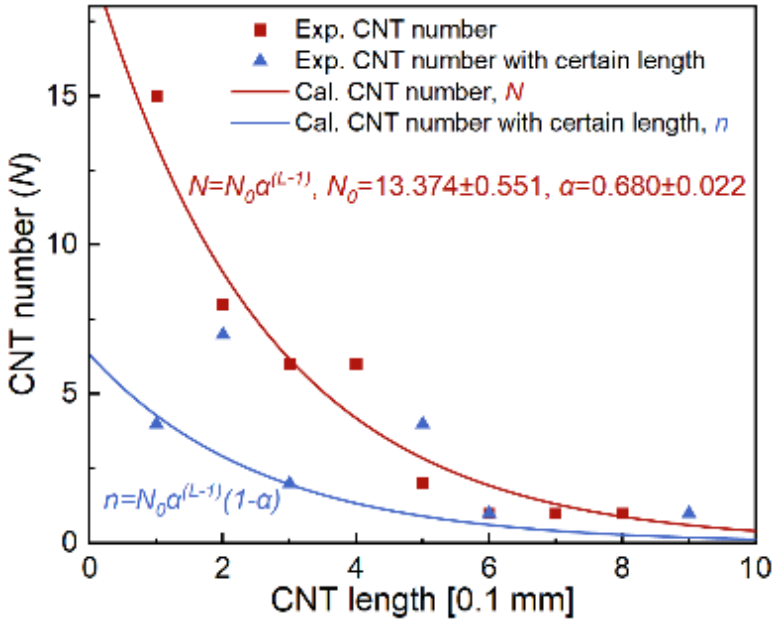


Figure 3.13 The number distribution of CNTs grown from nonmetallic NPs via gas-flow-directed growth.

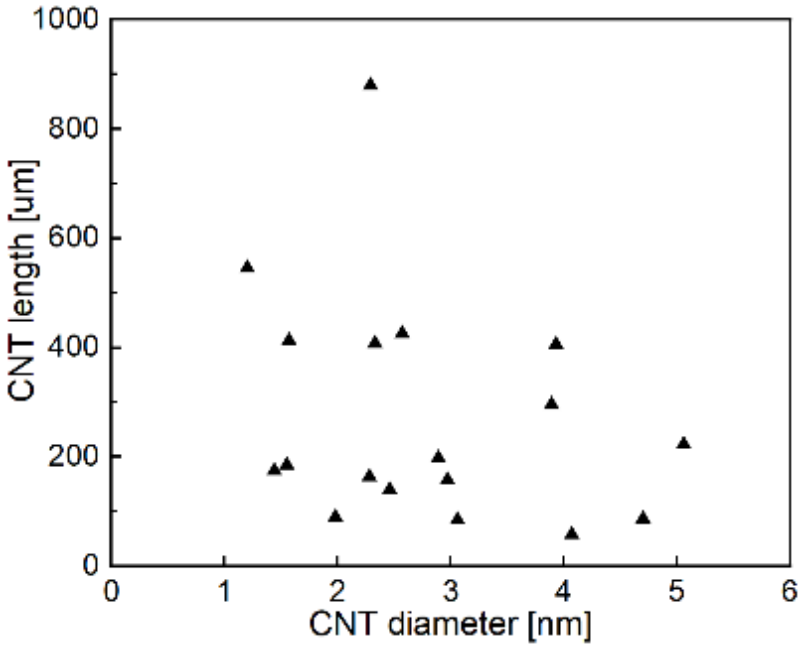


Figure 3.14 The distribution of CNT diameter and the corresponding CNT length grown from nonmetallic NPs via gas-flow-directed growth.

3.6 Crystallinity and diameter analysis of CNTs grown from nonmetallic NPs

We characterized the structure of aligned CNTs longer than 50 μm grown from nonmetallic NPs by SEM and Raman spectroscopy, as shown in Figs. 3.15 (a) and (b). Structural analysis was performed using the Raman mapping image of a long CNT (longer than 100 μm) in comparison with the SEM images observed at the same position. The G-band mapping image shows the same shape as the SEM image. The Raman spectra at the three positions indicated by the circles in the G-band image (Fig. 3.15 (b)) are shown in Figs. 3.15 (c) and (d). The spectra are consecutive but split into two images for clarity and accurate presentation. The intensity ratio from G-band to D-band in the Raman spectra (Fig. 3.15 (c)) was evaluated as 260 ± 50, indicating that the aligned CNTs uniformly have high crystallinity. It should be noted that although Raman measurements indicate a high G/D ratio, suggesting low defect density, SEM images reveal that some CNTs exhibit pronounced curvature. This apparent discrepancy can be rationalized by distinguishing between structural defects and elastic mechanical deformation. In gas-flow-directed growth, CNTs are subjected to continuous aerodynamic drag during growth, and the growing CNT can experience bending due to non-uniform flow fields, local turbulence, or transient fluctuations in buoyant and thermophoretic forces. Such bending is therefore primarily mechanical in origin and can occur either during growth or after the CNT has partially lost buoyant support and settled onto the substrate. Importantly, elastic bending of CNTs does not necessarily introduce topological defects into the sp^2 carbon lattice. CNTs can sustain large curvature and strain without generating Stone–Wales defects or vacancies, provided that the deformation remains within the elastic regime [188]. As a result, mechanically induced curvature is compatible with a high G/D ratio in Raman spectra. The coexistence of strong curvature in SEM images and high crystalline quality inferred from Raman spectroscopy therefore indicates that the observed CNT bending is dominated by reversible mechanical deformation rather than defect-generating structural damage.

The RBM peaks of the CNT were measured at three different positions, (i)–(iii), and it was found that all three positions displayed an identical peak at 172 cm^{-1} (Fig. 3.15 (d)). If the diameter is calculated using the formula $\omega_{\mathrm{RBM}} = A/d_t + B$, with $A = (217.8 \pm 0.3)\ cm^{-1}\ nm$ and $B = (15.7 \pm 0.3) cm^{-1}$ [189], the RBM signal at 172 cm^{-1} corresponds to a diameter of 1.39 nm. The RBM frequencies are uniform in the entire imaging range; thus, the diameters of the carbon nanotubes are constant over 50 μm.

The diameter of the CNT shown in Figs. 3.15 (a)–(d) was evaluated near its tip using AFM. Fig. 3.15 (e) show the AFM image and its line profile. The height of the CNT in the AFM image is 2.1 ± 0.1 nm, which is much larger than the height expected from the RBM signal. We have two possible explanations for this observation. The first involves a tight bundle of single-walled CNTs, in which only one CNT resonates with the excitation laser. The second possibility is that the two diameter values observed as CNT diameters represent the diameters for the outermost tube and one of the inner tubes in a multiwall CNT. Herein, the second possibility is considered because the bundle formation in the first possibility is rather unlikely due to the very low CNT yield from gas-flow-directed growth. Assuming that two shells with the diameters determined from AFM and RBM form a concentric structure, the interlayer distance between the shells is calculated as 0.355 ± 0.05 nm, which is a reasonable value compared to the interlayer distance of graphite (0.34 nm). Therefore, we infer this long CNT as a double-walled CNT with inner and outer wall diameters of ~1.4 and ~2.1 nm, respectively. Note that the RBM frequency for the outer wall should be observed around 119 ± 5 cm^{-1} from the diameter of the AFM image and the calculation using the above equation. The corresponding RBM peak, however, was not observed in the measured Raman spectrum although the frequency was within the measurable range of the Raman system used herein. Results indicate that the outer wall does not resonate with the Raman excitation laser, which is consistent with previous research results [190]. Fig. 3.15 (f) shows the diameter distribution of CNTs

longer than 50 μm from nonmetallic NPs evaluated by AFM. Most of the nanotubes are regarded as single- and double-walled CNTs with small diameters, and some are multiwalled CNTs, which confirm the effectiveness of nonmetallic growth seeds for growing CNTs with a relatively small diameter, which are suitable for electronic applications.

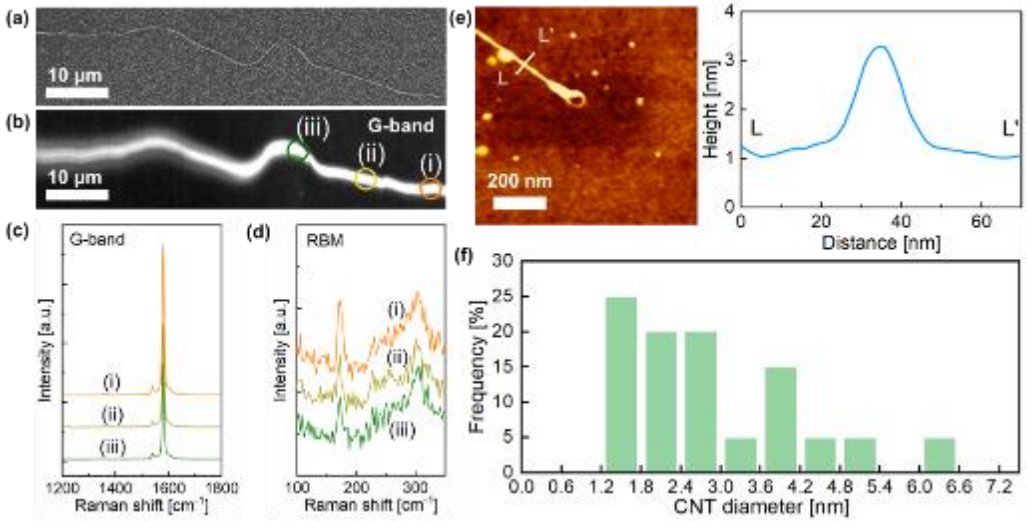


Figure 3.15 (a) SEM and (b) G-band Raman mapping images of an aligned CNT. The excitation wavelength for the Raman measurement is 532 nm. Raman spectra of (c) G-band and (d) RBM obtained at the circles in (b) marked as (i), (ii), and (iii). (e) AFM image and line profile of the same CNT as (a) and (b) measured near its tip. The line profile was obtained along a segment of the AFM image represented by a line between two points, denoted as L and L′. (f) Diameter distribution of CNTs formed by the gas-flow-directed growth mechanism from nonmetallic growth seeds.

It is also worth noting that, in addition to metallic residues, ND introduced during CNT growth may be present in the final structures and therefore warrant consideration from a device perspective. The key concern for CNT FETs is the presence of localized defects or charged impurities close to the CNT channel, which can directly reshape the band profile and transmission. Neophytou et al. showed that even a single vacancy can

reduce the drive current by about 28%, and a single negatively charged impurity located inside the CNT can reduce the drive current by about 33% while also producing a large threshold shift on the order of 40 mV, due to the formation of a strong scattering barrier and electrostatic carrier pileup near the impurity [191]. This provides a clear physical basis for why residual metal contamination is harmful in CNT electronics, since metallic residues can behave as strong local charged scattering centers and induce substantial current degradation and threshold instability when they are close to, or in direct contact with, the CNT channel.

By comparison, studies on CNT and ND hybrid materials indicate that adding ND does not inherently worsen electronic functionality, and can even improve electron emission behavior, which is also an electronic performance metric sensitive to local transport and electrostatics at emission sites. Ho et al. reported that hybrid CNT ND samples show improved field emission compared with pure CNTs, and attributed this to the ND being well mixed with CNTs and effectively creating many additional tips and emission sites on CNT sidewalls, as well as reducing electrostatic screening in dense CNT ensembles [192]. Similarly, Varshney et al. showed that a monolithic CNT diamond composite exhibits excellent field emission properties with improved reproducibility and long term stability, and they ascribed the stability enhancement to the seamless CNT diamond integration that enables effective heat removal from CNTs during high current operation [193]. Taken together, these results indicate that sparse ND attachment does not inherently degrade CNT electrical performance. Its primary effects are related to geometric, thermal, or electrostatic field modulation, rather than the strong charged-impurity scattering known to impair CNT FET characteristics.

3.7 Conclusion

Herein, we achieved gas-flow-directed growth of long, aligned CNTs from nonmetallic growth seeds by treating ND particles and controlling the conditions in the reactor. The temperature and flow rate dependence of the length and yield of aligned CNTs indicate the importance of the gas flow condition for initiating the gas-flow-directed growth from nonmetallic growth seeds, as in the case of metal catalysts. Using the SE yield analysis of CNT tips for the ND-deposited samples and the control Fe-deposited samples, we excluded the possibility of metal impurities affecting the aligned CNT growth from ND. A combined analysis of SE yield maps and AFM was used to detect the existence of NPs at the CNT tips, which confirms the tip-growth mode of CNTs grown from nonmetallic NPs. Although direct characterizations are expected to confirm their identity in the future, these nonmetallic NPs are presumed to be NDs or carbon NPs derived from NDs. Structural characterization revealed the high crystallinity of the CNTs and their relatively small diameters. This study is the first to demonstrate the use of nonmetallic growth seeds for gas-flow-directed growth and will provide alternative starting materials for fabricating long, aligned CNTs. As nonmetallic NPs have no catalytic effect, the yield of the grown CNTs lower than that from metal-catalyzed gas-flow-directed growth, and this also results in trace amounts of impurities that can still grow a significant percentage of CNTs. Importantly, the ability to grow long, aligned CNTs without metallic contamination provides a robust structural foundation for the subsequent investigations presented in this dissertation. In particular, the clean and continuous CNTs obtained here enable the systematic study of alignment mechanisms under geometric constraints and facilitate device-level electrical transport measurements without complications arising from metallic residues. With further optimization, nonmetallic NPs are expected to offer a versatile route toward the fabrication of aligned CNT networks and transfer-free CNT devices on a wide range of substrates, supporting the development of high-performance CNT-based electronics.

Chapter 4. Crossover between gas-flow-directed growth and vibrational bridging in pillar-assisted controlled formation of carbon nanotube networks

4.1 Background

Carbon nanotubes (CNTs) [1,2] possess exceptional mechanical strength, electrical conductivity, and thermal stability at the individual level [5,33,52]. However, using them as isolated elements poses challenges in practical applications. To overcome this issue, CNTs are often assembled into interconnected networks, which not only preserve their intrinsic properties but also enhance their flexibility, durability, and large-area scalability. These CNT networks have attracted significant attention for applications in nanodevices [194], energy storage [195], and sensing technologies [196]. In particular, both aligned arrays and random CNT networks have been actively investigated as potential interconnect wiring or electrodes in next-generation electronics [144,197–199]. Although techniques, such as spin coating and inkjet printing [200,201], have been used to fabricate CNT networks, they often offer limited control over network density and bridging configurations, which are crucial for consistent electrical characteristics in large-scale integration.

Pillar-assisted growth provides spatial anchors for CNTs, enabling the formation of suspended structures and geometric control over their orientation and connectivity. Originally proposed by Dai et al. [132,149], this method adopts regularly spaced nanopillars during chemical vapor deposition (CVD) to guide the self-assembly of CNTs into suspended bridges. Dai's work used microscale pillar spacings (typically ~5–10 μm) and achieved remarkably long CNT spans (up to 150 μm), attributing their formation primarily to the directionality of the gas flow. Notably, although the concept of gas-flow-directed growth [21,27,140,202,203] had not yet been formalized at the time, many observed features in Dai's work strongly reflect its characteristics, such as ultralong CNTs with strong alignment along the gas flow direction and bridging across multiple pillars.

This mechanism, characterized by tip growth influenced by buoyant gas flow forces, allows CNTs to extend into higher laminar flow zones and form longer suspended structures. In contrast, Homma et al. later proposed a vibrational growth model in which CNTs oscillate during growth and connect to nearby pillars. Their experiments, using submicron spacing pillar arrays (400–1,400 nm) [204–207], demonstrated that CNT tip vibrations were sufficient to account for short-range bridging, challenging the earlier gas-flow-based explanation [149]. Both interpretations are valid within their respective experimental regimes—Dai under conditions favoring extended, flow-guided growth [149], and Homma under conditions where vibrational growth likely dominates the growth behavior [204]. More recently, Lee et al. expanded the scope of pillar-assisted growth to three-dimensional CNT networks with tunable density and connectivity [208–211]. Their work highlighted the potential of nanopillar arrays as flexible platforms for customized interconnect architectures, with applications in multi-I/O routing and device wiring [212,213]. Although their study did not explicitly analyze the underlying growth mechanism, their experimental conditions suggest a regime in which vibrational growth dominates. Overall, previous studies have primarily focused on regimes where either flow-guided or vibrational growth dominates, without investigating the transitional or overlapping regimes where both mechanisms coexist or compete. Understanding these crossover conditions is essential for the precise control of the CNT bridging behavior.

In this study, we developed a unified growth framework that explicitly incorporates gas-flow-directed growth into a pillar-assisted technique for fabricating structurally tunable CNT networks. Building on our previous demonstration of gas-flow-directed growth [140], we systematically investigated the influence of the gas flow direction and pillar spacing on the CNT bridging behavior using extensive experimental data and fluid dynamics simulations. Our analysis provides insight into the interplay between the vibrational and gas-flow-directed growth mechanisms and demonstrates how a controlled-array design can optimize network connectivity. The resulting controllability

of the CNT bridging structures may also facilitate broader applications, including single-tube characterizations [214] and scalable nanoscale interconnect wiring [212].

4.2. Experimental section

4.2.1 CNT growth and characterization

Quartz substrates were patterned to form SiO_2 nanopillar arrays via a microfabrication process. The nanopillars had a square cross-section with a side length of 1.6 μm and a height of 8 μm. The edge-to-edge spacing between the nearest neighbor (NN) pillars was set to 3, 5, and 10 μm to assess the influence of the pillar arrangement on the CNT network formation.

A 0.03 M ethanol solution of $FeCl_3$ was spin-coated onto the substrates to serve as a catalyst precursor. After catalyst deposition, the substrates were placed in a horizontal CVD furnace for thermal treatment and CNT growth. Under a continuous flow of 20 sccm H_2 (3%)/Ar at 85 kPa, the temperature was ramped to 850°C–950°C and held for 10 min to reduce the catalyst. Subsequently, ethanol vapor was introduced as the carbon source. The ethanol vapor was generated by bubbling 35 sccm H_2 (3%)/Ar through a 40°C ethanol reservoir, supplemented by an additional 420 sccm H_2 (3%)/Ar flow through a separate line. CNT growth proceeded for 30 min under atmospheric pressure, with an estimated partial ethanol pressure of approximately 1.4 kPa. The gas flow was horizontally directed across the substrate surface throughout the process. The growth conditions were designed to promote tip-growth behavior consistent with previously established gas-flow-directed growth mechanisms [140], thereby facilitating the formation of suspended CNT networks that bridge the nanopillar arrays. After growth, the reaction was terminated by switching the gas flow to pure Ar and cooling the furnace to room temperature under an Ar atmosphere.

The morphology and structural features of the CNT networks were characterized using scanning electron microscopy (SEM). SEM images were obtained using a Hitachi S-4800 system with an accelerating voltage of 5 kV and an emission current of 10 μA. SEM images were acquired at tilted angles to provide three-dimensional views of the

CNT morphology, with the sample rotated horizontally by 30° and tilted vertically by 30°.

4.2.2 Finite element method simulations

Finite element method (FEM) simulations were conducted using COMSOL Multiphysics (COMSOL Inc.) to investigate the gas flow behavior and mechanical response of CNTs during growth.

The Laminar Flow module was used to model the gas flow field around the nanopillar arrays. The simulation solved the steady-state incompressible Navier–Stokes equations as follows:

$$\nabla \boldsymbol{u} = 0, \tag{4.1}$$

$$\rho(\boldsymbol{u} \cdot \nabla)\boldsymbol{u} = \nabla \cdot \sigma + \boldsymbol{F}, \tag{4.2}$$

where $\boldsymbol{u}$ denotes the velocity field, ρ denotes the fluid density, and $\boldsymbol{F}$ represents the body force per unit volume. The Cauchy stress tensor σ is defined as

$$\sigma = -p\boldsymbol{I} + \mu[\nabla \boldsymbol{u} + (\nabla \boldsymbol{u})^T], \tag{4.3}$$

where p denotes the pressure, μ denotes the dynamic viscosity, and $\boldsymbol{I}$ denotes the identity tensor. The boundary conditions were set to match the experimental gas flow velocity (0.01 m/s) with no-slip conditions applied at the nanopillar surfaces. Mesh refinement was applied near the nanopillars to accurately capture the local velocity gradients. Given the low flow velocity and microscale geometry, the flow was assumed to be laminar and incompressible throughout. Further details on the simulation parameters, mesh configurations, and material properties are provided in the Supporting Information.

4.3 Gas flow direction dependence and model fitting

CNT networks were fabricated on substrates consisting of nanopillar arrays with various geometric layouts under different growth conditions. For simplicity, the directions that are parallel and perpendicular to the gas flow direction are designated as // and ⊥, respectively. These symbols specify the orientation of the nanopillar configuration relative to the gas flow direction. For consistency, samples are designated based on the spacing of nanopillars in the parallel (//) and perpendicular (⊥) directions to the flow; e.g., a sample labeled 3 × 10 corresponds to nanopillar spacings of 3 μm (//) and 10 μm (⊥).

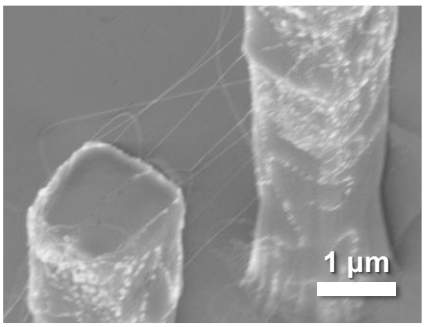


Figure 4.1 SEM image of CNT bridges between two nanopillars.

SEM analysis (Fig. 4.1) revealed that the catalyst particles were likely distributed across the entire pillar surface due to the liquid coating process. However, CNTs that nucleate at the apexes can effectively contribute to suspended bridging. CNTs that grow from the sidewalls of pillars or the substrate tend to quickly adhere to nearby surfaces, which prevents them from contributing to network formation. Using anisotropic pillar configurations and past research, the concept of "nearest neighbors (NNs) between pillars" is modified and refined to characterize bridging patterns in CNT networks [204]. The parallel NNs (//NN) and perpendicular NNs (⊥NN) are nanopillars that are exactly near each other in either the parallel (//) or perpendicular (⊥) directions. The diagonally aligned pillars are classified as diagonal NNs (∠NN). A schematic illustration of these configurations and bridging modes is shown in Fig. 4.2. Since this study focused on

suspended CNT structures, CNTs that adhered to the substrate surface were excluded from the analysis.

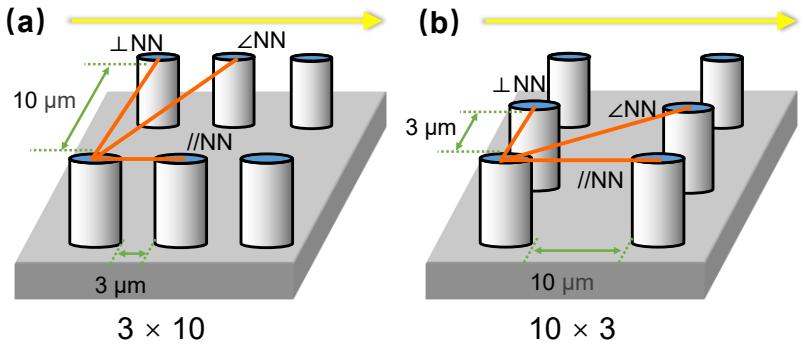


Figure 4.2 Schematic illustration of the CNT bridging behavior in different nanopillar configurations. (a) and (b) correspond to pillar arrays with short spacing aligned parallel (3 × 10) and perpendicular (10 × 3) to the gas flow, respectively. //NN, ⊥NN and ∠NN denote CNTs bridging between nearest neighbor pillars that are parallel, perpendicular, and diagonal to the gas flow direction, respectively. The yellow arrow indicates the gas flow direction. This figure illustrates representative configurations only. Additional pillar array designs, including 5 × 10, 10 × 5, and 10 × 10, were also employed in the experiments.

Figs. 4.3 (a) and (b) show the representative SEM images of the CNT networks synthesized under gas-flow-directed growth conditions [140] using substrates with identical nanopillar arrangements but subjected to distinct gas flow directions, explicitly comparing the 3 × 10 and 10 × 3 configurations. In both circumstances, the CNTs mostly bridged across the adjacent nanopillars; however, depending on the direction of the gas flow, minor variations in the bridging behavior were observed. Although the overall network structures appeared similar in the SEM images, subtle differences in the bridging behavior were further analyzed quantitatively. Specifically, two groups of samples, including those shown in Figs. 4.3 (a) and (b), were systematically evaluated. The // group comprises the 3 × 10, 5 × 10, and 10 × 10 configurations in which the nanopillar spacing in the // direction is altered (3, 5, and 10 μm) while preserving a constant 10 μm spacing

in the ⊥ direction. The ⊥ group includes the 10 × 3, 10 × 5, and 10 × 10 samples in which the ⊥ direction spacing varies, while the // spacing remains constant at 10 μm. Fig. 4.4 shows typical SEM images of the CNT networks formed in the 5 × 10, 10 × 5, and 10 × 10 layouts. Fig. 4.3 (c) summarizes the bridging statistics as a function of pillar spacing for both sample sets in the respective gas flow directions, including all tested spacings (3, 5, and 10 μm). These statistics represent the average number of CNT bridges per nanopillar pair, classified by connection type—specifically, //NN, ⊥NN, and ∠NN categories defined in the previous paragraph. As shown in Fig. 4.3 (c), two main trends are evident. First, as the spacing between the pillars increased, the likelihood of CNT bridging decreased, leading to a reduced number of bridges in both groups. Second, the direction of the gas flow affects the //NN and ⊥NN bridging connections, whereas its impact on ∠NN connections appears minimal. For each group, the number of CNT bridges in the // direction was consistently higher than in the ⊥ direction.

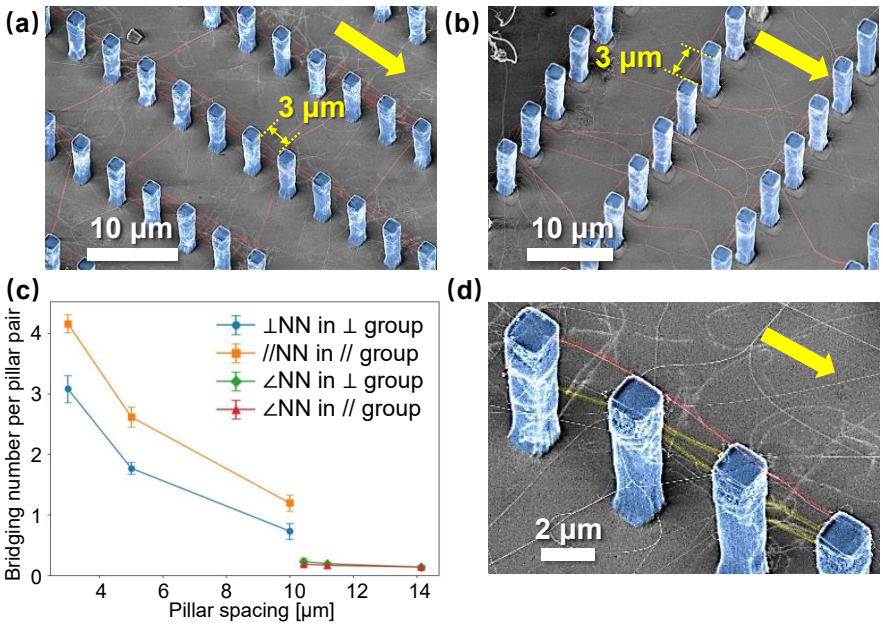


Figure 4.3 (a, b) False color SEM images of the CNT networks grown on substrates with identical nanopillar arrangements but different gas flow directions. (a) Sample with the 3 × 10 configuration, that is 3 μm spacing in the // direction and 10 μm spacing in the ⊥ direction. (b) Sample with the 10 × 3 configuration, that is 10 μm spacing in the // direction and 3 μm spacing in the ⊥ direction. Blue

indicates nanopillars and red lines mark CNT bridges. The yellow arrows indicate the direction of the gas flow during growth. The SEM images shown here are representative examples. Additional pillar array configurations, including 5 × 10, 10 × 5, and 10 × 10, were also used in the experiments. (c) Pillar-spacing dependence of the average number of CNT bridges per pillar pair, categorized by //NN, ⊥NN, and ∠NN connections in both // and ⊥ groups. For each pillar spacing, we grew multiple samples, captured SEM images at several regions per sample, counted bridges per pillar pair in each image, averaged these values, and plotted the standard deviation as the error bar. (d) False color SEM image highlighting two bridging modes: gas-flow-directed growth CNTs (red) span multiple pillar tops and vibrational-bridging CNTs (yellow) span short distances. Blue denotes the nanopillars. The yellow arrows indicate the direction of the gas flow during growth.

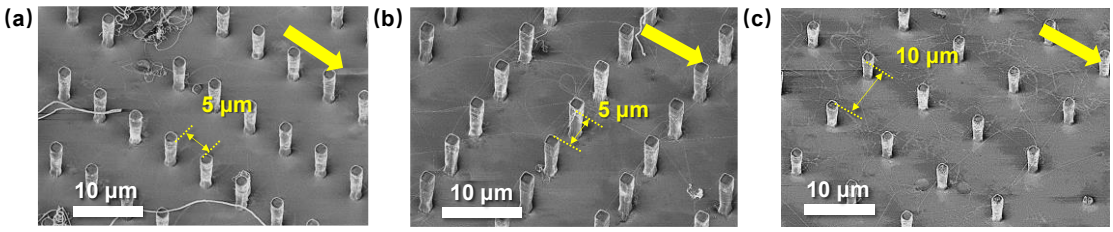


Figure 4.4 SEM images of CNT networks grown on substrates. (a) Sample with 5 µm spacing in the // direction and 10 µm spacing in the ⊥ direction; (b) Sample with 10 µm spacing in the // direction and 5 µm spacing in the ⊥ direction. (c) Sample with 10 µm spacing in the // direction and 10 µm spacing in the ⊥ direction. Yellow arrows indicate the direction of gas flow during growth.

The observed anisotropy in the bridging behavior is attributed to the interplay of two main growth mechanisms: vibrational growth, which enables both //NN and ⊥NN bridging [205], and gas-flow-directed growth, which predominantly promotes //NN along the gas flow direction [140]. The environmental SEM has directly detected the vibratory action in situ, indicating the validity of the proposed vibrational growth model [206]. In contrast, the gas-flow-directed growth process primarily occurs under directional gas

flow conditions. Here, CNTs are lifted from the tops of the nanopillars and carried along by laminar flow, which enables them to bridge greater distances and span multiple nanopillars [140]. As shown in Fig. 4.3 (d), gas-flow-directed growth CNTs (red) span multiple pillar tops, while vibrationally-bridged CNTs (yellow) form short-range connections between adjacent pillars. While multiple bridges are often observed between neighboring pillars, their formation can be attributed to CNTs initiating growth from different surface positions and angles. As illustrated in Fig. 4.5, this spatial and directional separation allows vibrational bridging to occur with reduced likelihood of bundling, even when final contact points appear closely spaced.

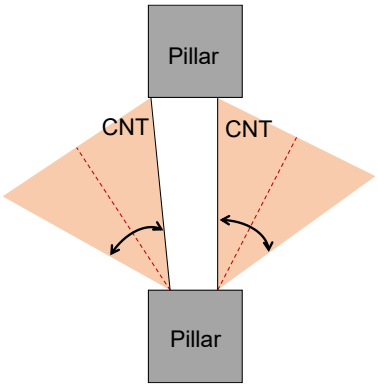


Figure 4.5 Schematic illustration showing how multiple CNTs with distinct initial growth directions can independently bridge between pillars via vibrational contact. Red dash lines indicate the initial growth directions, while black lines represent the final bridging positions after vibration. The spatial and directional separation reduces the likelihood of bundling, even when final contact points are closely spaced.

To quantitatively describe the CNT bridging behavior, we revisited a previously proposed isotropic bridging model [205], which assumes that CNTs grow straight without any directional preference in any direction from the pillar top and contact an adjacent pillar. Fig. 4.6 (a) illustrates the geometric definitions of the two angular constraints

involved in CNT bridging between nanopillars: the transverse angle Ω, representing the horizontal angular coverage from one pillar top toward a neighboring one, defined by a tangential projection from the pillar edge, and the longitudinal angle Ω', characterizing the vertical accessibility range from the pillar top to a neighboring pillar defined from the tangential point down to the base for successful bridging. In the original model, the bridging probability P is assumed to scale with the transverse angle as [205]:

$$P = K\Omega^n, \tag{4.4}$$

where K represents a proportionality constant, and n represents a fitting exponent. It is worth noting that the "bridging probability" used in previous studies was based on binarized counts (0 or 1) by limiting the catalyst density so that only a single CNT bridge could form per pillar pair. In contrast, this study does not impose such constraints; thus, multiple CNTs may bridge a single pillar pair, leading to values greater than 1. For a consistent comparison across different experimental approaches, we define B, the average bridging number per pillar pair, as the primary metric. Unlike the probability values P used in previous studies that limited CNT counts per pair, B generalizes the bridging behavior to reflect the actual CNT density, including multibridge events.

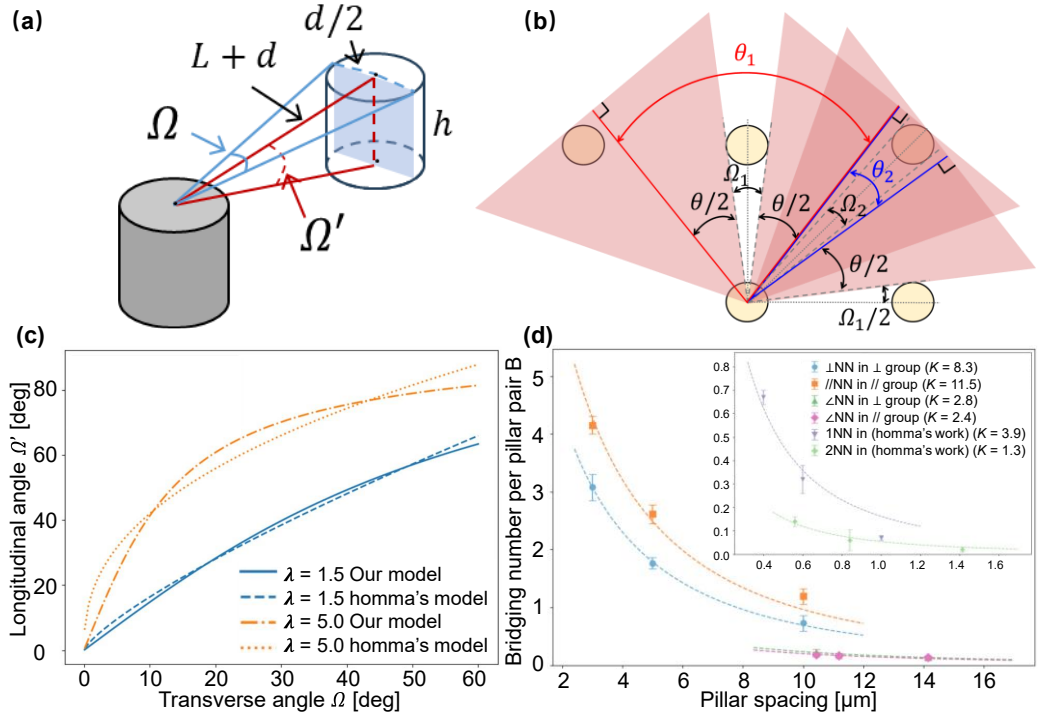


Figure 4.6 (a) Schematic illustration of the geometric constraints defining the transverse angle $\boldsymbol{\Omega}$ and the longitudinal angle $\boldsymbol{\Omega'}$ between the nanopillar pairs. (b) Schematic illustration of the geometric model used to derive the ratio of bridging constants $\boldsymbol{K_1}$ to $\boldsymbol{K_2}$. The shaded isosceles triangles represent the vibrational angular range $\boldsymbol{\theta}$ accessible to a CNT growing from the center pillar. $\boldsymbol{\Omega_1}$ and $\boldsymbol{\Omega_2}$ represent the transverse angles corresponding to ⊥NN and ∠NN connections, respectively. $\boldsymbol{\theta_1}$ and $\boldsymbol{\theta_2}$ represent the accessible vibrational angular ranges for ⊥NN and ∠NN connections, respectively. (c) Comparison between the analytical expression of $\boldsymbol{\Omega'(\Omega)}$ and a power-law approximation $\boldsymbol{\Omega' = k\Omega^n}$ under two pillar aspect ratios ($\boldsymbol{\lambda}$ = 1.5 and 5.0). (d) Average bridging number per pillar pair $\boldsymbol{B}$ versus pillar spacing $\boldsymbol{L}$ fitted using the analytical model.

To analytically estimate the average number of CNT bridges B, we consider the transverse angle Ω and the longitudinal angle Ω' that describe the accessible angular space between neighboring pillars. Based on the geometrical relationships illustrated in Fig. 4.7, we derive an analytical expression for the bridging number per pillar pair B as:

$$B = k\Omega \cdot k'\Omega' = K\Omega\Omega', \tag{4.5}$$

where K is a proportionality constant determined by the CNT density and growth conditions.

From the geometric configuration, the transverse angle Ω in the horizontal plane is given by:

$$\Omega = 2\arcsin\left(\frac{d}{2(L+d)}\right). \tag{4.6}$$

This relationship follows from:

$$\sin(\Omega/2) = \frac{d}{2(L+d)}, \tag{4.7}$$

$$\tan(\Omega/2) = \frac{d}{2y}, \tag{4.8}$$

$$\cos(\Omega/2) = \frac{z}{y}. \tag{4.9}$$

The the longitudinal angle Ω', which quantifies the vertical accessibility range for bridging, is related to the pillar height h and lateral distance z by:

$$\tan(\Omega') = \frac{h}{z}. \tag{4.10}$$

By substituting Eqs. (4.8) and (4.9) into Eq. (4.10), and expressing all quantities in terms of Ω, we obtain:

$$\Omega' = \arctan\left(\frac{2h\tan(\Omega/2)}{d\cos(\Omega/2)}\right) = \arctan\left(\frac{2h\sin(\Omega/2)}{d\left(1-\sin^2(\Omega/2)\right)}\right). \tag{4.11}$$

Alternatively, Ω' can also be expressed directly as:

$$\Omega' = \arctan\left(\frac{h(L+d)}{(L+d)^2-(d/2)^2}\right). \tag{4.12}$$

By substituting Eqs. (4.6) and (4.12) into (4.5), we arrive at the analytical form:

$$B = 2K \cdot \arcsin\left(\frac{d}{2(L+d)}\right) \cdot \arctan\left(\frac{h(L+d)}{(L+d)^2 - (d/2)^2}\right), \tag{4.13}$$

This equation shows that the bridging number B depends on the geometric parameters of the system: pillar spacing L, pillar diameter d, and pillar height h. Notably, if the aspect ratio h/d is fixed, the expression can be fully described as a function of Ω, simplifying the angular modeling framework.

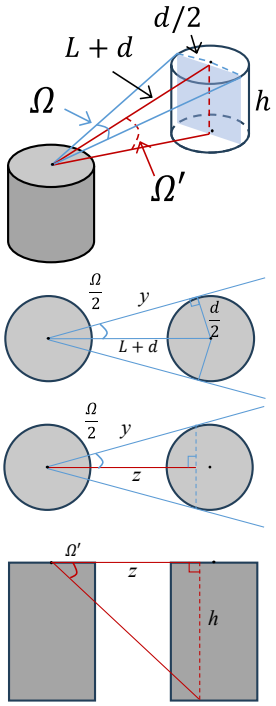


Figure 4.7 Geometric model used to derive angular accessibility between CNTs and neighboring pillars.

This geometric formulation provides a systematic framework for evaluating the bridging number based on and expanding previous simplified approaches. Given fixed pillar dimensions (d and h), the trend of B as a function of spacing L is uniquely determined by the model. The parameter K summarizes the effective density of the CNTs. A higher CNT density during growth increases the successful bridging number, thereby increasing the value of K. Thus, this formulation allows B to serve as a geometry-

dependent indicator of bridging behavior.

Previous studies [205] adopted a simplified empirical expression, a power-law form (Eq. (4.4)). This form was motivated by the assumption of a linear relationship between angles ($\Omega' \propto \Omega$), indicating that a theoretical exponent $n = 2$, and their experimental results yielded $n = 2.1$, seemingly confirming this assumption. To further investigate the validity of the simplified power-law approximation, we directly compared our analytical model (Eq. (4.11), derived from the geometric relation between Ω and Ω') to the power-law fitting results under various pillar geometries (Fig. 4.6 (c)). The aspect ratio λ is defined as the ratio of the pillar height to diameter ($\lambda = h/d$). For moderate aspect ratios ($\lambda = 1.5$, corresponding to conditions similar to previous studies [204,205]), the power-law approximation closely matches the analytical prediction, with a small error (the root mean square error $(\mathrm{RMSE}) = 1.25°$, the coefficient of determination $(\mathrm{R}^2) = 0.996$). In contrast, under our experimental conditions with a higher aspect ratio ($\lambda = 5.0$), the deviation between the analytical model and the power-law fit was slightly larger ($\mathrm{RMSE} = 4.66°, \mathrm{R}^2 = 0.950$), indicating that the power-law approximation became less reliable at high aspect ratios. Thus, our analysis reveals that Eq. (4.4) remains effective for fitting the experimental data within typical aspect ratio ranges, as in previous studies [205] and this work. However, applying the same power-law approximation for higher aspect ratio pillars may result in increasing deviations from the actual behavior.

To verify the reliability of our analytical model, we applied it to fit the experimental data spanning various pillar spacings and anisotropic array orientations. As shown in Fig. 4.6(d), which includes the experimental data shown in Fig. 4.3(c) along with the literature data, the model consistently fits different neighbor types and experimental conditions. Notably, our data in this ⊥ direction shows nearly perfect agreement with the model, indicating that the bridging behavior in this direction is well governed by the geometric constraints formalized in our theory. In contrast, when applying our analytical model to the prior work's dataset [205], we observed excellent agreement for their second

NN (2NN) bridging data, whereas moderate deviations appeared in their first NN (1NN) data. This slight discrepancy may be attributed in part to the differences in the definition of bridging in each study. In the referenced work, bridging was counted as a binary outcome—whether a CNT bridged a given neighbor pair or not—regardless of the number of bridging CNTs. In contrast, the overall consistency and accuracy of our analytical model across other datasets, including our measurements, supports its general validity and robustness. It is worth noting that although the analytical bridging model assumes cylindrical pillars for simplicity, the actual structures used in the experiments are square in cross-section. This approximation remains valid because the interpillar distances are much larger than the difference between the square and circular cross-sectional dimensions, resulting in only minor variations in the angular accessibility. As shown in Fig. 4.8, the fits based on the cylinder approximation and the two limiting square configurations (face-to-face and diagonal) exhibit similar trends across the explored CNT length regime, supporting the validity of the cylindrical approximation. Moreover, unlike the square pillars, the cylinder model is rotationally invariant, which makes it more general and applicable regardless of the array orientation. The consistent agreement with the experimental data further supports the validity of the geometric simplification.

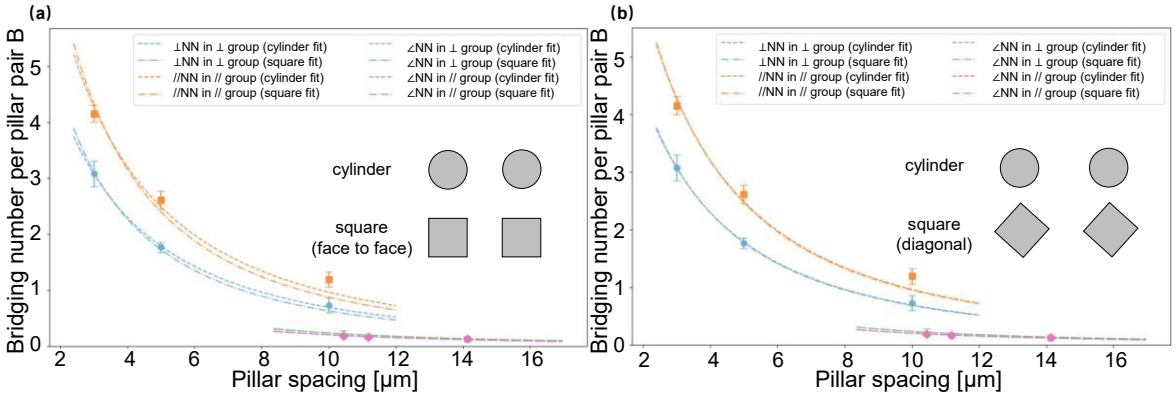


Figure 4.8 Comparison of model fits using the cylinder approximation and the two limiting square configurations: (a) face-to-face and (b) diagonal.

To explain the directional dependence observed in the CNT bridging, a vibrational growth model was previously proposed [204] as an extension to the isotropic model. Although the isotropic model provides excellent fits across all datasets, there are inconsistencies when comparing the fitted values of the proportionality constant K within the same sample group. For example, in the // group, K values differ significantly between //NN and ∠NN cases; similarly, the difference between ⊥NN and ∠NN is also significant in the ⊥ group. Since these data were obtained under identical experimental conditions, such differences cannot be attributed to variations in the CNT density. This indicates that the isotropic model alone is insufficient to explain the directional dependence of the bridging behavior. To address this issue, previous studies proposed the CNT vibration interpretation based on the isotropic model. Although their analytical expression remained the same, the authors attributed the variation in K to differences in the CNT vibrational mechanism. Based on the geometric considerations (Fig. 4.6 (b)), the ratio of K_1 to K_2 can be expressed as follows:

$$\frac{\theta + \Omega_1}{90° - \Omega_1 - \theta} = \frac{\theta_1}{\theta_2} = \frac{B_1(L_1)}{B_2(L_2)} = \frac{K_1 \Omega_1 \Omega_1'}{K_2 \Omega_2 \Omega_2'}, \tag{4.14}$$

where K_1 and K_2 represent the fitted proportionality constants for the CNT bridging along the ⊥ and ∠ directions, θ denotes the effective vibrational angle range of the CNT during growth, Ω_1 and Ω_2 represent the transverse angles corresponding to ⊥NN and ∠NN connections, respectively, Ω_1' and Ω_2' represent the longitudinal angle, θ_1 and θ_2 represent the accessible vibrational angular ranges for ⊥NN and ∠NN connections, respectively. As shown in Fig. 4.6 (b), each CNT oscillates within an angular range of θ and can bridge to neighboring pillars if its trajectory intersects the accessible angular range. In the ⊥ direction, any CNT that swings within the combined angle $\theta + \Omega_1$ will eventually land on a ⊥NN pillar. In contrast, to bridge diagonally, the CNT must avoid the ⊥NN pillar entirely and remain within the narrower diagonal angle defined by $90° - \Omega_1 - \theta$. Assuming a symmetric geometry where $\Omega_1 \approx \Omega_2$, $\Omega_1' \approx \Omega_2'$ and that Ω_1

remains small ($< 10°$), since the pillar diameter is much smaller than the interpillar spacing, the expression simplifies to:

$$\frac{K_1}{K_2} \approx \frac{\theta}{90° - \theta}. \tag{4.15}$$

In our experiments, the estimated K ratio for ⊥NN is approximately 3, corresponding to a vibration angle of $\theta \approx 68°$, which closely matches the value derived from prior data [23]. Since the ⊥NN connection is aligned ⊥ to the gas flow direction; thus, it is not affected by the flow-directed elongation and can be regarded as predominantly governed by the vibrational mechanism. Moreover, previous studies have reported CNT oscillation angles of around $30°$, giving a total swing range of approximately $60°$, which is consistent with the $68°$ estimate, further supporting the validity of the vibrational growth model. In contrast, the //NN connection is aligned horizontally to the gas flow direction and is more susceptible to bridging by the gas-flow-induced force. Therefore, the corresponding angle estimated from the K ratio ($\theta \approx 75°$) should not be interpreted as a pure vibrational amplitude. Instead, it likely reflects a combined contribution from both the vibrational and gas-flow-directed growth mechanisms.

4.4 Gas flow-induced deflection and vibrations

To further elucidate the influence of the gas flow on the CNT growth behavior, steady-state fluid dynamics simulations based on the FEM were conducted. Fig. 4.9 shows the simulated velocity fields around the nanopillar arrays with three different configurations: 3 × 10, 5 × 10, and 10 × 10. As shown in the figure, each row corresponds to a horizontal cross-sectional slice at a different vertical height: near the substrate (~4 μm above the base), at the pillar top (8 μm), and above the pillar (~12 μm). The gas flows horizontally from left to right, and the color scale from low (blue) to high (red) represents the velocity magnitude.

Although the velocity in the upper layer above the pillars remains largely unaffected across all configurations, the flow behavior at the pillar tops and near the substrate is more sensitive to the interpillar spacing. These two regions are essential because CNT bridging predominantly occurs near the pillar top and the substrate. At a 3 μm spacing, the dense pillar array significantly impeded the gas flow, thereby reducing the flow velocity between the pillars at the height of the pillar tops to approximately one-half of the inlet velocity and making the flow near the substrate nearly stagnant. When the spacing increased to 5 μm, the obstruction effect diminished. The flow velocity between the pillars at the height of the pillar tops noticeably increases, and small regions even reach the inlet velocity. At the widest spacing of 10 μm, confinement is essentially eliminated because the increased gap between the pillars allows the gas flow to pass through with minimal obstruction. As a result, the flow between the pillars, both near the tops and close to the substrate, achieves an inlet velocity. These results indicate that as the interpillar spacing increases, the influence of the gas flow becomes more pronounced in regions where CNT bridging occurs. This raises a critical question: how does this evolving flow environment impact CNT growth and bridging mechanisms?

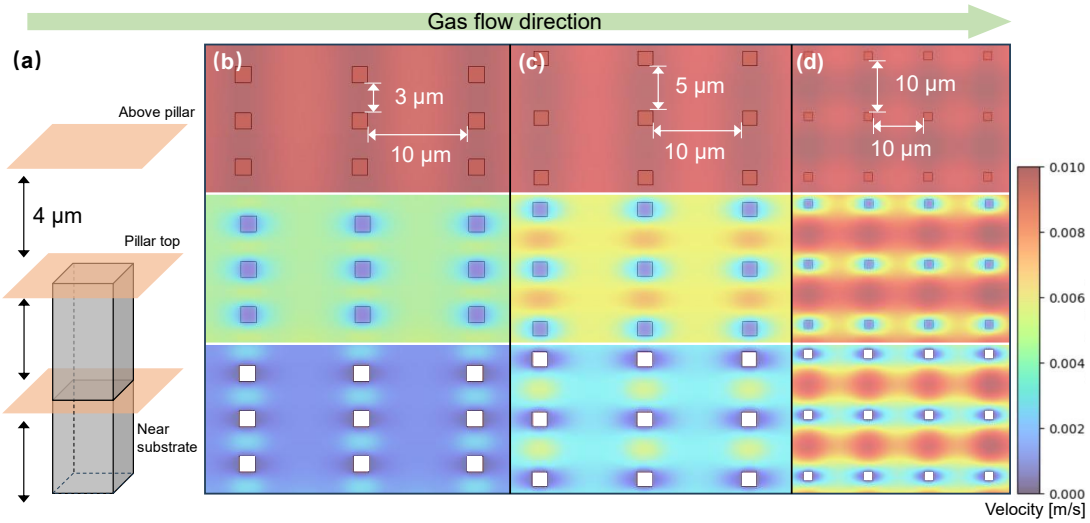


Figure 4.9 (a) Schematic illustration of a square nanopillar array and the positions of three horizontal cross-sectional slices: above the pillar (12 μm from substrate), at the pillar top (8 μm), and near the substrate (4 μm). (b–d) Simulated velocity magnitude distributions under horizontal gas flow (left to right) for pillar spacings of 3, 5, and 10 μm, respectively. Each row corresponds to one of the three slice heights defined in (a). Color indicates the magnitude of the flow velocity in arbitrary units, with warmer colors representing higher velocities. Note that in the bottom row (near the substrate), the square regions correspond to the cross-sections of the nanopillars. No fluid flow occurs within these structures, so no velocity is defined inside them. The apparent coloration inside the pillars is due to the material rendering in the simulation software and should not be interpreted as the fluid velocity.

To quantify the effect of gas flow on individual CNT growth, it is critical to recognize that the CNT diameter is considerably smaller than the mean free path of the gas molecules under typical CVD conditions. Thus, the flow regime corresponds to the free molecular flow characterized by a Knudsen number $K_n = \Lambda/d \gg 1$, where Λ denotes the gas mean free path, and d denotes the CNT diameter, rendering conventional continuum-based drag models inapplicable. Accordingly, the drag force F exerted on a CNT can be estimated using an empirical expression suitable for the free molecular flow regime [215]:

$$F = \sqrt{2\pi m_g kT}\left[\varphi + \left(2 - \frac{6-\pi}{4}\varphi\right) sin^2\ \alpha\right] NRL_c V. \tag{4.16}$$

Here, m_g denotes the mass of a gas molecule, k denotes Boltzmann's constant, T denotes the absolute temperature, φ denotes the momentum accommodation coefficient, typically taken as 0.9 based on standard gas–solid interaction models [215], and is insensitive to variations within a reasonable range, α denotes the angle between the gas flow direction and the CNT axis (set to 90°), N denotes the number density of the gas molecules, R denotes the CNT radius, L_c denotes the CNT length, and V denotes the relative gas flow velocity.

The corresponding lateral deflection of the CNT under the influence of this drag force can be modeled by treating the CNT as a cantilever beam subjected to a uniform load. The deflection δ at the free end is calculated as follows [216]:

$$\delta = \frac{qL_c^4}{8YI}. \tag{4.17}$$

Here, q denotes the distributed load per unit length given by $F = qL_c$, Y denotes the Young's modulus of the CNT, and I denotes the second moment of the area. Under the flow conditions used in this study, analytical calculations based on Eq. (4.17) suggest that CNTs with lengths smaller than approximately 1 μm exhibit minor deflection, typically below 1 nm, as summarized in Table 4.1. In principle, the flexibility of the catalyst particle at the CNT root can influence the amplitude of the CNT tip deflection during growth. However, explicitly incorporating the catalyst deformation into the analytical model would significantly complicate the derivation. To address this issue, FEM simulations were conducted to assess the potential impact of the catalyst flexibility. First, without considering catalyst softening, the FEM results (summarized in Table 4.1) showed that the tip deflection remained small, with values around 0.059 nm for a CNT with a length of 400 nm. Subsequently, a 5-nm hemispherical iron particle with reduced mechanical stiffness was introduced at the CNT root, where the elastic moduli were

reduced to one-tenth of their expected high-temperature values to approximately account for the thermal softening effects. This modification slightly increased the tip deflection from 0.059 to 0.079 nm for a CNT of the same length. However, the overall influence remained limited. Therefore, in the subsequent analyses, the catalyst flexibility was reasonably neglected to simplify the modeling without a significant loss of accuracy. The gas-flow-induced deflection as a function of the CNT length is plotted as the blue curve in Fig. 4.10 (a).

Table 4.1 Estimated CNT tip displacement under different driving mechanisms

Driving mechanism	**CNT length**	**CNT displacement**	
		Formula (Eqs. (12) and (13))	FEM simulation
Flow disturbance	400 nm	0.047 nm	CNT: 0.059 nm
			CNT+Fe: 0.079 nm
	1 μm	1.8 nm	–
	4 μm	470 nm	–
Thermal vibration	400 nm	18.0 nm	CNT: 16.80 nm
			CNT+Fe: 40.20 nm
	1 μm	71.0 nm	–
	4 μm	568 nm	–

In contrast, vibrations were identified as the main factors that modulated the growth of shorter CNTs. Although previous studies have primarily attributed such vibrations to mechanical vibrations from the CVD system [204,207], it is essential to recognize that thermal excitation may also contribute significantly. In a previous study [204], the vibrational amplitude, defined as the lateral displacement range of the CNT tips during growth, was first calculated using a cantilever beam model, which was found to be insufficient to explain the observed high proportion of NN bridging. To address this issue, the authors proposed that the catalyst particles become molten during growth, which

could enhance the large-amplitude motion driven by external mechanical vibrations. This view is further supported by subsequent experimental studies showing that catalyst particles can indeed become molten during growth due to the formation of carbon–metal eutectic compounds in the CVD environment [110]. However, the same softening at the CNT root would also reduce the effective stiffness of the system [217], thereby increasing the vibrational amplitude under thermal excitation, according to the equipartition theorem [218]. To evaluate both possibilities, we derived and compared the analytical expressions for the vibration amplitude arising from the thermal and external mechanical vibrations. The amplitude σ of thermal vibrations is given by [219]

$$\sigma = 0.9212\left(\frac{kT}{YWG(W^2+G^2)}\right)^{0.5} L_c^{1.5}, \tag{4.18}$$

where W denotes the measured diameter of the CNT, and G (0.34 nm) is the graphite interlayer spacing used to represent the effective thickness. The red curve in Fig. 4.10 (a) shows the thermal vibration amplitude estimated from the analytical calculations based on Eq. (4.18).

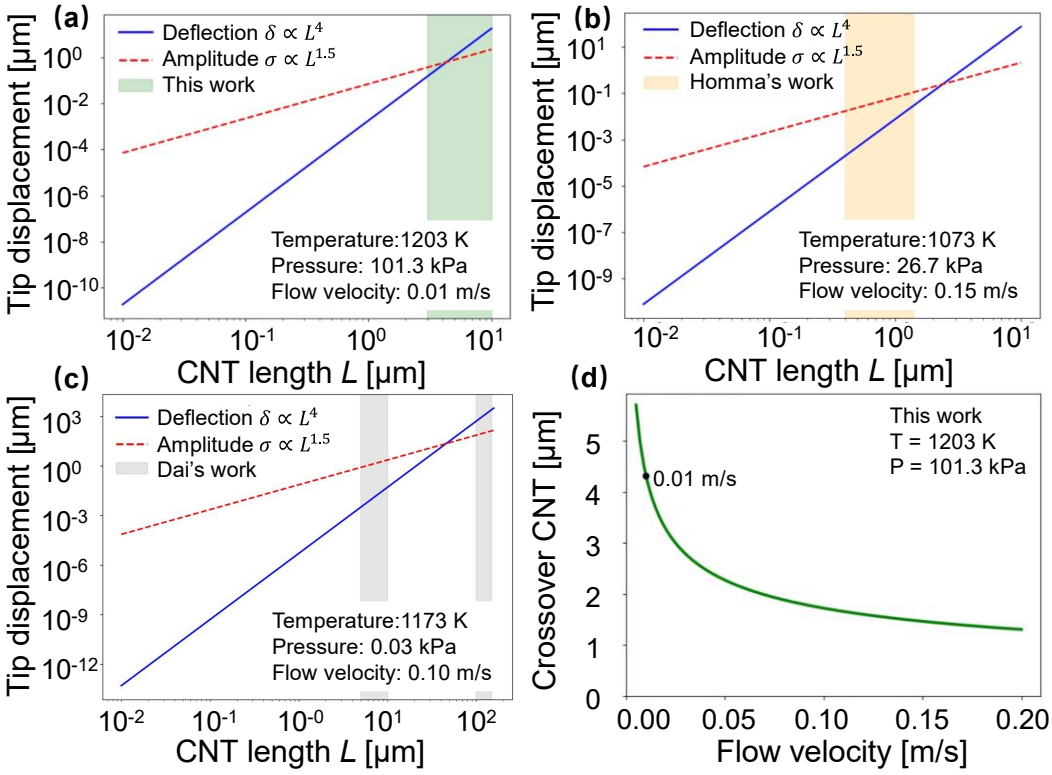


Figure 4.10 (a, b, c) Log–log plot comparing the gas-flow-induced deflection (blue line) and thermal vibration amplitude (red dashed line) as a function of the CNT length under different experimental conditions: (a) this work, (b) a previous study **[205]**, and (c) another previous study **[149]**. The shaded regions represent the typical CNT length range under each condition. (d) The crossover length shifts with increasing gas flow velocity. The curves were generated from the model calculations under the experimental conditions used in this work.

The amplitude of the mechanical vibration can be estimated by modeling the CNT as a cantilever beam under low-frequency forced vibration conditions. The mechanical vibration originating from the rotary pump is assumed to be directly transmitted to the CNT without attenuation. In other words, the acceleration acting on the CNT is equal to the pump-induced acceleration:

$$a_0 = A_p \cdot (2\pi f)^2, \tag{4.19}$$

where A_p and f denote the amplitude and frequency, respectively, of the pump vibration. We adopted relatively high values for these parameters—A_p = 50 μm and f = 100 Hz—which are within the upper range of typical mechanical vibration in CVD systems. Under the low-frequency limit, the vibration amplitude A of the CNT refers to the maximum lateral displacement of its free end during growth and can be approximated as follows [220]:

$$A \approx \frac{F_0}{m_{eff}\omega_0^2} = \frac{F_0}{0.236m\omega_0^2} = \frac{a_0}{0.236\omega_0^2}, \tag{4.20}$$

where F_0 denotes the external force on the CNT, the coefficient 0.236 represents the normalized effective mass of the CNT in its first flexural mode, and ω_0 denotes the natural angular frequency of the first flexural mode given by [218]:

$$\omega_0 = \frac{\beta_0^2}{2L_c^2}\sqrt{\frac{Y(W^2+G^2)}{2\rho}}. \tag{4.21}$$

Here, ρ denotes the density of the CNT, and $\beta_0 \approx 1.875$ represents the mode constant of the first flexural mode. By substituting Eqs. (4.19) and (4.21) into Eq. (4.20), the vibration amplitude induced by the mechanical vibration from the CVD system is given by

$$A = \left(\frac{32\pi^2\rho f^2 A_p}{0.236\beta_0^4 Y(W^2+G^2)}\right)L_c^4. \tag{4.22}$$

The results in Fig. 4.11 show that even under conservative assumptions, the mechanical vibrations remain significantly smaller than those induced by the thermal vibrations under typical growth conditions. Therefore, we consider the thermal vibration to be the dominant vibrational mechanism that influences the CNT bridging, whereas the contribution of the externally induced mechanical vibrations can be reasonably regarded as negligible. It worth noting that although mechanical vibrations from the rotary pump

were conservatively estimated in the model, their influence on bridging behavior was found to be negligible. Thus, even without pump-induced vibrations, similar outcomes are expected. Future studies may explore direct characterization or isolation of such vibrations to further validate this assumption.

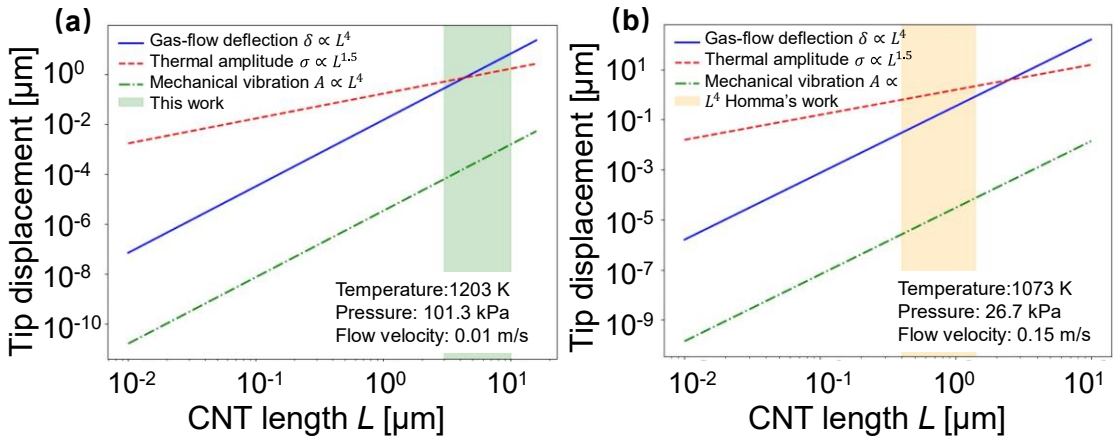


Figure 4.11 (a) Log-log plot comparing gas-flow-induced deflection (blue line), thermal vibration amplitude (red dashed line) and vibration amplitude induced by mechanical vibration (green dashed line) as a function of CNT length under different experimental condition: (a) this work, (b) a previous study.

Based on this understanding, we further compared the magnitudes of the gas-flow-induced deflection and thermal vibration amplitude as functions of the CNT length to identify a distinct crossover behavior. This crossover is inevitable, as the thermal vibration amplitude scales with the CNT length as $L_c^{1.5}$, whereas the gas-flow-induced deflection grows much faster, scaling as L_c^4. Fig. 4.10 (a) shows this relationship under the growth conditions used in our experiments. For CNT lengths shorter than approximately 4 μm, the thermal vibration dominates the tip motion, and the bridging behavior is primarily governed by the intrinsic vibrational dynamics around the catalyst. This regime favors short-range 1NN connections and is largely insensitive to gas flow. However, for CNTs longer than ~4 μm, flow forces induce greater deflection, and gas-

flow-directed growth becomes the dominant mechanism, enabling longer-range, flow-aligned bridging paths.

Importantly, the crossover point between these two regimes is not fixed; it varies with experimental conditions like temperature and gas flow rate. Fig. 4.10 (b) compares the crossover length under different growth conditions used in previous studies [205]. Due to differences in the experimental conditions—specifically, a higher gas flow velocity, lower system pressure, and lower temperature—the crossover point in their system occurs at a longer CNT length than the actual length grown in their experiments. This explains their conclusion that the gas flow plays little to no role in CNT bridging. Under these conditions, the CNTs remained too short to be affected by the flow-induced forces. In contrast, CNTs grow sufficiently long in our system to exceed the crossover length, making the gas flow a decisive factor in the growth dynamics. In addition to the previous study [205], another previous study [149] also provided important evidence supporting the crossover model proposed in this work.

Fig. 4.10 (c) shows the crossover length under the growth conditions from a different prior study [149]. Under these conditions, the crossover point appeared at a CNT length between the lengths of the short CNTs forming the network and the longer CNTs observed bridging multiple pillars. For short CNT networks, this is consistent with their SEM observations, where CNTs bridging the // and ⊥ directions appear in similar numbers, indicating the absence of strong directional alignment with the gas flow. Additionally, when a CNT bridges from the top of one pillar to a neighboring pillar, the attachment points are distributed across the top, middle, and bottom regions of the receiving pillar. This spatial distribution suggests that the CNT tips oscillate due to the thermal vibrations during growth rather than the flow-induced force. In contrast, for isolated ultralong CNTs exceeding 100 μm, flow-induced forces were dominant. In these cases, the CNT midsections were mostly found lying near the tops of the adjacent pillars, which is consistent with the gas-flow-directed growth mechanism, in which the CNTs are lifted by

the gas flow and fall onto the neighboring structures from above. These observations provide strong evidence that both vibrational and gas-flow-directed growth modes are present, depending on the CNT length, which aligns well with the crossover model proposed in this work.

Fig. 4.10 (d) shows how the crossover point between the thermal-vibration-dominated and gas-flow-dominated regimes varies with the gas-flow velocity. For comparison, the effects of temperature and pressure on the crossover length were also evaluated (Fig. 4.12). Although these parameters influence the crossover point, their impact is notably less significant than the gas flow velocity. Under increasing flow rates, the aerodynamic drag exerted on the CNTs significantly increased, accelerating the onset of the flow-induced deflection relative to the thermally induced vibration amplitude. As a result, the length at which the gas flow begins to dominate over the thermal motion—the crossover length—shifts progressively to lower values. For example, at a low flow velocity of 0.001 m/s, crossover occurs at approximately 5 μm, indicating that only relatively long CNTs are subject to flow-dominated behavior. As the flow velocity increased to 0.01 m/s, the crossover point decreased to approximately 4 μm. Further increasing the flow velocity to 0.02 m/s or a faster gas flow velocity shifts the transition point down to the 2–3 μm range.

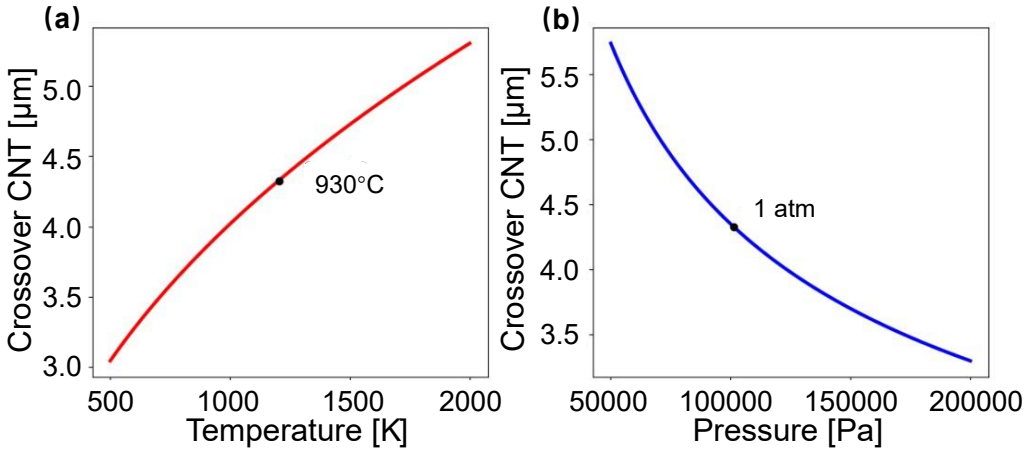


Figure 4.12 Dependence of the crossover CNT length on (a) temperature and (b) pressure.

This means that under a strong gas flow, even short CNTs are susceptible to aerodynamic deflection, enabling the gas-flow-directed growth mechanism to engage earlier during growth. This predicted trend is consistent with the experimental observations in Fig. 4.13: at lower flow rates, CNTs of comparable lengths are less affected by flow-induced forces, leading to a higher bridging number—particularly for those perpendicular to the flow direction. In contrast, higher flow rates enhance flow-induced forces that interfere with the vibrational mode, thereby reducing the bridging number.

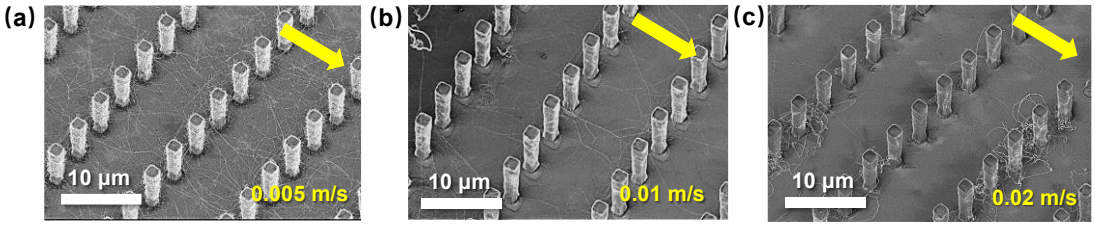


Figure 4.13 SEM images of CNT networks grown at 930 °C under different gas flow velocities: (a) 0.005 m/s, (b) 0.01 m/s, and (c) 0.02 m/s.

However, such tuning is only meaningful when the growth conditions remain within a regime that supports stable gas-flow-directed growth. Outside this window, changes in temperature or pressure may lead to growth interruption or instability, making the concept of a well-defined crossover no longer applicable. In practice, the growth behavior is governed by multiple coupled parameters, including catalyst activity, carbon supply, gas transport, and force balance at the CNT tip. Because of this complexity, it is difficult to quantitatively predict a specific crossover value using a single control parameter. Nevertheless, from a qualitative perspective, the observed trend remains robust: modifying flow velocity, temperature, or pressure systematically alters the relative importance of vibrational motion and flow-induced alignment, thereby enabling

directional tuning of the crossover behavior. As long as the conditions satisfy the basic requirements for gas-flow-directed growth, the conclusions drawn in this work remain valid.

These results highlight the tunability of the CNT growth regime via the gas flow control. Therefore, flow velocity is not just a passive growth parameter—it actively governs the nature and scale of the CNT network formation. In the absence of gas flow during growth, the crossover length can be considered effectively infinite, indicating that the entire CNT growth process is governed by a vibrational mechanism. This limiting case was observed in previous studies and agreed well with the vibrational growth model [205], as shown in the fitting results in Fig. 4.14.

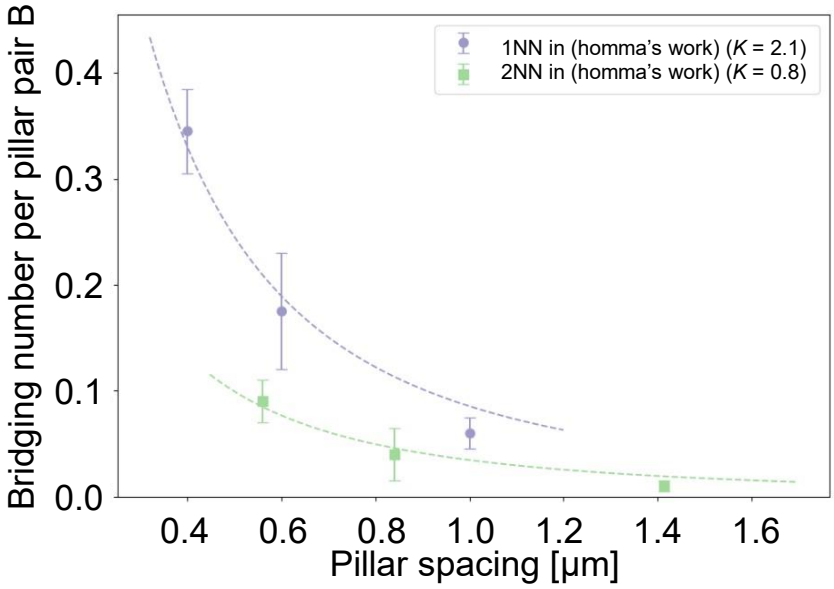


Figure 4.14 Average bridging number per pillar pair ***B*** versus pillar spacing ***L*** fitted using the analytical model under no gas flow condition.

4.5 Statistical analysis of the CNT bridging types

To comprehensively characterize the structural properties of the CNT networks formed under various growth conditions, we also classified bridging CNTs that do not fall into the previously defined //NN, ⊥NN, or ∠NN categories as "other." These "other" CNTs refer to those that still form suspended bridges but fall outside the defined NN types (//NN, ⊥NN, and ∠NN). They may span more than two pillars, follow highly bent or twisted paths between pillars, or even form entangled structures with neighboring CNTs, making them distinctly different from straight NN bridges. Although these CNTs are relatively rare, their presence becomes more noticeable under gas-flow-directed growth conditions, which facilitates longer CNT extensions. These bridges contribute to increased network complexity and may enhance signal propagation diversity, potentially contributing to applications, such as physical reservoir computing and neuromorphic circuits [221–225].

Fig. 4.15 categorizes the CNT bridges into three types. The first category is the //NN bridges, which align with the gas flow direction and are influenced by gas-flow-directed growth and vibrations. The second is the ⊥NN bridges, which are difficult to align due to gas-flow-induced forces, primarily formed due to vibrations. The third category is the ∠NN and "other" bridges, which generally span greater distances, making vibrations negligible, although they are influenced by the gas flow (Fig. 4.10 (a)). A notable indication of gas-flow-directed growth can be observed when comparing the 3 × 10 and 10 × 3 layouts. Despite having the same short pillar spacing (3 μm), the 3 × 10 layout shows a higher density of //NN bridges compared to the ⊥NN bridges in the 10 × 3 layout. Given that the vibrations remained consistent in both instances, this difference can be attributed to the directional contributions of the gas-flow-directed growth, allowing the CNTs to extend longer and align better with the gas flow. The numerical values related to Fig. 4.15 are summarized in Table 4.2.

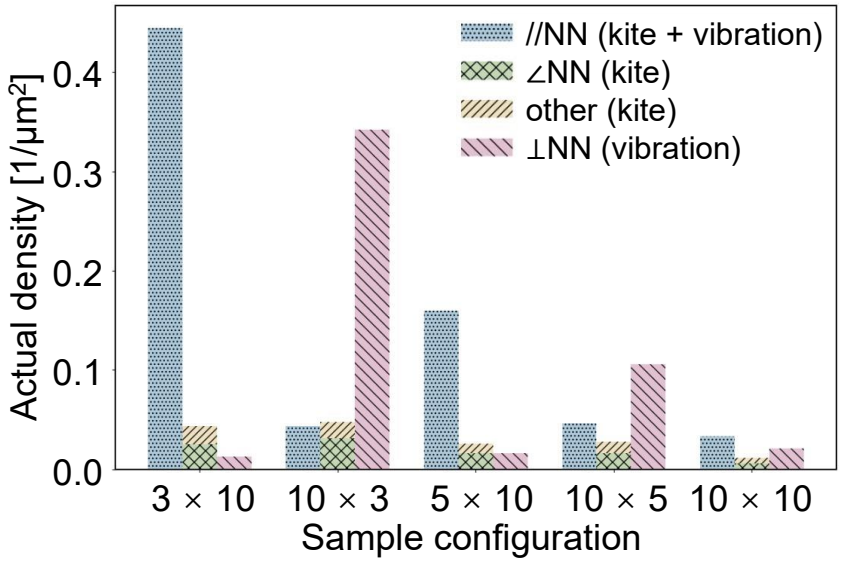


Figure 4.15 Actual density distributions of the CNT bridges for different sample configurations. Stacked bar chart depicting the contributions of //NN, ⊥NN, ∠NN, and "other" CNT bridges to the total network density. The //NN bridges are aligned in the direction of the gas flow and are affected by gas-flow-directed growth and vibrations. The ⊥NN bridges, which are difficult to align with gas-flow-induced forces, mainly form because of vibrations. In contrast, ∠NN and "other" bridges tend to cover larger distances, rendering vibration insignificant, and they are still influenced by gas flow.

Table 4.2 CNT bridging type proportions and total density across different nanopillar configurations

sample	// Spacing (μm)	⊥ Spacing (μm)	//NN (%)	⊥NN (%)	∠NN (%)	Other (%)	Total Density (1/μm²)
3 × 10	3	10	88.8	2.6	5	3.7	0.501
10 × 3	10	3	10	79	7.2	3.8	0.433
5 × 10	5	10	79.3	8	8	4.8	0.201
10 × 5	10	5	25.6	58.9	8.9	6.7	0.18
10 × 10	10	10	50.9	32.1	9.4	7.5	0.066

As shown in the 3 × 10 vs. 10 × 3 and 5 × 10 vs. 10 × 5 layouts, the actual density of ∠NN and "other" bridges remains nearly constant regardless of the flow direction. This

suggests that their formation is not influenced by the direction of the gas flow. These bridges tend to be longer and can be influenced by flow-induced effects; however, they exhibit an angular deviation from the flow direction. In such cases, the gas flow may even create disturbances that lead to deflected or bent connections, contributing to the ∠NN and "other" types. Thus, their actual density is primarily influenced by the arrangement of the pillars rather than the flow alignment. However, their percentage relative to the total number of CNT bridges does change with variations in the gas flow direction. The 3 × 10 layout shows an increase in //NN bridges, which reduced the proportion of ∠NN and "other" types. Although the actual density in the 3 × 10 layout exceeded that of the 10 × 10 layout, the proportion decreased to below 5%, compared to almost 10% in the 10 × 10 layout. This indicates that both the gas flow direction and the arrangement of pillars can be adjusted to control the density and relative proportions of ∠NN and "other" types, offering a level of structural tunability during network formation.

Notably, the bridge-type distribution reported in the previous study [204], which used iron catalysts, was close to our 5 × 10 result. Specifically, their CNT networks contained 86% NN bridges, 9% second-NN bridges, and 5% classified as "other." These values closely match our 5 × 10 data: 87% //NN + ⊥NN (NN), 8% ∠NN (second-NN), and 5% "other." Although the numbers are similar, the growth mechanisms differ. In their study, the pillar arrangement was fixed, and they only experienced vibrational growth. In contrast, our findings indicate that by controlling the pillar arrangement and gas flow, we can consistently achieve bridge-type distributions comparable to those associated only with vibrational growth. These findings highlight how the pillar arrangement and gas flow influence the CNT bridging behavior. Gas-flow-directed growth enhances directional alignment and enables long-range connectivity, whereas the pillar arrangement influences vibrational bridging for short-range CNT connections.

We further find that, for short inter-pillar bridging distances, straight CNT configurations are statistically dominant. This observation can be rationalized by

considering the mechanical stiffness and thermal fluctuation characteristics of CNTs under fixed boundary conditions. Once a CNT becomes anchored to two neighboring pillars, the suspended segment is effectively pinned at both ends, and its equilibrium configuration is governed by the balance between bending energy and residual lateral perturbations.

A quantitative criterion for this behavior is provided by the persistence length l_p, defined as

$$l_p = \frac{YI}{kT}, \tag{4.23}$$

which characterizes the length scale over which thermal fluctuations significantly randomize the CNT orientation [226]. Approximating the CNT as a solid cylindrical rod with moment of inertia $I = \pi R^4/64$, a Young's modulus $Y \approx 1$ TPa, diameter $d =$ 2 nm, and growth temperature $T \approx 1173$ K (900 °C), yields a persistence length on the order of $l_p \approx 50\ \mu m$. For suspended CNT segments whose length is well below this scale, bending fluctuations are strongly suppressed and the nanotube behaves effectively as a rigid rod. Consequently, in the short-span regime where the inter-pillar distance is much smaller than the persistence length (5 μm), the lowest-energy configuration is a near-straight segment connecting the two anchoring points. Any transient curvature introduced during the vibrational bridging event is not mechanically stabilized after anchoring. This explains why short-distance bridges appear predominantly straight despite the dynamic nature of the initial contact process. Curved bridges can nevertheless be observed in some cases. Such curvature does not originate from the bridging mechanism itself, but rather from continued CNT growth after the nanotube tip has already been fixed to the neighboring pillar. In this situation, excess length generated after anchoring cannot be accommodated by axial extension and is instead released through bending of the suspended segment, as discussed by Homma *et al.* [206].

4.6 Conclusion

In this study, we revisited pillar-assisted CNT growth and developed a generalized analytical model to describe the vibrational bridging of CNTs between nanopillars. By incorporating geometric constraints, the proposed model extends the previous vibrational model and quantitatively captures the relationship between the pillar spacing and bridging number. Introducing the gas-flow-directed growth mechanism allowed us to reveal a crossover behavior between the two competing growth modes. Although the vibrational model governs short CNTs, longer CNTs are increasingly influenced by the gas-flow-induced deflection. The position of this crossover point depends on the CNT length and growth conditions and can be systematically tuned through the gas flow rate and other conditions. Statistical analysis of the CNT bridging further demonstrates that the structural composition of the resulting network can be controlled by adjusting the gas flow direction and pillar arrangement. These findings provide a unified understanding of CNT network formation under gas flow-guided, pillar-assisted growth and offer practical design guidelines for nanostructured interconnects and wiring applications. Importantly, although this study focuses on structural formation rather than electrical functionality, it establishes a controllable framework for producing long, continuous CNTs with well-defined connectivity under geometric constraints. Such structural control is a necessary prerequisite for subsequent device-level investigations, where uninterrupted CNT pathways and reproducible architectures are required. In this sense, the present work provides a structural foundation for the transport studies discussed in the following chapters. Moreover, these structurally tunable networks show potential as a platform for future physical reservoir computing systems [221–225], where complex connectivity and material nonlinearity offer key functional advantages. Future work will focus on the functional characterization of these networks, enabling direct electrical measurements relevant to both interconnect applications and neuromorphic device architectures.

Chapter 5. Substrate-dependent electrical transport in individual single-walled carbon nanotubes grown across SiO_2 and hexagonal boron nitride

5.1 Background

Carbon nanotubes (CNTs) [1,2] have attracted sustained attention due to their exceptional electrical, mechanical, and thermal properties [4,33,52]. Their one-dimensional structure leads to quantum confinement and reduced scattering, which can result in ballistic transport over micrometer scales [227–229]. However, the electronic performance of CNT-based devices is strongly influenced by their surrounding environment, including the choice of substrate, surface adsorbates, and fabrication residues [151,6,152]. Among these, the substrate plays a particularly critical role: it governs charge screening, introduces remote phonon scattering, and determines the level of electrostatic disorder that carriers experience [230]. Therefore, understanding and quantifying substrate effects are essential for realizing CNTs' intrinsic transport potential in nanoelectronic applications.

To address these challenges, high-quality synthesis methods that minimize extrinsic disorder are indispensable. One promising strategy is gas-flow-directed growth [15,21,27,150], in which laminar gas flow and buoyancy effects guide CNT elongation along a uniform direction. As a chemical vapor deposition (CVD) variant, this technique enables the direct growth of ultralong, highly aligned CNTs without the need for any post-growth transfer or mechanical manipulation. Compared with conventional CVD or transfer-based methods, gas-flow-directed growth produces cleaner CNTs free from polymer residues or bending-induced defects, thus preserving their intrinsic transport characteristics. Furthermore, because CNTs can extend across large areas following the gas flow direction, this approach naturally allows the formation of continuous CNTs that traverse multiple substrate regions on a single chip [27,231,232,23]. Such an architecture provides an ideal platform for systematic studies of substrate-dependent transport within

the same physical CNT, eliminating variability associated with tube-to-tube differences.

SiO_2, as the most commonly used dielectric in CNT field-effect transistors (FETs) [30], introduces several detrimental effects such as surface roughness, trapped charges, and coupling to remote interfacial phonons, which collectively degrade carrier mobility and shorten the mean free path [154–156,233]. In contrast, hexagonal boron nitride (hBN) offers an atomically flat and chemically inert surface with low charge impurity density and weak phonon coupling [153,234–237]. These attributes make hBN a promising substrate for achieving cleaner and more stable CNT transport. Several studies have shown practical benefits of integrating CNTs with hBN, including a markedly higher current-carrying capacity enabled by improved heat dissipation in hBN stacks [238], cleaner and more stable quantum-dot operation [239], reduced hysteresis through tailored interfacial dielectrics [240]. hBN also enables solid-state optical and spectroscopic advantages for CNTs, such as bright room-temperature photoluminescence with narrow linewidths on hBN [241], direct chirality assignment on insulating hBN [242], and well-defined tunneling barriers for broadband CNT–CNT spectroscopy [243], all indicative of a cleaner dielectric environment. Nevertheless, past works have found negligible improvement compared to SiO_2, especially in subthreshold behavior and low-field conduction [240]. Such inconsistencies likely arise from differences in fabrication techniques, particularly those involving CNT transfer processes that introduce contamination or mechanical strain. Despite these efforts, a quantitative and direct comparison of CNT transport on hBN and SiO_2 under identical CNT conditions remains limited. Most prior studies rely on separate CNTs for each substrate, making it difficult to disentangle substrate effects from variations in chirality, diameter, or defect density. Moreover, systematic analyses of key transport parameters, such as field-effect mobility, mean free path, and thermal activation energy, have been incomplete.

In this work, we overcome these limitations by employing gas-flow-directed growth to synthesize long CNTs that span both SiO_2 and exfoliated hBN regions on the same

substrate. Using this configuration, we fabricated multiple channels device along a single CNT, enabling direct comparison of transport behavior on the two substrates under identical structural and environmental conditions. Nanodiamond (ND) particles were used as nonmetallic seeds for CNT growth, offering excellent growth stability and enabling the formation of isolated, long CNTs suitable for device fabrication [106,140]. Through systematic measurements of length- and temperature-dependent transport, we extracted the field-effect mobility and activation energies associated with thermally activated conduction. This integrated approach highlights the advantages of gas-flow-directed growth and provides a robust experimental framework for revealing how dielectric environments influence CNT electronic performance.

.

5.2. Experimental section

5.2.1 CNT growth

A ~1 cm × 1 cm SiO_2/Si wafer was used as the substrate. Fresh adhesive tape was first used to mechanically exfoliate hBN. The same piece of hBN-bearing tape was then laminated onto one half of the wafer to transfer hBN flakes and to mask that half from ND deposition. The other half, which remained bare SiO_2, was drop-cast with an ethanol dispersion of ND seeds. The ND suspension was allowed to dry in air. The wafer was placed on a hot plate at 90 °C for 2.5 min. The tape was then peeled off to leave a half-hBN, half-ND substrate: one half covered by transferred hBN flakes, the other half seeded with ND on bare SiO_2. Growth conditions followed our previous gas-flow-directed protocol [140]. Substrates were loaded into a horizontal quartz-tube CVD reactor. The tube was preheated to 600 °C. Samples were pushed to the hot zone and held at 600 °C in air for 10 min to remove tape residues and surface contaminants, as well as to downsize ND seeds appropriate for CNT growth [117]. The furnace was then brought to the synthesis temperature in the range 850–950 °C under a continuous H_2 (3%)/Ar flow. CNT growth was initiated by introducing ethanol vapor using H_2 (3%)/Ar bubbling through ethanol at ~40 °C in combination with a main H_2 (3%)/Ar stream. The growth process was conducted at atmospheric pressure, and the partial pressure of ethanol was estimated to be ~1.4 kPa. Growth proceeded at atmospheric pressure for ~30 min. After growth, the gas was switched to Ar and the system was cooled to room temperature. Under these conditions, laminar flow and buoyancy guided CNTs along the gas-flow direction. As a result, long and well-aligned CNTs were obtained, some of which spanned from the ND-seeded SiO_2 region into the hBN region, enabling subsequent multi-channel device fabrication on the same CNT for cross-substrate transport studies.

5.2.2 Alignment markers and electrodes fabrication

To facilitate scanning electron microscopy (SEM)-based CNT localization, alignment markers were first patterned via photolithography. A three-layer resist structure consisting of hexamethyldisiloxane (HMDS), LOR-3A, and OFPR was spin-coated sequentially, with each layer baked at the appropriate temperature (120 °C for HMDS, 150 °C for LOR-3A, and 110 °C for OFPR). Exposure was performed using a UV lamp through a photomask, followed by development in a tetramethylammonium hydroxide (TMAH) developer for 60 s. Au alignment markers were then deposited by DC magnetron sputtering (Quick Coater SC-701MkII ADVANCE, Sanyu Electron) under Ar plasma (~1.5 Pa, ~1 min), producing conductive markers with sufficient optical and SEM contrast. Lift-off was achieved in N-methyl-2-pyrrolidone (NMP) at 90 °C for 1 h.

After CNT mapping by SEM, nanoscale electrodes were fabricated by electron-beam lithography (EBL, ELS-BODEN-OU4801, ELIONIX). A diluted ZEP520A resist (1:3 in anisole) was spin-coated at 2000 rpm for 60 s and baked at 180 °C for 3 min. Patterns were written at 150 keV, ensuring sub-100 nm precision. Post-exposure, samples were developed in ZED-N50 for 90 s before drying under nitrogen. Metal electrodes were deposited in an Anelva L-043E electron beam evaporation system, where the chamber base pressure was ~10^{-4} Pa. A Ti adhesion layer (50 nm) was deposited first, followed by Au with a typical thickness of 450–950 nm. Thickness and deposition rates were monitored by quartz crystal microbalance. Lift-off was again performed in NMP at 90 °C for 1 h. After the lift-off process, the samples were annealed at 300 °C for 30 min in a 3 % H_2 in Ar to remove resist residues and improve the metal–CNT contact quality.

5.2.3 Characterization

Raman spectroscopy was employed to assess the structural quality of the CNTs. Spectra were acquired using a Raman microscope (RAMANtouch, Nanophoton) with a

532 nm excitation laser. The characteristic G-band (~1580 cm^{-1}) and D-band (~1350 cm^{-1}) were monitored to evaluate defect density. The G/D intensity ratio served as a key indicator of CNT crystallinity and defect concentration. Atomic force microscopy (AFM; AFM5000, Hitachi High-Tech) was used to determine CNT diameters and to inspect surface morphology, including the thickness of exfoliated hBN flakes and the step height between hBN and SiO_2 regions. AFM imaging was performed in tapping mode under ambient conditions. SEM (S-4800, Hitachi High-Tech) was utilized to map CNT positions across the substrate, enabling precise localization for subsequent lithography. SEM imaging also confirmed the successful spanning of individual CNTs across SiO_2 and hBN regions and was used to verify electrode alignment after fabrication.

Electrical characterization was carried out using a electrical characterization system (Keysight B2912A precision source/measure unit, SMU) connected to four complementary probe stations. For ambient-condition measurements, a manual probe station equipped with a micromanipulator stage was used. Under an optical microscope, probes were brought into direct contact with the electrode pads, allowing the assignment of source, drain, and gate electrodes and enabling standard current–voltage (I–V) characterization. For variable-temperature transport, a vacuum-compatible probe station (Nagase Techno-Engineering, model HMP400/600) was employed. This system incorporates a turbomolecular pumping unit, providing a base pressure of ~10^{-3} Pa, and a liquid nitrogen cooling system, enabling temperature control from 110 K to 300 K.

5.3 Morphology and device overview

The first step in validating the gas-flow-directed growth approach for substrate-dependent transport studies is to establish the morphological and structural quality of the synthesized CNTs. Fig. 5.1 (a) presents a representative SEM image of a CNT grown across the boundary between the ND-seeded SiO_2 region and the exfoliated hBN region. The CNT extends continuously for tens of micrometers with a uniform contrast and constant diameter, indicating a straight and well-aligned geometry guided by the laminar gas flow. No apparent kinks, bundles, or discontinuities were observed over the entire growth span. This capability of growing a single CNT seamlessly over different materials is one of the most distinctive advantages of the gas-flow-directed growth technique. It completely eliminates the need for post-growth transfer, a process that often introduces wrinkles, residues, or mechanical deformation, all of which can obscure subtle substrate effects [244,245]. The structural integrity and cleanliness retained through direct growth therefore form the foundation for reliable, cross-substrate electrical comparisons. Following the growth, electrode fabrication was performed as described in Section 2. The resulting optical micrograph in Fig. 5.1 (b) shows the same CNT after device fabrication. Multiple pairs of electrodes were patterned along the CNT, forming a series of channels with systematically varied lengths. The left portion of the device corresponds to the CNT segments on the SiO_2 surface, while the right portion lies on the hBN region. This configuration allows measurements of several channel lengths on both substrates. The lithographic alignment ensured that the electrode arrays were precisely positioned with respect to the CNT axis, while SEM observation confirmed that the targeted CNT remained isolated without any bundles or overlaps. The resulting multi-channel configuration enables eliminating tube-to-tube variability such as differences in chirality, diameter, or intrinsic defect density.

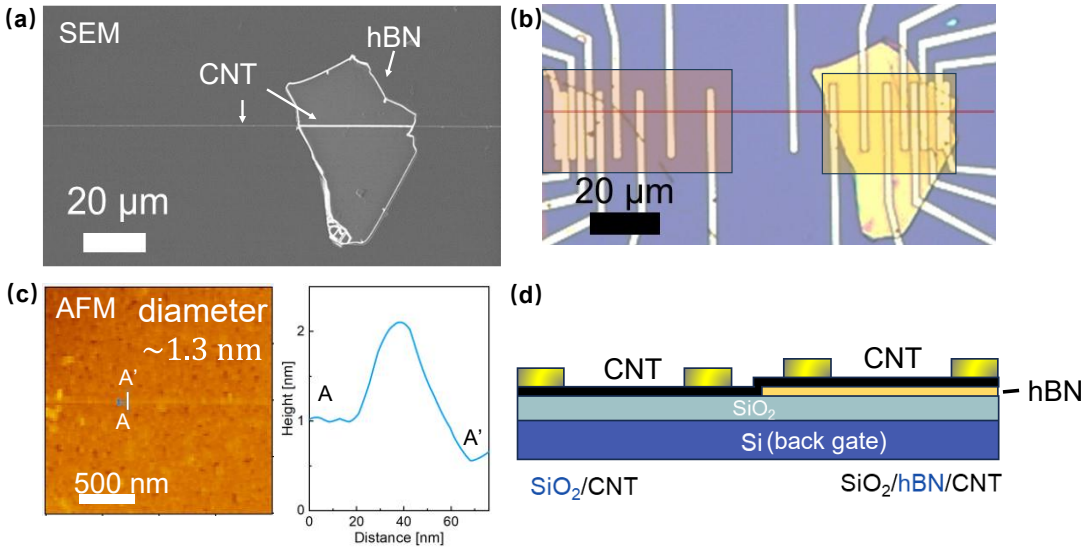


Figure 5.1 (a) SEM image of a single CNT grown across the exfoliated hBN flake. The CNT maintains a straight and well-aligned along the gas-flow direction. (b) Optical micrograph of the same CNT after multi-channel device fabrication, showing electrodes patterned on both SiO_2 (left) and hBN (right) regions. (c) AFM image and corresponding height profile of the CNT lying on hBN, with an apparent height of ~1.3 nm. (d) Schematic illustration of the cross-substrate device geometry, in which multiple channels are defined along the same CNT across SiO_2 and hBN regions using the common Si back gate.

AFM characterization provided further insight into the surface morphology. The topographic image acquired on the hBN region (Fig. 5.1 (c)) shows a smooth CNT lying on the atomically flat hBN surface. The apparent height of the CNT on hBN is approximately 1.3–1.6 nm, consistent with a single-walled structure. This difference likely arises from physiosorbed contaminants or trapped interfacial adsorbates on the SiO_2 surface, which effectively increase the apparent separation between the CNT and the substrate, whereas hBN provides a flatter and cleaner interface. In addition, AFM indentation can partially compress the CNT, and this effect may become more pronounced on the atomically flat hBN surface, where local support is more uniform [246,247]. Such

a contrast between the two substrates underscores the advantage of hBN in providing a cleaner and more uniform interface, which is expected to suppress charge scattering and minimize hysteresis in electrical transport measurements.

The overall device geometry is schematically illustrated in Fig. 5.1 (d). A single CNT grown across both SiO_2 and hBN regions is contacted by multiple metal electrodes with varied spacings, forming two sets of devices: CNT/SiO_2 and CNT/hBN. The degenerately doped Si substrate serves as a global back gate, separated by the native SiO_2 dielectric layer and, in the hBN region, an additional hBN thickness. The device architecture not only facilitates the extraction of intrinsic parameters such as field-effect mobility and mean free path but also provides insight into how substrate phonons, surface roughness, and charge traps influence one-dimensional electron transport. In addition to qualitative morphology, the yield statistics further demonstrate the practicality of this approach. Based on SEM surveys across multiple samples, approximately 10% of CNTs were sufficiently long to span across the exfoliated hBN regions. Among these, the majority remained well isolated without apparent bundling, suitable for multi-channel device fabrication. Although this yield does not yet reach wafer-scale uniformity, it is adequate for systematic and reproducible transport comparisons. To summarize, the combined SEM, optical, AFM, and Raman analyses confirm that the gas-flow-directed growth method reliably produces long, defect-scarce, and well-aligned CNTs capable of spanning different substrate regions without transfer.

5.4 Electrical transport on SiO_2 and hBN

Fig. 5.2 (a) presents the transfer characteristics of CNT FETs fabricated on SiO_2 substrates at 170 K under vacuum (~ 10^{-4} Pa). Devices with channel lengths ranging from 0.3 μm to 20 μm were measured at a drain bias of 0.1 V. All devices exhibit pronounced n-type behavior. For channel lengths below 1 μm, the conductance minimum (or off-state) shifts progressively toward more negative gate voltages as the channel length increases. This behavior saturates beyond approximately 1 μm, where longer channels exhibit similar threshold positions. The negative shift of the turn-off voltage in short-channel devices can be attributed to contact-induced electrostatic effects. The metal–CNT interface forms an extended overlap region extending several hundred nanometers, within which charge transfer and weak coupling modify the local band alignment and threshold behavior. For Ti contacts, electron donation from the metal effectively shifts the local Fermi level upward, reducing gate control and resulting in an apparent negative shift of the threshold voltage [248]. As the channel length increases, the influence of this contact-induced doping diminishes, allowing the intrinsic channel region to dominate the gating response. At the same time, the overall transconductance decreases with increasing channel length, while the on/off ratio increases. The decrease in transconductance arises naturally from the longer conduction path and higher series resistance. In contrast, the enhancement of the on/off ratio with length suggests that short-channel devices experience incomplete depletion due to residual carrier density at the contacts. For channels longer than several micrometers, enhanced gate control over the central region leads to a more pronounced reduction of off-state current, though complete suppression is not achieved. These observations confirm that transport in gas-flow-directed CNTs on SiO_2 is diffusive, with gate control progressively improving as the channel becomes longer relative to the mean free path [231]. Temperature-dependent transfer curves for a representative 0.3 μm device are shown in Fig. 5.2 (b). With increasing temperature from 110 K to 300 K, the turn-off voltage shifts slightly toward negative gate bias, while the

on-state current decreases modestly. The shift in threshold can be associated with thermally activated trap states in SiO_2 that release electrons to the CNT channel at higher temperatures, resulting in an apparent negative shift of the neutrality point. The reduction of on-state current with temperature is consistent with enhanced phonon scattering, while the nearly constant on/off ratio indicates that both carrier mobility and residual carrier density scale similarly with temperature [152].

Fig. 5.2 (c) plots the two-probe resistance as a function of channel length for several temperatures at a fixed gate bias of 30 V. In all cases, the resistance increases linearly with channel length, confirming the diffusive transport regime and a constant contact resistance independent of L. The extracted resistivity ρ from the slope of each line (Fig. 5.2 (d)) shows a clear increase with temperature T, following approximately a linear $\rho \propto T$ dependence between 100 K and 300 K. This temperature dependence is characteristic of acoustic phonon–limited transport in one-dimensional conductors, consistent with theoretical predictions for metallic or small-bandgap semiconducting CNTs. The linear fits yield resistivity values of about 4 kΩ/μm at 110 K and 11 kΩ/μm at 300 K, corresponding to mean free paths $\lambda \approx$ 1.6 μm and 0.6 μm, respectively, using the relation $\rho = (h/4e^2)(1/\lambda)$ [249], where h is Planck's constant and e is the elementary charge. These values are comparable to those reported for pristine, suspended CNTs of similar diameter, indicating that gas-flow-directed CNTs maintain their intrinsic transport quality even on SiO_2 substrates [232].

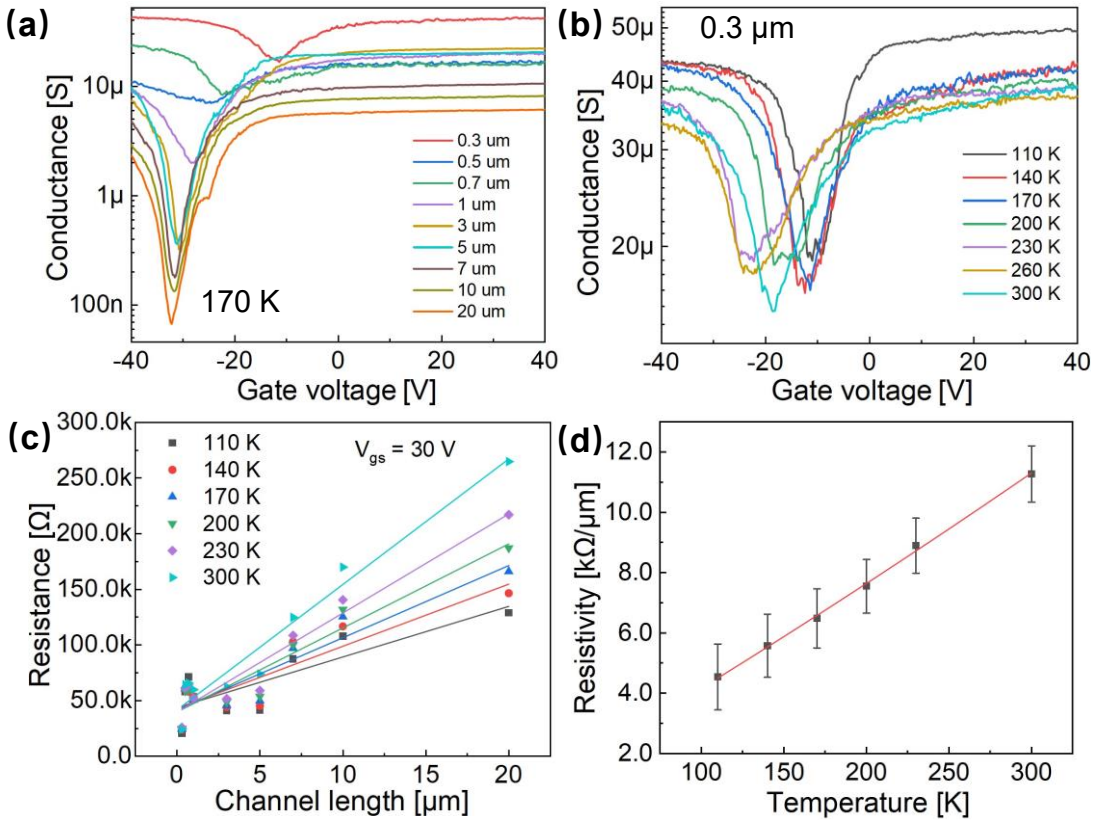


Figure 5.2 (a) Conductance versus gate voltage for CNT/SiO_2 FETs with channel lengths ranging from 0.3 to 20 μm, measured at 170 K under $\mathbf{V_{ds} = 0.1\ V}$. (b) Transfer characteristics of a 0.3 μm channel at different temperatures (110–300 K). (c) Two-probe resistance versus channel length at different temperatures, showing a linear dependence indicative of diffusive transport. (d) Extracted resistivity as a function of temperature, showing monotonic increase with T.

We measured the gate-dependent characteristics of a single CNT spanning both SiO_2 and hBN regions, which exhibits typical ambipolar behavior as shown in Fig. 5.3. Although the CNT devices exhibit typical ambipolar characteristics, the charge neutrality point, corresponding to the minimum conductance where electron and hole currents are balanced, appears at gate voltages more negative than zero. This shift can be attributed to several concurrent doping mechanisms. First, Ti adhesion layers, having relatively low work functions, tend to inject electrons into the CNT, and similar n-type doping effects

have been reported in CNT devices using Ti contacts [250] Second, residual amine-containing species from the alkaline developer TMAH used in lithography may act as weak electron donors, slightly raising the Fermi level. Previous studies have reported that such amine groups transfer electrons to CNTs, causing a negative shift in gate characteristics [251]. Beyond these n-type effects, substrate-induced doping also plays a role. On SiO_2, surface traps and adsorbed species such as H_2O and O_2 are known to introduce p-type doping, while hBN provides an atomically flat and chemically inert interface that suppresses such p-type contributions. As a result, when the CNT is placed on hBN, the p-type component is diminished but the contact and residue-induced n-type doping remains nearly unchanged. The net effect is an apparent shift of the neutrality point toward more negative gate voltages on hBN, even though the interfacial environment becomes cleaner. As shown in Fig. 5.3 (a), the on-state current on hBN is significantly larger, while the subthreshold slope is steeper, suggesting enhanced electrostatic control and improved contact injection in room temperature. These results directly demonstrate that hBN provides a more favorable dielectric environment for charge transport compared to conventional SiO_2, which introduces charge inhomogeneities and traps that degrade transistor performance. Figs 5.3 (b) and (c) show the temperature-dependent transfer curves of 7 μm channels fabricated on SiO_2 and hBN, respectively. Fig. 5.3 (d) summarizes the field-effect mobility μ_{FE} as a function of temperature for the 7 μm channels on both substrates. The mobility was extracted from the linear regime using $\mu_{FE} = (L/C_g V_{ds})(dI_d/dV_g)$ [59], where C_g is the gate capacitance per unit length L calculated from a cylindrical model. For a single dielectric of thickness t and permittivity $\varepsilon = \varepsilon_0 \kappa$, and a CNT of diameter d, $C_g = 2\pi\varepsilon/\ln(4h/d)$, which is the classical wire–plane result used and validated for CNTs, where ε_0 is vacuum permittivity, κ is relative dielectric constant [252]. For the CNT/hBN channel, a series dielectric model was used to account for the stacked hBN/SiO_2 configuration. The effective dielectric constant was evaluated using $\kappa_{\text{eff}} = (t_{\text{hBN}} + t_{\text{SiO}_2})/(t_{\text{hBN}}/\kappa_{\text{hBN}} +$

t_{SiO_2}/κ_{SiO_2}) [253], where t_{hBN} and t_{SiO_2} are the thicknesses, and κ_{hBN} and κ_{SiO_2} are the dielectric constants of hBN and SiO_2, respectively. The resulting μ_{FE} values are consistently higher on hBN across the entire temperature range. At 110 K, μ_{FE} reaches ~350 $cm^2V^{-1}s^{-1}$ on hBN compared to ~240 $cm^2V^{-1}s^{-1}$ on SiO_2. The temperature dependence of the field-effect mobility follows a power-law behavior that can be described by $\mu_{FE} \propto T^{-\gamma}$ [152]. Fitting the experimental data in the range of 110–300 K yields $\gamma \approx 1.3$ for devices on SiO_2 and $\gamma \approx 1.1$ for those on hBN. This trend is consistent with phonon-limited transport commonly observed in semiconducting CNTs, where carrier mobility decreases with increasing temperature due to enhanced phonon scattering. The slightly smaller γ value on hBN suggests that remote surface phonon scattering is partially suppressed by the atomically flat and nonpolar dielectric surface, leading to a weaker temperature dependence and higher overall mobility.

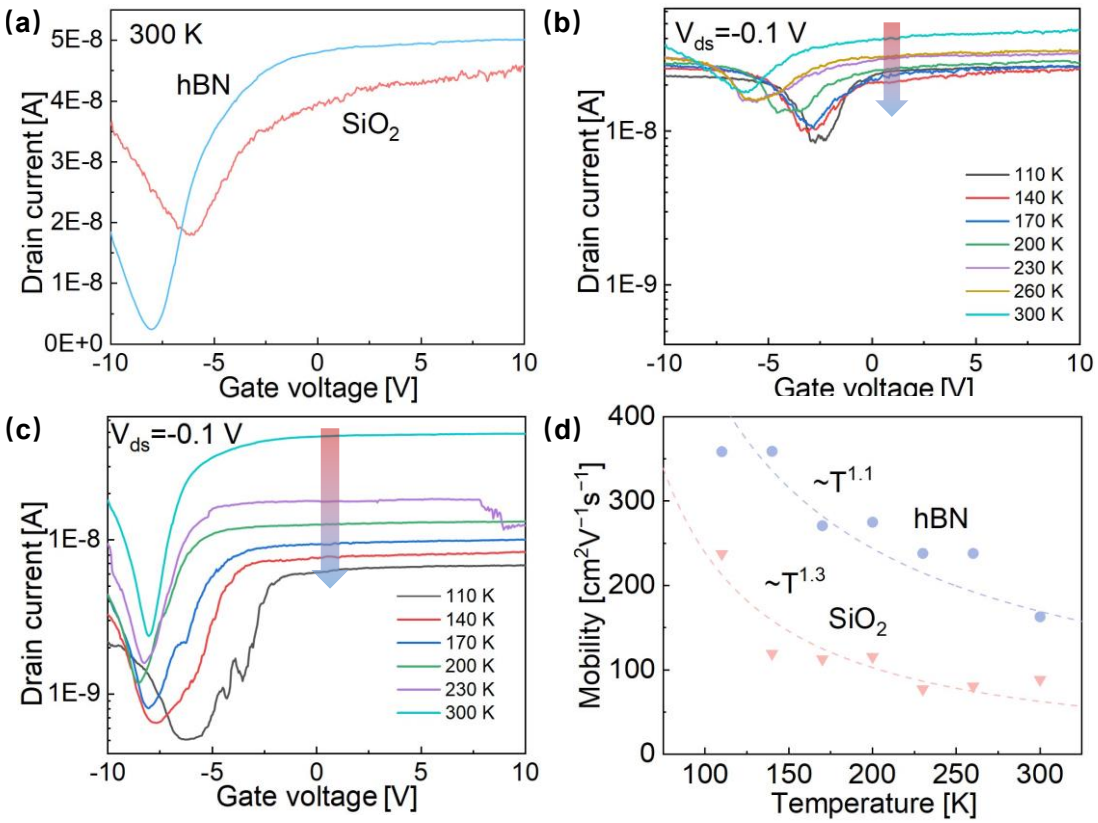


Figure 5.3 (a) Transfer characteristics of a 7 µm CNT device on SiO_2 and hBN measured at 300 K

and $\boldsymbol{V_{ds} = 0.1\ V}$. (b) Transfer curves of a 7 µm channel on SiO_2 and (c) on hBN, measured over a temperature range of 110–300 K. (d) Field-effect mobility as a function of temperature for 7 µm CNT channels on SiO_2 and hBN. The mobility can be approximated by the power-low fits shown by the dashed-dotted lines.

To further elucidate the transport mechanism and assess device reproducibility, additional measurements were performed on CNT channels with lengths of 3 µm and 5 µm (Fig. 5.4). The temperature-dependent mobility trends in these devices closely follow those observed in the 7 µm channels. The consistent scaling of conductance with channel length indicates diffusive transport dominated by phonon and interfacial scattering, from which the mean free path is estimated to be 0.4-0.7 µm. This agreement across multiple channel lengths highlights the intrinsic nature of the substrate effect rather than device-to-device variation. Moreover, the multi-channel device configuration enables systematic comparison of transport properties within a single CNT, confirming both the reproducibility and physical validity of the observed mobility enhancement on hBN. Nevertheless, the overall mobility values are significantly lower than those reported for semiconducting CNTs, where μ_{FE} can exceed 10^4–10^5 $cm^2V^{-1}s^{-1}$ at room temperature under diffusive transport conditions [59,254].

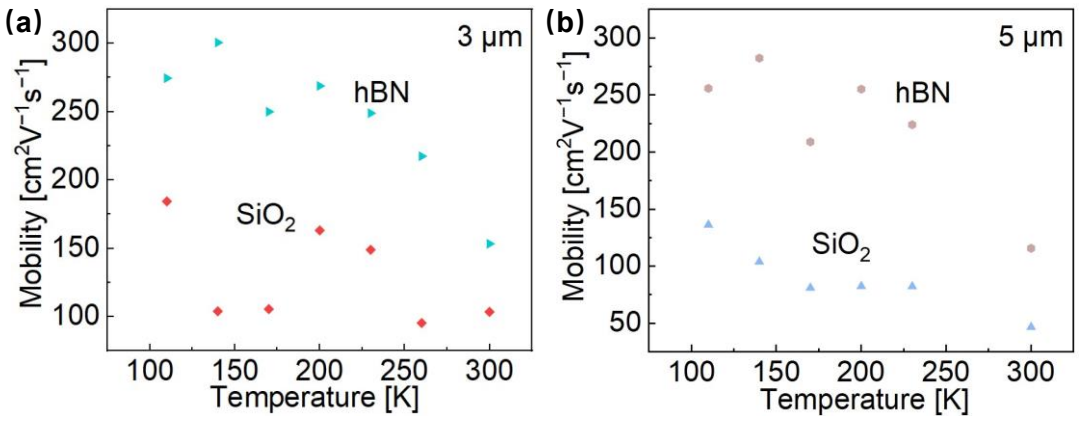


Figure 5.4 Temperature-dependent mobility of CNT devices with a 3 µm channel length on SiO_2 and

hBN substrates. (b) Temperature-dependent mobility of CNT devices with a 5 μm channel length on SiO_2 and hBN substrates.

To clarify the role of interfacial morphology in carrier transport, AFM was used to characterize the surface roughness of the two substrates. The root-mean-square roughness R_q was calculated from the height distribution using $R_q = \sqrt{\frac{1}{N}\sum_{i=1}^{N}(z_i - \bar{z})^2}$, where z_i is the measured height at each point and $\bar{z}$ is the mean height. The extracted R_q values were 1.62 nm for SiO_2 and 0.89 nm for hBN. The AFM images are provided in Fig. 5.5. Although the hBN surface is significantly smoother than SiO_2, the measured value remains higher than the sub-nanometer roughness typically reported for mechanically exfoliated hBN crystals (~0.3 nm) [234]. This discrepancy likely originates from the use of CVD-grown or transferred hBN flakes and residual processing contaminants such as amorphous carbon or lithography residues. Despite these effects, the lower roughness of hBN still indicates a flatter and more uniform interface, which suppresses interfacial scattering and charge inhomogeneity at the CNT–substrate interface. Such a smoother surface environment is considered one of the key factors contributing to the enhanced carrier mobility observed on hBN compared with SiO_2.

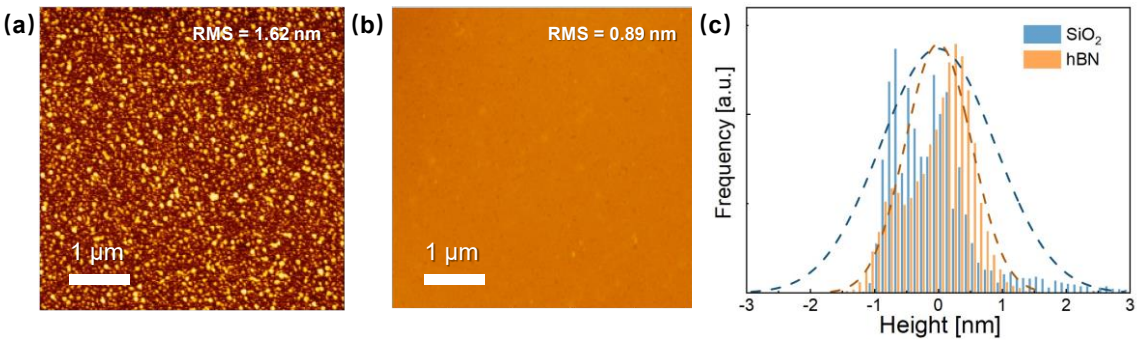


Figure 5.5 AFM images of the substrate surfaces showing surface roughness. (a) SiO_2 with a root mean square (RMS) roughness of 1.62 nm. (b) hBN with a RMS roughness of 0.89 nm. (c) Histogram of the height distribution (surface roughness) measured by AFM for SiO2 and hBN.

5.5 Band evolution at metal–CNT contacts under equilibrium and biased conditions

In the previous section, the gate-voltage-dependent transport characteristics and carrier mobility of CNT-based devices were analyzed. While these electrical parameters provide direct insight into device performance, a more complete understanding requires examination of the underlying band alignment and contact physics that govern charge injection and modulation. In the following, we therefore discuss the band structure evolution at metal–CNT contacts, starting from the equilibrium condition and extending to the biased regime, in order to clarify the physical origin of the observed device behavior.

At zero source–drain bias, the band alignment between Ti electrodes and a semiconducting CNT cannot be described solely by the Schottky–Mott rule based on work-function differences. Instead, the contact behavior is strongly influenced by Fermi-level pinning at the metal–CNT interface. As shown schematically in Fig. 5.6, although the electron affinity of CNTs is comparable to or even larger than the work function of Ti, the conduction and valence bands of the CNT still bend downward near the contacts after electrical equilibration. This downward band bending is consistent with the presence of interface-induced Fermi-level pinning, which fixes the local Fermi level near the contact to a position largely independent of the metal work function. Past researches demonstrated that, for metal–CNT junctions, interface states and the one-dimensional electrostatics of CNTs lead to partial Fermi-level pinning, resulting in Schottky barrier characteristics that deviate from conventional planar metal–semiconductor contacts [255,256]. As a consequence, band bending at the CNT contact region reflects charge redistribution required for Fermi-level alignment rather than a simple work-function matching picture.

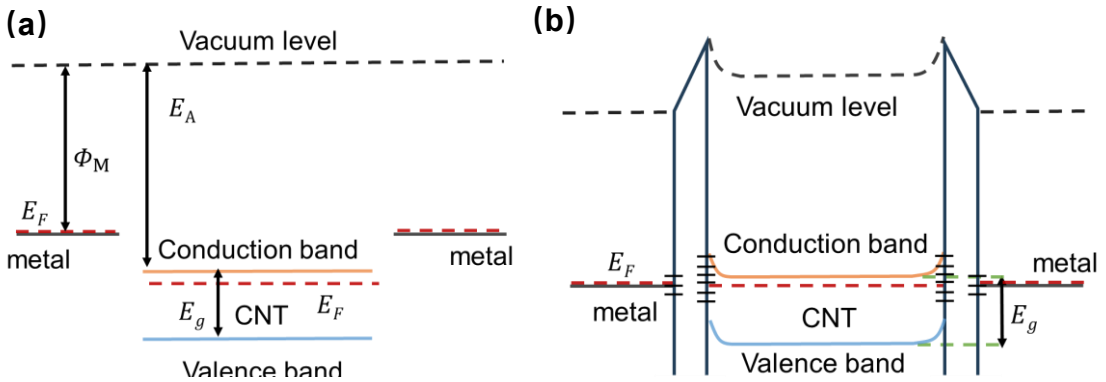


Figure 5.6 Schematic band diagrams of a semiconducting CNT before and after contact with Ti electrodes at zero source–drain bias. (a) Before contact, the energy levels of the CNT and Ti are referenced to their respective vacuum levels. (b) After contact, Fermi-level alignment is established at the metal–CNT interface, leading to downward bending of the CNT conduction and valence bands near the contacts. This band profile reflects the combined effects of intrinsic n-type doping of the CNT and Fermi-level pinning at the Ti–CNT interface, rather than a simple work-function-driven Schottky–Mott alignment.

In addition, the CNTs studied here exhibit intrinsic n-type doping, with the bulk Fermi level located closer to the conduction band. Upon contact with Ti, electrons are transferred toward the interface region to equilibrate the Fermi level, giving rise to an electron accumulation layer near the contact. This accumulation manifests as a downward bending of both the conduction and valence bands, as illustrated in Fig. 5.6 (b). Therefore, the observed band profile should be interpreted as the combined result of intrinsic n-type doping and contact-induced Fermi-level pinning, rather than as evidence of an ohmic or ideal Schottky contact determined solely by the relative values of the CNT electron affinity and the Ti work function.

Fig. 5.7 illustrates the band diagrams of a CNT FET under a low source–drain bias, where the applied bias is smaller than the CNT band gap. At the charge neutrality point (OFF state), the Fermi level lies near the middle of the band gap, and both electrons and

holes must overcome their respective Schottky barriers at the metal–CNT contacts. Under this condition, carrier injection is suppressed for both carrier types, resulting in a minimum current. When a negative gate bias is applied, the CNT channel is electrostatically shifted toward p-type conduction. The valence band edge is pulled closer to the Fermi level at the contacts, reducing the effective Schottky barrier for holes. As a result, hole transport becomes dominant and proceeds through a combination of thermionic emission over the Schottky barrier and tunneling through the thinned barrier near the contacts. This corresponds to the ON state for hole conduction. Conversely, under a positive gate bias, the CNT channel is driven into an n-type regime. The conduction band edge approaches the Fermi level, lowering the Schottky barrier for electrons at the metal–CNT interface. Electron transport is then enabled through thermionic emission and, more importantly under low-bias conditions, tunneling across the Schottky barrier. This regime corresponds to the ON state for electron conduction. Because both electron and hole injection can be activated by gate modulation when the CNT band gap is sufficiently small, the device exhibits ambipolar transport characteristics. In this case, the activation energy for conduction is determined by the smaller of the two Schottky barrier heights, leading to gate-controlled transitions between hole-dominated and electron-dominated transport under low source–drain bias conditions.

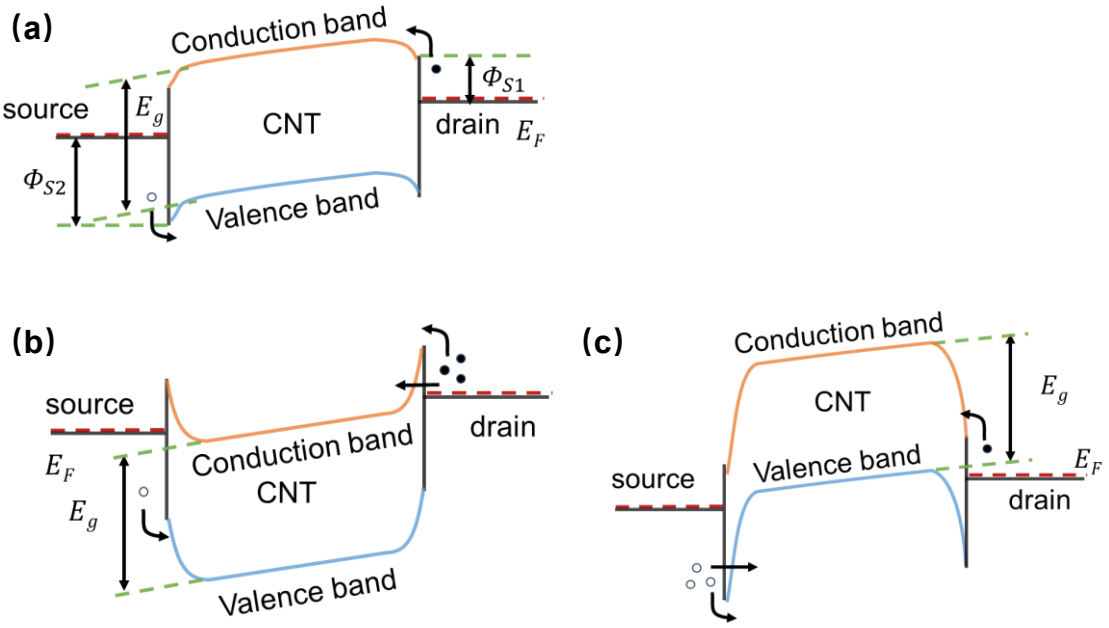


Figure 5.7 Schematic band diagrams of a CNT FET under low source–drain bias. (a) At the charge neutrality point (OFF state), both electrons and holes must overcome the Schottky barriers at the metal–CNT contacts, resulting in a minimum current. (b) Under a negative gate bias, the valence band is shifted upward, enabling hole transport through thermionic emission and tunneling across the Schottky barrier (ON state for holes). (c) Under a positive gate bias, the conduction band is pulled downward, allowing electron transport via Schottky barrier lowering and tunneling (ON state for electrons). For CNTs with a small band gap, both carrier types can be activated by gate modulation, leading to ambipolar transport behavior under low-bias conditions.

Fig. 5.8 illustrates the band diagrams of a CNT FET with a relatively large band gap under gate bias conditions, where transport is dominated by contact barriers. For an n-type CNT, applying a negative gate bias drives the channel deep into depletion. In this case, the built-in electric field opposing electron injection becomes large, while the Schottky barrier for hole injection at the metal–CNT contact remains substantial due to the wide band gap. As a result, neither electrons nor holes can be efficiently injected into the channel, and the device remains in the OFF state with negligible current. In contrast,

under a positive gate bias, the conduction band is pulled closer to the Fermi level, significantly reducing the effective Schottky barrier for electron injection at the contacts. Electron transport is then enabled through a combination of thermionic emission over the Schottky barrier and tunneling through the thinned barrier region. Owing to the large band gap, hole injection remains strongly suppressed even at high gate bias, resulting in unipolar n-type behavior dominated by electron conduction.

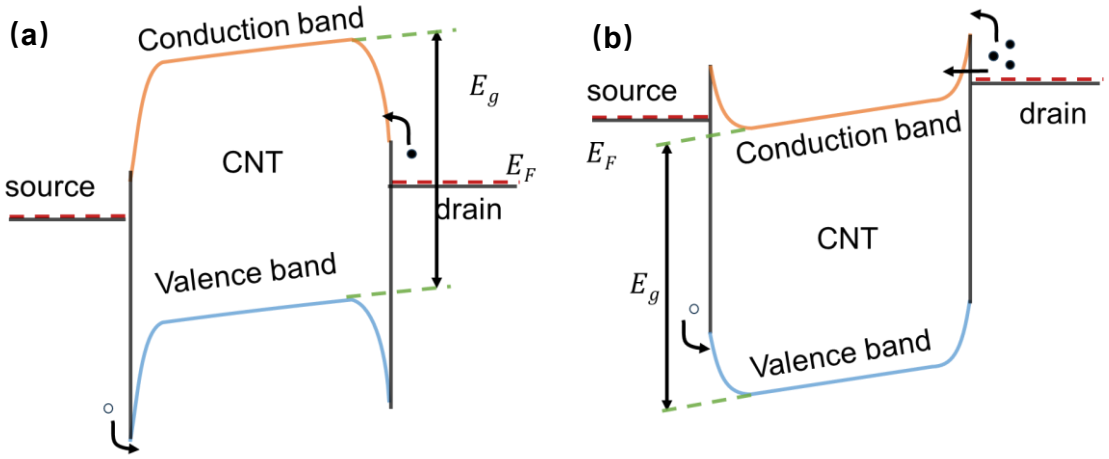


Figure 5.8 Schematic band diagrams of a large-band-gap CNT field-effect transistor under gate bias. (a) Under negative gate bias, the n-type CNT channel is strongly depleted, leading to a large built-in electric field for electrons and a high Schottky barrier for holes, resulting in an OFF state with suppressed current. (b) Under positive gate bias, the conduction band is lowered relative to the Fermi level, enabling electron transport via thermionic emission and tunneling across the Schottky barrier, while hole injection remains inhibited due to the large band gap.

Fig. 5.9 shows the band diagrams reconstructed for the devices studied in this work under a source–drain bias of 0.1 V, which nominally exceeds the band gap of small-band-gap CNTs. From a strict energetic viewpoint, this bias corresponds to a high-bias regime. However, the experimentally observed transport characteristics remain qualitatively similar to those discussed for the low-bias case, including the presence of a well-defined charge neutrality point, gate-controlled electron and hole conduction, and clear ambipolar

behavior. This apparent similarity arises because, even under a finite source–drain bias, carrier injection and transport near the charge neutrality point are still dominated by the Schottky barriers at the metal–CNT contacts rather than by bulk channel conduction. The applied bias primarily tilts the band profile along the CNT, but does not fundamentally alter the barrier-controlled injection processes at the source and drain. As a result, both electron and hole transport can still be activated by gate modulation in a manner analogous to the low-bias regime, particularly for small-band-gap CNTs.

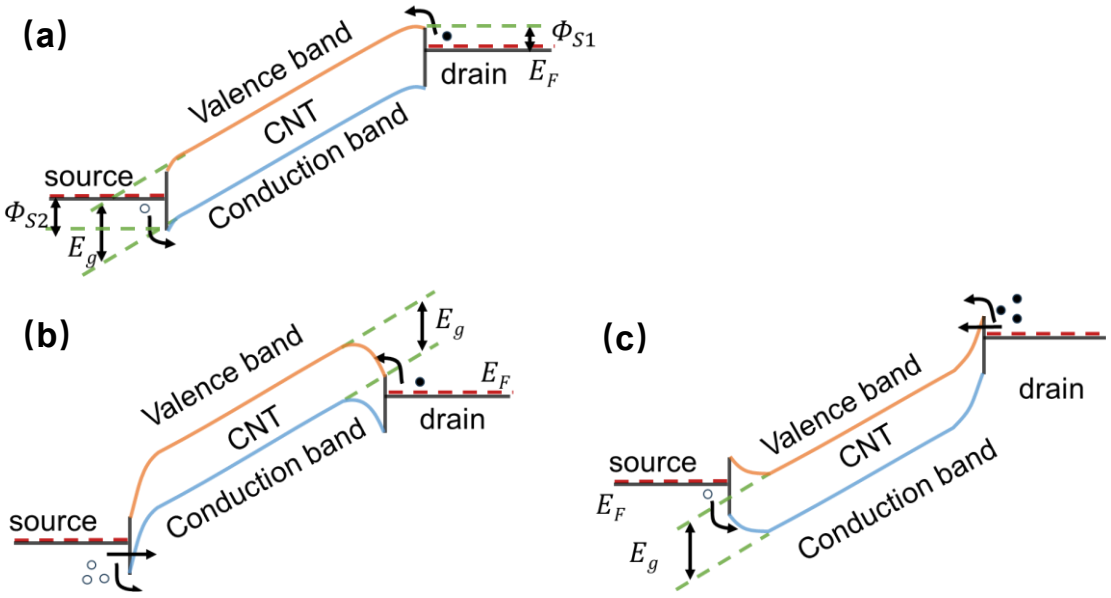


Figure 5.9 Schematic band diagrams of a CNT FET under high source–drain bias. (a) At the charge neutrality point (OFF state), both electrons and holes must overcome the Schottky barriers at the metal–CNT contacts, resulting in a minimum current. (b) Under a negative gate bias, the valence band is shifted upward, enabling hole transport through thermionic emission and tunneling across the Schottky barrier (ON state for holes). (c) Under a positive gate bias, the conduction band is pulled downward, allowing electron transport via Schottky barrier lowering and tunneling (ON state for electrons).

Therefore, although the bias voltage used in this work exceeds the intrinsic band gap,

its effect on the qualitative transport mechanism is limited in the gate-voltage range relevant to the charge neutrality point. The essential features governing current modulation—namely, Schottky barrier heights, tunneling probability, and thermally assisted carrier injection—remain unchanged. Consequently, the analysis of Schottky barrier behavior and activation energies near the charge neutrality point presented in the following sections remains valid and is not qualitatively affected by the finite source–drain bias employed in the measurements.

5.6 Temperature-dependent transport and activation behavior

To gain deeper insight into the transport mechanism underlying the behavior discussed above, we further analyzed the temperature dependence of the resistance near the charge neutrality point for the same CNT channels [257]. The resistance at this point is particularly informative because it corresponds to the condition where the Fermi level lies close to the middle of the CNT band gap, and carrier density is minimized. Under such conditions, current flow is governed by thermally activated carrier injection over the smaller of the two Schottky barriers at the metal–CNT interfaces, which sets the effective activation energy for carrier injection. This activation energy therefore corresponds to the lower of the electron or hole barriers that dominate charge transport near the charge neutrality point. As depicted in Fig. 5.9 (a), both electrons and holes must overcome the Schottky barriers at the metal–CNT interfaces, leading to thermally activated transport and the current minimum. Under positive gate bias (Fig. 5.9 (b)), the conduction band approaches the Fermi level, reducing the tunneling distance and enabling n-type conduction, whereas under negative gate bias (Fig. 5.9 (c)), hole tunneling into the valence band leads to p-type conduction.

Because the CNT channel is slightly n-doped, n-type conduction occurs at smaller positive gate voltages, resulting in a steeper slope and higher apparent mobility in the n-branch. Based on the temperature-dependent transfer characteristics already shown in Figs. 5.3 (a) and (b), the resistance at the current minimum was extracted and plotted as a function of inverse temperature (Figs. 5.10 (a) and (b)). For both substrates, the data follow an exponential dependence $R \propto \exp(E_a/k_B T)$ at high temperatures (110–300 K), confirming that the current minimum is indeed governed by thermal activation [257]. The extracted activation energies are approximately 21 meV for the CNT/SiO_2 device and 16 meV for the CNT/hBN device. The activation energies obtained for CNTs on hBN and SiO_2 are comparable, although a slightly smaller value is observed on hBN. This subtle difference can be understood in light of theoretical studies suggesting that dielectric

screening from hBN modestly reduces the quasiparticle band gap of supported CNTs relative to those on SiO_2 [258,259]. According to curvature-induced gap theory, such CNTs exhibit band gaps scaling as $E_g \propto 1/d^2$, typically on the order of 10–60 meV for diameters around 1 nm [260]. The smaller activation energy observed on hBN implies that the effective potential barrier for carrier excitation is slightly reduced, likely due to a cleaner dielectric interface that suppresses interfacial charge disorder and potential fluctuations. It is noteworthy that the plot for CNT/hBN devices exhibits a noticeable deviation from linearity at 300 K, where the resistance falls below the value predicted by a simple thermally activated model. This behavior indicates that at high temperature, thermally assisted transport is no longer the sole conduction mechanism. The atomically flat and low-disorder interface provided by hBN likely enhances carrier injection efficiency and reduces interfacial scattering, enabling non-activated transport channels to become significant. A slight reduction in the Schottky barrier with temperature, facilitated by weaker Fermi-level pinning on hBN, may further contribute to this effect. By contrast, devices on SiO_2 remain dominated by thermally activated conduction across the entire temperature range, consistent with stronger interface disorder and less efficient injection.

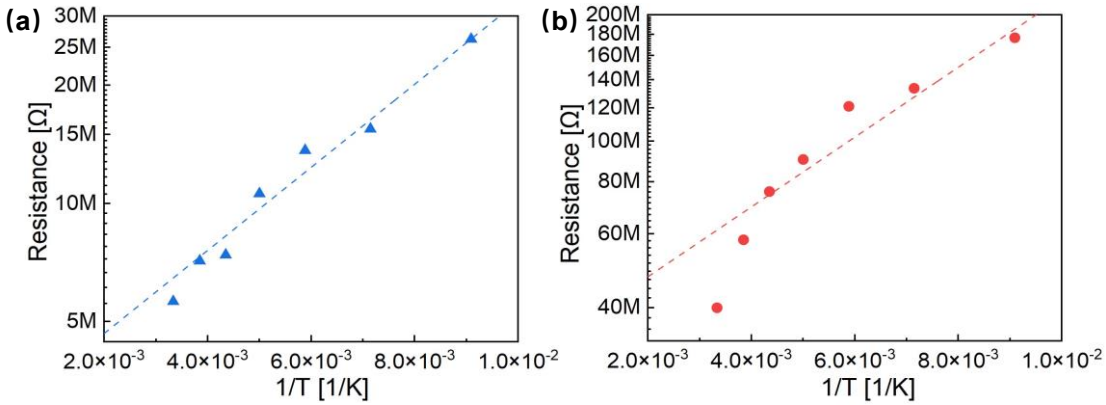


Figure 5.10 (a) Plot of resistance for CNT/SiO_2, fitted to $\boldsymbol{R \propto \exp(E_a/k_BT)}$, yielding an activation energy $\boldsymbol{E_a \approx 21\ meV}$. (b) Corresponding analysis for CNT/hBN, giving $\boldsymbol{E_a \approx 16\ meV}$. The agreement with the thermal activation model confirms that the CNT is a small-band-gap (quasi-metallic) tube, and the smaller $\boldsymbol{E_a}$ on hBN suggests reduced interfacial disorder.

Because the charge neutrality point shifts with temperature, a direct comparison of thermally activated transport at fixed absolute gate voltages would mix intrinsic transport physics with extrinsic electrostatic drift. To address this issue, we adopt a neutrality-point alignment approach analogous to the Dirac-point alignment commonly used in graphene transport studies [261] as shown in Figs. 5.11 (a) and (b). Specifically, the gate voltage is redefined relative to the charge neutrality point for each temperature, allowing activation energies to be analyzed as a function of relative gate voltage rather than absolute bias. This alignment procedure isolates the temperature-dependent transport behavior from the trivial shift of the neutrality point and enables a direct, point-by-point comparison of thermal activation energies. Near the neutrality point, carrier injection is dominated by Schottky-barrier-limited transport, and the extracted activation energy reflects the effective barrier height for thermally assisted carrier injection (Figs. 5.11 (c) and (d)). Away from the neutrality point, the activation energy decreases as gate-induced band bending lowers the effective injection barrier and enhances tunneling contributions. By analyzing the activation energy as a function of relative gate voltage, we are able to directly compare the effective transport barriers on different substrates under equivalent electrostatic conditions. This approach is particularly important for evaluating substrate-dependent effects, as it ensures that differences in extracted activation energies arise from variations in CNT–substrate interaction rather than from temperature-induced shifts of the neutrality point itself.

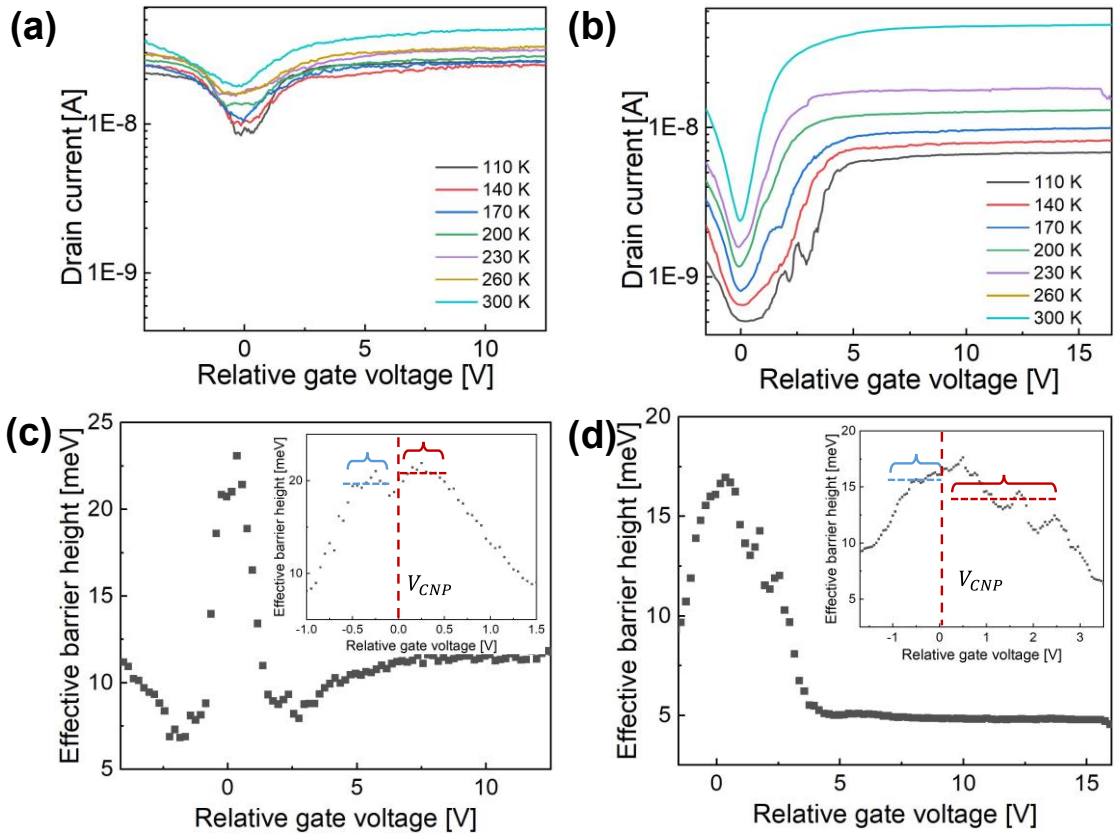


Figure 5.11 (a,b) Temperature-dependent drain current as a function of relative gate voltage measured on the same SWCNT device on (a) SiO_2 and (b) hBN substrates, recorded from 110 K to 300 K. The gate voltage is referenced to the charge neutrality point for each temperature. (c,d) Effective activation energy extracted from Arrhenius analysis of the corresponding data, plotted as a function of relative gate voltage for devices on (c) SiO_2 and (d) hBN. Insets show enlarged views of the activation-energy profiles in the vicinity of the charge neutrality point.

To elucidate the origin of the effective activation-energy profile near the charge neutrality point, we focus on the gate-voltage region where the CNT band alignment is most sensitive to the Schottky barriers at the metal contacts. In this regime, the extracted activation energy provides direct information on the relative position of the CNT Fermi level. The analysis is based on the combined contributions of electron and hole transport,

following a framework similar to that reported for CNT Schottky-barrier transistors [262].

For clarity, we first consider a simplified picture in which only electrons contribute to transport. As the gate voltage is swept from negative to positive values, three distinct regimes can be identified (Fig. 5.12 (a)). In the first regime, under sufficiently negative gate bias, the conduction band bends upward and electron transport requires overcoming both the Schottky barrier and the built-in electric field, resulting in an activation energy that increases with increasingly negative gate voltage. In the second regime, as the gate voltage becomes slightly positive and the conduction band just begins to bend downward, tunneling remains negligible and electron transport is dominated by thermionic emission over the Schottky barrier. Consequently, the required activation energy remains approximately constant. In the third regime, with further increase in positive gate voltage, the Schottky barrier width is reduced and tunneling becomes significant, leading to a decrease in the effective activation energy. The hole contribution exhibits a complementary behavior. As the gate voltage is swept toward positive values, the activation energy for holes increases, remains approximately constant over a narrow gate-voltage window, and then increases further as tunneling becomes suppressed. Because the gate-voltage dependences of electron and hole activation energies are approximately symmetric with respect to the charge neutrality point, the experimentally extracted activation energy reflects the combined contributions of both carrier types. The total drain current can be expressed as the sum of electron and hole currents, $I = I_n + I_p$, with $I_n \propto \exp\left(-\frac{E_{an}}{kT}\right)$, $I_p \propto \exp\left(-\frac{E_{ap}}{kT}\right)$. Accordingly, the experimentally measured activation energy corresponds to a weighted harmonic average, $E_a = \frac{E_{an}I_n + E_{ap}I_p}{I_n + I_p}$. In this formulation, the smaller of the two activation energies dominates the measured value, while comparable electron and hole contributions yield an intermediate value.

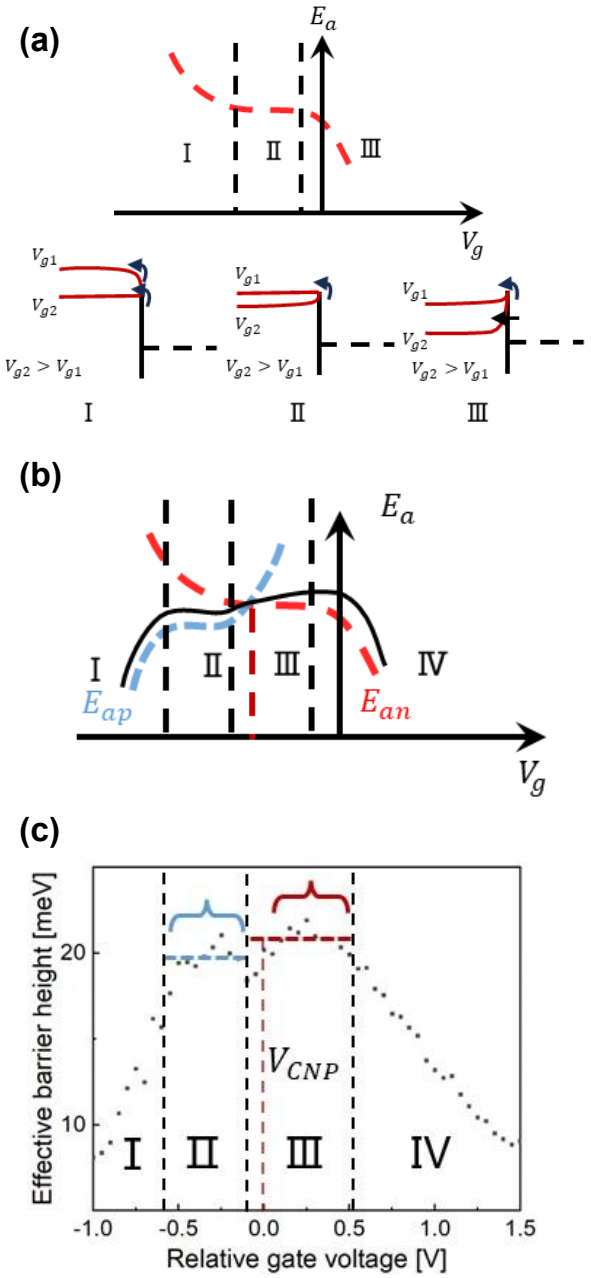


Figure 5.12 (a) Schematic representation of a simplified model considering only electron contribution, showing the gate-voltage dependence of the electron activation energy. (b) Schematic representation of the full model in which both electron and hole contributions are included, illustrating the gate-voltage-dependent activation energies for electrons and holes. (c) Experimentally extracted effective activation energy as a function of relative gate voltage, divided into four regions (I–IV). The charge neutrality point is indicated by the dashed red line, and the regions correspond to the gate-voltage

intervals represented in panel (b).

As a result, four effective regimes emerge when sweeping the gate voltage from negative to positive values (Figs. 5.12 (b) and (c)). In the first two regimes on the negative-gate side, the electron activation energy exceeds that of holes, whereas in the third and fourth regimes on the positive-gate side, the hole activation energy becomes larger than that of electrons. The shallow step-like features observed on either side of the charge neutrality point correspond to the crossover between regimes in which the activation energy is approximately equal to the Schottky barrier height for one carrier type. These plateaus therefore provide a direct experimental signature of the relative Schottky barriers for electrons and holes. Applying this analysis to different substrates reveals a systematic shift in the relative activation energies. For CNTs on SiO_2, the extracted activation energies indicate that the Fermi level is located closer to the valence band, whereas for CNTs on hBN, the Fermi level is shifted toward the conduction band. This substrate-induced Fermi-level shift is consistent with differences in dielectric cleanliness and substrate-induced doping, and explains the observed lower activation energy and higher mobility on hBN compared with SiO_2. The present analysis thus demonstrates that the substrate modifies the CNT transport characteristics primarily by shifting the intrinsic Fermi-level position, rather than by altering the fundamental Schottky-barrier transport mechanism.

These results highlight that the improved transport on hBN originates primarily from extrinsic factors such as reduced surface roughness, lower trap density, rather than from any modification of the intrinsic CNT band structure. They also explain why earlier studies observed little improvement on hBN, as transferred CNTs often suffered from polymer residues and structural damage. The gas-flow-directed approach employed here avoids such artifacts, allowing direct cross-substrate comparison along the same CNT and

revealing the genuine influence of hBN on electronic transport. Despite these advantages, several limitations of the present study must be acknowledged. First, the exfoliated hBN flakes used here vary in thickness across devices, with typical values of 60–80 nm (Fig. 5.13). The relatively thick hBN increases the gate-to-channel spacing and slightly reduces the gate capacitance, which may introduce minor uncertainty in the extracted field-effect mobility. Although this variation does not alter the comparative trend between hBN and SiO_2 devices, since both share the same back-gate configuration. Nevertheless, thinner and more uniform hBN layers would be more favorable for achieving stronger electrostatic control and more accurate mobility quantification. The adoption of large-area few-layer hBN films grown by chemical vapor deposition could help overcome this limitation and improve device uniformity. Second, surface contamination and adsorbates may still play a role. Although the direct growth method avoids transfer-related residues, exposure to lithographic chemicals and ambient air introduces additional scatterers. The observed device-to-device variability, even on hBN, suggests that extrinsic adsorbates remain a limiting factor. Future efforts could include encapsulation techniques to further stabilize the CNT surface.

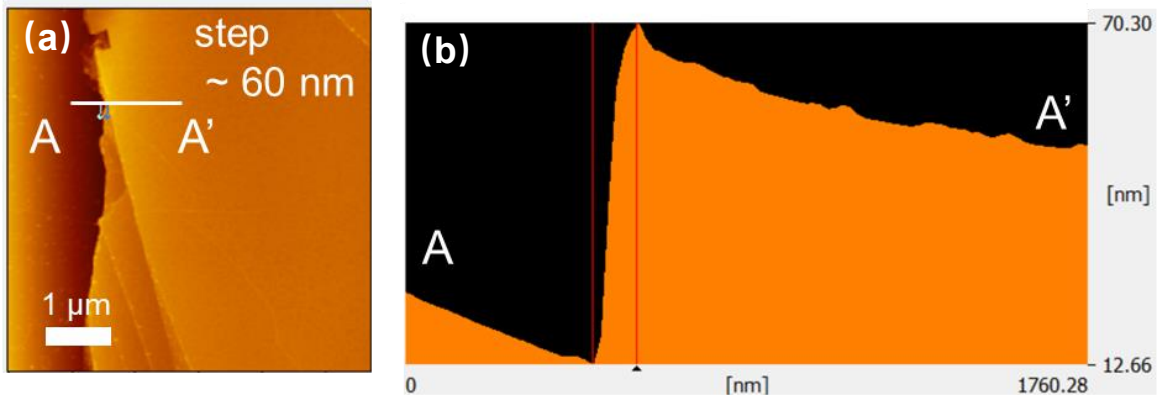


Figure 5.13 AFM characterization of an exfoliated hBN flake. (a) Topographic image showing a clear step edge. (b) Corresponding height profile.

5.7 Conclusion

In this work, we investigated substrate-dependent transport in CNTs synthesized by gas-flow-directed growth, a method that enables the formation of long, highly aligned CNTs without any transfer or mechanical manipulation. By fabricating multiple device channels along the same CNT across SiO_2 and hBN regions, we achieved direct comparison of transport properties under identical structural conditions. The results demonstrate that gas-flow-directed growth yields clean and continuous CNTs suitable for quantitative transport studies. Field-effect mobility extracted from the linear regime showed higher values for CNTs on hBN across all measured temperatures. For example, at 110 K, the mobility of the 7 μm channel reached approximately 350 $cm^2V^{-1}s^{-1}$ on hBN, compared to about 240 $cm^2V^{-1}s^{-1}$ on SiO_2. This improvement indicates that hBN provides a cleaner and more homogeneous electrostatic environment. Temperature-dependent transfer characteristics exhibit clear thermally activated behavior near the off state. The extracted activation energies are approximately 21 meV on SiO_2 and 16 meV on hBN, values characteristic of small-band-gap, semiconducting CNTs. The slight difference in activation energy can be understood in terms of dielectric screening from hBN, which modestly alters the electronic environment without fundamentally changing the transport mechanism. At room temperature, CNT channels on hBN display longer mean free paths than those on SiO_2, confirming a cleaner and lower-scattering environment. Despite these advantages, certain extrinsic effects such as contact resistance variability remain significant. Overall, this study establishes gas-flow-directed growth as a reliable route for producing pristine, continuous CNTs that traverse multiple dielectric environments. The multi-channel platform developed here minimizes device-to-device variability and provides a robust framework for probing substrate effects on CNT transport. These results highlight the potential of combining clean CNT synthesis with hBN dielectrics to advance the understanding and performance of one-dimensional nanoelectronic systems.

Chapter 6. Conclusion and future perspective

This dissertation presents a comprehensive investigation of gas-flow-directed CNT growth, spanning metal-free synthesis, the interplay between flow-guided alignment and vibrational bridging in constrained geometries, and substrate-dependent electronic transport in individual CNTs. The three studies collectively establish a consistent mechanistic framework that links growth physics, structural morphology, and electronic properties, while providing practical strategies for producing device-ready CNTs with minimal contamination and well-controlled alignment.

In Chapter 3, this part of the work demonstrates that ND particles can serve as robust, nonmetallic seeds for gas-flow-directed CNT growth. Through controlled ethanol CVD, ND particles remain solid throughout the process and support CNT nucleation via a vapor–solid surface–solid mechanism. Systematic analysis of growth temperature, gas flow rate, and pretreatment conditions reveals that nanotubes can reliably lift off from ND seeds and enter a tip-growth regime similar to metal-catalyzed gas-flow-directed growth, but without introducing any metallic residues. Secondary electron yield mapping and AFM imaging collectively confirm the absence of transition metals at CNT tips, while Raman analysis shows that the resulting CNTs possess high crystallinity and small diameters suitable for electronic transport studies. By extending gas-flow-directed growth into a catalyst-free regime, this chapter provides a clean structural and material foundation for subsequent investigations of CNT architecture and device physics.

In Chapter 4, this part investigates how CNT alignment evolves when gas-flow-directed growth occurs in pillar-assisted architectures. In such confined environments, two mechanisms influence CNT trajectories. Gas-flow-directed extension dominates for sufficiently long CNTs, where aerodynamic forces stabilize the floating tip and guide its orientation along the flow direction. In contrast, vibrational bridging becomes prominent at shorter CNT lengths: small-amplitude thermal oscillations allow the tip to

intermittently contact neighboring pillars and anchor spontaneously. By using pillar arrays with controlled spacing and geometry, this study systematically characterizes the transition between these two regimes and establishes a quantitative geometric model to describe length-dependent behavior. The model explains how CNT-pillar interactions, oscillation amplitude, and local flow profile jointly determine whether a CNT continues to elongate freely or forms a structural bridge. The experimental observations agree closely with model predictions, providing a physically grounded framework that enables rational design and deterministic control of CNT network morphology. Importantly, this chapter clarifies the conditions under which long, uninterrupted CNTs can be obtained in complex geometries, thereby establishing structural capabilities relevant to device-level studies.

In Chapter 5, this part examines how the substrate environment modulates the electronic transport of aligned CNTs. To eliminate variability in chirality, defect density, and contact quality across devices, a single long CNT produced by gas-flow-directed growth is used to span both SiO_2 and hBN region. This configuration allows direct, within-tube comparison of transport behavior under identical structural and electrostatic conditions. Electrical measurements show that CNT segments on hBN consistently exhibit higher field-effect mobility than those on SiO_2, while the extracted activation energies are comparable, with only a slight reduction observed on hBN. This behavior reflects the cleaner dielectric environment provided by hBN, including its atomically flat surface and low charge-impurity density, which collectively suppress extrinsic scattering without fundamentally altering the transport mechanism. The results provide unambiguous evidence that the substrate alone can significantly influence one-dimensional transport, even when intrinsic CNT properties remain unchanged. This study highlights substrate engineering as a powerful route for enhancing CNT device performance and provides a quantitative basis for using hBN and other high-quality dielectrics to minimize extrinsic scattering.

Taken together, the three studies demonstrate that gas-flow-directed growth is not only a viable method for producing ultraclean and highly aligned CNTs, but also a platform for exploring detailed structure–property relationships. The combination of nonmetallic seeding, quantitative alignment control, and substrate-resolved transport measurements offers a holistic perspective on how CNT quality and device integration can be simultaneously optimized.

Future research may focus on improving the uniformity and reproducibility of nonmetallic-seed growth, especially over large areas where seed distribution and surface chemistry remain limiting factors. A more refined understanding of the dynamical interplay between gas-flow guidance and vibrational motion would further enhance control over CNT network morphology in complex geometries. In addition, expanding cross-substrate transport studies to a wider range of dielectric environments may clarify how interfacial phonons and charge impurities shape one-dimensional conduction. Continued progress in these directions will support the scalable integration of clean, aligned CNTs into high-performance nanoelectronic systems.

Reference

[1] S. Iijima, Helical microtubules of graphitic carbon, Nature 354 (1991) 56–58. https://doi.org/10.1038/354056a0.

[2] S. Iijima, T. Ichihashi, Single-shell carbon nanotubes of 1-nm diameter, Nature 363 (1993) 603–605. https://doi.org/10.1038/363603a0.

[3] D.S. Bethune, C.H. Kiang, M.S. de Vries, G. Gorman, R. Savoy, J. Vazquez, R. Beyers, Cobalt-catalysed growth of carbon nanotubes with single-atomic-layer walls, Nature 363 (1993) 605–607. https://doi.org/10.1038/363605a0.

[4] M.S. Dresselhaus, G. Dresselhaus, R. Saito, Physics of carbon nanotubes, Carbon 33 (1995) 883–891. https://doi.org/10.1016/0008-6223(95)00017-8.

[5] G. Dresselhaus, M.S. Dresselhaus, R. Saito, Physical Properties Of Carbon Nanotubes, World Scientific, 1998.

[6] J.-C. Charlier, X. Blase, S. Roche, Electronic and transport properties of nanotubes, Rev. Mod. Phys. 79 (2007) 677–732. https://doi.org/10.1103/RevModPhys.79.677.

[7] M.S. Dresselhaus, G. Dresselhaus, A. Jorio, UNUSUAL PROPERTIES AND STRUCTURE OF CARBON NANOTUBES, Annu. Rev. Mater. Res. 34 (2004) 247–278. https://doi.org/10.1146/annurev.matsci.34.040203.114607.

[8] A. Thess, R. Lee, P. Nikolaev, H. Dai, P. Petit, J. Robert, C. Xu, Y.H. Lee, S.G. Kim, A.G. Rinzler, D.T. Colbert, G.E. Scuseria, D. Tománek, J.E. Fischer, R.E. Smalley, Crystalline Ropes of Metallic Carbon Nanotubes, Science 273 (1996) 483–487. https://doi.org/10.1126/science.273.5274.483.

[9] J. Kong, A.M. Cassell, H. Dai, Chemical vapor deposition of methane for single-walled carbon nanotubes, Chem. Phys. Lett. 292 (1998) 567–574. https://doi.org/10.1016/S0009-2614(98)00745-3.

[10] A.M. Cassell, J.A. Raymakers, J. Kong, H. Dai, Large Scale CVD Synthesis of Single-Walled Carbon Nanotubes, J. Phys. Chem. B 103 (1999) 6484–6492. https://doi.org/10.1021/jp990957s.

[11] J. Prasek, J. Drbohlavova, J. Chomoucka, J. Hubalek, O. Jasek, V. Adam, R. Kizek, Methods for carbon nanotubes synthesis—review, J. Mater. Chem. 21 (2011) 15872–15884. https://doi.org/10.1039/C1JM12254A.

[12] A.D. Franklin, M.C. Hersam, H.-S.P. Wong, Carbon nanotube transistors: Making electronics from molecules, Science 378 (2022) 726–732. https://doi.org/10.1126/science.abp8278.

[13] J. Si, P. Zhang, Z. Zhang, Road map for, and technical challenges of, carbon-nanotube integrated circuit technology, Natl. Sci. Rev. 11 (2024) nwad261. https://doi.org/10.1093/nsr/nwad261.

[14] S. Huang, X. Cai, J. Liu, Growth of Millimeter-Long and Horizontally Aligned Single-Walled Carbon Nanotubes on Flat Substrates, J. Am. Chem. Soc. 125 (2003) 5636–5637. https://doi.org/10.1021/ja034475c.

[15] S. Huang, M. Woodson, R. Smalley, J. Liu, Growth Mechanism of Oriented Long Single Walled Carbon Nanotubes Using “Fast-Heating” Chemical Vapor Deposition Process, Nano Lett. 4 (2004) 1025–1028. https://doi.org/10.1021/nl049691d.

[16] L.X. Zheng, M.J. O’Connell, S.K. Doorn, X.Z. Liao, Y.H. Zhao, E.A. Akhadov, M.A. Hoffbauer, B.J. Roop, Q.X. Jia, R.C. Dye, D.E. Peterson, S.M. Huang, J. Liu, Y.T. Zhu, Ultralong single-wall carbon nanotubes, Nat. Mater. 3 (2004) 673–676. https://doi.org/10.1038/nmat1216.

[17] B.H. Hong, J.Y. Lee, T. Beetz, Y. Zhu, P. Kim, K.S. Kim, Quasi-Continuous Growth of Ultralong Carbon Nanotube Arrays, J. Am. Chem. Soc. 127 (2005)

15336–15337. https://doi.org/10.1021/ja054454d.

[18] L. Huang, B. White, M.Y. Sfeir, M. Huang, H.X. Huang, S. Wind, J. Hone, S. O'Brien, Cobalt Ultrathin Film Catalyzed Ethanol Chemical Vapor Deposition of Single-Walled Carbon Nanotubes, J. Phys. Chem. B 110 (2006) 11103–11109. https://doi.org/10.1021/jp060693r.

[19] H. Liu, D. Takagi, S. Chiashi, Y. Homma, The controlled growth of horizontally aligned single-walled carbon nanotube arrays by a gas flow process, Nanotechnology 20 (2009) 345604. https://doi.org/10.1088/0957-4484/20/34/345604.

[20] R. Cui, Y. Zhang, J. Wang, W. Zhou, Y. Li, Comparison between Copper and Iron as Catalyst for Chemical Vapor Deposition of Horizontally Aligned Ultralong Single-Walled Carbon Nanotubes on Silicon Substrates, J. Phys. Chem. C 114 (2010) 15547–15552. https://doi.org/10.1021/jp100286c.

[21] R. Zhang, Y. Zhang, Q. Zhang, H. Xie, W. Qian, F. Wei, Growth of Half-Meter Long Carbon Nanotubes Based on Schulz–Flory Distribution, ACS Nano 7 (2013) 6156–6161. https://doi.org/10.1021/nn401995z.

[22] T. Fujimori, K. Matsuo, H. Masuda, Y. Kikuchi, J. Otsuka, D. Tanioka, T. Hikata, S. Okubo, Y. Ito, J. Fujita, Fabrication of high-strength carbon nanotube bundles using iron oxides co-assisted chemical vapor deposition, Appl. Phys. Lett. 115 (2019) 023106. https://doi.org/10.1063/1.5098370.

[23] Z. Zhu, N. Wei, W. Cheng, B. Shen, S. Sun, J. Gao, Q. Wen, R. Zhang, J. Xu, Y. Wang, F. Wei, Rate-selected growth of ultrapure semiconducting carbon nanotube arrays, Nat. Commun. 10 (2019) 4467. https://doi.org/10.1038/s41467-019-12519-5.

[24] T. Tsuji, K. Hata, D.N. Futaba, S. Sakurai, Additional obstacles in carbon nanotube

growth by gas-flow directed chemical vapour deposition unveiled through improving growth density, Nanoscale Adv. 1 (2019) 4076–4081. https://doi.org/10.1039/C9NA00209J.

[25] Z. Zhu, Y. Bai, N. Wei, J. Gao, S. Sun, C. Zhang, F. Wei, Controlled growth of crossed ultralong carbon nanotubes by gas flow, Nano Res. 13 (2020) 1988–1995. https://doi.org/10.1007/s12274-020-2898-2.

[26] Z. Zhu, N. Wei, B. Yan, B. Shen, J. Gao, S. Sun, H. Xie, H. Xiong, C. Zhang, R. Zhang, W. Qian, S. Fu, L. Peng, F. Wei, Monochromatic Carbon Nanotube Tangles Grown by Microfluidic Switching between Chaos and Fractals, ACS Nano 15 (2021) 5129–5137. https://doi.org/10.1021/acsnano.0c10300.

[27] Q. Jiang, F. Wang, R. Li, B. Li, N. Wei, N. Gao, H. Xu, S. Zhao, Y. Huang, B. Wang, W. Zhang, X. Wu, S. Zhang, Y. Zhao, E. Shi, R. Zhang, Synthesis of Ultralong Carbon Nanotubes with Ultrahigh Yields, Nano Lett. (2023). https://doi.org/10.1021/acs.nanolett.2c03858.

[28] A.H. Castro Neto, The electronic properties of graphene, Rev. Mod. Phys. 81 (2009) 109–162. https://doi.org/10.1103/RevModPhys.81.109.

[29] G. Yang, L. Li, W.B. Lee, M.C. Ng, Structure of graphene and its disorders: a review, Sci. Technol. Adv. Mater. 19 (2018) 613–648. https://doi.org/10.1080/14686996.2018.1494493.

[30] P. Avouris, Z. Chen, V. Perebeinos, Carbon-based electronics, Nat. Nanotechnol. 2 (2007) 605–615. https://doi.org/10.1038/nnano.2007.300.

[31] S.B. Sinnott, R. Andrews, Carbon Nanotubes: Synthesis, Properties, and Applications, Crit. Rev. Solid State Mater. Sci. 26 (2001) 145–249. https://doi.org/10.1080/20014091104189.

[32] M. Ouyang, J.-L. Huang, C.L. Cheung, C.M. Lieber, Energy Gaps in “Metallic”

Single-Walled Carbon Nanotubes, Science 292 (2001) 702–705. https://doi.org/10.1126/science.1058853.

[33] T. Ando, The electronic properties of graphene and carbon nanotubes, NPG Asia Mater. 1 (2009) 17–21. https://doi.org/10.1038/asiamat.2009.1.

[34] H. Kataura, Y. Kumazawa, Y. Maniwa, I. Umezu, S. Suzuki, Y. Ohtsuka, Y. Achiba, Optical properties of single-wall carbon nanotubes, Synth. Met. 103 (1999) 2555–2558. https://doi.org/10.1016/S0379-6779(98)00278-1.

[35] A. Jorio, R. Saito, Raman spectroscopy for carbon nanotube applications, J. Appl. Phys. 129 (2021) 021102. https://doi.org/10.1063/5.0030809.

[36] T.W. Odom, J.-L. Huang, P. Kim, C.M. Lieber, Structure and Electronic Properties of Carbon Nanotubes, J. Phys. Chem. B 104 (2000) 2794–2809. https://doi.org/10.1021/jp993592k.

[37] M.-F. Yu, B.I. Yakobson, R.S. Ruoff, Controlled Sliding and Pullout of Nested Shells in Individual Multiwalled Carbon Nanotubes, J. Phys. Chem. B 104 (2000) 8764–8767. https://doi.org/10.1021/jp002828d.

[38] M. Syduzzaman, M.S. Islam Saad, M.F. Piam, T.A. Talukdar, T.T. Shobdo, N.M. Pritha, Carbon nanotubes: Structure, properties and applications in the aerospace industry, Results Mater. 25 (2025) 100654. https://doi.org/10.1016/j.rinma.2024.100654.

[39] J.H. Warner, F. Schäffel, G. Zhong, M.H. Rümmeli, B. Büchner, J. Robertson, G.A.D. Briggs, Investigating the Diameter-Dependent Stability of Single-Walled Carbon Nanotubes, ACS Nano 3 (2009) 1557–1563. https://doi.org/10.1021/nn900362a.

[40] J.H. Lehman, M. Terrones, E. Mansfield, K.E. Hurst, V. Meunier, Evaluating the characteristics of multiwall carbon nanotubes, Carbon 49 (2011) 2581–2602.

https://doi.org/10.1016/j.carbon.2011.03.028.

[41] B. Ben Doudou, J. Chen, A. Vivet, C. Poîlane, M. Ayachi, Role of Stone–Wales defects on the functionalization of (8,0) single wall carbon nanotubes by the amine group: Ab initio study, Phys. E Low-Dimens. Syst. Nanostructures 44 (2011) 120–123. https://doi.org/10.1016/j.physe.2011.07.017.

[42] H. Yoshida, S. Takeda, Elucidation of the origin of grown-in defects in carbon nanotubes, Carbon 70 (2014) 266–272. https://doi.org/10.1016/j.carbon.2014.01.006.

[43] Defects in carbon nanotubes, in: Defects Adv. Electron. Mater. Nov. Low Dimens. Struct., Woodhead Publishing, 2018: pp. 87–136. https://doi.org/10.1016/B978-0-08-102053-1.00004-1.

[44] C. Wang, G. Zhou, H. Liu, J. Wu, Y. Qiu, B.-L. Gu, W. Duan, Chemical Functionalization of Carbon Nanotubes by Carboxyl Groups on Stone-Wales Defects: A Density Functional Theory Study, J. Phys. Chem. B 110 (2006) 10266–10271. https://doi.org/10.1021/jp060412f.

[45] L. Liang, W. Xie, S. Fang, F. He, B. Yin, C. Tlili, D. Wang, S. Qiu, Q. Li, High-efficiency dispersion and sorting of single-walled carbon nanotubes via non-covalent interactions, J. Mater. Chem. C 5 (2017) 11339–11368. https://doi.org/10.1039/C7TC04390B.

[46] S. Han, X. Liu, C. Zhou, Template-Free Directional Growth of Single-Walled Carbon Nanotubes on a- and r-Plane Sapphire, J. Am. Chem. Soc. 127 (2005) 5294–5295. https://doi.org/10.1021/ja042544x.

[47] Z. Jin, H. Chu, J. Wang, J. Hong, W. Tan, Y. Li, Ultralow Feeding Gas Flow Guiding Growth of Large-Scale Horizontally Aligned Single-Walled Carbon Nanotube Arrays, Nano Lett. 7 (2007) 2073–2079.

https://doi.org/10.1021/nl070980m.

[48] E.S. Snow, J.P. Novak, P.M. Campbell, D. Park, Random networks of carbon nanotubes as an electronic material, Appl. Phys. Lett. 82 (2003) 2145–2147. https://doi.org/10.1063/1.1564291.

[49] R. Maheswaran, B.P. Shanmugavel, A Critical Review of the Role of Carbon Nanotubes in the Progress of Next-Generation Electronic Applications, J. Electron. Mater. 51 (2022) 2786–2800. https://doi.org/10.1007/s11664-022-09516-8.

[50] X. Hu, X. Bao, M. Zhang, S. Fang, K. Liu, J. Wang, R. Liu, S.H. Kim, R.H. Baughman, J. Ding, Recent Advances in Carbon Nanotube-Based Energy Harvesting Technologies, Adv. Mater. n/a (2023) 2303035. https://doi.org/10.1002/adma.202303035.

[51] K.J. Hughes, K.A. Iyer, R.E. Bird, J. Ivanov, S. Banerjee, G. Georges, Q.A. Zhou, Review of Carbon Nanotube Research and Development: Materials and Emerging Applications, ACS Appl. Nano Mater. 7 (2024) 18695–18713. https://doi.org/10.1021/acsanm.4c02721.

[52] R.S. Ruoff, D.C. Lorents, Mechanical and thermal properties of carbon nanotubes, Carbon 33 (1995) 925–930. https://doi.org/10.1016/0008-6223(95)00021-5.

[53] J.-P. Salvetat, J.-M. Bonard, N.H. Thomson, A.J. Kulik, L. Forró, W. Benoit, L. Zuppiroli, Mechanical properties of carbon nanotubes, Appl. Phys. A 69 (1999) 255–260. https://doi.org/10.1007/s003390050999.

[54] M.S. Dresselhaus, G. Dresselhaus, P. Avouris, eds., Carbon Nanotubes, Springer, Berlin, Heidelberg, 2001. https://doi.org/10.1007/3-540-39947-X.

[55] P. Poncharal, Z.L. Wang, D. Ugarte, W.A. de Heer, Electrostatic Deflections and Electromechanical Resonances of Carbon Nanotubes, Science 283 (1999) 1513–1516. https://doi.org/10.1126/science.283.5407.1513.

[56] E.T. Thostenson, Z. Ren, T.-W. Chou, Advances in the science and technology of carbon nanotubes and their composites: a review, Compos. Sci. Technol. 61 (2001) 1899–1912. https://doi.org/10.1016/S0266-3538(01)00094-X.

[57] Z. Yao, C.L. Kane, C. Dekker, High-Field Electrical Transport in Single-Wall Carbon Nanotubes, Phys. Rev. Lett. 84 (2000) 2941–2944. https://doi.org/10.1103/PhysRevLett.84.2941.

[58] P. Poncharal, C. Berger, Y. Yi, Z.L. Wang, W.A. de Heer, Room Temperature Ballistic Conduction in Carbon Nanotubes, J. Phys. Chem. B 106 (2002) 12104–12118. https://doi.org/10.1021/jp021271u.

[59] T. Dürkop, S.A. Getty, E. Cobas, M.S. Fuhrer, Extraordinary Mobility in Semiconducting Carbon Nanotubes, Nano Lett. 4 (2004) 35–39. https://doi.org/10.1021/nl034841q.

[60] S. Berber, Y.-K. Kwon, D. Tománek, Unusually High Thermal Conductivity of Carbon Nanotubes, Phys. Rev. Lett. 84 (2000) 4613–4616. https://doi.org/10.1103/PhysRevLett.84.4613.

[61] E. Pop, D. Mann, Q. Wang, K. Goodson, H. Dai, Thermal Conductance of an Individual Single-Wall Carbon Nanotube above Room Temperature, Nano Lett. 6 (2006) 96–100. https://doi.org/10.1021/nl052145f.

[62] K.M. Liew, C.H. Wong, X.Q. He, M.J. Tan, Thermal stability of single and multi-walled carbon nanotubes, Phys. Rev. B 71 (2005) 075424. https://doi.org/10.1103/PhysRevB.71.075424.

[63] B. Kumanek, Thermal conductivity of carbon nanotube networks: a review, J Mater Sci (2019) 31.

[64] A. Hirsch, Functionalization of Single-Walled Carbon Nanotubes, Angew. Chem. Int. Ed. 41 (2002) 1853–1859. https://doi.org/10.1002/1521-

3773(20020603)41:11%253C1853::AID-ANIE1853%253E3.0.CO;2-N.

[65] P. Ayala, R. Arenal, M. Rümmeli, A. Rubio, T. Pichler, The doping of carbon nanotubes with nitrogen and their potential applications, Carbon 48 (2010) 575–586. https://doi.org/10.1016/j.carbon.2009.10.009.

[66] Z. Liu, S. Tabakman, K. Welsher, H. Dai, Carbon nanotubes in biology and medicine: In vitro and in vivo detection, imaging and drug delivery, Nano Res. 2 (2009) 85–120. https://doi.org/10.1007/s12274-009-9009-8.

[67] R.P. Raffaelle, T. Gennett, J. Maranchi, P. Kumta, A.F. Hepp, M.J. Heben, A.C. Dillon, K.C. Jones, Carbon Nanotube Anodes for Lithium Ion Batteries, MRS Online Proc. Libr. 706 (2011) 1051. https://doi.org/10.1557/PROC-706-Z10.5.1.

[68] T. Chen, L. Wei, Z. Zhou, D. Shi, J. Wang, J. Zhao, Y. Yu, Y. Wang, Y. Zhang, Highly enhanced gas sensing in single-walled carbon nanotube-based thin-film transistor sensors by ultraviolet light irradiation, Nanoscale Res. Lett. 7 (2012) 644. https://doi.org/10.1186/1556-276X-7-644.

[69] T.W. Ebbesen, P.M. Ajayan, Large-scale synthesis of carbon nanotubes, Nature 358 (1992) 220–222. https://doi.org/10.1038/358220a0.

[70] C. Journet, W.K. Maser, P. Bernier, A. Loiseau, M.L. de la Chapelle, S. Lefrant, P. Deniard, R. Lee, J.E. Fischer, Large-scale production of single-walled carbon nanotubes by the electric-arc technique, Nature 388 (1997) 756–758. https://doi.org/10.1038/41972.

[71] M. Keidar, Factors affecting synthesis of single wall carbon nanotubes in arc discharge, J. Phys. Appl. Phys. 40 (2007) 2388. https://doi.org/10.1088/0022-3727/40/8/S18.

[72] A. Eatemadi, H. Daraee, H. Karimkhanloo, M. Kouhi, N. Zarghami, A. Akbarzadeh, M. Abasi, Y. Hanifehpour, S.W. Joo, Carbon nanotubes: properties, synthesis,

purification, and medical applications, Nanoscale Res. Lett. 9 (2014) 393. https://doi.org/10.1186/1556-276X-9-393.

[73] T. Guo, P. Nikolaev, A. Thess, D.T. Colbert, R.E. Smalley, Catalytic growth of single-walled nanotubes by laser vaporization, Chem. Phys. Lett. 243 (1995) 49–54. https://doi.org/10.1016/0009-2614(95)00825-O.

[74] M. Kim, S. Osone, T. Kim, H. Higashi, T. Seto, Synthesis of Nanoparticles by Laser Ablation: A Review, KONA Powder Part. J. 34 (2017) 80–90. https://doi.org/10.14356/kona.2017009.

[75] J.S. Lee, G.H. Gu, H. Kim, K.S. Jeong, J. Bae, J.S. Suh, Growth of Carbon Nanotubes on Anodic Aluminum Oxide Templates: Fabrication of a Tube-in-Tube and Linearly Joined Tube, Chem. Mater. 13 (2001) 2387–2391. https://doi.org/10.1021/cm0014076.

[76] P. Hou, C. Liu, C. Shi, H. Cheng, Carbon nanotubes prepared by anodic aluminum oxide template method, Chin. Sci. Bull. 57 (2012) 187–204. https://doi.org/10.1007/s11434-011-4892-2.

[77] L.N. Sacco, S. Vollebregt, Overview of Engineering Carbon Nanomaterials Such As Carbon Nanotubes (CNTs), Carbon Nanofibers (CNFs), Graphene and Nanodiamonds and Other Carbon Allotropes inside Porous Anodic Alumina (PAA) Templates, Nanomaterials 13 (2023) 260. https://doi.org/10.3390/nano13020260.

[78] S. Manafi, M. Amin, M. Rahimipour, E. Salahi, A. Kazemzadeh, High-yield Synthesis of Multiwalled Carbon Nanotube by Mechanothermal Method, Nanoscale Res. Lett. 4 (2009) 296. https://doi.org/10.1007/s11671-008-9240-3.

[79] E.Z. Karimi, S.M. Zebarjad, J.V. Khaki, H. Izadi, Production of carbon nanotubes using mechanical milling in the presence of an exothermic reaction, J. Alloys Compd. 505 (2010) 37–42. https://doi.org/10.1016/j.jallcom.2010.06.021.

[80] J. Kong, H.T. Soh, A.M. Cassell, C.F. Quate, H. Dai, Synthesis of individual single-walled carbon nanotubes on patterned silicon wafers, Nature 395 (1998) 878–881. https://doi.org/10.1038/27632.

[81] R. Andrews, D. Jacques, A.M. Rao, F. Derbyshire, D. Qian, X. Fan, E.C. Dickey, J. Chen, Continuous production of aligned carbon nanotubes: a step closer to commercial realization, Chem. Phys. Lett. 303 (1999) 467–474. https://doi.org/10.1016/S0009-2614(99)00282-1.

[82] K. Hernadi, A. Fonseca, J.B. Nagy, A. Siska, I. Kiricsi, Production of nanotubes by the catalytic decomposition of different carbon-containing compounds, Appl. Catal. Gen. 199 (2000) 245–255. https://doi.org/10.1016/S0926-860X(99)00561-X.

[83] W.Z. Li, J.G. Wen, Z.F. Ren, Effect of temperature on growth and structure of carbon nanotubes by chemical vapor deposition, Appl. Phys. A 74 (2002) 397–402. https://doi.org/10.1007/s003390201284.

[84] K. Hata, D.N. Futaba, K. Mizuno, T. Namai, M. Yumura, S. Iijima, Water-Assisted Highly Efficient Synthesis of Impurity-Free Single-Walled Carbon Nanotubes, Science 306 (2004) 1362–1364. https://doi.org/10.1126/science.1104962.

[85] X. Xiang, L. Zhang, H.I. Hima, F. Li, D.G. Evans, Co-based catalysts from Co/Fe/Al layered double hydroxides for preparation of carbon nanotubes, Appl. Clay Sci. 42 (2009) 405–409. https://doi.org/10.1016/j.clay.2008.04.004.

[86] M. Kumar, Y. Ando, Chemical Vapor Deposition of Carbon Nanotubes: A Review on Growth Mechanism and Mass Production, J. Nanosci. Nanotechnol. 10 (2010) 3739–3758. https://doi.org/10.1166/jnn.2010.2939.

[87] S. Vm, A.R. Mohamed, A.Z. Abdullah, S.-P. Chai, Role of Reaction and Factors of Carbon Nanotubes Growth in Chemical Vapour Decomposition Process Using Methane—A Highlight, J. Nanomater. 2010 (2010) 395191.

https://doi.org/10.1155/2010/395191.

[88] S. Maruyama, R. Kojima, Y. Miyauchi, S. Chiashi, M. Kohno, Low-temperature synthesis of high-purity single-walled carbon nanotubes from alcohol, Chem. Phys. Lett. 360 (2002) 229–234. https://doi.org/10.1016/S0009-2614(02)00838-2.

[89] M. Escobar, M.S. Moreno, R.J. Candal, M.C. Marchi, A. Caso, P.I. Polosecki, G.H. Rubiolo, S. Goyanes, Synthesis of carbon nanotubes by CVD: Effect of acetylene pressure on nanotubes characteristics, Appl. Surf. Sci. 254 (2007) 251–256. https://doi.org/10.1016/j.apsusc.2007.07.044.

[90] N.J. Morales, S. Goyanes, C. Chiliotte, V. Bekeris, R.J. Candal, G.H. Rubiolo, One-step chemical vapor deposition synthesis of magnetic CNT–hercynite (FeAl2O4) hybrids with good aqueous colloidal stability, Carbon 61 (2013) 515–524. https://doi.org/10.1016/j.carbon.2013.04.106.

[91] W. Zhou, Z. Han, J. Wang, Y. Zhang, Z. Jin, X. Sun, Y. Zhang, C. Yan, Y. Li, Copper Catalyzing Growth of Single-Walled Carbon Nanotubes on Substrates, Nano Lett. 6 (2006) 2987–2990. https://doi.org/10.1021/nl061871v.

[92] H. Ago, S. Imamura, T. Okazaki, T. Saito, M. Yumura, M. Tsuji, CVD Growth of Single-Walled Carbon Nanotubes with Narrow Diameter Distribution over Fe/MgO Catalyst and Their Fluorescence Spectroscopy, J. Phys. Chem. B 109 (2005) 10035–10041. https://doi.org/10.1021/jp050307q.

[93] M.R. Aguiar, C. Verissimo, A.C.S. Ramos, S.A. Moshkalev, J.W. Swart, Synthesis of Carbon Nanotubes and Nanofibers by Thermal CVD on SiO2 and Al2O3 Support Layers, J. Nanosci. Nanotechnol. 9 (2009) 4143–4150. https://doi.org/10.1166/jnn.2009.M23.

[94] S. Hofmann, C. Ducati, J. Robertson, B. Kleinsorge, Low-temperature growth of carbon nanotubes by plasma-enhanced chemical vapor deposition, Appl. Phys. Lett.

83 (2003) 135–137. https://doi.org/10.1063/1.1589187.

[95] M.T. Cole, W.I. Milne, Plasma Enhanced Chemical Vapour Deposition of Horizontally Aligned Carbon Nanotubes, Materials 6 (2013) 2262–2273. https://doi.org/10.3390/ma6062262.

[96] A. Kohls, M. Maurer Ditty, F. Dehghandehnavi, S.-Y. Zheng, Vertically Aligned Carbon Nanotubes as a Unique Material for Biomedical Applications, ACS Appl. Mater. Interfaces 14 (2022) 6287–6306. https://doi.org/10.1021/acsami.1c20423.

[97] Y. Murakami, Y. Miyauchi, S. Chiashi, S. Maruyama, Characterization of single-walled carbon nanotubes catalytically synthesized from alcohol, Chem. Phys. Lett. 374 (2003) 53–58. https://doi.org/10.1016/S0009-2614(03)00687-0.

[98] Y. Murakami, Y. Miyauchi, S. Chiashi, S. Maruyama, Direct synthesis of high-quality single-walled carbon nanotubes on silicon and quartz substrates, Chem. Phys. Lett. 377 (2003) 49–54. https://doi.org/10.1016/S0009-2614(03)01094-7.

[99] N. Inami, M.A. Mohamed, E. Shikoh, A. Fujiwara, Synthesis-condition dependence of carbon nanotube growth by alcohol catalytic chemical vapor deposition method, Sci. Technol. Adv. Mater. 8 (2007) 292. https://doi.org/10.1016/j.stam.2007.02.009.

[100] H. Sato, K. Hata, K. Hiasa, Y. Saito, Low temperature growth of carbon nanotubes by alcohol catalytic chemical vapor deposition for field emitter applications, J. Vac. Sci. Technol. B Microelectron. Nanometer Struct. Process. Meas. Phenom. 25 (2007) 579–582. https://doi.org/10.1116/1.2433964.

[101] D.N. Futaba, K. Hata, T. Yamada, K. Mizuno, M. Yumura, S. Iijima, Kinetics of Water-Assisted Single-Walled Carbon Nanotube Synthesis Revealed by a Time-Evolution Analysis, Phys. Rev. Lett. 95 (2005) 056104. https://doi.org/10.1103/PhysRevLett.95.056104.

[102] S.P. Patole, P.S. Alegaonkar, H.-C. Lee, J.-B. Yoo, Optimization of water assisted chemical vapor deposition parameters for super growth of carbon nanotubes, Carbon 46 (2008) 1987–1993. https://doi.org/10.1016/j.carbon.2008.08.009.

[103] P.B. Amama, C.L. Pint, L. McJilton, S.M. Kim, E.A. Stach, P.T. Murray, R.H. Hauge, B. Maruyama, Role of Water in Super Growth of Single-Walled Carbon Nanotube Carpets, Nano Lett. 9 (2009) 44–49. https://doi.org/10.1021/nl801876h.

[104] S. Huang, Q. Cai, J. Chen, Y. Qian, L. Zhang, Metal-Catalyst-Free Growth of Single-Walled Carbon Nanotubes on Substrates, J. Am. Chem. Soc. 131 (2009) 2094–2095. https://doi.org/10.1021/ja809635s.

[105] B. Liu, W. Ren, L. Gao, S. Li, S. Pei, C. Liu, C. Jiang, H.-M. Cheng, Metal-Catalyst-Free Growth of Single-Walled Carbon Nanotubes, J. Am. Chem. Soc. 131 (2009) 2082–2083. https://doi.org/10.1021/ja8093907.

[106] D. Takagi, Y. Kobayashi, Y. Homma, Carbon Nanotube Growth from Diamond, J. Am. Chem. Soc. 131 (2009) 6922–6923. https://doi.org/10.1021/ja901295j.

[107] B. Liu, D.-M. Tang, C. Sun, C. Liu, W. Ren, F. Li, W.-J. Yu, L.-C. Yin, L. Zhang, C. Jiang, H.-M. Cheng, Importance of Oxygen in the Metal-Free Catalytic Growth of Single-Walled Carbon Nanotubes from SiOx by a Vapor−Solid−Solid Mechanism, J. Am. Chem. Soc. 133 (2011) 197–199. https://doi.org/10.1021/ja107855q.

[108] M. Kumar, Y. Ando, Carbon Nanotube Synthesis and Growth Mechanism, Nanotechnol. Percept. 6 (2010) 7–28.

[109] Y. Saito, Nanoparticles and filled nanocapsules, Carbon 33 (1995) 979–988. https://doi.org/10.1016/0008-6223(95)00026-A.

[110] Y. Homma, Y. Kobayashi, T. Ogino, D. Takagi, R. Ito, Y.J. Jung, P.M. Ajayan, Role of Transition Metal Catalysts in Single-Walled Carbon Nanotube Growth in

Chemical Vapor Deposition, J. Phys. Chem. B 107 (2003) 12161–12164. https://doi.org/10.1021/jp0353845.

[111] R.S. Wagner, W.C. Ellis, Vapor-liquid-solid mechanism of single crystal growth, Appl. Phys. Lett. 4 (1964) 89–90. https://doi.org/10.1063/1.1753975.

[112] A.I. Persson, M.W. Larsson, S. Stenström, B.J. Ohlsson, L. Samuelson, L.R. Wallenberg, Solid-phase diffusion mechanism for GaAs nanowire growth, Nat. Mater. 3 (2004) 677–681. https://doi.org/10.1038/nmat1220.

[113] D. Takagi, Y. Homma, H. Hibino, S. Suzuki, Y. Kobayashi, Single-Walled Carbon Nanotube Growth from Highly Activated Metal Nanoparticles, Nano Lett. 6 (2006) 2642–2645. https://doi.org/10.1021/nl061797g.

[114] M. He, H. Jiang, J. Lehtonen, E.I. Kauppinen, Growth of single-walled carbon nanotubes with large chiral angles on rhodium nanoparticles, Nanoscale 5 (2013) 10200–10202. https://doi.org/10.1039/C3NR03259K.

[115] H. Xue, L. Xin, Z. Xu, R. Bai, Q. Wu, B. Xin, X. Zhang, H. Cui, F. Chen, M. He, Iridium-catalyzed growth of single-walled carbon nanotubes with a bicentric diameter distribution, Mater. Chem. Front. 3 (2019) 1882–1887. https://doi.org/10.1039/C9QM00267G.

[116] Y. Homma, H. Liu, D. Takagi, Y. Kobayashi, Single-walled carbon nanotube growth with non-iron-group “catalysts” by chemical vapor deposition, Nano Res. 2 (2009) 793–799. https://doi.org/10.1007/s12274-009-9082-z.

[117] M. Wang, K. Nakamura, M. Arifuku, N. Kiyoyanagi, T. Inoue, Y. Kobayashi, Growth of Single-Walled Carbon Nanotubes from Solid Carbon Nanoparticle Seeds via Cap Formation Engineering with a Two-Step Growth Process and Water Vapor Supply, ACS Omega 7 (2022) 3639–3648. https://doi.org/10.1021/acsomega.1c06268.

[118] Z.-Y. Zeng, J.-H. Lin, Metal-catalyst-free growth of carbon nanotubes/carbon nanofibers on carbon blacks using chemical vapor deposition, RSC Adv. 4 (2014) 40251–40258. https://doi.org/10.1039/C4RA03456B.

[119] S.A.I. Steiner, T.F. Baumann, B.C. Bayer, R. Blume, M.A. Worsley, W.J. MoberlyChan, E.L. Shaw, R. Schlögl, A.J. Hart, S. Hofmann, B.L. Wardle, Nanoscale Zirconia as a Nonmetallic Catalyst for Graphitization of Carbon and Growth of Single- and Multiwall Carbon Nanotubes, J. Am. Chem. Soc. 131 (2009) 12144–12154. https://doi.org/10.1021/ja902913r.

[120] L. Kang, Y. Hu, L. Liu, J. Wu, S. Zhang, Q. Zhao, F. Ding, Q. Li, J. Zhang, Growth of Close-Packed Semiconducting Single-Walled Carbon Nanotube Arrays Using Oxygen-Deficient TiO2 Nanoparticles as Catalysts, Nano Lett. 15 (2015) 403–409. https://doi.org/10.1021/nl5037325.

[121] S. Helveg, C. López-Cartes, J. Sehested, P.L. Hansen, B.S. Clausen, J.R. Rostrup-Nielsen, F. Abild-Pedersen, J.K. Nørskov, Atomic-scale imaging of carbon nanofibre growth, Nature 427 (2004) 426–429. https://doi.org/10.1038/nature02278.

[122] H. Yoshida, S. Takeda, T. Uchiyama, H. Kohno, Y. Homma, Atomic-Scale In-situ Observation of Carbon Nanotube Growth from Solid State Iron Carbide Nanoparticles, Nano Lett. 8 (2008) 2082–2086. https://doi.org/10.1021/nl080452q.

[123] I.W. Chiang, B.E. Brinson, R.E. Smalley, J.L. Margrave, R.H. Hauge, Purification and Characterization of Single-Wall Carbon Nanotubes, J. Phys. Chem. B 105 (2001) 1157–1161. https://doi.org/10.1021/jp003453z.

[124] Y. Maeda, M. Kanda, M. Hashimoto, T. Hasegawa, S. Kimura, Y. Lian, T. Wakahara, T. Akasaka, S. Kazaoui, N. Minami, T. Okazaki, Y. Hayamizu, K. Hata, J. Lu, S. Nagase, Dispersion and Separation of Small-Diameter Single-Walled

Carbon Nanotubes, J. Am. Chem. Soc. 128 (2006) 12239–12242. https://doi.org/10.1021/ja063776u.

[125] Y. Hu, L. Kang, Q. Zhao, H. Zhong, S. Zhang, L. Yang, Z. Wang, J. Lin, Q. Li, Z. Zhang, L. Peng, Z. Liu, J. Zhang, Growth of high-density horizontally aligned SWNT arrays using Trojan catalysts, Nat. Commun. 6 (2015) 6099. https://doi.org/10.1038/ncomms7099.

[126] Y. Liao, H. Jiang, N. Wei, P. Laiho, Q. Zhang, S.A. Khan, E.I. Kauppinen, Direct Synthesis of Colorful Single-Walled Carbon Nanotube Thin Films, J. Am. Chem. Soc. 140 (2018) 9797–9800. https://doi.org/10.1021/jacs.8b05151.

[127] M. He, S. Zhang, J. Zhang, Horizontal Single-Walled Carbon Nanotube Arrays: Controlled Synthesis, Characterizations, and Applications, Chem. Rev. 120 (2020) 12592–12684. https://doi.org/10.1021/acs.chemrev.0c00395.

[128] Y. Zhang, A. Chang, J. Cao, Q. Wang, W. Kim, Y. Li, N. Morris, E. Yenilmez, J. Kong, H. Dai, Electric-field-directed growth of aligned single-walled carbon nanotubes, Appl. Phys. Lett. 79 (2001) 3155–3157. https://doi.org/10.1063/1.1415412.

[129] E. Joselevich, C.M. Lieber, Vectorial Growth of Metallic and Semiconducting Single-Wall Carbon Nanotubes, Nano Lett. 2 (2002) 1137–1141. https://doi.org/10.1021/nl025642u.

[130] A. Ural, Y. Li, H. Dai, Electric-field-aligned growth of single-walled carbon nanotubes on surfaces, Appl. Phys. Lett. 81 (2002) 3464–3466. https://doi.org/10.1063/1.1518773.

[131] H. Ago, K. Nakamura, K. Ikeda, N. Uehara, N. Ishigami, M. Tsuji, Aligned growth of isolated single-walled carbon nanotubes programmed by atomic arrangement of substrate surface, Chem. Phys. Lett. 408 (2005) 433–438.

https://doi.org/10.1016/j.cplett.2005.04.054.

[132] A.M. Cassell, N.R. Franklin, T.W. Tombler, E.M. Chan, J. Han, H. Dai, Directed Growth of Free-StandingSingle-Walled Carbon Nanotubes, J. Am. Chem. Soc. 121 (1999) 7975–7976. https://doi.org/10.1021/ja992083t.

[133] B. Peng, Y. Yao, J. Zhang, Effect of the Reynolds and Richardson Numbers on the Growth of Well-Aligned Ultralong Single-Walled Carbon Nanotubes, J. Phys. Chem. C 114 (2010) 12960–12965. https://doi.org/10.1021/jp103731p.

[134] Z. Zhu, N. Wei, H. Xie, R. Zhang, Y. Bai, Q. Wang, C. Zhang, S. Wang, L. Peng, L. Dai, F. Wei, Acoustic-assisted assembly of an individual monochromatic ultralong carbon nanotube for high on-current transistors, Sci. Adv. 2 (2016) e1601572. https://doi.org/10.1126/sciadv.1601572.

[135] R. Zhang, Y. Zhang, F. Wei, Controlled Synthesis of Ultralong Carbon Nanotubes with Perfect Structures and Extraordinary Properties, Acc. Chem. Res. 50 (2017) 179–189. https://doi.org/10.1021/acs.accounts.6b00430.

[136] R. Zhang, Y. Zhang, F. Wei, Horizontally aligned carbon nanotube arrays: growth mechanism, controlled synthesis, characterization, properties and applications, Chem. Soc. Rev. 46 (2017) 3661–3715. https://doi.org/10.1039/C7CS00104E.

[137] Q. Jiang, F. Wang, R. Li, X. Wu, W. Zhang, S. Zhao, Y. Huang, B. Wang, S. Zhang, Y. Zhao, R. Zhang, The Inherent Thermal Effect of Substrates on the Growth of Ultralong Carbon Nanotubes, Adv. Funct. Mater. 33 (2023) 2212665. https://doi.org/10.1002/adfm.202212665.

[138] E.J. Shaughnessy, I.M. Katz, J.P. Schaffer, Introduction to fluid mechanics, Oxford University Press, New York, 2005.

[139] L.C. Burmeister, Convective Heat Transfer, John Wiley & Sons, 1993.

[140] Y. Liu, T. Inoue, M. Wang, M. Arifuku, N. Kiyoyanagi, Y. Kobayashi, Gas flow–directed growth of aligned carbon nanotubes from nonmetallic seeds, Carbon 214 (2023) 118309. https://doi.org/10.1016/j.carbon.2023.118309.

[141] Y. Wu, M. Huang, F. Wang, X.M.H. Huang, S. Rosenblatt, L. Huang, H. Yan, S.P. O'Brien, J. Hone, T.F. Heinz, Determination of the Young's Modulus of Structurally Defined Carbon Nanotubes, Nano Lett. 8 (2008) 4158–4161. https://doi.org/10.1021/nl801563q.

[142] Y. Bai, R. Zhang, X. Ye, Z. Zhu, H. Xie, B. Shen, D. Cai, B. Liu, C. Zhang, Z. Jia, S. Zhang, X. Li, F. Wei, Carbon nanotube bundles with tensile strength over 80 GPa, Nat. Nanotechnol. 13 (2018) 589–595. https://doi.org/10.1038/s41565-018-0141-z.

[143] V. Lee, C.-H. Wu, Z.-X. Lou, W.-L. Lee, C.-W. Chang, Divergent and Ultrahigh Thermal Conductivity in Millimeter-Long Nanotubes, Phys. Rev. Lett. 118 (2017) 135901. https://doi.org/10.1103/PhysRevLett.118.135901.

[144] C. Qiu, Z. Zhang, M. Xiao, Y. Yang, D. Zhong, L.-M. Peng, Scaling carbon nanotube complementary transistors to 5-nm gate lengths, Science 355 (2017) 271–276. https://doi.org/10.1126/science.aaj1628.

[145] Z. Chen, J. Appenzeller, Y.-M. Lin, J. Sippel-Oakley, A.G. Rinzler, J. Tang, S.J. Wind, P.M. Solomon, P. Avouris, An Integrated Logic Circuit Assembled on a Single Carbon Nanotube, Science 311 (2006) 1735–1735. https://doi.org/10.1126/science.1122797.

[146] G. Hills, C. Lau, A. Wright, S. Fuller, M.D. Bishop, T. Srimani, P. Kanhaiya, R. Ho, A. Amer, Y. Stein, D. Murphy, Arvind, A. Chandrakasan, M.M. Shulaker, Modern microprocessor built from complementary carbon nanotube transistors, Nature 572 (2019) 595–602. https://doi.org/10.1038/s41586-019-1493-8.

[147] C. Rutherglen, A.A. Kane, P.F. Marsh, T.A. Cain, B.I. Hassan, M.R. AlShareef, C. Zhou, K. Galatsis, Wafer-scalable, aligned carbon nanotube transistors operating at frequencies of over 100 GHz, Nat. Electron. 2 (2019) 530–539. https://doi.org/10.1038/s41928-019-0326-y.

[148] G. Long, W. Jin, F. Xia, Y. Wang, T. Bai, X. Chen, X. Liang, L.-M. Peng, Y. Hu, Carbon nanotube-based flexible high-speed circuits with sub-nanosecond stage delays, Nat. Commun. 13 (2022) 6734. https://doi.org/10.1038/s41467-022-34621-x.

[149] N.R. Franklin, H. Dai, An Enhanced CVD Approach to Extensive Nanotube Networks with Directionality, Adv. Mater. 12 (2000) 890–894. https://doi.org/10.1002/1521-4095(200006)12:12%253C890::AID-ADMA890%253E3.0.CO;2-K.

[150] Y. Liu, T. Inoue, Y. Kobayashi, Crossover between Kite Growth and Vibrational Bridging in Pillar-Assisted Controlled Formation of Carbon Nanotube Networks toward Nanoscale Interconnections, ACS Appl. Nano Mater. 8 (2025) 16861–16871. https://doi.org/10.1021/acsanm.5c03056.

[151] J. Zhang, X. Wang, W. Yang, W. Yu, T. Feng, Q. Li, X. Liu, C. Yang, Interaction between carbon nanotubes and substrate and its implication on field emission mechanism, Carbon 44 (2006) 418–422. https://doi.org/10.1016/j.carbon.2005.09.004.

[152] V. Perebeinos, S.V. Rotkin, A.G. Petrov, P. Avouris, The Effects of Substrate Phonon Mode Scattering on Transport in Carbon Nanotubes, Nano Lett. 9 (2009) 312–316. https://doi.org/10.1021/nl8030086.

[153] S.-H. Kang, G. Kim, Y.-K. Kwon, Is hexagonal boron nitride always good as a substrate for carbon nanotube-based devices?, Phys. Chem. Chem. Phys. 17 (2015)

5072–5077. https://doi.org/10.1039/C4CP05478D.

[154] K. Hess, P. Vogl, Remote polar phonon scattering in silicon inversion layers, Solid State Commun. 30 (1979) 797–799. https://doi.org/10.1016/0038-1098(79)90051-6.

[155] J.P. Leburton, G. Dorda, Remote polar phonon scattering for hot electrons in Si-inversion layers, Solid State Commun. 40 (1981) 1025–1026. https://doi.org/10.1016/0038-1098(81)90060-0.

[156] Y.K. Koh, A.S. Lyons, M.-H. Bae, B. Huang, V.E. Dorgan, D.G. Cahill, E. Pop, Role of Remote Interfacial Phonon (RIP) Scattering in Heat Transport Across Graphene/SiO2 Interfaces, Nano Lett. 16 (2016) 6014–6020. https://doi.org/10.1021/acs.nanolett.6b01709.

[157] O.A. Shenderova, D.M. Gruen, Ultrananocrystalline Diamond: Synthesis, Properties and Applications, William Andrew, 2012.

[158] M. Wang, Y. Liu, M. Maekawa, M. Arifuku, N. Kiyoyanagi, T. Inoue, Y. Kobayashi, Combination effect of growth enhancers and carbon sources on synthesis of single-walled carbon nanotubes from solid carbon growth seeds, Diam. Relat. Mater. 130 (2022) 109516. https://doi.org/10.1016/j.diamond.2022.109516.

[159] M.S. Dresselhaus, G. Dresselhaus, A. Jorio, A.G. Souza Filho, R. Saito, Raman spectroscopy on isolated single wall carbon nanotubes, Carbon 40 (2002) 2043–2061. https://doi.org/10.1016/S0008-6223(02)00066-0.

[160] A. Jorio, A.G. Souza Filho, G. Dresselhaus, M.S. Dresselhaus, A.K. Swan, M.S. Ünlü, B.B. Goldberg, M.A. Pimenta, J.H. Hafner, C.M. Lieber, R. Saito, G-band resonant Raman study of 62 isolated single-wall carbon nanotubes, Phys. Rev. B 65 (2002) 155412. https://doi.org/10.1103/PhysRevB.65.155412.

[161] M.S. Dresselhaus, G. Dresselhaus, R. Saito, A. Jorio, Raman spectroscopy of

carbon nanotubes, Phys. Rep. 409 (2005) 47–99. https://doi.org/10.1016/j.physrep.2004.10.006.

[162] C.C. Moura, R.S. Tare, R.O.C. Oreffo, S. Mahajan, Raman spectroscopy and coherent anti-Stokes Raman scattering imaging: prospective tools for monitoring skeletal cells and skeletal regeneration, J. R. Soc. Interface 13 (2016) 20160182. https://doi.org/10.1098/rsif.2016.0182.

[163] G. Binnig, H. Rohrer, SCANNING TUNNELING MICROSCOPY., IBM J. Res. Dev. 30 (1986) 355–369.

[164] Y. Homma, S. Suzuki, Y. Kobayashi, M. Nagase, D. Takagi, Mechanism of bright selective imaging of single-walled carbon nanotubes on insulators by scanning electron microscopy, Appl. Phys. Lett. 84 (2004) 1750–1752. https://doi.org/10.1063/1.1667608.

[165] Homma Y., Kato H., SEM Observation of Carbon Nanotube and Graphene, Hyomen Kagaku 36 (2015) 178–183. https://doi.org/10.1380/jsssj.36.178.

[166] K. Akhtar, S.A. Khan, S.B. Khan, A.M. Asiri, Scanning Electron Microscopy: Principle and Applications in Nanomaterials Characterization, in: S.K. Sharma (Ed.), Handb. Mater. Charact., Springer International Publishing, Cham, 2018: pp. 113–145. https://doi.org/10.1007/978-3-319-92955-2_4.

[167] K. Liu, Y. Sun, X. Lin, R. Zhou, J. Wang, S. Fan, K. Jiang, Scratch-Resistant, Highly Conductive, and High-Strength Carbon Nanotube-Based Composite Yarns, ACS Nano 4 (2010) 5827–5834. https://doi.org/10.1021/nn1017318.

[168] M.F.L. De Volder, S.H. Tawfick, R.H. Baughman, A.J. Hart, Carbon Nanotubes: Present and Future Commercial Applications, Science 339 (2013) 535–539. https://doi.org/10.1126/science.1222453.

[169] L.-M. Peng, Z. Zhang, S. Wang, Carbon nanotube electronics: recent advances,

Mater. Today 17 (2014) 433–442. https://doi.org/10.1016/j.mattod.2014.07.008.

[170] X. He, H. Htoon, S.K. Doorn, W.H.P. Pernice, F. Pyatkov, R. Krupke, A. Jeantet, Y. Chassagneux, C. Voisin, Carbon nanotubes as emerging quantum-light sources, Nat. Mater. 17 (2018) 663–670. https://doi.org/10.1038/s41563-018-0109-2.

[171] Y. Bai, B. Shen, S. Zhang, Z. Zhu, S. Sun, J. Gao, B. Li, Y. Wang, R. Zhang, F. Wei, Storage of Mechanical Energy Based on Carbon Nanotubes with High Energy Density and Power Density, Adv. Mater. 31 (2019) 1800680. https://doi.org/10.1002/adma.201800680.

[172] M.M. Shulaker, G. Hills, N. Patil, H. Wei, H.-Y. Chen, H.-S.P. Wong, S. Mitra, Carbon nanotube computer, Nature 501 (2013) 526–530. https://doi.org/10.1038/nature12502.

[173] A. Ismach, L. Segev, E. Wachtel, E. Joselevich, Atomic-Step-Templated Formation of Single Wall Carbon Nanotube Patterns, Angew. Chem. Int. Ed. 43 (2004) 6140–6143. https://doi.org/10.1002/anie.200460356.

[174] P.-X. Hou, C. Liu, H.-M. Cheng, Purification of carbon nanotubes, Carbon 46 (2008) 2003–2025. https://doi.org/10.1016/j.carbon.2008.09.009.

[175] K.T. Koga, M.J. Walter, E. Nakamura, K. Kobayashi, Carbon self-diffusion in a natural diamond, Phys. Rev. B 72 (2005) 024108. https://doi.org/10.1103/PhysRevB.72.024108.

[176] E. Budke, Ch. Herzig, H. Wever, Volume and grain boundary diffusion of 14C in α-Fe, Phys. Status Solidi A 127 (1991) 87–101. https://doi.org/10.1002/pssa.2211270109.

[177] E.W. Lemmon, R.T. Jacobsen, Viscosity and Thermal Conductivity Equations for Nitrogen, Oxygen, Argon, and Air, Int. J. Thermophys. 25 (2004) 21–69. https://doi.org/10.1023/B:IJOT.0000022327.04529.f3.

[178] H. Seiler, Secondary electron emission in the scanning electron microscope, J. Appl. Phys. 54 (1983) R1–R18. https://doi.org/10.1063/1.332840.

[179] D. Takagi, A. Yamazaki, Y. Otsuka, H. Yoshimura, Y. Kobayashi, Y. Homma, Gold-filled apo-ferritin for investigation of single-walled carbon nanotube growth on substrate, Chem. Phys. Lett. 445 (2007) 213–216. https://doi.org/10.1016/j.cplett.2007.07.104.

[180] B.W. Smith, D.E. Luzzi, Electron irradiation effects in single wall carbon nanotubes, J. Appl. Phys. 90 (2001) 3509–3515. https://doi.org/10.1063/1.1383020.

[181] S. Araki, The Secondary Electron Emission Characteristics of Carbon Materials, J. Surf. Anal. 14 (2007) 118–123. https://doi.org/10.1384/jsa.14.118.

[182] Y. Lin, D.C. Joy, A new examination of secondary electron yield data, Surf. Interface Anal. 37 (2005) 895–900. https://doi.org/10.1002/sia.2107.

[183] E. Schreiber, H.-J. Fitting, Monte Carlo simulation of secondary electron emission from the insulator SiO2, J. Electron Spectrosc. Relat. Phenom. 124 (2002) 25–37. https://doi.org/10.1016/S0368-2048(01)00368-1.

[184] M.-F.C. Fiawoo, A.-M. Bonnot, H. Amara, C. Bichara, J. Thibault-Pénisson, A. Loiseau, Evidence of Correlation between Catalyst Particles and the Single-Wall Carbon Nanotube Diameter: A First Step towards Chirality Control, Phys. Rev. Lett. 108 (2012) 195503. https://doi.org/10.1103/PhysRevLett.108.195503.

[185] L. Zhang, M. He, T.W. Hansen, J. Kling, H. Jiang, E.I. Kauppinen, A. Loiseau, J.B. Wagner, Growth Termination and Multiple Nucleation of Single-Wall Carbon Nanotubes Evidenced by in Situ Transmission Electron Microscopy, ACS Nano 11 (2017) 4483–4493. https://doi.org/10.1021/acsnano.6b05941.

[186] G.-H. Jeong, S. Suzuki, Y. Kobayashi, A. Yamazaki, H. Yoshimura, Y. Homma, Effect of nanoparticle density on narrow diameter distribution of carbon nanotubes

and particle evolution during chemical vapor deposition growth, J. Appl. Phys. 98 (2005) 124311. https://doi.org/10.1063/1.2146054.

[187] F. Yang, H. Zhao, R. Li, Q. Liu, X. Zhang, X. Bai, R. Wang, Y. Li, Growth modes of single-walled carbon nanotubes on catalysts, Sci. Adv. 8 (2022) eabq0794. https://doi.org/10.1126/sciadv.abq0794.

[188] M.R. Falvo, G.J. Clary, R.M. Taylor, V. Chi, F.P. Brooks, S. Washburn, R. Superfine, Bending and buckling of carbon nanotubes under large strain, Nature 389 (1997) 582–584. https://doi.org/10.1038/39282.

[189] P.T. Araujo, S.K. Doorn, S. Kilina, S. Tretiak, E. Einarsson, S. Maruyama, H. Chacham, M.A. Pimenta, A. Jorio, Third and Fourth Optical Transitions in Semiconducting Carbon Nanotubes, Phys. Rev. Lett. 98 (2007) 067401. https://doi.org/10.1103/PhysRevLett.98.067401.

[190] F. Villalpando-Paez, H. Son, D. Nezich, Y.P. Hsieh, J. Kong, Y.A. Kim, D. Shimamoto, H. Muramatsu, T. Hayashi, M. Endo, M. Terrones, M.S. Dresselhaus, Raman Spectroscopy Study of Isolated Double-Walled Carbon Nanotubes with Different Metallic and Semiconducting Configurations, Nano Lett. 8 (2008) 3879–3886. https://doi.org/10.1021/nl802306t.

[191] N. Neophytou, D. Kienle, E. Polizzi, M.P. Anantram, Influence of defects on nanotube transistor performance, Appl. Phys. Lett. 88 (2006) 242106. https://doi.org/10.1063/1.2211932.

[192] Y.M. Ho, G.M. Yang, W.T. Zheng, X. Wang, H.W. Tian, Q. Xu, H.B. Li, J.W. Liu, J.L. Qi, Q. Jiang, Synthesis and field electron emission properties of hybrid carbon nanotubes and nanoparticles, Nanotechnology 19 (2008) 065710. https://doi.org/10.1088/0957-4484/19/6/065710.

[193] D. Varshney, B.R. Weiner, G. Morell, Growth and field emission study of a

monolithic carbon nanotube/diamond composite 单片碳纳米管/金刚石复合材料的生长与场发射研究, Carbon 48 (2010) 3353–3358. https://doi.org/10.1016/j.carbon.2010.05.025.

[194] Q. Cao, J.A. Rogers, Random networks and aligned arrays of single-walled carbon nanotubes for electronic device applications, Nano Res. 1 (2008) 259–272. https://doi.org/10.1007/s12274-008-8033-4.

[195] A.C. Dillon, Carbon Nanotubes for Photoconversion and Electrical Energy Storage, Chem. Rev. 110 (2010) 6856–6872. https://doi.org/10.1021/cr9003314.

[196] V. Schroeder, S. Savagatrup, M. He, S. Lin, T.M. Swager, Carbon Nanotube Chemical Sensors, Chem. Rev. 119 (2019) 599–663. https://doi.org/10.1021/acs.chemrev.8b00340.

[197] N.F. Zorn, J. Zaumseil, Charge transport in semiconducting carbon nanotube networks, Appl. Phys. Rev. 8 (2021) 041318. https://doi.org/10.1063/5.0065730.

[198] Y. Yue, D. Zhang, P. Wang, X. Xia, X. Wu, Y. Zhang, J. Mei, S. Li, M. Li, Y. Wang, X. Zhang, X. Wei, H. Liu, W. Zhou, Large-Area Flexible Carbon Nanofilms with Synergistically Enhanced Transmittance and Conductivity Prepared by Reorganizing Single-Walled Carbon Nanotube Networks, Adv. Mater. 36 (2024) 2313971. https://doi.org/10.1002/adma.202313971.

[199] X. Zhu, M. Xi, J. Wang, P. Zhang, Y. Li, X. Luo, L. Bai, X. Chen, L. Peng, Y. Cao, Q. Li, X. Liang, High-performance ternary logic circuits and neural networks based on carbon nanotube source-gating transistors, Sci. Adv. 11 (2025) eadt1909. https://doi.org/10.1126/sciadv.adt1909.

[200] R.H. Schmidt, I.A. Kinloch, A.N. Burgess, A.H. Windle, The Effect of Aggregation on the Electrical Conductivity of Spin-Coated Polymer/Carbon Nanotube Composite Films, Langmuir 23 (2007) 5707–5712.

https://doi.org/10.1021/la062794m.

[201] R.P. Tortorich, J.-W. Choi, Inkjet Printing of Carbon Nanotubes, Nanomaterials 3 (2013) 453–468. https://doi.org/10.3390/nano3030453.

[202] S. Huang, B. Maynor, X. Cai, J. Liu, Ultralong, Well-Aligned Single-Walled Carbon Nanotube Architectureson Surfaces, Adv. Mater. 15 (2003) 1651–1655. https://doi.org/10.1002/adma.200305203.

[203] Y. Bai, H. Yue, J. Wang, B. Shen, S. Sun, S. Wang, H. Wang, X. Li, Z. Xu, R. Zhang, F. Wei, Super-durable ultralong carbon nanotubes, Science 369 (2020) 1104–1106. https://doi.org/10.1126/science.aay5220.

[204] Y. Homma, Y. Kobayashi, T. Ogino, T. Yamashita, Growth of suspended carbon nanotube networks on 100-nm-scale silicon pillars, Appl. Phys. Lett. 81 (2002) 2261–2263. https://doi.org/10.1063/1.1507840.

[205] T. Matsumoto, Y. Homma, Y. Kobayashi, Bridging Growth of Single-Walled Carbon Nanotubes on Nanostructures by Low-Pressure Hot-Filament Chemical Vapor Deposition, Jpn. J. Appl. Phys. 44 (2005) 7709. https://doi.org/10.1143/JJAP.44.7709.

[206] Y. Homma, D. Takagi, Y. Kobayashi, Suspended architecture formation process of single-walled carbon nanotubes, Appl. Phys. Lett. 88 (2006) 023115. https://doi.org/10.1063/1.2162799.

[207] Y. Homma, S. Chiashi, Y. Kobayashi, Suspended single-wall carbon nanotubes: synthesis and optical properties, Rep. Prog. Phys. 72 (2009) 066502. https://doi.org/10.1088/0034-4885/72/6/066502.

[208] J. Seo, T.J. Lee, S. Ko, H. Yeo, S. Kim, T. Noh, S. Song, M.M. Sung, H. Lee, Hierarchical and Multifunctional Three-Dimensional Network of Carbon Nanotubes for Microfluidic Applications, Adv. Mater. 24 (2012) 1975–1979.

https://doi.org/10.1002/adma.201104958.

[209] J. Seo, T.J. Lee, C. Lim, S. Lee, C. Rui, D. Ann, S.-B. Lee, H. Lee, A Highly Sensitive and Reliable Strain Sensor Using a Hierarchical 3D and Ordered Network of Carbon Nanotubes, Small 11 (2015) 2990–2994. https://doi.org/10.1002/smll.201401812.

[210] Y. Sun, R. Chen, J. Oh, B. Yoo, H. Lee, Novel synthesis of dual-suspended architectures between Si-pillars for enhanced photocatalytic performance, RSC Adv. 7 (2017) 2880–2883. https://doi.org/10.1039/C6RA25464K.

[211] R. Chen, J. Kang, M. Kang, H. Lee, H. Lee, Silicon Pillar Structure Assisted Three Dimensional Carbon Nanotube Assembly: Fabrications and Rational Surface Modifications, Bull. Chem. Soc. Jpn. 91 (2018) 979–990. https://doi.org/10.1246/bcsj.20180042.

[212] B. Xu, R. Chen, J. Zhou, J. Liang, Recent Progress and Challenges Regarding Carbon Nanotube On-Chip Interconnects, Micromachines 13 (2022) 1148. https://doi.org/10.3390/mi13071148.

[213] H.-Y. Liu, Y. Sun, D.-M. Sun, H.-M. Cheng, Carbon Nanotube 3D Integrated Circuits: From Design to Applications, Adv. Funct. Mater. n/a (n.d.) 2424012. https://doi.org/10.1002/adfm.202424012.

[214] F. Yao, W. Yu, C. Liu, Y. Su, Y. You, H. Ma, R. Qiao, C. Wu, C. Ma, P. Gao, F. Xiao, J. Zhao, X. Bai, Z. Sun, S. Maruyama, F. Wang, J. Zhang, K. Liu, Complete structural characterization of single carbon nanotubes by Rayleigh scattering circular dichroism, Nat. Nanotechnol. 16 (2021) 1073–1078. https://doi.org/10.1038/s41565-021-00953-w.

[215] B.E. Dahneke, Slip correction factors for nonspherical bodies—II free molecule flow, J. Aerosol Sci. 4 (1973) 147–161. https://doi.org/10.1016/0021-

8502(73)90066-9.

[216] G. Timoshenko, S. P. J.N., Theory of Elasticity, McGraw-Hill Educ. (1951).

[217] M. Born, On the stability of crystal lattices. I, Math. Proc. Camb. Philos. Soc. 36 (1940) 160–172. https://doi.org/10.1017/S0305004100017138.

[218] M.M.J. Treacy, T.W. Ebbesen, J.M. Gibson, Exceptionally high Young's modulus observed for individual carbon nanotubes, Nature 381 (1996) 678–680. https://doi.org/10.1038/381678a0.

[219] A. Krishnan, E. Dujardin, T.W. Ebbesen, P.N. Yianilos, M.M.J. Treacy, Young's modulus of single-walled nanotubes, Phys. Rev. B 58 (1998) 14013–14019. https://doi.org/10.1103/PhysRevB.58.14013.

[220] S.S. Rao, Y.F. Fah, Mechanical vibrations, 5. ed. in SI units, Prentice Hall/Pearson, Singapore, 2011.

[221] H. Tanaka, M. Akai-Kasaya, A. TermehYousefi, L. Hong, L. Fu, H. Tamukoh, D. Tanaka, T. Asai, T. Ogawa, A molecular neuromorphic network device consisting of single-walled carbon nanotubes complexed with polyoxometalate, Nat. Commun. 9 (2018) 2693. https://doi.org/10.1038/s41467-018-04886-2.

[222] G. Tanaka, T. Yamane, J.B. Héroux, R. Nakane, N. Kanazawa, S. Takeda, H. Numata, D. Nakano, A. Hirose, Recent advances in physical reservoir computing: A review, Neural Netw. 115 (2019) 100–123. https://doi.org/10.1016/j.neunet.2019.03.005.

[223] D. Banerjee, S. Azhari, Y. Usami, H. Tanaka, Room temperature demonstration of in-materio reservoir computing for optimizing Boolean function with single-walled carbon nanotube/porphyrin-polyoxometalate composite, Appl. Phys. Express 14 (2021) 105003. https://doi.org/10.35848/1882-0786/ac24db.

[224] H. Tanaka, S. Azhari, Y. Usami, D. Banerjee, T. Kotooka, O. Srikimkaew, T.-T. Dang, S. Murazoe, R. Oyabu, K. Kimizuka, M. Hakoshima, In-materio computing in random networks of carbon nanotubes complexed with chemically dynamic molecules: a review, Neuromorphic Comput. Eng. 2 (2022) 022002. https://doi.org/10.1088/2634-4386/ac676a.

[225] S. Azhari, D. Banerjee, T. Kotooka, Y. Usami, H. Tanaka, Influence of junction resistance on spatiotemporal dynamics and reservoir computing performance arising from an SWNT/POM 3D network formed via a scaffold template technique, Nanoscale 15 (2023) 8169–8180. https://doi.org/10.1039/D2NR04619A.

[226] N. Fakhri, D.A. Tsyboulski, L. Cognet, R.B. Weisman, M. Pasquali, Diameter-dependent bending dynamics of single-walled carbon nanotubes in liquids, Proc. Natl. Acad. Sci. 106 (2009) 14219–14223. https://doi.org/10.1073/pnas.0904148106.

[227] C.T. White, T.N. Todorov, Carbon nanotubes as long ballistic conductors, Nature 393 (1998) 240–242. https://doi.org/10.1038/30420.

[228] H. Suzuura, T. Ando, Phonons and electron-phonon scattering in carbon nanotubes, Phys. Rev. B 65 (2002) 235412. https://doi.org/10.1103/PhysRevB.65.235412.

[229] A. Javey, J. Guo, Q. Wang, M. Lundstrom, H. Dai, Ballistic carbon nanotube field-effect transistors, Nature 424 (2003) 654–657. https://doi.org/10.1038/nature01797.

[230] Oxide and Interface Trapped Charges, Oxide Thickness, in: Semicond. Mater. Device Charact., John Wiley & Sons, Ltd, 2005: pp. 319–387. https://doi.org/10.1002/0471749095.ch6.

[231] A.D. Franklin, Z. Chen, Length scaling of carbon nanotube transistors, Nat. Nanotechnol. 5 (2010) 858–862. https://doi.org/10.1038/nnano.2010.220.

[232] B. Chandra, V. Perebeinos, S. Berciaud, J. Katoch, M. Ishigami, P. Kim, T.F. Heinz,

J. Hone, Low Bias Electron Scattering in Structure-Identified Single Wall Carbon Nanotubes: Role of Substrate Polar Phonons, Phys. Rev. Lett. 107 (2011) 146601. https://doi.org/10.1103/PhysRevLett.107.146601.

[233] C. Canali, G. Majni, R. Minder, G. Ottaviani, Electron and hole drift velocity measurements in silicon and their empirical relation to electric field and temperature, IEEE Trans. Electron Devices 22 (1975) 1045–1047. https://doi.org/10.1109/T-ED.1975.18267.

[234] C.R. Dean, A.F. Young, I. Meric, C. Lee, L. Wang, S. Sorgenfrei, K. Watanabe, T. Taniguchi, P. Kim, K.L. Shepard, J. Hone, Boron nitride substrates for high-quality graphene electronics, Nat. Nanotechnol. 5 (2010) 722–726. https://doi.org/10.1038/nnano.2010.172.

[235] A.K. Geim, I.V. Grigorieva, Van der Waals heterostructures, Nature 499 (2013) 419–425. https://doi.org/10.1038/nature12385.

[236] L. Wang, I. Meric, P.Y. Huang, Q. Gao, Y. Gao, H. Tran, T. Taniguchi, K. Watanabe, L.M. Campos, D.A. Muller, J. Guo, P. Kim, J. Hone, K.L. Shepard, C.R. Dean, One-Dimensional Electrical Contact to a Two-Dimensional Material, Science 342 (2013) 614–617. https://doi.org/10.1126/science.1244358.

[237] M. Houssa, A. Dimoulas, A. Molle, 2D Materials for Nanoelectronics, CRC Press, 2016.

[238] J.-W. Huang, C. Pan, S. Tran, B. Cheng, K. Watanabe, T. Taniguchi, C.N. Lau, M. Bockrath, Superior Current Carrying Capacity of Boron Nitride Encapsulated Carbon Nanotubes with Zero-Dimensional Contacts, Nano Lett. 15 (2015) 6836–6840. https://doi.org/10.1021/acs.nanolett.5b02716.

[239] A. Baumgartner, G. Abulizi, K. Watanabe, T. Taniguchi, J. Gramich, C. Schönenberger, Carbon nanotube quantum dots on hexagonal boron nitride, Appl.

Phys. Lett. 105 (2014) 023111. https://doi.org/10.1063/1.4890600.

[240] K. Otsuka, T. Sugihara, T. Inoue, W. Jia, S. Matsushita, T. Saito, M. Lee, T. Taniguchi, K. Watanabe, G. Pitner, M.-Y. Li, T.-A. Chao, R. Xiang, S. Chiashi, S. Maruyama, Coaxial boron nitride nanotubes as interfacial dielectric layers to lower interface trap density in carbon nanotube transistors, Nano Res. 16 (2023) 12840–12848. https://doi.org/10.1007/s12274-023-6241-6.

[241] N. Fang, K. Otsuka, A. Ishii, T. Taniguchi, K. Watanabe, K. Nagashio, Y.K. Kato, Hexagonal Boron Nitride As an Ideal Substrate for Carbon Nanotube Photonics, ACS Photonics 7 (2020) 1773–1779. https://doi.org/10.1021/acsphotonics.0c00406.

[242] Q. Gao, J. Chen, B. Lyu, A. Deng, L. Wang, T. Wu, K. Watanabe, T. Taniguchi, Z. Shi, Detection of chirality of single-walled carbon nanotubes on hexagonal boron nitride, Appl. Phys. Lett. 117 (2020) 023101. https://doi.org/10.1063/5.0005831.

[243] S. Zhao, S. Yoo, S. Wang, B. Lyu, S. Kahn, F. Wu, Z. Zhao, D. Cui, W. Zhao, Y. Yoon, M.I.B. Utama, W. Shi, K. Watanabe, T. Taniguchi, M.F. Crommie, Z. Shi, C. Zhou, F. Wang, Tunneling Spectroscopy in Carbon Nanotube-Hexagonal Boron Nitride-Carbon Nanotube Heterojunctions, Nano Lett. 20 (2020) 6712–6718. https://doi.org/10.1021/acs.nanolett.0c02585.

[244] K. Glasmästar, J. Gold, A.-S. Andersson, D.S. Sutherland, B. Kasemo, Silicone Transfer during Microcontact Printing, Langmuir 19 (2003) 5475–5483. https://doi.org/10.1021/la026558x.

[245] A.L. Briseno, M. Roberts, M.-M. Ling, H. Moon, E.J. Nemanick, Z. Bao, Patterning Organic Semiconductors Using “Dry” Poly(dimethylsiloxane) Elastomeric Stamps for Thin Film Transistors, J. Am. Chem. Soc. 128 (2006) 3880–3881. https://doi.org/10.1021/ja058226v.

[246] R. Alizadegan, A.D. Liao, F. Xiong, E. Pop, K.J. Hsia, Effects of tip-nanotube interactions on atomic force microscopy imaging of carbon nanotubes, Nano Res. 5 (2012) 235–247. https://doi.org/10.1007/s12274-012-0203-8.

[247] D. Vobornik, M. Chen, S. Zou, G.P. Lopinski, Measuring the Diameter of Single-Wall Carbon Nanotubes Using AFM, Nanomaterials 13 (2023) 477. https://doi.org/10.3390/nano13030477.

[248] Z. Chen, J. Appenzeller, J. Knoch, Y. Lin, P. Avouris, The Role of Metal−Nanotube Contact in the Performance of Carbon Nanotube Field-Effect Transistors, Nano Lett. 5 (2005) 1497–1502. https://doi.org/10.1021/nl0508624.

[249] P. Sundqvist, F.J. Garcia-Vidal, F. Flores, M. Moreno-Moreno, C. Gómez-Navarro, J.S. Bunch, J. Gómez-Herrero, Voltage and Length-Dependent Phase Diagram of the Electronic Transport in Carbon Nanotubes, Nano Lett. 7 (2007) 2568–2573. https://doi.org/10.1021/nl070746w.

[250] Jianshi Tang, D. Farmer, S. Bangsaruntip, Kuan-Chang Chiu, B. Kumar, Shu-Jen Han, Contact engineering and channel doping for robust carbon nanotube NFETs, in: 2017 Int. Symp. VLSI Technol. Syst. Appl. VLSI-TSA, IEEE, Hsinchu, Taiwan, 2017: pp. 1–2. https://doi.org/10.1109/VLSI-TSA.2017.7942478.

[251] C. Klinke, J. Chen, A. Afzali, P. Avouris, Charge Transfer Induced Polarity Switching in Carbon Nanotube Transistors, Nano Lett. 5 (2005) 555–558. https://doi.org/10.1021/nl048055c.

[252] S. Ilani, L. a. K. Donev, M. Kindermann, P.L. McEuen, Measurement of the quantum capacitance of interacting electrons in carbon nanotubes, Nat. Phys. 2 (2006) 687–691. https://doi.org/10.1038/nphys412.

[253] Sadiku M N O, Nelatury S. Elements of electromagnetics[M]. New York: Oxford university press, 2001. (accessed October 26, 2025).

[254] X. Zhou, Band Structure, Phonon Scattering, and the Performance Limit of Single-Walled Carbon Nanotube Transistors, Phys. Rev. Lett. 95 (2005). https://doi.org/10.1103/PhysRevLett.95.146805.

[255] F. Léonard, J. Tersoff, Role of Fermi-Level Pinning in Nanotube Schottky Diodes, Phys. Rev. Lett. 84 (2000) 4693–4696. https://doi.org/10.1103/PhysRevLett.84.4693.

[256] J. Svensson, E.E.B. Campbell, Schottky barriers in carbon nanotube-metal contacts, J. Appl. Phys. 110 (2011) 111101. https://doi.org/10.1063/1.3664139.

[257] C. Zhou, J. Kong, H. Dai, Intrinsic Electrical Properties of Individual Single-Walled Carbon Nanotubes with Small Band Gaps, Phys. Rev. Lett. 84 (2000) 5604–5607. https://doi.org/10.1103/PhysRevLett.84.5604.

[258] N.A. Lanzillo, N. Kharche, S.K. Nayak, Substrate-induced Band Gap Renormalization in Semiconducting Carbon Nanotubes, Sci. Rep. 4 (2014) 3609. https://doi.org/10.1038/srep03609.

[259] X. Zhou, J. Xie, G. Li, J. Zhang, M. Xia, W. Luo, Z. Shi, Moiré-induced band-gap opening in one-dimensional superlattices of carbon nanotubes on hexagonal boron nitride, Phys. Rev. B 105 (2022) 115433. https://doi.org/10.1103/PhysRevB.105.115433.

[260] E.A. Laird, F. Kuemmeth, G.A. Steele, K. Grove-Rasmussen, J. Nygård, K. Flensberg, L.P. Kouwenhoven, Quantum transport in carbon nanotubes, Rev. Mod. Phys. 87 (2015) 703–764. https://doi.org/10.1103/RevModPhys.87.703.

[261] G. Xu, C.M.Jr. Torres, Y. Zhang, F. Liu, E.B. Song, M. Wang, Y. Zhou, C. Zeng, K.L. Wang, Effect of Spatial Charge Inhomogeneity on 1/f Noise Behavior in Graphene, Nano Lett. 10 (2010) 3312–3317. https://doi.org/10.1021/nl100985z.

[262] M. Tamaoki, S. Kishimoto, Y. Ohno, T. Mizutani, Electrical properties of the

graphitic carbon contacts on carbon nanotube field effect transistors, Appl. Phys. Lett. 101 (2012) 033101. https://doi.org/10.1063/1.4737169.

List of publications

Relating publications to this dissertation:

1. **Yuanjia Liu**, Taiki Inoue, Mengyue Wang, Michiharu Arifuku, Noriko Kiyoyanagi, Yoshihiro Kobayashi. "**Gas-flow-directed growth of aligned carbon nanotubes from nonmetallic seeds**", Carbon, **214** (2023) 118309.

   DOI: 10.1016/j.carbon.2023.118309

2. **Yuanjia Liu**, Taiki Inoue, Yoshihiro Kobayashi. "**Crossover Between Kite Growth and Vibrational Bridging in Pillar-Assisted Controlled Formation of Carbon Nanotube Networks Towards Nanoscale Interconnections**", ACS Appl. Nano Mater., accepted for publication (19 Aug. 2025).

   DOI: 10.1021/acsanm.5c03056

3. **Yuanjia Liu**, Taiki Inoue, Yoshihiro Kobayashi. "**Substrate-dependent electrical transport in individual single-walled carbon nanotubes grown across SiO_2 and hexagonal boron nitride**". In preparation.

Co-author:

1. Mengyue Wang, **Yuanjia Liu**, Manaka Maekawa, Michiharu Arifuku, Noriko Kiyoyanagi, Taiki Inoue, Yoshihiro Kobayashi. " **Combination effect of growth enhancers and carbon sources on synthesis of single-walled carbon nanotubes from solid carbon growth seeds**", Diam. Relat. Mater., **130** (2022) 109516.

   DOI: 10.1016/j.diamond.2022.109516

2. Mengyue Wang, Manaka Maekawa, Man Shen, **Yuanjia Liu**, Michiharu Arifuku, Noriko Kiyoyanagi, Taiki Inoue, Yoshihiro Kobayashi. " **Thermal defect healing of single-walled carbon nanotubes assisted by supplying carbon-containing reactants**", Appl. Phys. Exp. **16** (2023) 015002.

DOI: 10.35848/1882-0786/acaaec

3. Man Shen, Taiki Inoue, Mengyue Wang, **Yuanjia Liu**, Yoshihiro Kobayashi. " **Efficient defect healing of single-walled carbon nanotubes through C2H2-assisted multiple-cycle treatment with air exposure**", ACS Appl. Mater. Interfaces, **17** (2025) 20105-20115.

DOI: 10.1021/acsami.5c00619

List of conferences

International conferences:

1. **Yuanjia Liu**, Michiharu Arifuku, Noriko Kiyoyanagi, Masamitsu Satake, Taiki Inoue, Yoshihiro Kobayashi. “Kite-growth of long, aligned carbon nanotubes from non-metallic growth seeds”, The 22nd Int. Conf. on the Science and Applications of Nanotubes and Low-Dimensional Materials (NT-22), Suwon, Korea and online (June 19-24, 2022). (Poster)

Domestic conferences:

1. **劉 元嘉**, 井ノ上泰輝, 小林慶裕. “カイト成長による単一カーボンナノチューブ多チャネルデバイスを用いた環境影響下での輸送特性評価”, 2025 年 第 86 回 応用物理学会 秋季学術講演会（名城大学天白キャンパス＆オンライン、2025 年 9 月 7−10 日）(Poster)
2. **劉 元嘉**, 井ノ上泰輝, 小林慶裕. “カイト成長メカニズムを利用したナノピラー配列上のカーボンナノチューブランダムネットワーク形成の統計解析と流体シミュレーション″, 2025 年第 72 回応用物理学会 春季学術講演会（東京理科大野田キャンパス＆オンライン、2025 年 3 月 14−17 日）(Poster)
3. **劉 元嘉**, 井ノ上泰輝, 小林慶裕. “Random network formation of carbon nanotubes suspended between nano-pillars via kite-growth mechanism”, 2024 年 第 85 回応用物理学会秋季学術講演会（朱鷺メッセ・新潟コンベンションセンター＆オンライン、2024 年 9 月 16−20 日）(Oral)
4. **Yuanjia Liu**, Taiki Inoue, Michiharu Arifuku, Noriko Kiyoyanagi, Masamitsu Satake, Yoshihiro Kobayashi. “Microscopic analysis of aligned carbon nanotubes: evidence for the first observation of kite-growth from non-metallic seeds”, 2022 年第 83 回応用物理学会秋季学術講演会（東北大学河内北キャンパス＆オンライン、2022 年 9 月 20−23 日）. (Oral)
5. **Yuanjia Liu**, Taiki Inoue, Michiharu Arifuku, Noriko Kiyoyanagi, Masamitsu Satake, Yoshihiro Kobayashi. “Synthesis of aligned carbon nanotubes from nanodiamond seeds by

kite-growth mechanism", The 62nd Fullerenes-Nanotubes-Graphene General Symposium（Nagoya University、Mar.2(Wed)-Mar.4(Fri), 2022 ）. (Poster)

6. **Yuanjia Liu**, Taiki Inoue, Michiharu Arifuku, Noriko Kiyoyanagi, Masamitsu Satake, Yoshihiro Kobayashi. "Synthesis of aligned carbon nanotube from nanodiamond seeds by kite-growth mechanism", 応用物理学会関西支部 2021 年度第 2 回講演会（オンライン、2021 年 10 月 5 日） (Poster)

Co-author:

1. Mengyue Wang, **Yuanjia Liu**, Manaka Maekawa, Michiharu Arifuku, Noriko Kiyoyanagi, Masamitsu Satake, Taiki Inoue, Yoshihiro Kobayashi. "Effect of CO2 in high temperature SWCNT growth from solid carbon growth seeds", The 22nd Int. Conf. on the Science and Applications of Nanotubes and Low-Dimensional Materials (NT-22), Suwon, Korea and online (June 19-24, 2022).
2. Man Shen, **Yuanjia Liu**, Taiki Inoue, Yoshihiro Kobayashi. "Multiple-step defect healing of single-walled carbon nanotubes in reactive environment", 2024 年 第 71 回 応用物理学会春季学術講演会（東京都市大学世田谷キャンパス＆オンライン、2024 年 3 月 22-25 日）.
3. Man Shen, Mengyue Wang, **Yuanjia Liu**, Taiki Inoue, Yoshihiro Kobayashi. "Thermal defect healing of carbon nanotubes using a combination of carbon feedstock and etchant", The 65th Fullerenes-Nanotubes-Graphene General Symposium (Nishijin Plaza, Kyushu University, Sep.4-Sep.6, 2023).
4. Man Shen, Mengyue Wang, **Yuanjia Liu**, Manaka Maekawa, Taiki Inoue. "Assistive effects of carbon feedstock and etchant on defect healing of carbon nanotubes by thermal process", 2023 年第 70 回応用物理学会春季学術講演会（上智大学四谷キャンパス＋オンライン、2023 年 3 月 15-18 日）.

Acknowledgments

First and foremost, I would like to express my sincere gratitude to all those who have guided, supported, and encouraged me throughout my doctoral studies. Their generous assistance and continuous encouragement have played an essential role in both my academic development and personal growth.

I am deeply grateful to Professor Kobayashi for his outstanding supervision and unwavering support during my doctoral program. His profound knowledge, insightful guidance, and constant encouragement have been a tremendous source of inspiration throughout my research on carbon nanotubes. His trust and patience allowed me to explore scientific problems independently while providing clear direction whenever it was needed. I sincerely appreciate the time and effort he devoted to my academic training.

I would also like to express my heartfelt thanks to Assistant Professor Inoue for his careful guidance and thoughtful advice. His broad expertise and clear explanations helped me overcome many experimental and conceptual challenges. In particular, his detailed feedback greatly improved my scientific thinking and scientific writing, and I am truly grateful for his continuous support.

I would like to acknowledge Nippon Kayaku for generously providing nanodiamond materials used in this study. Their support contributed to the exploration of material-related effects in carbon nanotube devices and was an important component of this research.

I also gratefully acknowledge the use of shared experimental facilities and technical support provided by the University of Osaka. Access to advanced characterization and nanofabrication facilities was essential for the successful completion of this research. I further acknowledge financial support from competitive research funding programs in Japan, which enabled the progress of this work.

I am deeply grateful to the professors who served as examiners of my doctoral dissertation. Their careful reading, insightful comments, and constructive suggestions significantly improved the clarity, depth, and overall quality of this thesis.

I would also like to thank all my colleagues in the laboratory for creating a supportive and stimulating research environment. In particular, I am grateful to Ms. Wang, and Mr. Shen for their collaboration and discussions, which were invaluable in overcoming experimental difficulties. I also wish to thank Mr. Ding, Ms. Yao, Mr. Xu, Mr. Zhou, Mr. Li, Mr. Wei, Mr. Akamatsu, Mr. Suzuki, Mr. Hirai, Mr. Hayato Watanabe, Mr. Yoshida, Mr. Atsutaka Watanabe, Mr. Shimizu, Mr. Mizuno, Mr. Ikeda, Mr. Kamei, Mr. Sakamoto, Mr. Toda, Ms. Himura, Ms. Maekawa, Mr. Kato, Mr. Kikudo, Ms. Ishiguro, Mr. Tsutsumi, Mr. Nishikawa, Mr. Yura, Mr. Keisuke Nakamura and Mr. Shingo Nakamura, for their kind cooperation and support, which made our laboratory a productive and welcoming place. I would like to give special thanks to Ms. Yao for his encouragement and thoughtful care, which helped me feel at ease while pursuing my studies abroad.

Finally, I would like to express my deepest gratitude to everyone who has supported me throughout this academic journey. Your guidance, encouragement, and kindness have helped me overcome challenges, broaden my perspective, and continue striving toward future goals. This work would not have been possible without your selfless support.

Thank you all from the bottom of my heart.